NIST GCR 04-861

Simultaneous Measurements of Drop Size and Velocity in Large-Scale Sprinkler Flows Using Particle Tracking and Laser-Induced Fluorescence

Anthony D. Putorti, Jr.
Department of Mechanical Engineering
University of Michigan
Ann Arbor, MI 48109-2125

National Institute of Standards and Technology
Technology Administration, U.S. Department of Commerce

NIST GCR 04-861

Simultaneous Measurements of Drop Size and Velocity in Large-Scale Sprinkler Flows Using Particle Tracking and Laser-Induced Fluorescence

Prepared for
U.S. Department of Commerce
Building and Fire Research Laboratory
National Institute of Standards and Technology
Gaithersburg, MD 20899-8661

February 2004

U.S. Department of Commerce
Donald L. Evans, Secretary

Technology Administration
Phillip J. Bond, Under Secretary for Technology

National Institute of Standards and Technology
Arden L. Bement, Jr., Director

Notice

This report was prepared for the Building and Fire Research Laboratory of the National Institute of Standards and Technology under Grant number 60NANB8D0080. The statement and conclusions contained in this report are those of the authors and do not necessarily reflect the views of the National Institute of Standards and Technology or the Building and Fire Research Laboratory.

SIMULTANEOUS MEASUREMENTS OF DROP SIZE AND VELOCITY IN LARGE-SCALE SPRINKLER FLOWS USING PARTICLE TRACKING AND LASER-INDUCED FLUORESCENCE

by

Anthony Demetrio Putorti Jr.

A dissertation submitted in partial fulfillment
of the requirements for the degree of
Doctor of Philosophy
(Mechanical Engineering)
in The University of Michigan
2004

Doctoral Committee:
- Professor Arvind Atreya, Chair
- Professor Michael M. Chen
- Professor Gerard M. Faeth
- Associate Professor Margaret S. Wooldridge
- Howard Baum, National Institute of Standards and Technology
- Kevin B. McGrattan, National Institute of Standards and Technology

ACKNOWLEDGEMENTS

The author would like to thank the Fire Research Division of the National Institute of Standards and Technology’s Building and Fire Research Laboratory for support of this work. This includes Division Chiefs David Evans and William Grosshandler, as well as Daniel Madrzykowski, the grant supervisor, and Anthony Hamins, the manager of the Advanced Measurement and Prediction Methods program. The various group leaders over the years that provided the workplace flexibility to conduct this investigation were Daniel Madrzykowski, George Mulholland, and Nelson Bryner. The author also grateful for the assistance provided by Jay McElroy, Laurean DeLauter, Gary Roadarmel, and William Twilley in laboratory construction. Jack Lee provided assistance in conducting the measurements of sprinkler water flux. Kazuki Shiozawa provided assistance in conducting some of the experiments, and automated the extraction of raw data from the sprinkler images. Many thanks to Arvind Atreya for advice and guidance through the entire degree process, and the doctoral committee for providing input into this research. The support and encouragement of the Large Fire/Firefighting Technology Group is greatly appreciated. Most of all, this effort would not have been possible without the love, support, and encouragement of my family and wife Patti.

ABSTRACT

Automatic fire sprinkler systems greatly reduce fire losses and deaths. While sprinklers provide an estimated 75% reduction in death rate within residential structures, they are installed in less than 2% of new U.S. homes. A major impediment is sprinkler system cost, which can be reduced by optimization of the water flux distribution to the burning surfaces. If sprinkler drop size and velocity distributions are known, water flux distributions can be predicted. Existing measurement techniques, however, are incapable of large scale simultaneous measurement of droplet size and velocity, and cannot operate in fire environments.

The Particle Tracking Velocimetry and Imaging (PTVI) technique was developed to provide large-scale, simultaneous, non-intrusive measurement of droplet size and velocity in two phase flows. The apparatus illuminates a 0.5 m by 0.5 m region of the spray field with two consecutive laser sheet pulses of different wavelengths. Dyes in the water fluoresce in two different colors, resulting in two differentiable color images for each drop, which are recorded by a camera. Drop velocity is determined from the distance traveled in the time between the pulses, and size from the areas of the droplet images. Droplet sizes from 200 μm to 3000 μm, and velocities from 1 m/s to 30 m/s have been measured with low uncertainty. While not studied here, the PTVI technique is general enough to measure many types of two-phase flows, such as those that occur in fire environments, engines, and manufacturing processes.

Droplet sizes and velocities from axis-symmetrical sprinkler sprays were measured using the PTVI technique. Water flux distributions on the floor under the sprinkler were calculated using droplet trajectories, and agreed with measured water fluxes when entrainment could be neglected. Agreement also occurred when the droplets were assumed to start at the sprinkler and at the speed of the water exiting the sprinkler, suggesting that the sheet breakup region and mechanism can be ignored. Scaling parameters are suggested for droplet trajectory analysis. These developments simplify the prediction of water flux distribution and allow for the changing of sprinkler parameters to produce desired water distributions.

TABLE OF CONTENTS

LIST OF FIGURES

LIST OF TABLES

LIST OF APPENDICES

CHAPTER 1

INTRODUCTION

Automatic fire sprinkler systems in structures not only provide fire detection, but also offer fire suppression or extinguishment. Sprinkler systems greatly reduce fire deaths and losses, with average deaths and losses in sprinklered buildings being 1/2 to 2/3 less than in non-sprinklered buildings. The impact of sprinklers is even greater in homes, where they provide an estimated 75% reduction in death rate (Rohr 2001). Overall, statistics for the United States show that approximately 400,000 fires were reported in 2001 within residential structures, causing 3745 fire deaths (83% of all U.S. fire deaths) and $8.9 Billion in direct fire property damage (63% of total U.S. fire losses), excluding the 9/11 attacks (Karter Jr. 2002). Even with the benefits residential sprinklers provide, they are installed in less than 2% of new U.S. homes (Milke 2003).

One of the major impediments to the use of sprinkler systems, especially residential systems, is water supply availability and cost. The more efficient a sprinkler system, the less water is needed, potentially decreasing the required water flux and reducing the quantity and size of piping. An optimum sprinkler system for a given application will apply the maximum amount of water spray to the burning surface(s) and suppress the fire in the shortest amount of time after ignition. The design of a sprinkler system depends on the geometrical relationships between the sprinkler(s) and the fire source(s), the fire heat release rate, the geometry of the room, ventilation conditions, and the sprinkler spray characteristics. A well designed sprinkler system not only reduces costs, but provides a higher level of suppression performance. At the current time, full-scale fire experiments are used to determine sprinkler effectiveness.

In order to optimize the design of a sprinkler system, the characteristics of the sprinkler spray field are needed. This data typically consists of the distribution of droplet sizes and velocities within the sprinkler spray. The breakup of the water sheet exiting the sprinkler, however, is not completely understood in the literature, and droplet size and velocity can not be predicted to a high level of certainty. Droplet size and velocity data have been gathered in the past by many investigators, but the data currently available are time averaged point measurements that do not provide the instantaneous spatial drop distribution in the spray. Consequently, the spray must be considered time invariant, and a large number of measurements must be taken at different points to determine the drop size distribution. It is very important to note that existing measurement techniques are also incapable of operating in a fire environment.

In addition to knowing the droplet size and velocity distributions from a sprinkler, the final destinations of the droplets are also of interest. Depending on the attributes of the droplets, water from the sprinkler may reach the floor or burning surface, and apply a water flux distribution. The droplet travel process can be scaled, and the trajectories of the droplets predicted. The scaling is valuable since it gives insight into the important parameters of the process. Once verified, scaling rules can be used to predict the results of large scale experiments by conducting small scale experiments. Scaling is particularly valuable in fire research due to the high costs of conducting large scale experiments.

Fire models can be used to predict sprinkler activation, fire suppression, and the conditions within the structure during a fire event. In order to predict multiple sprinkler activation, the interaction of fire plumes and sprinkler sprays, and the suppression of fires by sprinklers, high quality input and validation data are needed. This includes droplet size and velocity data for the sprinkler spray. Due to the large number of sprinkler configurations and models currently in use, general sprinkler criteria for approximating the droplet size and velocity distributions would be useful. Once in flight, the trajectories of the droplets can be predicted using models that include the effects of entrainment and evaporation. Due to a lack of verification data, it is unclear as to whether the calculations and assumptions involved are correctly predicting their flight. Advanced techniques, capable of simultaneously measuring large scale unsteady droplet size and velocity distributions, are clearly needed.

The ideal measurement method would be non-intrusive, and provide droplet size and velocity distributions with a low level of uncertainty. The method would also provide data over a large area instantaneously, so that large scale unsteady behaviors could be studied. This data could be directly compared with water sheet breakup predictions, used as sprinkler input data, or used to verify the droplet trajectories predicted by fire models. The Particle Tracking Velocimetry and Imaging (PTVI) technique developed as part of this work, and described in this thesis, meets these requirements.

Using the measured droplet size and velocity data from the PTVI technique developed in this work, the trajectories of the droplets are predicted. These trajectories result in predicted water flux distributions to the floor under the sprinkler, and compare favorably with measured water flux distributions.

In the future, these techniques can be applied to myriad problems. The methods are applicable to the measurement of droplet size and velocity from fire sprinklers and firefighter hose streams, the measurement of sprinkler and fire flow interaction, and the prediction of sprinkler water distribution. This information may be used to better understand the flows associated with sprinklers and fires, to provide input data and validation data for field models, and provide insight into sprinkler design. The PTVI technique is also general enough to measure many types of two-phase flows, such as those that occur in engines and in manufacturing processes.

CHAPTER 2

BACKGROUND

2.1 Fire Models

Fire protection engineers and fire researchers have employed room fire models for decades to help understand the spread of fire and combustion products in structures. These models are not only a research tool, but are used to conduct fire hazard analyses, design fire protection systems, and to help investigate fire incidents. The most commonly utilized fire models are zone models, which break up building compartments into a hot upper layer and a cool lower layer. Zone models assume that the conditions within each layer are homogeneous, so transit times are neglected. A fire subroutine within the model is responsible for transferring heat, mass, and combustion products from the fire and lower layer into the upper layer. Mechanisms are also included for moving mass and energy from room to room, and for heat losses through openings and boundaries. The user generally inputs a function that defines the heat release rate of the fire over time since the fire growth itself is not predicted. The zone models are typically used to predict the movement of hot gases through the structure, i.e. the height and temperature of the hot layer, and to predict the activation of fire detectors or a sprinkler. They are limited to predicting the activation of the first sprinkler due to their use of empirically based ceiling jet correlations.

The increasing capabilities and decreasing costs of computer technology have made it possible for researchers to create Computational Fluid Dynamics (CFD) based fire models of increasing complexity. CFD based models, also known as field models, operate by solving the fundamental equations of mass conservation, energy conservation, momentum conservation, and species conservation for the cells within the modeled space. Some of these models have advanced to the point where they contain combustion algorithms, which allow combustion to occur at locations where suitable fuel, oxidizer, and temperatures are present. In addition, the flows induced by a fire, as well as the impact of the fire and combustion products on the environment or on an enclosure are predicted. Fire protection engineers and fire researchers have been eager to apply the increased model capabilities to more complex scenarios with better resolution than was previously available with zone fire models. Versions of a Large Eddy Simulation (LES), a CFD model developed at the National Institute of Standards and Technology (NIST), have been released to the public. The ALOFT model is available for downrange dispersion of pollutants in the environment (Walton et. al. 1996, 1998), and the Fire Dynamics Simulator (FDS) is available for fire flows in compartments (McGrattan et al. 2002; McGrattan and Forney 2002).

The widespread use of CFD models for fire environment prediction has been accompanied by the desire for more sophisticated modeling of fire suppression. While interest in suppression has been around for quite some time, it has traditionally been studied by conducting full scale fire testing. Relating small scale suppression experiments to full scale scenarios has proved difficult, although progress is being made. (McGrattan, Hamins, Blevins 1998) Full scale experiments are still necessary, however, to gauge the overall effectiveness of sprinklers. Only recently have advances in technology allowed modeling of large spaces using cells with length scales small enough to incorporate fire suppression by sprinklers in adequate detail. The prediction of multiple sprinkler activation was of particular interest recently, with CFD modeling serving as a valuable tool. (McGrattan, Hamins, and Evans 1998)

In order to predict multiple sprinkler activation, the interaction of fire plumes and sprinkler sprays, and the suppression of fires by sprinklers, high quality input and validation data are needed. Field models such as FDS require the initial droplet size and velocity to be prescribed. At the current time, the sprinkler drops are assumed to be spherical, and experimental data for industrial sprinklers is used (Chan 1994; You 1986). The droplet size distributions for sprinklers are represented by a combination of log-normal and Rosin-Rammler distributions. The size distribution information is derived from measurements made with the Particle Measuring Systems (PMS) Optical Array Probe (OAP) device, to be described in detail later. Recently, drop size and velocity data for use in FDS have become available for industrial sprinklers using Particle Induced Velocimetry (PIV) and Phase Doppler Interferometry (PDI) (Sheppard 2002; Sheppard and Lueptow 2003). Drop size distributions from commercial sprinklers were also used in the past to study other fire scenarios. (Madrzykowski and Vettori 2000; Putorti Jr., Belsinger, and Twilley 1995)

When FDS predicts that a sprinkler has activated and begins to discharge water, representative droplets are tracked. Droplet size is randomly selected from a probability density function (PDF) constructed from the sprinkler data. The model calculates the droplet trajectory, as well as the momentum transfer from the droplets to the surrounding air. Droplet evaporation is predicted using a heat balance including convective and radiative heat transfer to a sphere and the latent heat of evaporation for water. FDS has shown good agreement with the data in large scale fire experiments; although a lack of precise large scale fire test data has limited validation efforts. The PTVI technique can be used to gather high quality input and validation data.

2.2 Existing Droplet Measurement Techniques

There are many methods currently available for measuring the size and/or velocity distributions of water sprays from fire sprinklers, and each has benefits and limitations. One method is oil capture, where a pan of viscous oil is exposed to the droplet spray. Once trapped in the oil, the droplets are measured with a microscope. This method provides droplet size, but not velocity data. The technique is effectively a point measurement given the large scale of the sprinkler sprays with which we are interested (on the order of meters).

A historically popular device for droplet sizing and velocity measurement is the Optical Array Probe (OAP), available from Particle Measuring Systems (PMS). This device employs an imaging method, where droplets passing through a laser beam measurement volume are imaged on a one-dimensional segmented line detector array. The droplet will shadow some number of the components of the detector array, thereby providing size information. The array is scanned temporally, providing the second dimension of the drop, as well as the speed. The optical array probe measures one component of the velocity, so the direction of the drops must be known beforehand. Due to limitations of instrument design, the device is easily overwhelmed by heavy sprinkler flows. Its design also favors smaller droplets over larger droplets due to the greater likelihood of a larger droplet image overlapping the edge of the measurement volume and being rejected. Although there are few large droplets, the impact of these drops on the size statistics is magnified by the large volume of water within. The optical array probe is also very intrusive, and provides point measurements given the scale of the sprinkler spray.

The optical array probe was used in the past at NIST to measure the droplet size and velocity distributions of fire sprinklers. The NIST data was gathered for sprinklers designed for use in light commercial facilities such as offices, and water mist type sprinklers for use in light hazard, residential, and marine applications. The probe is also in use at the University of California, Fresno for agricultural sprinklers, and at Factory Mutual Research Corporation (FMRC) for industrial fire sprinklers. The facility in Fresno has an algorithm designed to account for the large drop statistical challenges, but it is unclear whether the corrections have been verified with polydisperse droplet distributions. (Solomon, Zoldoske, and Oliphant 1996) The data incorporated into the LES models in the past was from experiments conducted at FMRC and at NIST.

A very popular droplet size measurement device (Malvern) operates by measuring the Fraunhofer diffraction patterns produced when droplets interact with a monochromatic light source. The commercially available device includes a computerized analysis package, which is capable of rapid data collection and analysis. The Malvern device conducts a line measurement, where the results are integrated over a line of sight. Conversion to point type measurements is possible by using a deconvolution algorithm. (Dodge 1987) Limitations of the device for our purposes include a lack of velocity data and size data that are limited to integrated lines or deconvoluted points. It is unclear whether the device would be non-intrusive if applied to fire sprinklers due to the long line of sight that would be necessary.

Laser Doppler Velocimetry (LDV) is a commercially available, non-intrusive, velocity measurement technology that has seen much use in the combustion arena. It operates on the principle of Doppler shift, where a particle passing through a small measurement volume formed by the intersection of two laser beams causes a frequency shift, the magnitude of which is related to the particle velocity. The significant drawback of LDV for our application is that it is a point measurement. While it is capable of providing a rapid number of measurements at a particular point in space, and is therefore capturing unsteady behavior, it does not provide instantaneous droplet velocities over a large region. LDV could be set up to scan a large area, but it would become an averaging measurement, which would assume steady flow conditions.

Phase Doppler Interferometry (PDI) measures drop size and velocity by illuminating droplets with laser light, then detecting and analyzing the scattered light signal. The light from two incident laser beams scatters off of the droplets, forming fringe patterns. The spatial frequencies of the fringe patterns are inversely related to the drop diameter. As in LDV, the temporal frequency is related to the velocity of the droplet. This relatively non-intrusive point measurement technique works well for spherical droplets, and has a large measurement size range, from approximately 0.5 μm to 3000 μm. (Lefebvre 1989) Sprinkler droplets, however, are not always spherical as will be seen in the images discussed later in this thesis.

PDI measurements of sprinkler drop size and velocity were recently conducted at NIST. (Widmann 2000) The investigator reported good results in measuring the droplet size distributions and velocities from a residential fire sprinkler. The reported combined standard uncertanties of these measurements was less than 10%. Whether or not the entire sprinkler spray is characterized by the measured distributions and associated uncertainties is open to debate, however. PDI relies on point measurements being made at various places in the sprinkler flow, with the results temporally and spatially averaged. The use of point measurements for determining the attributes of actual fire sprinklers is severely limited by several factors. First of all, a real sprinkler is an unsymmetrical and unsteady device. Qualitatively, there are certain areas of the spray pattern that are much denser than other areas. In addition, there are small areas that contain drastically different drop sizes than the bulk of the spray. These areas may be described as fingers. In order to obtain meaningful average bulk properties of the spray, a tremendous number of point measurements would be required within the three-dimensional spray field. These limitations apply to all of the point measurement techniques.

The size distribution of droplets may be measured by using the shadowgraph method. Available from Bete Fog Nozzle Corp., this method utilizes a strobe light and video camera to form a shadow image of the measurement area and the droplets therein. The size range that can be measured depends on the optical magnification chosen for the system. Previous tests with common fire sprinklers were conducted with a measurement range of 100 μm to 2000 μm with some success. (Lawson, Walton, and Evans 1988) Since this is an imaging technique, non spherical droplets can be identified and measured, but the analysis system converts them to a representative spherical droplet. Difficulties with this method include out-of-focus droplets and multiple droplets in the depth of field imaged on top of one another. Investigators indicated that the device did not provide accurate determinations of velocity due to the inability of the device to adequately match droplet pairs. Droplet sizing was successful, but required frequent operator involvement to separate overlapping droplet images.

Particle imaging velocimetry (PIV) is another commercially available non-intrusive velocity measurement technique frequently used in combustion research. A planar measurement region is sequentially illuminated with two laser sheet pulses. Laser light scattering off the particles within the region is captured by a camera perpendicular to the measurement region. By controlling the time between laser pulses, Δt, and measuring the distance and direction the particles have traveled, their velocities can be determined. Since Δt is small, on the order of milliseconds, the measurements are nearly instantaneous for typical time scales of interest.

In typical PIV applications, the velocities of individual particles are not directly measured. Instead, the camera images are broken up into square interrogation regions, each containing a large number of particles (There are two images of each particle, one at time t, and the second at time $t+\Delta t$). The locations of the particle images within each interrogation region are recorded, and an algorithm is used to compile a matrix of possible particle velocities. This matrix is formed by determining a spatial translation (displacement) vector between each particle image in the interrogation region and every other particle image in the interrogation region. The two translations with the highest frequency of occurrence, divided by Δt, are the forward velocity and the reverse velocity of the interrogation region. These two velocities have the same frequency of occurrence and magnitude, but their directions are 180 degrees apart. If two camera images of the measurement area were recorded, one for each laser pulse, the directional ambiguity is resolved by knowing which image was taken first. If a double exposed camera image was used to capture the light from both laser pulses, the direction of the flow must be known beforehand. It is important to note that the velocity of individual particles is not measured; only the representative velocities of the interrogation regions within the measurement region are reported.

At the current time, off the shelf PIV systems are typically limited to measurement areas on the order of centimeters due to resolution and signal level limitations. Recently, however, PIV has been successfully used for velocity measurement on 0.3 m by 0.3 m areas of sprinkler sprays (Sheppard 2002). Since PIV is an imaging technique, the scattered light signal from the droplets does provide an estimate of droplet size and shape (no assumption of spherical drops) if conducted at high resolutions. Significant uncertainties and errors exist when scattered light signals are used for particle sizing, however, which will be discussed later in this thesis.

Different techniques of simultaneous planar measurement of droplet size and velocity have recently appeared in the literature. Kadambi et al. (1998) have identified the errors associated with particle size measurements from Particle Image Velocimetry (PIV) images. Herpfer and Jeng (1997) have introduced streak PIV for planar measurements of droplet sizes and velocities. Domann and Hardalupas (2001a, b) have investigated fluorescing droplet intensity profiles and the effects of dye concentration. Cao et al. (1999) and Everest and Atreya (1999, 2003) have used planar laser-induced fluorescence for measurements of droplet size and Particle Tracking Velocimetry (PTV) for measuring drop velocities. The PTV technique is similar to the PIV technique and is useful when the density of seed particles is low. In this thesis, we present a Particle

Tracking Velocimetry and Imaging (PTVI) technique, similar to Cao et al. (1999), and Everest and Atreya (1999, 2003), which relies on taking instantaneous double-exposed color photographs of the spray and using them to obtain both velocities and particle sizes. Since the double-exposed photographs are created by laser shots of two different wavelengths, the color differentiation resolves ambiguities in flow direction.

2.3 Droplet Breakup and Trajectory

Previous researchers have sought to predict water distribution patterns from sprinklers as a step to predicting fire suppression. The groundwork for these predictions is the work of Taylor (1959, 1960), who studied the behavior of water bells, and the breakup of thin water sheets into droplets. Taylor's (1959, 1960) analysis defines the basic linear wave character of thin horizontal water sheets with radial velocity. With little to no turbulence, Taylor (1959, 1960) was able to form a radially symmetric horizontal water sheet by impaction of an upward traveling stream and horizontally oriented flat disk. At some radial distance, sheet breakup occurs, forming droplets with little to no radial velocity. When the water sheet breaks up into drops, Taylor (1959, 1960) found that 98% of the kinetic energy was lost in the breakup region. Since only a small portion of the energy was converted to the surface energy of the drops, the remainder was lost to turbulence within the drops, an idea supported by the observation that the drops were far from spherical after breakup. This conclusion is important since it shows that for some sprinkler flow conditions, significant kinetic energy can be converted to turbulence in the drops, rather than being transferred to the velocity of the drop. While Taylor (1959, 1960) presents expressions for describing the waves contained within the sheets and for predicting sheet thickness, he does not suggest expressions for drop size at breakup.

Other researchers, such as Huang (1970), have expanded on the work of Taylor (1959, 1960) and provided insight into the stability of water sheets. This information is useful for our study since we can estimate beforehand the stability of the water sheet formed by the sprinkler, which has an effect on the sheet breakup radius. The stability of the sheet was found to correlate with the value of the Weber number, defined using the properties of the water jet and the sprinkler orifice diameter as $\rho du^2/\sigma$, where ρ is density, d is diameter, u is velocity, and σ is the droplet surface tension. Huang (1970) found the existence of a critical regime, where the sheet is stable, but sensitive to perturbations. This regime is characterized by the value of the Weber number lying between 800 and 1000, and contains the maximum water sheet breakup radius. The breakup regime is expected to be important for experimental repeatability since a sprinkler operating in the critical regime would be more sensitive to small deviations in laboratory conditions. The works of Taylor (1959, 1960) and Huang (1970) may be used to predict the droplet properties at sheet breakup, however successive merging of droplets at the periphery of the water sheet causes deviations from the drop sizes predicted by Taylor (1959, 1960).

Dundas (1974) at Factory Mutual Research Corporation (FMRC) conducted another important piece of work. In this study, the researchers used dimensional analysis and experiments to show that the drop size distribution from a sprinkler can be scaled if the sprinklers are geometrically similar. The sprinklers studied were axis-symmetric and consisted of a simple nozzle and horizontal strike plate. They found that for the range of sprinklers tested, the volume median drop size to sprinkler size ratio varies as $We^{-1/3}$, with the value of the proportionality constant dependent on the type of sprinkler or nozzle used. (We is defined in the same manner as above by Huang (1970), where the length scale is the sprinkler orifice diameter) Their result implies that the volume median drop size, $d_m \propto d^{2/3}$ and $d_m \propto p^{-1/3}$, where d is the orifice diameter and p is the water discharge pressure. The authors also found that the value of the Reynolds number of the flow was unimportant within the range of sprinklers and water flows studied.

The breakup of water sheets from sprinklers into droplets was recently studied by Villermaux and Clanet (2002), which continues the work of Huang (1970). They identify two breakup regimes, similar to those identified by Taylor (1959, 1960) and Huang (1970). They found the transition from a smooth sheet regime to a flapping regime at $\alpha^{1/2}We=40$, where $\alpha=\rho_{drop}/\rho_a$, or the density ratio of the droplet and the ambient atmosphere. At small Weber numbers and small density ratios, the disturbances in the sheet are damped, while at large Weber numbers and density ratios the sinusoidal disturbances in the sheet grow. Typical sprinkler flows are within this flapping regime. In addition, the authors found that $d_{avg}/d_0 \sim \alpha^{-2/3}We^{-1}$ and $R/d_0 \sim \alpha^{-2/3}We^{-1/3}$ where d_{avg} is the numerical average droplet diameter, R is the sheet breakup radius, and d_0 is the initial water jet diameter issuing from the sprinkler orifice. The breakup mechanism is attributed to a shear instability resulting from interaction of the sheet with the surrounding medium, with inertial forces overcoming surface tension forces. The authors claim that gravity is negligible in the flapping regime. Unfortunately, it appears that they were unaware of the work done previously by Dundas (1974), and their data is given in numerical average diameter instead of volume median drop diameter.

Simple droplet trajectory models have been applied to sprinklers in the literature in an effort to predict the distribution of water to the areas below the sprinkler. The models assume that the droplets behave as single solid spheres, thereby neglecting droplet deformation, breakup, agglomeration, evaporation, and the effects of entrained air velocity. An example is presented in Prahl and Wendt (1988) and Wendt and Prahl (1986) where the authors compared axis-symmetric and commercial sprinkler water density distributions to predicted water distributions. In the study, the droplet size distribution near the sprinkler was backed out of the analysis instead of measured. A theoretical model of sheet dynamics and breakup was used to predict the initial flight trajectory of the droplets. Since the resulting droplet size distribution (Rosin-Rammler distribution) was within the range of values reported in the literature, the researchers were confident with predicting the gross water density distribution.

A similar study was recently reported in the literature. (Sheppard, Gandhi, and Lueptow 2000) In this report, the investigators applied a solid sphere trajectory model similar to that published by Prahl and Wendt (1988), but used PIV droplet velocity data gathered from the sprinkler flow as a model input instead of using a sheet breakup model. The droplet size distribution was not measured, but assumed to follow a Rosin-Rammler distribution. The authors reported fair agreement between the predicted and measured water flux, and indicated that further refinement was necessary for acceptable engineering results.

It is important to note that in the research conducted so far, and reported in the literature, simultaneous measurement of droplet size and velocity have not been conducted at a meaningful scale. This data is readily provided by the PTVI technique, which is able to measure the velocity associated with each individual droplet, and allows for determining relationships between droplet size, direction, and speed. It is not possible to study these relationships using the average droplet size and velocity data from other techniques.

2.4 Evaporating Droplets

The droplet evaporation process begins with a polydisperse distribution of droplets leaving the atomization device with an initial trajectory. There are various ways to quantify the droplet distribution. For applications with heat and mass transfer, the Sauter mean diameter (SMD) is often useful. The SMD is based on the volume to surface area ratio of the droplets. Mass median diameter is also frequently calculated for droplet distributions. For fire suppression applications, it would be useful to have the actual droplet volume or mass distribution. The distribution would allow calculation of droplet evaporation rates individually, the integration of which would provide information as to how much of the water volume evaporated during the travel from the sprinkler to the fire or fuel surface, and therefore the actual delivered density (ADD) could be determined.

The droplet evaporation rate is a function of the velocity difference between the droplet and the surrounding gas. It has been shown that the first droplets, and those near the edge of the spray pattern, are those most affected by a velocity difference. The spray pattern from nozzles serves to accelerate the gas to a similar velocity, resulting in little to no velocity difference between the droplets and the gas. (Law 1977; Lefebvre 1989) The velocity differences that are observed are due to the unsteady or turbulent components of the velocity. These assumptions must be revisited for the case of sprinkler sprays since the droplet density is lower than that of a typical spray nozzle, and the droplets are significantly larger. In this chapter, we will assume that the droplets are not affected by their neighbors. In a more complex analysis, the drag a drop experiences would be affected by the drops traveling in front of it. In addition, the heat and mass transfer boundary conditions will differ for drops on the interior versus drops at the edge of the spray pattern.

In this thesis, the PTVI method is developed that is capable of measuring drop size and velocity in fire environments where the drops are expected to lose mass through evaporation. Although not examined experimentally in this work, evaporation caused by elevated temperatures will affect the boundary layer of the droplet, which may have an effect on drag forces. The following sections briefly examine these topics, and suggest that evaporation, and its effect of drag, may be neglected for the environmental conditions used in the study.

2.4.1 Heat and Mass Transfer

For monodisperse droplets in a constant atmosphere of still air, there will be some amount of heat transfer between the drops and air if a temperature difference exists. Neglecting radiation, there could be convection between the air and the surface of the drop, as well as some combination of conduction and convection within the drop. The process inside the drop would be bounded by two extremes, one where convection causes the temperature within the drop to be a function only of time, ie. the drop is well mixed. The other extreme would be where the internal circulation is negligible, and the heat transfer within the drop is only by conduction. Sujith et. al. (1996) suggest that internal circulation is absent in small drops, but significant in large drops. The droplet size at which this transition occurs has not been clearly established in the literature. From the plots of Sujith's data, however, the transition appears to occur at drop sizes less than approximately 100 µm, which is near the lower limit of what we expect to measure.

An analysis by Law (1977) indicates that the heating of a thin outside layer, where evaporation is occurring, is very rapid and nearly independent of the internal heating. This results in insensitivity of the overall droplet vaporization characteristics to the internal heat transfer mechanism. For the case of a sprinkler discharging in an ambient atmosphere, a well-mixed droplet assumption could also be utilized with similar results due to the small temperature differences expected between the water and the air, except when the droplet flight occurs in a fire.

For a single spherical stationary droplet in quiescent air, constant properties, no radiation effects, constant pressure, no internal heat generation, and neglecting Dufour and Soret effects, the general spherical conservation equations (Kuo 1986) for a droplet can be reduced to simplified formulations for continuity, energy, and species. If the energy transferred from the ambient to the droplet surface is only used to evaporate the droplet, and the ambient temperature is present at large radial distances from the droplet, then the mass flux from the droplet can be expressed by Equation 1.

$$\dot{m}_s = 4\pi\, r_s\, \rho_s\, \alpha_s \ln\left[1 + \frac{C_p\left(T_\infty - T_s\right)}{h_{fg}}\right] \tag{1}$$

where: r_s=radius of droplet surface
ρ_s=density of droplet
α=thermal diffusivity, $k/(\rho C_p)$
k=thermal conductivity
C_p=specific heat
T_∞=ambient temperature
T_s=droplet surface temperature
h_{fg}=latent heat of vaporization

This approach is typically very useful for combustion type problems since the surface temperature of the drop is replaced by the boiling point of the fuel. Likewise, the calculation is also straightforward when a sprinkler spray interacts with the fire plume, which is expected to be at a temperature in excess of 100 ^oC. If the water and air are near room temperature, then $T_\infty - T_s \approx 0$, and evaporation will be small. Some evaporation will occur if the relative humidity is <100%, but the evaporation rate is small and therefore neglected in this work.

For stationary droplets under quiescent conditions, the dominant heat transfer mode is conduction, which provides the energy for the latent heat of vaporization. When relative motion exists between the droplet and the air, forced convection was found to affect the rate of heat transfer to the drop and the rate of evaporation to the same extent, resulting in the same steady state evaporation temperature for the drop. The rates of evaporation are enhanced however, increasing the rate of change of the droplet radius. Correction factors were developed to account for the increased evaporation rate and are available in the literature (Lefebvre 1989). The correction factors are useful for cases where droplets are passing through fires or fire plumes, but since the droplet and ambient temperatures are nearly equal for the experiments in this work, evaporation is neglected.

2.4.2 Velocity of Evaporating Droplets

The boundary layer surrounding evaporating droplets can affect the drag forces on the droplet. One approach to predicting the velocity of falling droplets is discussed by Sujith (1996). In this analysis, the droplets are assumed to be solid spheres, with the coefficient of drag, C_D, determined by equating drag and gravitational forces:

$$C_D = \frac{24}{\mathrm{Re}}\left(1 + 0.173\,\mathrm{Re}^{0.657}\right) + \frac{0.413}{1 + 16300\,\mathrm{Re}^{-1.09}} \tag{2}$$

In order to treat the droplet as a solid sphere, the effects of mass transfer and drop deformation must be neglected. Mass transfer from the droplet undergoing evaporation results in two effects on drag. The phenomenon known as "blowing" tends to increase the form or pressure drag by a factor of approximately $(1+B)^{0.6}$,while evaporation reduces friction drag on a flat plate by a factor of approximately $(1+B)^{0.75}$, where B is the Spalding transfer number defined in Equation 3 (Spalding 1955).

$$B = \frac{C_p\left(T_\infty - T_s\right)}{h_{fg}} \tag{3}$$

Falling droplets of 0.6 mm to 5.5 mm in diameter were measured in a heated wind tunnel, and the results compared to the "standard" drag curve for non-evaporating spherical drops by Yuen and Chen (1976). Excellent agreement was found for $1<\mathrm{Re}<2000$ and $0<B<3$, if Re is evaluated at free stream conditions except for viscosity, which is evaluated using the 1/3 rule as described in the literature (Sparrow and Gregg 1958, Hubbard et al. 1975, and Yuen and Chen 1978). The 1/3 rule comes from studies of natural convection, but was also expected to apply to forced convection as well. The temperature at which to evaluate the kinematic viscosity is determined by:

$$T_{ref} = T_s + \frac{(T_\infty - T_s)}{3} \tag{4}$$

Note that typical film conditions would utilize a factor of 1/2 instead of 1/3 in the above relation.

Some of the drag measurements were confirmed by Sujith et al. (1996), with droplets from 50 μm to 250 μm at temperatures less than ~200 ^{o}C. Therefore, in this thesis drag calculations are conducted assuming the droplets are quasi-steady non-evaporating spheres under steady flow. It is important to note that the standard drag curve could also be used if the droplets were evaporating due to travel through a fire plume. In this case the droplet diameter would decrease along the droplet path, resulting in a drag coefficient changing along the standard drag curve.

2.5 Summary and Conclusions

The previous sections of the background have laid the foundation for the work done in preparation of this thesis. It has been shown that large scale measurements of sprinkler drop size and velocity are needed to provide input and verification data for both CFD fire models and simple droplet trajectory calculations. It is these models and calculations that are used to predict the water density delivered by the sprinkler to burning surfaces.

Simultaneous measurements of drop size and velocity have not been conducted at a meaningful scale, and cannot be predicted to a high level of certainty. Existing measurement techniques are not capable of providing large scale, simultaneous measurement of drop size and velocity, and a new measurement technique is needed to provide this data. A Particle Tracking Velocimetry and Imaging (PTVI) technique is developed in Chapter 3, which is capable of providing large scale, non-intrusive, simultaneous measurements of drop size and velocity. Drop size and velocity measurements in sprinkler flows are described in Chapter 4, with the data presented and analyzed in Chapter 5.

Analyses and correlations are available in the literature to predict the mass loss rates, drag coefficients, and velocities of droplets traveling through fire flows. While the PTVI technique is capable of conducting measurements under these conditions, the experiments in this work are all done at standard temperature and pressure. Under these conditions, evaporation can be neglected, and velocities calculated assuming the drops are solid spheres. Using the droplet data from Chapter 5, droplet trajectories for the sprinklers are calculated in Chapter 6, and the resulting water distributions on the floor below the sprinkler are predicted. The predicted water distributions are also compared with measured water distributions. The conclusions of the study are presented in Chapter 7.

CHAPTER 3

PARTICLE TRACKING VELOCIMETRY AND IMAGING TECHNIQUE

The measurement method utilized in this work is a type of particle tracking technique developed at the University of Michigan and NIST. The technique is described at a smaller scale in the literature (Everest and Atreya 1999, 2003). In this method, a droplet laden flow is sequentially illuminated with two pulsed laser sheets of two different wavelengths produced by two Nd:YAG lasers. There are two fluorescent dyes in the droplets, each of which fluoresces primarily in response to one of the laser sheets, each in a different color. A film camera is situated perpendicular to the measurement region to capture the fluorescent signal emitted by the drops (See Figure 1). Each film exposure is double exposed, capturing two droplet images for each droplet in the measurement region. A specially chosen narrowband filter is installed on the camera lens to exclude scattered laser light which would otherwise interfere with the fluorescent images.

Once exposed, the film is developed and the images digitized by a high resolution film scanner. Due to the large number of droplet images on each film exposure, a computer program is used for analysis. The algorithms in the program determine the sizes and velocities of the droplets. The results consist of droplet size and velocity distributions that can be used for input into fire models or provide verification data. While sprinkler measurements are described here, this is a general measurement technique that may be used for any spray where high resolution measurements of droplet size and velocity are needed. This includes characterization of fuel sprays used in engines where simultaneous measurements of drop size and velocity are of interest, and in manufacturing processes utilizing sprays.

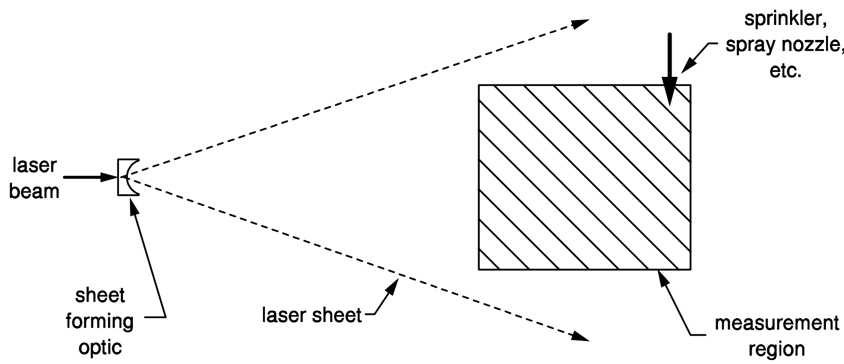

Figure 1. Elevation view of the measurement region and laser sheet. This is also the camera view.

While simple in concept, there are many experimental parameters that must be chosen for good results. Initially, the drop size range, drop velocity range, and measurement region size are tacitly chosen. The droplet sizes from fire sprinklers, for example, are between approximately 20 μm to approximately 3 mm, with velocities on the orders of 1m/s and 10 m/s. This estimate agrees with the literature (Kincaid, Soloman and Oliphant 1996), which indicates that droplets larger than approximately 5.5 mm in diameter are unstable, and break up into droplets predominately in the range of 1 mm to 2 mm. Other research has shown that while a large number of very small drops are present, they comprise a small portion of the total water volume (Putorti, Belsinger, and Twilley 1999). The authors found that 98% of the water from typical fire sprinklers is contained in droplets larger than 200 μm in diameter. Thus, an initial drop size range is chosen to be 200 μm to 3000 μm, with a velocity range of 1m/s and 10 m/s.

The measurement area size can now be estimated, keeping in mind that the measurement resolution is currently limited by the electronic scanning technology used to digitize the photographic images for analysis. It is estimated that 4 pixel by 4 pixel coverage of a 200 μm diameter droplet will result in an uncertainty of 25% in droplet size, requiring each pixel in the measurement region to be approximately 50 μm in size. Given a 50 μm pixel in the measurement region, the use of medium format photographic film (70 mm × 60 mm), and a 4000 DPI scanner, a magnification factor of 0.13 is indicated, resulting in a measurement area of approximately 54 cm by 46 cm. This is an acceptable drop size range, measurement area, and uncertainty for the purposes of sprinkler characterization.

The drop size range, measurement region, and uncertainty determined above are initial estimates that require further study. There are many factors and experimental parameters that affect the uncertainty. The initial estimate was based only on the advertised capabilities of the film scanner, and doesn't take into account factors such as film resolution, camera diffraction errors, optical component distortion, beam sheet thickness, or camera depth of focus effects. All of these factors will be studied in depth in this chapter.

It is also important to determine if a droplet can be detected by the measurement system, for an undetected drop cannot be measured. There are many factors and experimental parameters that affect the detectabilty of a droplet. These include film sensitivity, dye concentration, droplet composition, emission wavelength, emission intensity, color differentiation, exclusion of scattered light, and laser beam quality. These factors will also be studied in this chapter.

Once high quality droplet images are recorded and digitized, a technique is needed to measure the droplet size and velocity with low uncertainty. Due to the large amount of data available, the image analysis is automated. In order to determine the overall uncertainty in the measurement and analysis process, the technique is calibrated/verified using drops of known diameter. The calibration/verification process is detailed later in this chapter.

3.1 Uncertainty

In this study, the uncertainties reported are expanded uncertainties resulting from a combination of Type A (statistical methods) and Type B (other methods) evaluations (Taylor and Kuyatt 1994). The expanded uncertainty is expressed with a coverage factor, k=2, which corresponds to a coverage probability of 95% for the interval, assuming normally distributed data. Therefore, if the uncertainty in a measurement is defined as U, the true value of the measurand is defined as Y, and measurement result is defined as y, then there is a 95% probability that $Y=y\pm U$. In some cases, the uncertainty is derived from statistical methods alone (Type A). These cases will be specifically noted.

3.2 Droplet Sizing Considerations

Sizing and tracking a particle in a large field of view (FOV) requires simultaneously satisfying disparate requirements of low magnification and high spatial resolution. For proper sizing, the spatial resolution of the optical, film, and digital components must result in a fully resolvable drop, indicating as large a magnification as possible. Meeting the spatial requirements for drop sizing results in limiting the FOV and a subsequent loss in the dynamic velocity range (DVR) and the dynamic spatial range (DSR), as defined by Adrian (1997) and shown in Equation 5:

$$DVR = \frac{V_{\max}}{V_{resolve}} \qquad DSR = \frac{L_{meas\ region}}{l_{resolve\ meas\ region}} \tag{5}$$

where: V_{max}=full scale velocity
$V_{resolve}$=minimum resolvable velocity
$L_{meas\ region}$=length scale of measurement region
$l_{resolve\ meas\ region}$=minimum resolvable length scale in measurement region

A magnification higher than necessary for meeting the sizing requirements reduces the spatial and velocity spectrums over which the velocity measurements can be made. This can be seen by considering the DVR×DSR product. Clearly, a large value of this product is desirable. The DVR×DSR product is proportional to the dimensionless constant ***L/l*** that is characteristic of the imaging/recording system. Here, ***L*** is a characteristic dimension that defines the format of the recording medium and ***l*** is the smallest observable length scale. For PIV applications, '***l***' may be as small as two pixels for a digital recording media or one line pair for a film recording medium yielding a large DVR×DSR product. However, for simultaneous particle sizing, '***l***' is determined by the smallest particle size that needs to be resolved and the required accuracy; it is at least twice the requirements for PIV. Thus, to maintain a large DVR×DSR it is necessary to increase '***L***', i.e. a high resolution, large format image. A medium format film camera was used to satisfy these disparate requirements. Also, particle tracking was used to measure the velocity, and color differentiation was used to resolve the directional ambiguity.

The variables that must be considered for particle size measurements by the PTVI technique are schematically shown in Figure 2. First, the thickness of the laser sheets relative to the droplet size and the variation of the laser intensity across this thickness are important. Often the laser sheet thickness for PIV or PTV applications is determined by the transverse component of the particle velocity and the time separation between the two laser pulses. For the worst case scenario of equal in-plane and transverse velocities, the minimum beam sheet thickness (as defined by 50% intensity or full width at half maximum, FWHM) should be at least three times the maximum particle diameter. Thus, for a 3 mm sprinkler droplet, the laser sheet should be at least 10 mm thick[1]. Since the light intensity in Gaussian sheets falls to about 50% of the maximum at the edges, the image of a large droplet at the edge may be smaller than the image of the same size droplet at the center. This error must be quantified for drop size measurements. Next, the effect of the depth of focus (DOF) must be quantified. If the droplet is out of the depth of focus, it appears large because of blurring. Thus, the DOF and the beam sheet thickness should be approximately equal to enable the increase and the decrease in the particle image size to roughly cancel each other out. Increasing the DOF larger than the beam sheet thickness is not useful because it requires larger f#^{s} that only serve to reduce the amount of light captured by the camera and increase the error due to diffraction limitations of the optics. It is also possible to use a laser that produces a top hat type energy profile. In fact, in many Q-switched pulsed lasers, the initially Gaussian laser beam profile changes to approximately a top hat profile by the time it reaches the measurement region. Since the energy level of the top hat beam is relatively constant across the sheet thickness, the droplets imaged at the edge of the sheet would be expected to be larger due to blurring. All these questions and those regarding the ability to accurately measure drops sizes by recording the scattering signal are addressed below.

---

[1] The choice of the beam sheet thickness is also important to ensure that sufficient numbers of droplets are present in the measurement volume to obtain a representative sample. The particle seeding density in these experiments is not externally determined leaving beam sheet thickness as the primary control variable. As will be seen later, the criteria used above yields an adequate number of vectors to define the velocity field.

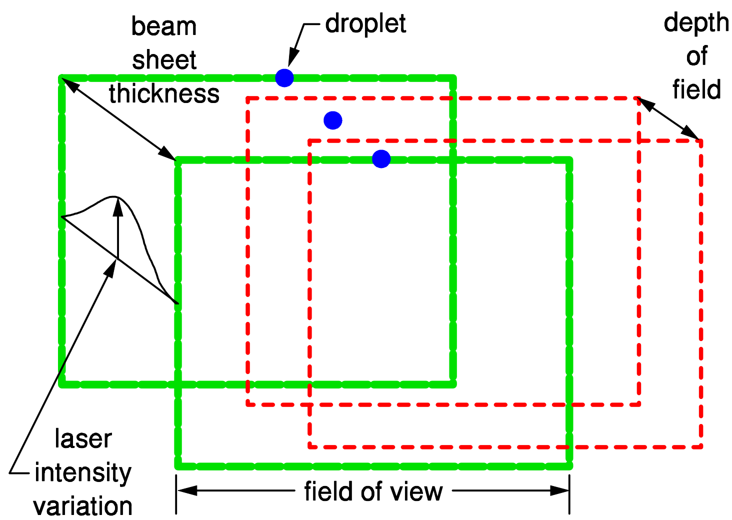

Figure 2. A schematic diagram showing the variables that must be considered for accurate particle size measurements by the Particle Tracking Velocimetry and Imaging (PTVI) technique.

Kadambi et al. (1998) considered some of the above effects for determining the particle size from the image. In their experiments, light scattering from solid particles suspended in a liquid was captured. They studied the effects of spatial resolution, light sheet intensity distribution, and depth of field (DOF) on particle size measurements. They observed that the particle image must be greater than 3 pixels in diameter to determine its size with reasonable accuracy. For quantifying the light sheet intensity distribution effect and the DOF effect, they used a 200 μm particle, a DOF of 200 μm, and a beam sheet thickness of 1600 μm. By moving the focused particle through the light sheet, they observed a decrease in the measured diameter of approximately 9% and a roughly 50% decrease in the scattered light intensity at the edges of the light sheet relative to the center. In another experiment, they traversed the imaging camera while holding the particle and laser sheet fixed to determine the effect of DOF. It was observed that the particle diameter increased by approximately 9%, while the intensity level again decreased by roughly 50%. Thus, when a particle is not centered in the light sheet and the focal plane, DOF and beam sheet intensity effects approximately cancel each other out resulting in a constant particle diameter. Their results show a standard deviation of 7% and pertain to measurements from the image formed by light scattered by the particles. Their results also indicate that it would be advantageous to have DOF ≤ FWHM. (Recall that FWHM ≥ 3×d_{DROP} for PIV requirements.) While Kadambi et al. (1998) and Adrian's (1991) results are very insightful, scattering measurements did not yield reliable droplet sizes in previous work (Everest and Atreya 2003). Thus, two-color fluorescence imaging was used to make drop size and velocity measurements in a large FOV with low-density sprinkler spray.

In order to estimate the effects of the experimental setup on the ability to produce suitable droplet images, it would be useful to have expressions for the light signals from the droplets. The fluorescence emission signal ‘F’ for droplets is given by the equation:

$$F \propto \frac{\phi\, I_0}{\lambda}\left(\frac{m}{(m+1)f\#}\right)^2 V\, f(c)\, f(R) \tag{6}$$

Here, ‘F’ is proportional to the fluorescence yield ‘ϕ’, intensity of light incident on the droplet ‘I_0’, wavelength of emitted light ‘λ’, and the volume of the illuminated droplet ‘V’. The signal is nonlinearly related to the magnification ‘m’, f#, the dye concentration function ‘f (c)’ and the film response function ‘f (R)’. The signal quality is improved by using higher magnifications and smaller *f#s*. However, to meet the FOV requirements the magnification is fixed at approximately 0.1, and only the *f#* can be reduced.

The response function ‘f(R)’ of the film is dependent on the spectral and exposure response characteristics of the film emulsions. Characteristic sensitivity curves for

Kodak Pro film (Eastman Kodak Company 1997) were used to define the film spectral response function. The overall response to a given wavelength was estimated by extrapolating the response curves for each film emulsion layer shown in Figure 3, and calculating the sum of the responses for all layers. The curves indicate that the film is approximately 30 times more sensitive to 588 nm (rhodamine fluorescence), 434 nm (stilbene fluorescence), and 532 nm (scattering) than for 355 nm UV scattered light. The increased energy in the shorter UV wavelength improves the signal but lower 355 nm laser power offsets that gain. Similar results are obtained from Fuji color films (Fuji Photo Film Co., Ltd. 2001), as shown in Figure 4, where the film response drops off rapidly for wavelengths less than approximately 400 nm. As a result, 355nm scattering was not observed in the images from either film type.

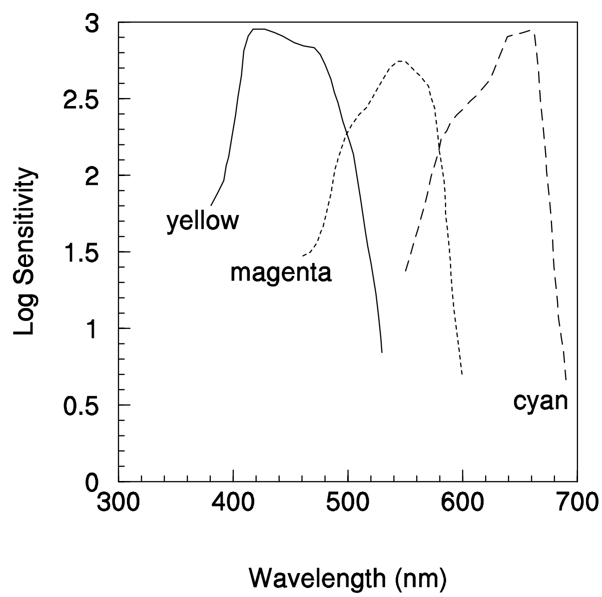

Figure 3. Spectral sensitivity curve for Kodak Pro 1000 film. Sensitivity is defined as the reciprocal of the exposure required to produce a specified density. Specific units are unimportant since the relative sensitivity between wavelengths is of interest. Data provided by Kodak.

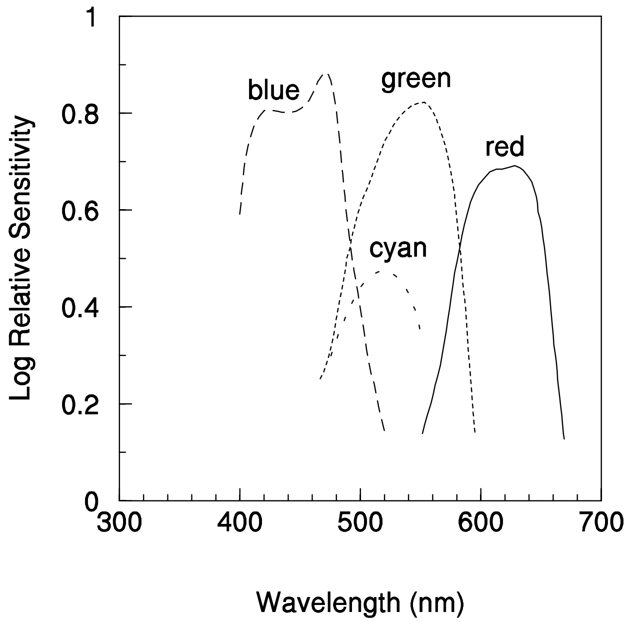

Figure 4. Spectral sensitivity curve for Fuji NPZ800 film. Sensitivity is defined as the reciprocal of the exposure required to produce a specified density. Specific units are unimportant since the relative sensitivity between wavelengths is of interest. Data provided by Fuji.

It is also instructive to qualitatively examine how various signal levels change with the choice of f# of the optics. Two formulas taken from Adrian (1991) are useful:

$$\frac{d_{IMAGE}}{d_{DROP}} = m\left(1+\left(2.44\frac{(1+m)f\#\lambda}{md_{DROP}}\right)^{2}\right)^{\frac{1}{2}} \tag{7}$$

$$DOF = 4\left(\frac{(1+m)f\#}{m}\right)^{2}\lambda \tag{8}$$

Equation 7 accounts for the diffraction limitation of the optics, whereas Equation 8 provides an estimate of the depth of field (DOF). Assuming a magnification 'm' of 0.13, Equation 6 through Equation 8 can be used to study the variation with the f#

of the recording optics. These equations are shown plotted in Figure 5. The curves with solid markers correspond to 355 nm excitation and the curves with hollow markers correspond to 532 nm excitation. The objective of the calculations illustrated in this plot is to understand the dependence of the signals on the optics parameters.

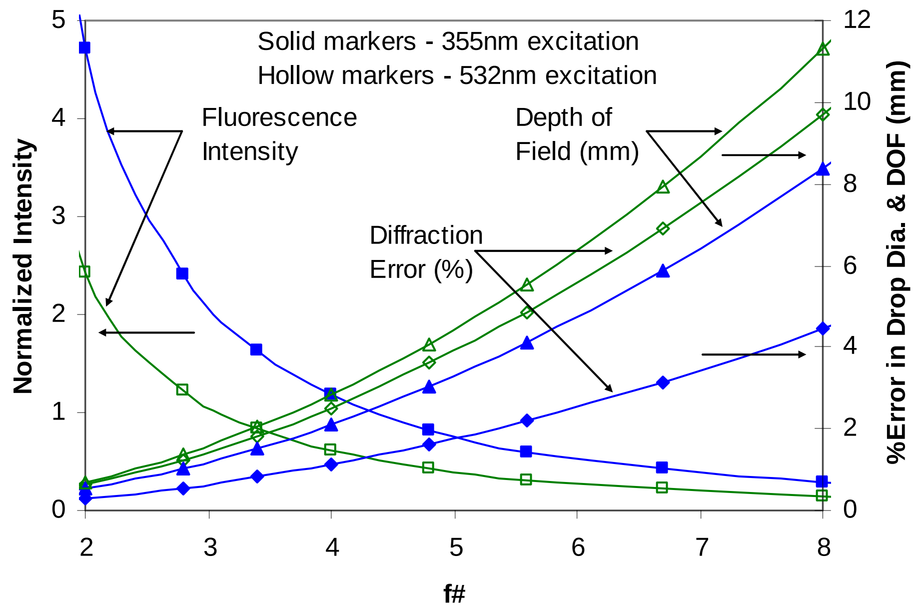

Figure 5. Variation of fluorescence intensity, percent diffraction error, and DOF (in mm) with f# for a 200 μm droplet. Emission intensity is normalized by the maximum intensity of the detection system as derived from experimental data. Filled markers indicate 355 nm excitation, while hollow markers indicate 532 nm excitation.

For a given droplet size, dye concentration and incident intensity, Equation 6 shows how the fluorescence intensities vary with the f#. Note that the data for fluorescence intensity is not arbitrary, but was calculated using experimental data from 200 μm diameter drops which will be discussed later. Using this data, the intensity was normalized by the maximum intensity measurable by the detection system, also known as the saturation intensity. As such, normalized intensity values >1 can not be differentiated by the measurement apparatus. Clearly, as the f# is increased, the intensity drops sharply as $1/f\#^2$. Consequently, a small f# is needed to increase the signal levels. The curves corresponding to Equation 7 show the %error due to diffraction limitations of the optics for a 200 µm drop. These appear acceptable for drops >200 µm in diameter, but the error increases sharply to 35% for 100 µm droplets imaged using 532 nm light and an f# of 8.0. As expected, the diffraction error for 355 nm images is significantly less than for 532 nm images.

The increase in the DOF with the f# is also shown. DOF must be appropriately chosen based on drop sizes and the beam width. The primary balance that needs to be achieved is between the fluorescence intensity and the DOF. It appears that the choice of an f# around 4.0 is appropriate for these parameters. However, if the maximum droplet size to be measured is much larger, on the order of 3 mm for example, the beam sheet thickness and DOF will need to be larger, making a larger f# necessary. In this case, the error in droplet size measurement due to diffraction effects will increase, but are still less than 5% for drop sizes ≥200 µm at f#=5.6. Adequate signal for droplet detection and imaging must be verified, however, given the decrease in aperture size and laser sheet profile. In addition, errors in drop size measurement must also be quantified. Thus, detectability and sizing error will be determined experimentally in the sections to follow.

With these considerations, experiments were conducted to identify the effect of the imaging system resolution, fluorescent dye concentration, variation in laser sheet thickness, and laser sheet intensity on drop size measurements. The results of these experiments were used to quantify the ability of the measuring system to accurately characterize the spray velocities and particle size while maximizing FOV.

3.3 Experimental Setup

Two methods are possible to resolve the directional ambiguity in the double-exposed, high-resolution color photographs: 1) color differentiation by fluorescence and scattering and 2) color differentiation by two different fluorescent colors. In the *fluorescence/scattering method*, the two images of the droplet on the film consist of one from the fluorescing dye and the other from scattering. In the *dual-fluorescence method*, both images are of the fluorescing dyes, but at two different wavelengths. The two experimental setups were investigated to determine their feasibility in the literature (Putorti, Everest, and Atreya 2003).

In the aforementioned study, the authors indicate that the results from the *fluorescence/scattering* method were less than satisfactory for two primary reasons. First of all, color differentiation was difficult due to the green/yellow color of both the fluorescent signal from rhodamine dye and the scattered light signal (See Figure 30 later in the discussion). In addition, the scattered signal tended to overwhelm the fluorescent signal. Using the *dual-fluorescence method*, the authors indicate that a rhodamine-stilbene-water mixture produced a blue emission from 355 nm excitation, and a yellow emission from 532 nm excitation, leading to easily differentiated images. For these and other reasons to be discussed later, the *dual-fluorescence method* is developed in this thesis.

The *dual-fluorescence method* was developed at NIST using a large enclosure with a high power laser as shown in Figure 6 and Figure 7. Water is discharged through a nozzle and hits a symmetrical strike plate, forming a conical to umbrella shaped water distribution pattern. The water is recycled via a holding tank and pumps (detailed later in Figure 57), so the fluorescent dyes are dissolved in water before the experiments to a concentration of approximately 3.3 mg/L of rhodamine and 10 mg/L of stilbene. Dual Nd:YAG lasers operating at 10 Hz produce co-linear beams, with the leading 10 ns pulse at 532 nm, followed by a 355 nm pulse of 10 ns duration at Δt milliseconds (Δt determined by PTV requirements) after the primary pulse. The laser energies are approximately 400 mJ/pulse at 355 nm and 700 mJ/pulse at 532 nm. A laser sheet of approximately 13 mm in thickness is produced by a cylindrical plano-concave lens with a nominal focal length $f = -37.5$ which was coated for both wavelengths. The sheet was limited to approximately 10 mm in thickness by installing an 8 mm wide steel slit after the sheet forming optic.

Images of a 460 mm by 540 mm region downstream of the nozzle were taken at a magnification of 0.13 using a Mamiya RZ series medium format camera (70 mm by 60 mm film) with a 210 mm achromatic lens and Fujicolor NPZ 800 color film. Since the frame rate of the camera is slow compared to the laser frequency, the shutter was left open for one laser beam shot pair thereby double exposing the film. A 532 nm notch filter is installed on the camera to exclude scattering from the 532 nm laser. The rhodamine fluorescence in response to the 532 nm pulse results in yellow droplet images, whereas the stilbene fluorescence in response to the 355 nm pulse results in blue droplet images. The best results were obtained by using an f# of 5.6.

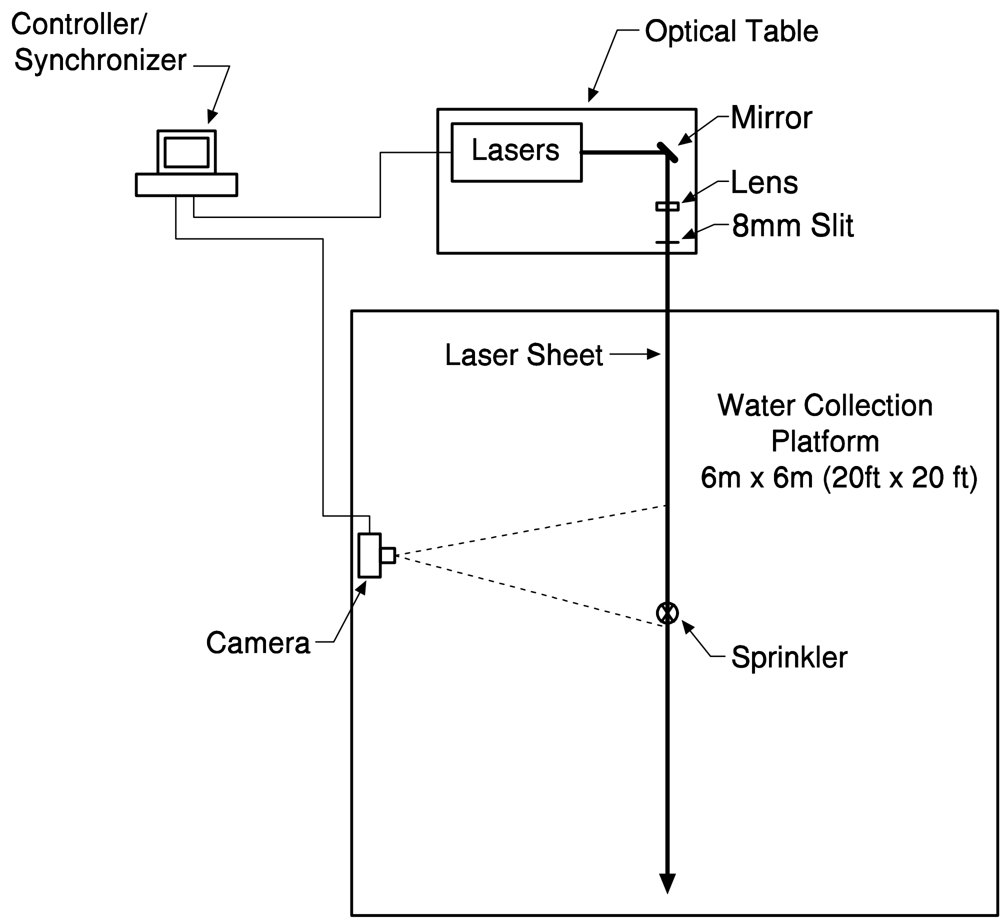

Figure 6. Experimental arrangement for spray measurements, plan view.

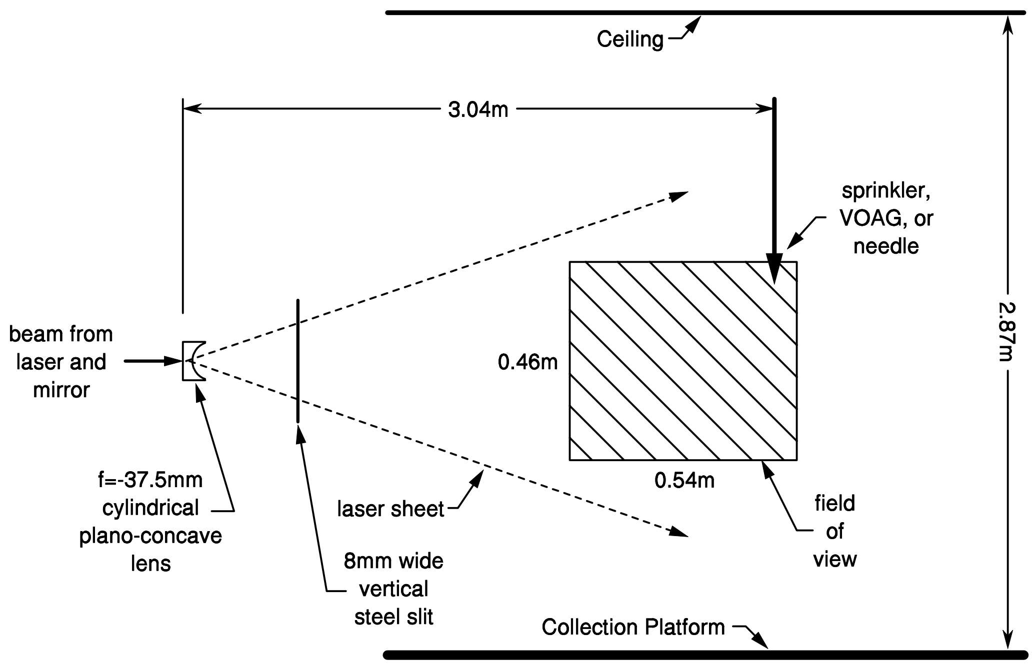

Figure 7. Measurement region, elevation view.

A control system is needed to synchronize the laser pulses with the opening of the camera shutter. The measurement system relies on a constant flow of water through the sprinkler, or a steady stream of calibration drops through the field of view. The lasers are operated using a synchronizer and software provided by TSI, Inc. The synchronizer was used to control the power level of the lasers via the flashlamp and Q-switch timing, and to vary the time between the pulses from the two lasers of different wavelengths. The lasers operate continuously, since the crystals within them need to reach a steady operating temperature to provide a stable power output and consistent beam quality. As such, the lasers become the timing master, and provide a signal to a separate delay unit each time the leading laser pulses. An initiation box is attached to the delay unit, and has a button which is pushed when a photo of the measurement region is desired. The initiation box signals the delay box to wait for the next laser pulse, wait a programmed delay time, and fire the camera. The delay, which varies with the lens and aperture setting, is due to the time necessary for the camera mirror to flip up, and the shutter to fully open. The camera shutter opens, the lasers flash, and the shutter closes. The process is captured on a dual channel oscilloscope to verify that the laser pulses occurred while the camera shutter was open. A camera auto-winder advances the film to the next frame, and the camera is ready for another exposure in approximately 1.5 s. The time sequence of this process is shown in Figure 8.

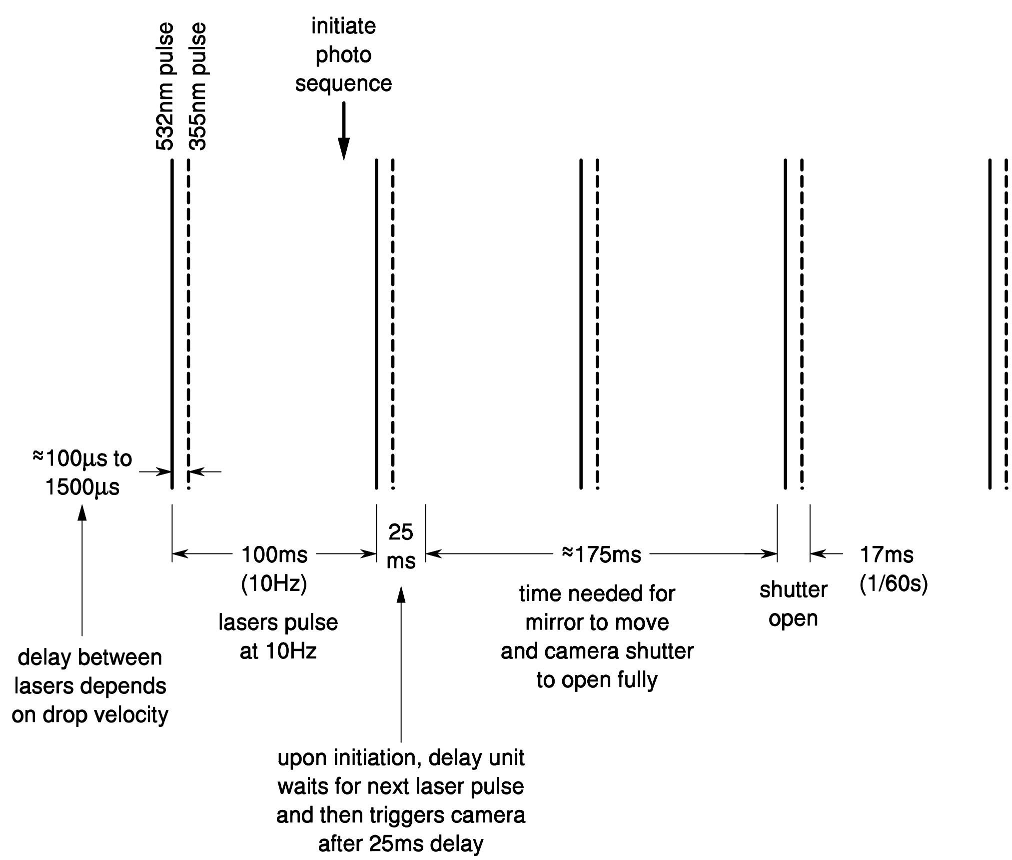

Figure 8. Laser and camera synchronization time sequence.

After development, the film negatives were digitized with a 4000 dpi × 4000 dpi Polaroid film scanner that resulted in a digital resolution of approximately 50 µm/pixel in the droplet plane. The optical spatial resolution of the imaging system was measured by using a standard USAF 1951 resolution chart. Images were obtained at a magnification of 0.13 for various f#s. The best resolution was obtained with an f# of 8.0 at 5.0 lp/mm, which corresponds to resolving a 100 μm thick line in the droplet plane. A line of this size corresponds to roughly 2 pixels in the image. Assuming that 3×3 pixels are needed to measure the drop size with reasonable accuracy, we obtain the minimum measurable droplet diameter of approximately 150 μm.

The digitized images were processed using a custom analysis macro running in ImagePro Plus software. Droplet sizes were determined from the blue fluorescent images, and the droplet velocities determined from the yellow and blue images. These images had sufficient spatial resolution for sizing 200 μm diameter droplets, as well as color-differentiation for resolving the directional ambiguity in velocity measurements. For laser pulse separations of $\Delta t = 1$ ms, the dynamic velocity range (DVR) was estimated at 75 from Equation 5, with a minimum resolvable velocity of 0.2 m/s (from a minimum separation of one drop diameter between 200 μm drops) and a maximum velocity of approximately 15 m/s (using five times the diameter of 3000 μm drops (Adrian 1991)). This estimate is based on traditional PIV, where droplet image translations must be within a certain range to obtain useful droplet correlations. The velocity algorithm used in this work, however, matches the individual droplet images using size, color, and position, which accommodates greater translations between images and suggests a DVR on the order of 200 based on droplets traveling at 35 m/s and $\Delta t = 1$ ms. During the sprinkler experiments, laser pulse separations of $\Delta t = 100$ μs to 1500 μs were utilized, and velocities in the range of approximately 1 m/s to approximately 35 m/s were observed.

3.4 Determination of Fluorescent Dye Concentrations

Proper choice of the fluorescent dye and its concentration must be made to obtain the best signal. The optimum droplet dye concentration was determined by placing dye/water solutions of various concentrations in a Perkins-Elmer luminescence spectrometer (fluorimeter.) The device illuminates the solution sample with a user selectable narrowband light source, and scans the fluorescent output over a large range of wavelengths, recording the intensity at each wavelength. The sample is held within a square cross section cuvet, constructed of polymethacrylate, which is nearly transparent and consistently transmissive at the wavelengths of interest. The transmission path length is nominally 10 mm.

Solutions of rhodamine, stilbene, and fluorescein were tested in the fluorimeter. The Rhodamine WT dye was provided in a 2.5% by mass in water concentrate, manufactured by Kingscote chemical company. The Stilbene 420 dye was manufactured by Exciton, and designated as non-laser grade, 99% pure stilbene. The fluorescein (uranine) dye was provided in a 7.5% by mass water concentrate, also manufactured by Kingscote chemical company. The results are shown in Figure 9 where relative intensity, integrated over all emission wavelengths, is plotted against concentration. From the graph, it can be seen that the best concentrations to use are approximately 3 mg/L of rhodamine in water, 10 mg/L of stilbene in water, and 100 mg/L of fluorescein in water. Note that the maximum response of the stilbene dye is nearly an order of magnitude greater than the response of the rhodamine dye, and that fluorescein reaches its peak at an order of magnitude greater concentration than rhodamine and stilbene. Chemical and identification data for each of the dyes is provided in Table 1. Unless stated otherwise, the rhodamine used in this work is Rhodamine WT.

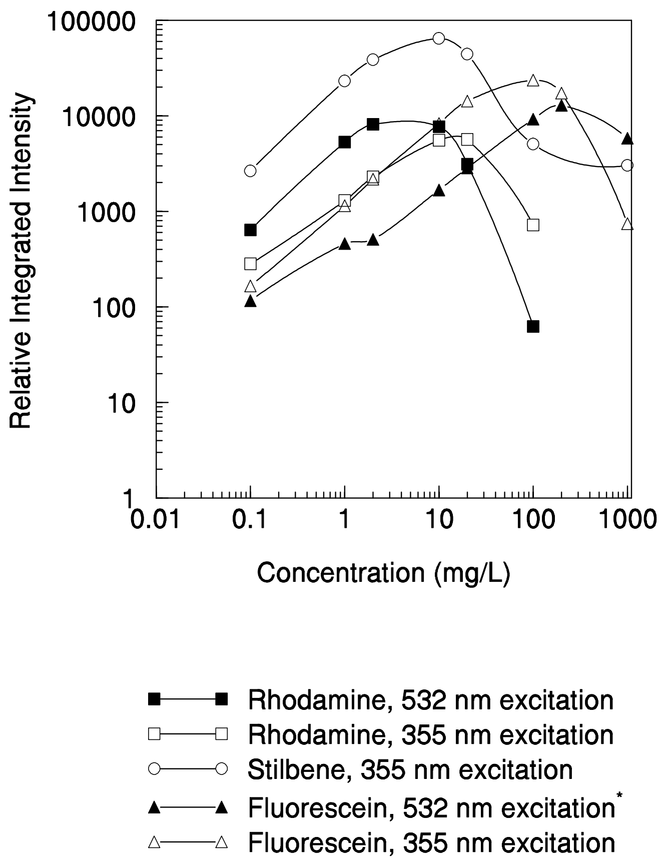

Figure 9. Relative fluorescent emission intensity from dye-water solutions integrated over all emission wavelengths.

Table 1. Fluorescent dye information.

Dye	CAS#	Molecular Formula	Molecular Weight	Notes
Rhodamine 6G	989-3838	C28 H30 N2 O3 HCl	478.4	
Rhodamine WT	37299-86-8	C29 H29 N2 O5 Cl.2 Na	579	Liquid Concentrate 2.5% by Mass
Fluorescein (Uranine)	518-47-8	C20 H12 O5	332.15	Liquid Concentrate 7.5% by Mass
Stilbene 420	27344-41-8	C28 H20 O6 S2 Na2	562.56	99% Pure Powder

The fluorimeter is especially useful since it gives the spectral response of the dye to a given excitation wavelength. Spectral response curves for the dyes, in response to 355 nm and 532 nm excitation signals, are shown in Figure 10 through Figure 14. The maximum emission wavelength varies somewhat with concentration. Two of the dyes, rhodamine and fluorescein respond to both excitation wavelengths, while stilbene does not fluoresce when exposed to 532 nm. These plots, along with Figure 9, suggest an optimal combination of dyes for two-color droplet differentiation. If rhodamine and stilbene are used together with excitation wavelengths of 355 nm and 532 nm, the 355 nm light will cause a very strong emission from the stilbene in blue, and a much weaker emission in yellow. With a 532 nm excitation signal, a strong emission from rhodamine will occur in yellow, with no response from stilbene. The final result from the rhodamine-stilbene-water mixture would be a blue emission from 355 nm, and a yellow emission from 532 nm excitation.

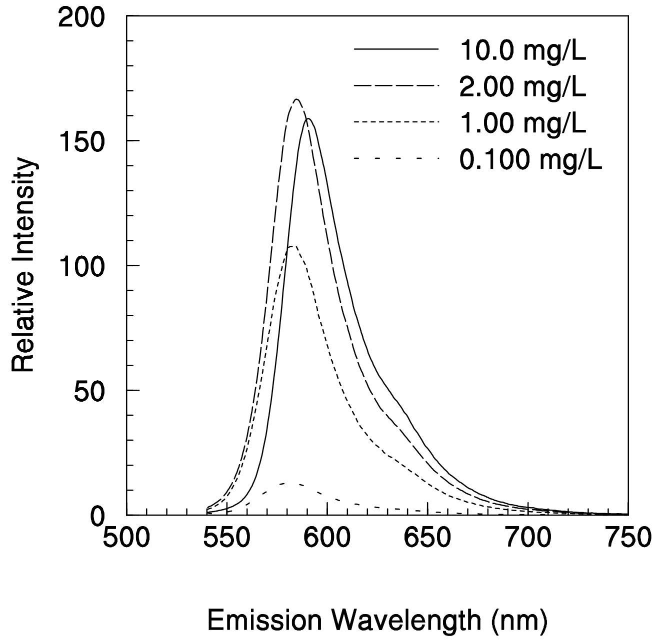

Figure 10. Relative fluorescent emission intensity spectra from rhodamine-water solutions excited by 532 nm light. The response maximum for 2.00 mg/L of dye is at 584.5 nm.

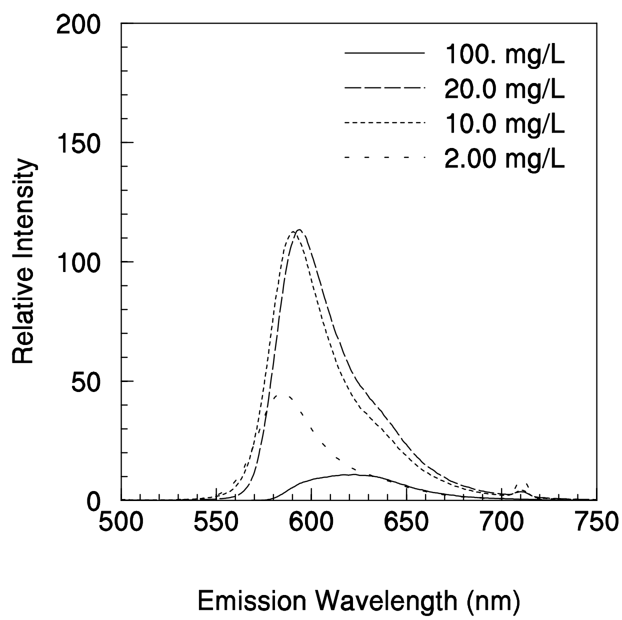

Figure 11. Relative fluorescent emission intensity spectra from rhodamine-water solutions excited by 355 nm light. The response maximum for 20.0 mg/L of dye is at 594 nm.

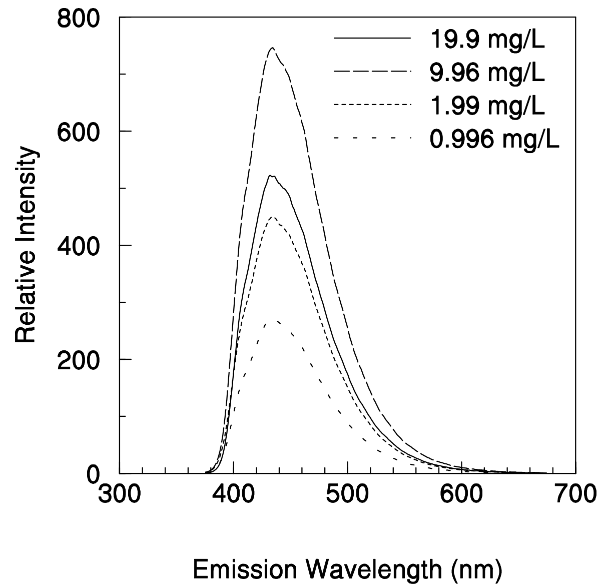

Figure 12. Relative fluorescent emission intensity spectra from stilbene-water solutions excited by 355 nm light. The response maximum for 9.96 mg/L of dye is at 434 nm.

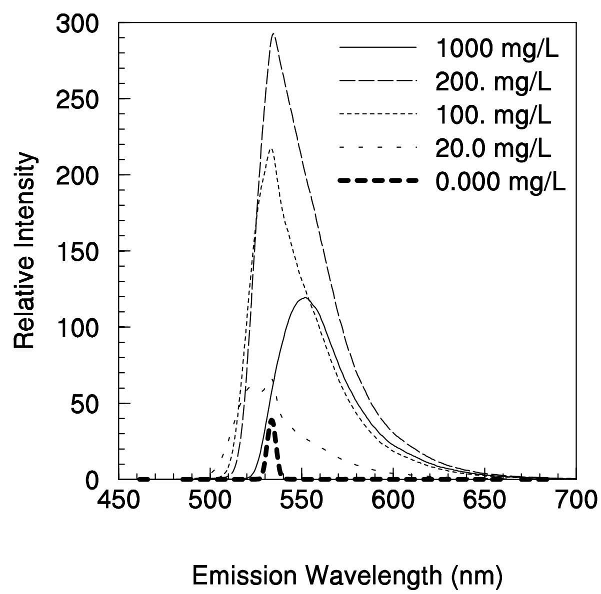

Figure 13. Relative fluorescent emission intensity spectra from fluorescein-water solutions excited by 532 nm light. The response maximum for 200. mg/L of dye is at 534.5 nm. Note that fluorescein may not be fluorescing at this wavelength due to uncertainty in the incident wavelength, but the response curve does indicate that it is fluorescing about the excitation wavelength of 532 nm.

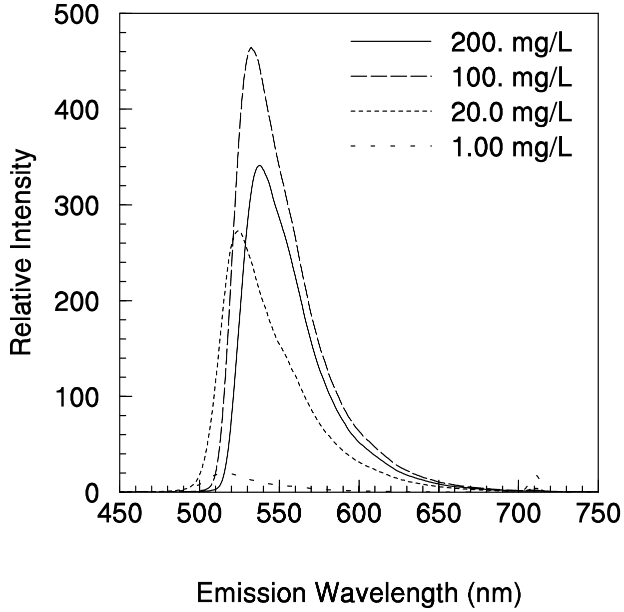

Figure 14. Relative fluorescent emission intensity spectra from fluorescein-water solutions excited by 355 nm light. The response maximum for 100. mg/L of dye is at 532.5 nm.

Signal intensities from solutions containing both rhodamine and stilbene are shown in Figure 15. Note that the emissions from the combination solutions are less than the emissions from the solution with stilbene alone (superposition is not valid), even though rhodamine fluoresces in response to 355 nm light. From the data in Figure 16, it can be seen that the primary emission wavelength from the stilbene dye is absorbed by the rhodamine dye. Therefore, when the two dyes are in solution together, the rhodamine will attenuate some portion of the signal from the stilbene. Stilbene, however, has no absorption effect on the fluorescence signal from rhodamine, nor does it fluoresce in response to 532 nm light. For these reasons, the stilbene concentration will be set to its emission maximum (10 mg/L), while the rhodamine concentration will be set to the lower concentration side (3 mg/L) of the emission maximum. This should provide the maximum possible signal.

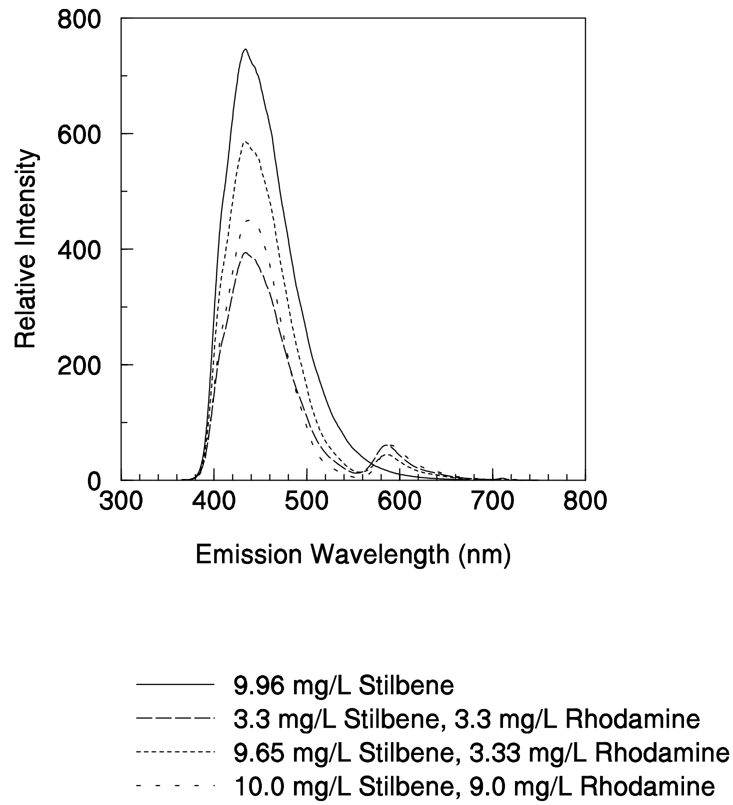

Figure 15. Relative fluorescent emission intensity spectra from rhodamine-stilbene-water solutions excited by 355 nm light. The response maximum for 3.33 mg/L rhodamine and 9.65 mg/L stilbene in water is at 433 nm.

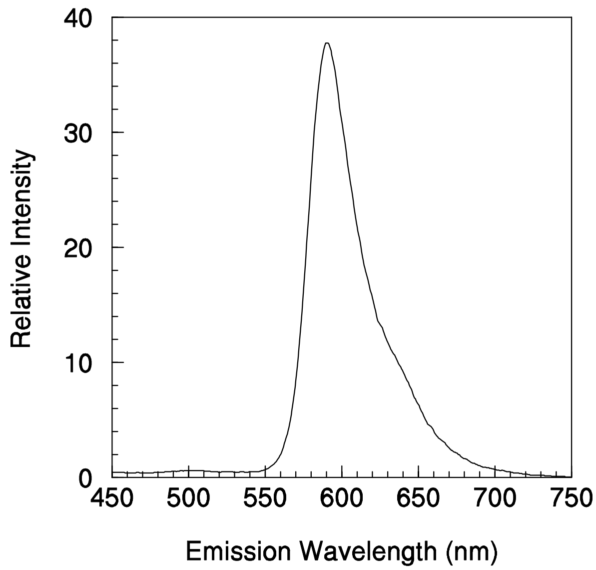

Figure 16. Relative fluorescent emission intensity spectra from rhodamine-stilbene-water solution excited by 434 nm light, which is the wavelength of the fluorescence emission maximum for stilbene-water mixtures excited by 355 nm. The rhodamine in the mixture is absorbing some of the 434 nm light, and fluorescing at 590 nm.

In a different set of experiments, various concentrations of rhodamine and fluorescein dyes were qualitatively tested by passing a beam through a glass tube filled with the mixture (Everest and Atreya 2003). The fluorescence emissions were imaged onto videotape by a Cohu CCD camera with a f/2.8 lens and Schott OG530 filter, and analyzed using a Data Translation frame-grabber board and ImagePro software. An OG530 filter was chosen to allow some 532 nm scattering to be imaged. The results were consistent with those obtained from the spectrometer data shown in Figure 9. These experiments confirm that small-scale spectrometer data is applicable to the larger-scale experiments.

The spectral responses for the dye solutions can be corrected for the effect of the 532 nm notch filter used in the present work (Figure 17), since it will remove some part of the fluorescent signal. Recall that the filter is needed to remove the green scattered light that would otherwise interfere with the fluorescent signals. The characteristics of this particular filter were specifically chosen to work with the two dyes used in the experiments.

The responses of the dye solutions with the calculated response of the notch filter are shown in Figure 18 and Figure 19. The filter has little effect on the integrated intensity function for 532 nm excitation since the portion of fluorescent emission spectrum near 532 nm is small. The filter does have an effect on the emissions from 355 nm excitation, however, since the fluorescent emission spectrum overlaps the region about 532 nm where the filter is active. Since the fluorescence signal from stilbene is very strong, however, there is still sufficient signal for imaging.

These plots are valuable since they illustrate the intensity-wavelength relationship that will be passing through the camera optics to the film. Not only is the peak emission wavelength indicated, but it is possible to calculate the 50% cumulative emission intensity wavelength, which is the wavelength above which and below which 50% of the integrated relative intensity versus wavelength function lies. With the filter installed and 532 nm excitation, 50% of the fluorescent light intensity is above 592 nm. For 355 nm excitation, 50% of the fluorescent light intensity is above 439 nm with the filter installed. These wavelengths indicate the color of the droplet images seen on film, and are also used for the depth of field calculations.

The figures also illustrate, along with Figure 9, the relative response of the dye solutions to the two excitation wavelengths. Since Figure 18 and Figure 19 contain data from water containing both dyes, as well as account for the 532 nm notch filter, they better represent the differences in signal levels from the two dyes that will be observed. Although the laser power in the experiments at 532 nm is nearly twice the power at

355 nm, the integrated response of the water-dye mixture to 355 nm is approximately 2× greater than to 532 nm, suggesting similar image intensities. This is in fact the case, which is shown in the experimental images to be discussed later.

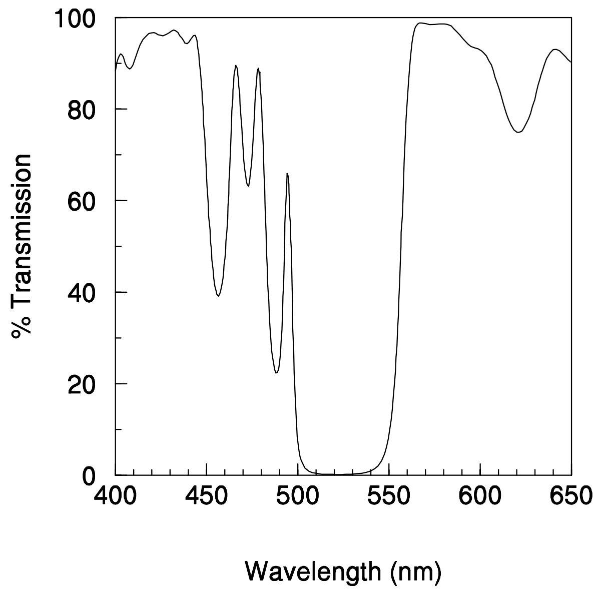

Figure 17. Transmission function for 532 nm notch filter. The filter is used on the camera during the two-color fluorescence measurements to exclude 532 nm light that will be scattered by the water droplets.

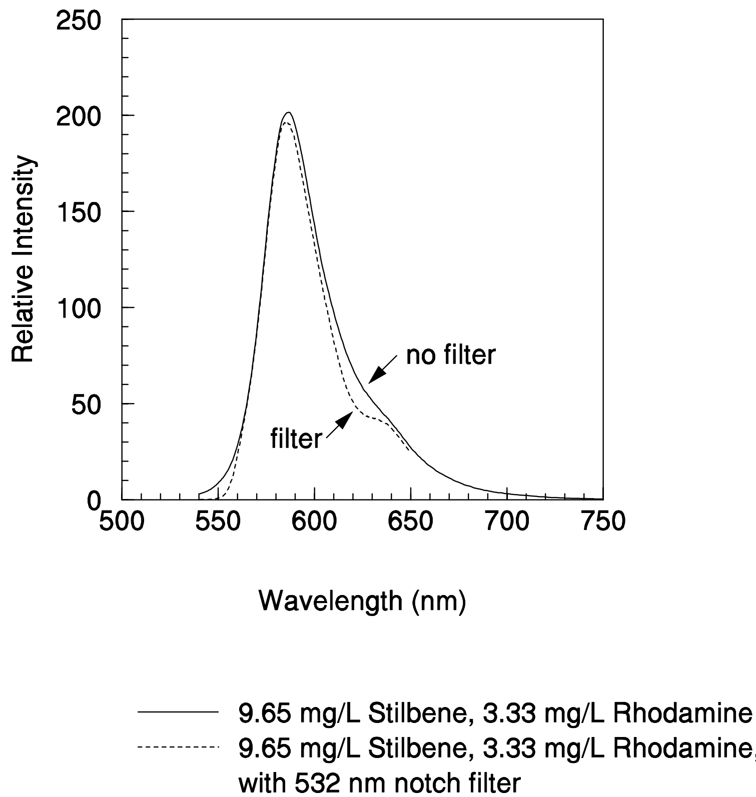

Figure 18. Fluorescent emission intensity spectra of rhodamine-stilbene-water solutions excited by 532 nm light. Comparison of results with and without 532 nm notch filter. The peak emission wavelength without the filter is at 587 nm, and the peak emission wavelength with the filter is at 586 nm. With the filter installed, 50% of the fluorescent light intensity is above 592 nm. This is one of the wavelengths used for the DOF calculations.

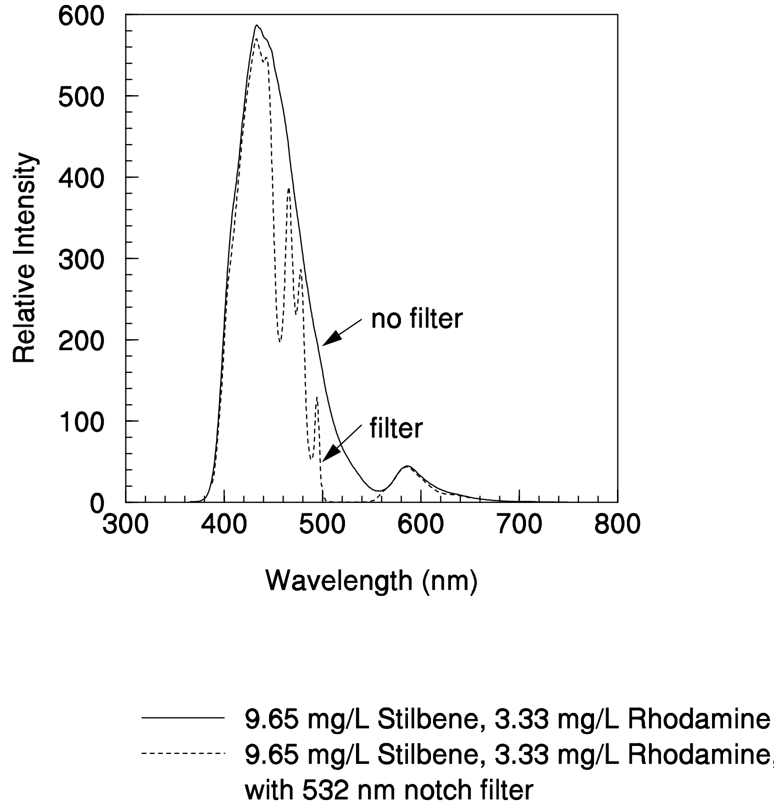

Figure 19. Fluorescent emission intensity spectra of rhodamine-stilbene-water solutions excited by 355 nm light. Comparison of results with and without 532 nm notch filter. The peak emission wavelengths with and without the filter are at 433 nm. With the filter installed, 50% of the fluorescent light intensity is above 439 nm. This is one of the wavelengths used for the DOF calculations.

3.5 Image Resolution

Assuming that the signal from the droplets is sufficient to form detectable images, the uncertainty of size measurements may be estimated by examining the resolution of the system. Resolution may be measured with the USAF 1951 resolution chart, which consists of an array of parallel alternating light and dark bars of various spatial frequencies. (Figure 20) A line pair per mm of resolution is defined as one dark bar and one light bar per mm of length, and abbreviated lp/mm. A magnified set of bars is shown in Figure 21. This figure illustrates 0.25 lp/mm of resolution, where each bar (line) is 2 mm wide, and a line pair covers 4 mm.

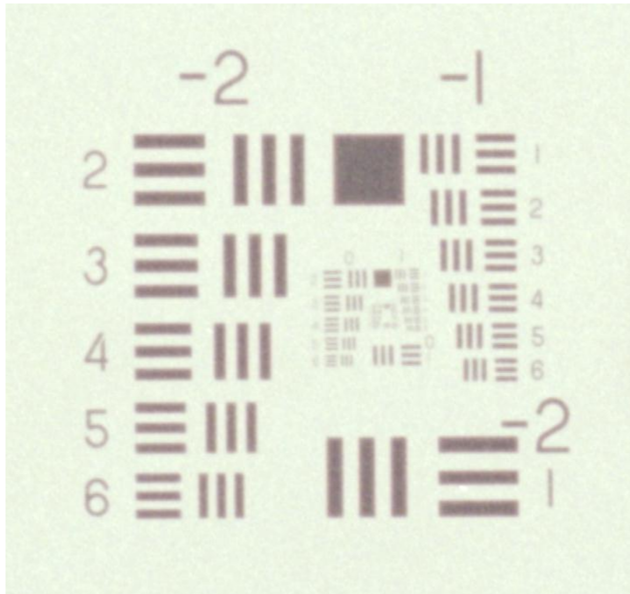

Figure 20. A portion of the USAF 1951 resolution chart. The chart is imaged and used to determine the resolution of the imaging system.

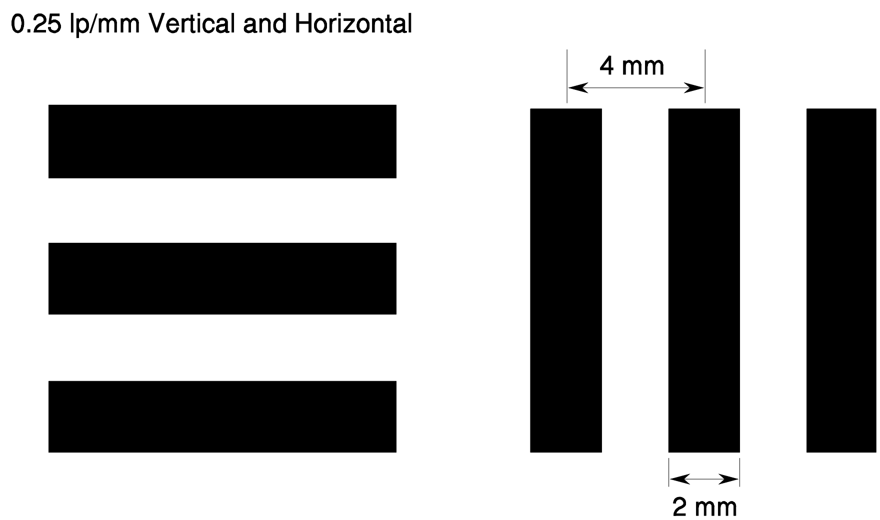

Figure 21. Magnified set of lines from the USAF resolution chart. Each light and dark bar (line) is 2 mm wide. A line pair covers 4 mm, resulting in a resolution of 0.25 lp/mm.

To determine resolution, the chart is photographed and digitized with the imaging system. The magnified images are then examined. The images can be viewed with the eye, and the set of differentiable lines with the highest spatial frequency is said to be the resolution limit of the system. Since the final component (retina) of this measurement is quite variable from person to person, the method is subjective. In order to make the method objective, the contrast between the light and dark bars is measured as the spatial frequency of the lines increases. Contrast is defined as: (Smith 2000)

$$C(\nu) = \frac{I_{\max} - I_{\min}}{I_{\max} + I_{\min}} \qquad (9)$$

where: I_{max}= intensity level at brightest location of the light bar
I_{min}= intensity level at darkest location of the dark bar
ν = spatial frequency (lp/mm)

At very low spatial frequencies, there is a single dark line on a large light area, and $\nu \rightarrow 0$. At this low frequency, light lines approach the highest intensity measurable by the imaging system, the dark lines approach the minimum measurable intensity of the measurement system, and $C(\nu \rightarrow 0)=1$. As the optical system measures lines of gradually increasing frequency, the system will reach a point where it can no longer fully capture the transitions from light to dark and dark to light. The contrast between light and dark decreases, until $C(\nu)$ in Equation 9 reaches zero at the cutoff frequency. For diffraction limited (perfect) systems, the cutoff frequency (Smith 2000), RES_C, expressed in lp/mm, is given in Equation 10.

$$RES_C = \left[\lambda \ (f\#)\right]^{-1} \qquad (10)$$

The reduction in contrast with increasing spatial frequency is illustrated in Figure 22 and Figure 23. In Figure 22, the response of the system to a low frequency signal illustrates that the output signal closely follows the input signal. The maximum and minimum normalized intensities are the same for both signals. There is some loss of sharpness at the light/dark bar transition, however. In Figure 23, the response of the system to a high frequency signal is shown. The maximum and minimum normalized intensities of the output signal differ from the input signal by approximately 20%, and the transitions between light and dark are becoming less distinct. The overall effect is to make the boundary between the lines and the background less distinct, and an increase in the uncertainty of the line width with increasing spatial frequency. In both examples, the intensity was normalized by the maximum intensity measurable by the system, or saturation intensity.

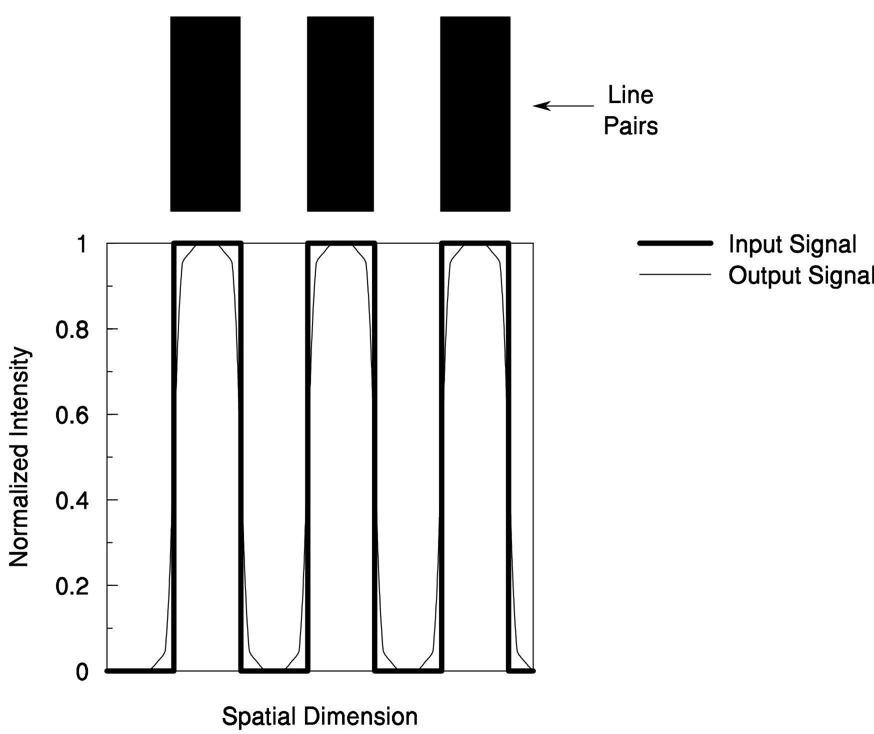

Figure 22. Spatial frequency response of a generic optical system to a low frequency signal illustrating high contrast.

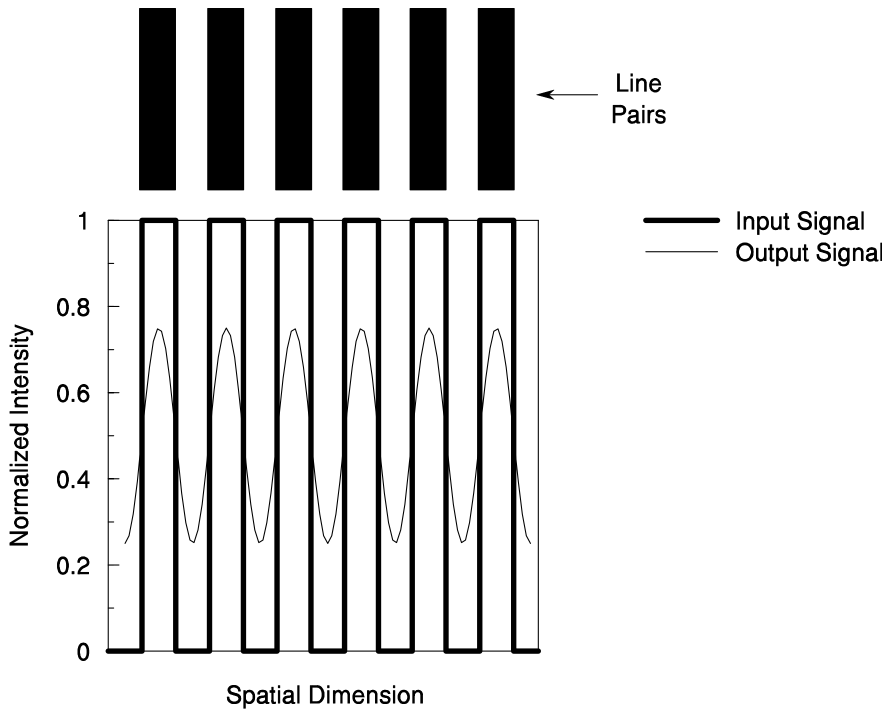

Figure 23. Spatial frequency response of a generic optical system to a high frequency signal illustrating reduction in contrast.

The function describing the performance of the system as a function of frequency is the modulation transfer function (MTF). The MTF illustrates the reduction in contrast of the image as the spatial frequency increases, and is defined as:

$$MTF(\nu) = \frac{C(\nu)}{C(0)} \tag{11}$$

The MTF can be used to quantify the performance of each component in the imaging system, and the overall system MTF later determined by calculating the product of the individual MTF functions according to Equation 12. In order for the calculation to be valid, the optical components cannot be coherently linked. Since we effectively have a diffuser between each of the groups of lenses (ie. film between the camera lens and scanner lens) our components are not coherently linked. For systems that are coherently linked, a more general optical transfer function with real and imaginary parts is used to account for the phase and magnitude of the light (Williams and Becklund 1989).

$$MTF(\nu) = MTF_{Lens}(\nu) \times MTF_{Film}(\nu) \times MTF_{Scanner}(\nu) \qquad (12)$$

For a perfect system, ie. diffraction limited with no aberrations, the maximum useful resolution is given by the Rayleigh limit. At the resolution corresponding to the Rayleigh limit, the separation of two images is such that the maximum of one diffraction pattern coincides with the first dark ring of the second diffraction pattern. At this distance apart, the droplet images are degraded, but the presence of two maxima can be clearly seen. The resolution at the Rayleigh limit, RES_R, in lp/mm is given by Equation 13 (Suiter 1994, Smith 2000).

$$RES_R = \left[1.22\lambda\ (f\#)\right]^{-1} \qquad (13)$$

For an f# of 5.6, the diffraction limited resolution of 355 nm excited droplet images (439 nm emission) is 333 lp/mm and the diffraction limited resolution of 532 nm excited droplet images (592 nm emission) is 247 lp/mm. Recall that this is the limitation of a perfect system, which is only limited by the diffraction of light due to the camera aperture. Resolution stated in this manner is most useful when closely spaced objects are observed. Since the droplets to be measured in our system are in a dilute two phase flow, we expect our droplets to be many diameters apart. This representation of resolution is useful for determining the limitations of the measurement system; however, since it also indicates how quickly the system can transition from light to dark areas at the edge of droplets. The value of the MTF is approximately equal to 0.09 at the Rayleigh resolution limit (Suiter 1994).

The system uncertainty is examined using the MTF concept since film and lenses do not have pixel equivalents. The scale of interest in this case is 200 μm, which is the smallest droplet of interest in the current experiments. Thus, a cycle occurs over 400 μm, which is equivalent to 2.5 lp/mm of resolution in our measurement region. Assuming a magnification M=0.13, the equivalent film resolution would be 19 lp/mm. Next, the value of the MTF function for each optical component is determined at the spatial frequency of 19 lp/mm. From Fuji NPZ800 film datasheets (Fuji Photo Film Co., Ltd 2001) (Figure 24), the MTF (at 19 lp/mm) = 0.85. For a f/4.0 maximum aperture Mamiya lens, the overall MTF (at 19 lp/mm) is given as 0.71 by Photodo, which is an average response over the entire lens surface (Photodo AB 2002) (Figure 25). Unfortunately, the MTF function for the film scanner is not available, but can be calculated if the MTF of the entire imaging system is available.

The system MTF was measured experimentally by photographing the USAF resolution chart and digitizing it with the film scanner. The digital images were analyzed by measuring the intensity profile perpendicular to the line pairs in the image with a spatial frequency of 19 lp/mm. The intensity profiles provide the values of I_{max} and I_{min} for Equation 9. The contrast values calculated from Equation 9 are input into Equation 11, which gives the value of the MTF for the spatial frequency at which the intensities were measured. The value of the MTF for the entire imaging system was determined to be 0.20 at a spatial frequency of 19 lp/mm.

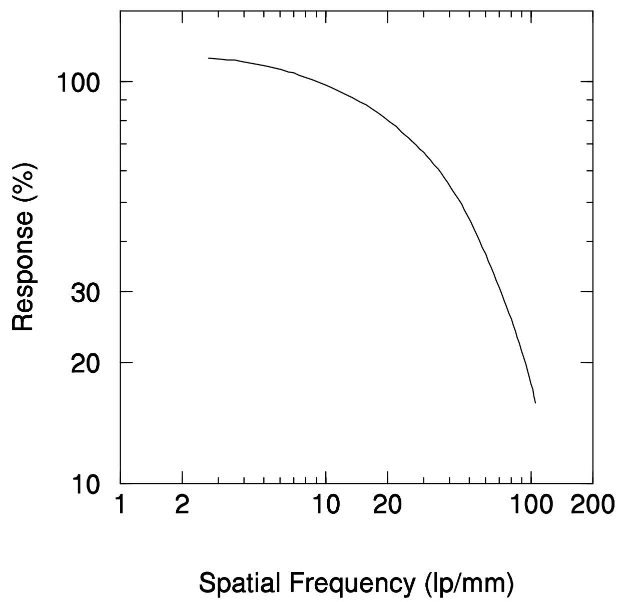

Figure 24. Spatial frequency response for Fuji NPZ800 film. Due to the chemistry of the film, per Fuji, the measurements show a response >100% at low frequencies.

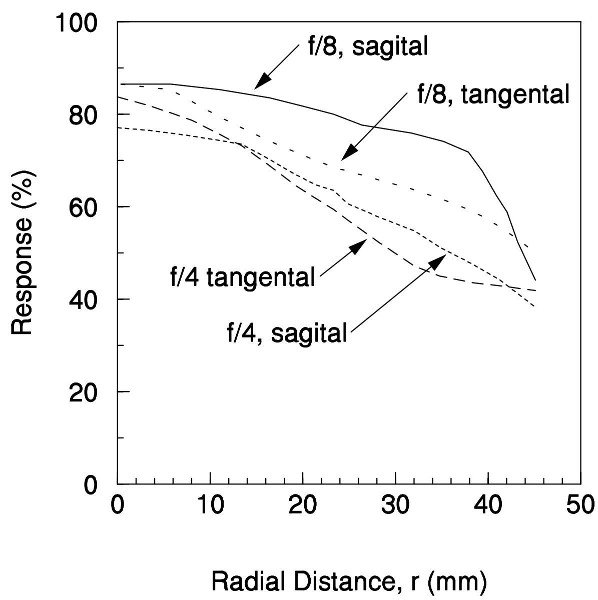

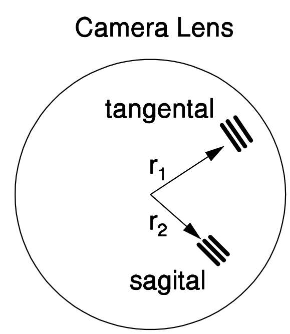

Figure 25. Spatial frequency response of Mamiya camera lens. Response of the lens varies with the radial location and orientation of the pattern used for resolution measurement, as well as the f# setting. Radial distance is the distance from the center of the lens. Tangental data indicates measurements of line patterns perpendicular to the lens radius, sagital data indicates measurements of line patterns parallel to the lens radius.

Since the MTF curve for the scanner is not available, back calculation yields the MTF (at 19 lp/mm) for the scanner alone as 0.30 (See Equation 12). It is clear from these calculations that the limiting component in the system is the scanner which has a performance level significantly lower than that of the camera lens and film. In addition, the spatial frequency of interest is less than RES_R~250 lp/mm, so the measurement system is limited by aberrations or defocusing effects, not by diffraction. The MTF calculation is valuable for determining the potential differences in performance of various films. One such comparison showed that there was no resolution penalty for using Fuji 800 ASA film versus Fuji 400 ASA film, but the speed difference resulted in a significant gain in light sensitivity. The ability to increase the film speed by a factor of 2 allows for the changing of the lens aperture by one f-stop, a precious bit of flexibility. These results are summarized in Table 2.

Table 2. Summary of modulation transfer function values for optical system components.

Component	Frequency, ν (lp/mm)	MTF(ν)
Camera lens	19	0.71
Film, Fuji NPZ 800	19	0.85
Film, Fuji NPH 400	19	0.80
Film scanner	19	0.30
Total optical system using Fuji NPZ 800 film	19	0.20

While the MTF analysis has indicated that the limiting component in the system is the scanner, the results are not directly applicable to determining how the system resolution limitations affect the uncertainty in droplet sizes. Disagreements exist in the literature (Biberman 1973) as to how the MTF relates to the quality of a complex image. Since the scanner is the limiting factor in the measurements, this implies that the effect of the pixels (spatial sampling frequency) is important. The ability of the finite pixels or pixel equivalents to represent the droplets, especially the edges, is of primary concern. This behavior will have a direct effect on how the edge is represented, and therefore the droplet size. The MTF concept tells us how the system spatially transitions from light to dark and vice versa. The effect of the scanner, due mostly to pixelization, greatly affects our measurements since the pixels (50 μm) are relatively large compared to the smallest droplet size (200 μm), and relative to the film, lens, and aperture capabilities.

The scanning of the resolution chart is examined at the pixel level. The photos are digitized with a 4000 dpi optical scanner, and if we neglect the circle of confusion formed by diffraction limitations of the lens or aperture, or by the image being slightly out of focus, the most detail we can expect from the image is on the order of the pixel size. As the line width begins to approach the pixel size of the scanner, several observations can be made. Clearly, lines can not be resolved if the pixel size is greater than the line width. The maximum performance of the scanner would take place when the line width is the same as the pixel width. In practice, however, the lines are not always aligned with the pixels, the result being a reduction in contrast due to pixel averaging of the line edge over two pixels. Therefore, it is necessary to have each line pair covered by more than 2 pixels, with perhaps 3 to 4 pixels per line pair necessary for satisfactory results. The effects of pixels that overlap line boundaries are shown in Figure 26. It can be seen that the signal level drops due to the pixel averaging over the line boundary. This may be partially responsible for the asymmetrical intensity peak on one side of the droplet image, although off-center peaks due to the spatial distribution of fluorescent intensity are usually caused by the internal reflections within the droplet (Domann and Hardalupas 2001a).

By examining Figure 26, it appears that the "correct" line width is found by using one pixel in from the edge where the signal rises above the background. In this case, the uncertainty in the line width would be ±1 pixels, since each side of the drop would be rounded to the nearest pixel. By using this calculation method, if a given line width of 2 pixels is resolved by 3 pixels, an error of 33% (1 of 3 pixels) could result. If the same line width is resolved by 4 smaller pixels, the resulting error would be 25% (1 of 4 pixels). For the lens/film/scanner combination operating at M=0.13, each pixel is approximately 50 µm in size. If a line is adequately resolved by 3 pixels, then the measurement can occur over a distance of 150 µm, resulting in a resolution of 6.7 lp/mm (1/150 µm). Resolving a line using 4 pixels, however, would occur over a distance of 200 µm, resulting in a resolution of 5.0 lp/mm (1/200 µm). Note that the gradients of the intensity are used to determine the edge of the line, which is the same method used in this thesis to determine droplet size. It was found that drop diameters derived from analysis of the intensity gradient were closer to the true value than methods utilizing threshold image intensity.

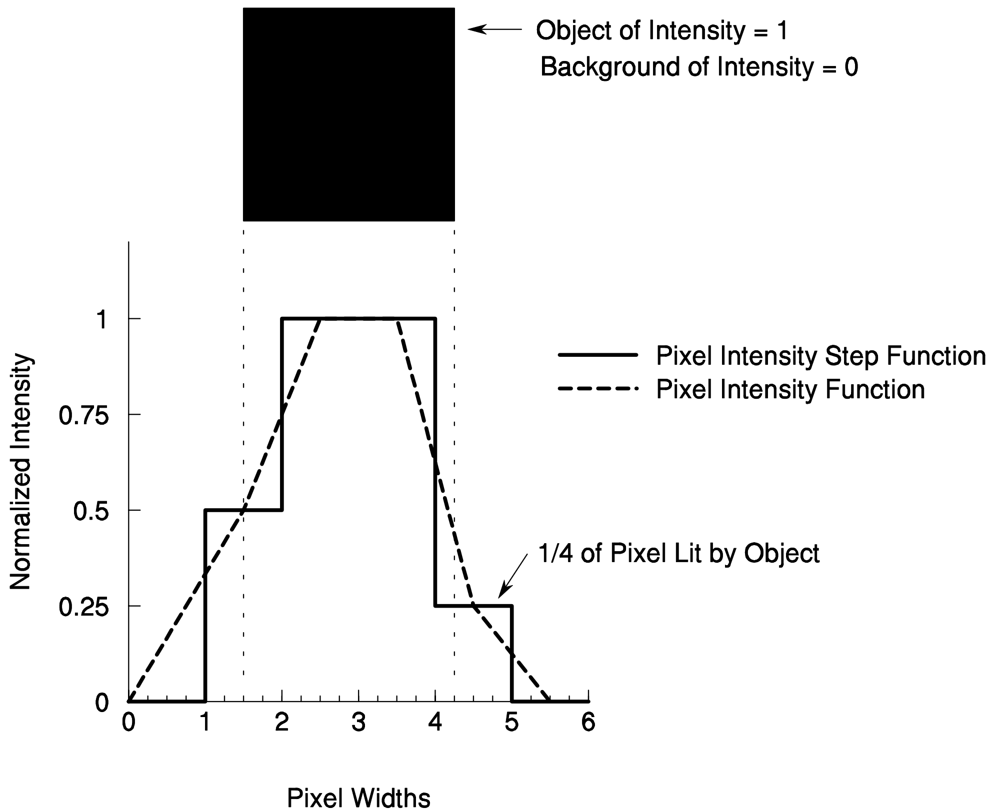

Figure 26. Pixel averaging effect on the edge of an object.

The effects of camera aperture and film scanner settings on resolution are investigated by measurements of images from the USAF 1951 resolution chart. Photographs of the resolution chart are digitized with the film scanner, and the contrast and MTF values for various spatial frequencies were calculated using measured intensity profiles, Equation 9, and Equation 11. The spatial frequencies corresponding to the Rayleigh limit, MTF(ν)=0.09, are determined for various camera aperture settings and scanner bits per channel. The amount of data used by the film scanner to define each pixel is limited by bit per channel setting. Each pixel is represented by 3 channels, the definition of which depends on the color model used. The RGB model, for example, is commonly used for general purpose image analysis, and assigns a red, green, and blue intensity to each pixel. The HSI model used in this work describes a pixel in terms of hue, color saturation, and intensity. Hue is defined as the color, and saturation as the pureness of the color. Red and pink, for example, are different saturations of the same color. In the HSI model, the intensity value alone determines the pixels brightness, which is equivalent to the average of the red, green, and blue values in an RGB image. For 8 bit/channel scanning, each pixel channel can have a value between 0 and 2^8, or an intensity of between 0 and 256. For 16 bit/channel scanning, each pixel channel can have a value of 0 to 2^{16}, or an intensity of 0 to 65536. The results of the resolution determinations are summarized in Table 3. Contrary to the diffraction errors predicted in Equation 7, the measured resolution is higher for the smaller aperture, due to less defocusing error. As can be seen from the f#=5.6 case, scanning the images at higher bit/channel settings may increase the resolution.

The measurements summarized in Table 3 also show agreement with the thought experiment conducted using Figure 26. It was argued that if 4 pixels, 50 µm in size, are needed to resolve 200 µm, then the resulting resolution is approximately 5.0 lp/mm. This agrees satisfactorily with the values presented in Table 3 for all camera apertures and bit per channel settings, especially for f#=8.0. In addition, the data in the table shows that the imaging system has more than enough resolution for resolving 200 µm drops (A resolution of 3.6 lp/mm from the table as compared to a minimum resolution of 2.5 lp/mm from the discussions of MTF and Figure 24).

Table 3. Aperture effect on resolution.

f# (camera aperture)	Bits per channel (HSI)	Resolution, film plane (lp/mm)	Resolution, measurement plane, M=0.13, (lp/mm)
5.6	8	27.7	3.6
5.6	16	30.8	4.0
8.0	8	38.5	5.0
8.0	16	38.5	5.0

3.6 Identification of Minimum Signal Levels

It is important to understand how the fluorescence signal intensity varies with the drop size and the f# of the optics. The intensity curve corresponding to Equation 6, and normalized using experimental data for dyes in water, was plotted in Figure 5. Experimentally this was investigated by imaging fluorescence from 201 μm ± 1.34 μm ethanol droplets doped with stilbene and rhodamine dyes. The ethanol/dye droplets were illuminated with a 355 nm laser sheet 13.5 mm ± 0.5 mm thick, and centered within the laser sheet and camera depth of focus. A 532 nm notch filter was installed, which was used to remove the 532 nm scattered light. Images were taken at a magnification of approximately 0.20 at f#s of 4.5, 5.6, 6.7, 8.0, and 9.5. The laser intensity was the same as that used in the 460 mm × 540 mm spray experiments to be described later so that they would be applicable to the large scale sprinkler measurements. The image intensity, corrected for a background intensity of approximately 10, is normalized by the film/scanner saturation intensity, and shown versus f# in Figure 27. While the concentrations of dye are different than those used in the sprinkler experiments, and using alcohol as the solvent increases the fluorescent signal as compared to water, this data is useful for studying the signal level dependence on f#.

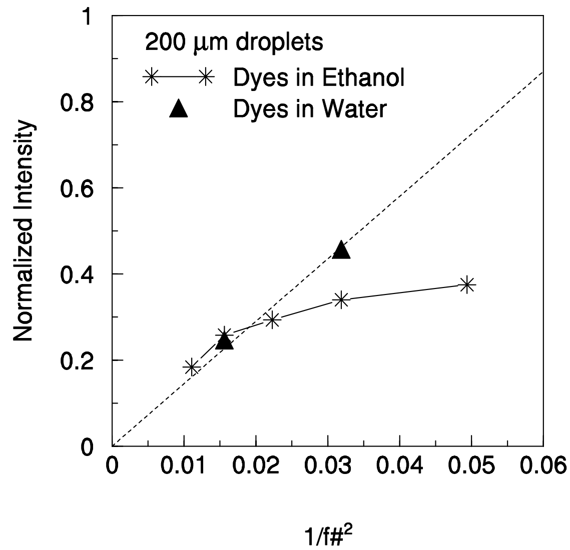

Figure 27. Normalized fluorescence response from a 200 μm nominal diameter drop excited with a 355 nm beam for a range of camera aperture f#s.

Water droplets with diameters of 201 μm ± 1.34 μm, doped with 9.65 mg/L of stilbene and 3.33 mg/L of rhodamine were also imaged. The signal intensity, corrected for a background of approximately 20, was normalized by the film/scanner saturation intensity and plotted in Figure 27 versus f#. The drops were illuminated with a 355 nm laser sheet 13.5 mm ± 0.5 mm thick, and centered within the laser sheet and camera depth of focus. The camera used a 210 mm lens with a 532 nm notch filter to remove the 532 nm scattered light. Images were taken at a magnification of 0.13, resulting in a 460 mm ×540 mm measurement region. The dye concentrations, laser powers, and camera setup were the same as used in the sprinkler experiments to be discussed later.

The fluorescence intensity was also measured from 2.8 mm ± 0.14 mm diameter drops by Everest and Atreya (Everest and Atreya 2003). The droplets were centered in both the nominally 5 mm thick laser light sheet and the depth of field of the camera. A long-pass 550 nm filter was used to collect 588 nm rhodamine fluorescence resulting from 355 nm excitation. Images were taken at a magnification of 0.09 for f#s of 1.2, 2.8, 4.0 and 5.6. The laser intensity was approximately 250 mJ per 10 ns pulse. The measured change in droplet image intensity, normalized by the film/scanner saturation intensity, is shown versus f# in Figure 28. The average background signal of 34 was subtracted from the data. The droplet diameters measured from these photographs were 2.7 mm ± 0.27 mm.

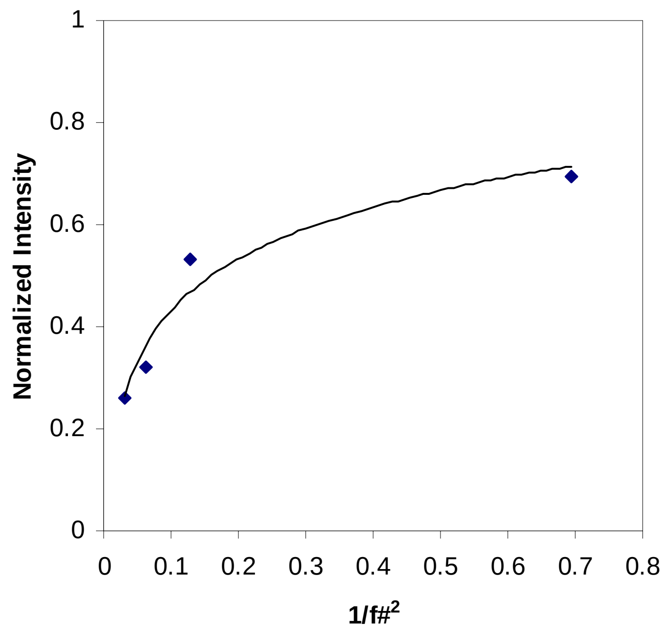

Figure 28. Normalized fluorescence response from a 2.8 mm diameter drop excited with 355 nm beam for a range of camera aperture f#s.

Contrary to expectation, the measured signals from the 200 μm ethanol droplets and the 2.8 mm water droplets are not linear with $1/f\#^2$ for the entire range. For a pin-hole camera with a perfect detector, the intensity vs. $1/f\#^2$ plot should be a straight line through the data and the origin. The intensity function appears to be roughly linear at the lower intensity levels (small apertures), but decreases in slope as the aperture size increases. For the 2.8 mm droplets, this behavior can be partly explained by the decreasing depth of field as the aperture increases in size according to Equation 8. For the given magnification and wavelength, the depth of field is greater than ~3 mm for f#s greater than 2.8 (Equation 8). However for f# of 1.2, the depth of field is only 0.5mm, much smaller than the drop diameter. The 355 nm laser sheet width, defined by full width at half maximum (FWHM) for a Gaussian intensity profile, was approximately 3.5 mm for the 2.8 mm droplets, much larger than the depth of field and slightly larger than the drop. The drop is therefore fully illuminated, but the fluorescence outside the depth of field is not in focus and therefore does not increase the signal as anticipated. Hence, the depth of field serves to limit the fluorescence volume used in Equation 6. For drops that are larger than the depth of field, the fluorescence volume is likely proportional to DOF $\times$ $(d_{drop})^2$ rather than $(d_{drop})^3$. Since DOF is also proportional to $f\#^2$, Equation 6 and Equation 8 indicate that for drops larger than DOF, the intensity should not depend on the f#. There is some increase in fluorescence signal at f#s smaller than 2.8, however, as indicated by the data in Figure 28, so the droplet portion out of the depth of field still makes some contribution to the measured signal. For f#s larger than 2.8 (small values of $1/f\#^2$), it may be useful to fit a straight line through the data and the origin to approximate the behavior of the function over this range of values.

Examination of the signal levels from the 200 μm nominal diameter droplets provides more information on the subject. Since the droplets are well within the laser sheet and depth of focus for all aperture settings, blurring is not a factor. Instead, the non-linearity of the intensity versus $1/f\#^2$ function may be due to the response function of the measurement system. The film response is one potential source of non-linearity, and a sample photographic density vs. exposure graph is shown in Figure 29. It can be seen that the film response to light is linear over a middle range of exposures (exposure intensity and exposure time are both important), but the slopes change dramatically at low and high exposures, a phenomenon referred to as the reciprocity effect. Therefore, at low and high signal levels, an increase in signal level has less of an effect on film density than at mid-range exposure levels. Since we are conducting our experiments in the mid-range of intensities, we will be working within the roughly linear region of the film response function. If the reciprocity effect was a factor, then the shape of the plot in Figure 27 would suggest that the film is reaching saturation at $1/f\#^2>0.02$. Measurements have shown, however, that the film is not saturated at this level ($I \approx 0.4$), and that saturation occurs at $I=1$ by definition. While the non-linearity of the normalized intensity vs. $1/f\#^2$ function may be in the detection system, consisting of the optics, film, and scanner, it has not been linked to any particular component of the system.

Examination of the 200 μm water droplet data, however, shows good agreement with the behavior of a perfect pin-hole camera. As seen in Figure 27, a straight line with a slope of 14.5 can be drawn fitting the data and passing through the origin. This relationship will be used in this work since the data range shown in the figure encompasses the operating conditions used in the sprinkler drop size experiments. It is possible, however, that if the 200 μm water droplet data was extended to larger values of $1/f\#^2$, that the slope of the function could decrease with $1/f\#^2$ like the 200 μm ethanol droplet function.

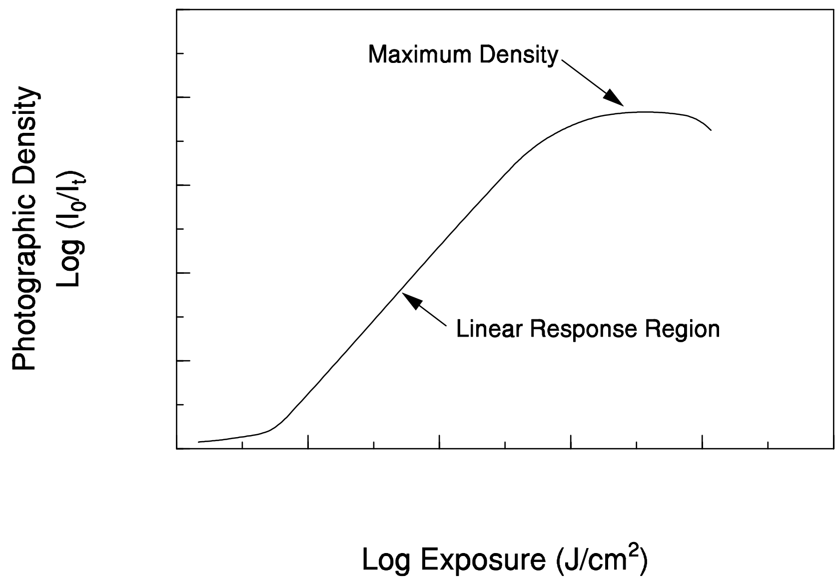

Figure 29. Response curve for a typical photographic film. Photographic density is measured by passing light through the negative, and is calculated as $\log_{10}$(incident intensity/transmitted intensity).

In addition to the resolution limited droplet size, the minimum detectable drop size must also be determined or estimated. It can be estimated by calculating the minimum measurable fluorescence signal required to illuminate a pixel in the digitized photograph. This signal can be generated by a small diameter drop or by the edges of a larger droplet. A relationship, based on Equation 6, may be used to estimate the minimum detectable drop size. Since many of the factors in Equation 6 have not been measured individually, the expression can be rearranged to combine them into a constant of proportionality, γ, as follows:

$$F = \gamma \left(\frac{I_0 V}{\lambda} \right) \left(\frac{m}{(m+1) f\#} \right)^2 \tag{14}$$

Note that the function F=constant×(1/f#^{2}) goes through the origin in Figure 27.

If the functions φ, f (c), and/or f (R) are available, they may be separated from ‘γ’ in order to study the effect of changing these variables on the fluorescence signal. This may be especially useful for studying the performance of a measurement system at fluorescent intensities where the measurement system response function becomes non-linear.

The minimum detectable droplet size is estimated for each of the excitation wavelengths. For small drops, the fluorescence volume in Equation 6 is proportional to the pixel area×drop diameter until the DOF limit is reached. Data from Figure 27 represents Equation 6 and can be used to calculate the value of γ, and Equation 14 used to find the expected signal for a small drop. The data for 355 nm excitation of water drops is plotted in Figure 27 along with the alcohol droplet data. Note that ‘F’ has been normalized by the maximum intensity of a film pixel, so that it is evident that the film is not saturated. From measurements of 200 μm water/dye droplets in a 355 nm laser sheet and M=0.13, the value of $\gamma=5.50\times10^5$ m^{-1} for an f-stop of 8.0, and $\gamma=4.22\times10^5$ m^{-1} for an f-stop of 5.6. Measurements of 200 μm water/dye droplets in a 532 nm laser sheet and M=0.13 result in $\gamma=2.67\times10^5$ m^{-1} for an f-stop of 8.0, and $\gamma=1.93\times10^5$ m^{-1} for an f-stop of 5.6. According to Equation 14, the two values of γ for the same excitation wavelength should be equal, however experimental uncertainty and the potential for non-linearity in the $1/f\#^2$ relationship is present. An alternative method for determining γ would be to use the line fit of the water/dye data in Figure 27. It is inappropriate to compare the magnitude of the intensities of the water solutions versus alcohol solutions due to differences in the experimental setup and dye concentration. For all factors being equal, the dyes in alcohol were found to produce a greater fluorescent intensity than in water.

Based on previous research by others (Everest and Atreya 2003), it may be assumed that a drop with a signal to noise ratio (SNR)≥2 is detectable. For the current setup, however, the minimum detectable drop size is based on a more severe criterion, where the droplet intensity must be greater than 2 times the background level. This more severe criterion was necessary to differentiate droplets from the background as well as measure their diameters to a low level of uncertainty. From Equation 14, the minimum detectable drop size for the two-color fluorescent setup would be approximately 130 µm for 355 nm excitation. (Normalized background noise level was 18/256, so the drop must have a normalized intensity of 36/256 for detection) For 532 nm excitation, the minimum detectible drop diameter is approximately 168 µm for the 2× background criterion. In both cases, the limiting fluorescence diameter is greater than the pixel dimension of 50 µm.

Table 4. Minimum detectible drop size for f/5.6

Incident Wavelength (nm)	Incident Flux (W/m^2)	Minimum diameter (µm) for F≥2×background	Minimum diameter (µm) for F=0.305
355	250	130	166
532	350	168	211

These estimates are based on dye concentrations, magnification, laser powers, and film/scanner characteristics that are the same as will be used to measure the sprinkler flows. The smallest detectable drop size may be different for actual sprinkler measurements versus the above calculation or for streams of calibration droplets for the following reasons. Since the sprinkler will contain many droplets that are not in the sheet, these out-of-plane droplets will effectively raise the noise level and the intensity of the background. When the background intensity is defined to exclude the out-of-plane droplets, very small in-plane droplets that may have been detectable will have the same intensity as the noise and will be excluded. For this reason, based on the background cutoff used in sprinkler sprays the minimum detectable droplet size for 355 nm excitation would be approximately 166 μm (The cutoff intensity level of 78/256=0.305 was defined in the droplet sizing and velocity algorithm to be discussed later. This value was based on the background intensities of droplets that were outside the laser sheet in actual calibration photographs). For 532 nm excitation, the minimum detectible drop diameter is approximately 211 μm for the sprinkler spray criterion. This subject will be discussed in depth in the droplet sizing method section. The results of calculating the minimum detectible drop size are summarized in Table 4

There is significant uncertainty in the above estimates since all of the factors in Table 5 are important, and not all of the factors can be well quantified. Therefore, the calibration is important in identifying whether or not the 200 μm droplets are detectable throughout the laser sheet. It would also be useful to have an estimate of the smallest drop detectable, in order to estimate the number of drops present in the sprinkler spray that are smaller than our 200 μm lower bound. These sub-200 μm drops can be estimated if they are detectable, and on the order of the 50 μm pixel size to reduce the loss from pixel averaging errors.

Table 5. Measurement system calibration parameters.

Laser Power	Film sensitivity	Film resolving power
Magnification	Aperture / sheet thickness	Lens resolution
Droplet size range	Scanner resolving power	Dye concentration

Assuming that the intensity of fluorescence from a 200 μm droplet is adequate for detection, the measurement area and pixel size can be determined. Using the guideline of having the 200 μm drop covered by a 3 pixel x 3 pixel matrix (4000 dpi scanner, M=0.10, 64 μm pixel size) should result in an error of approximately 30%, while a 4 pixel by 4 pixel matrix (4000 dpi scanner, M=0.13, 50 μm pixel size) should result in an error of approximately 25%.

Now, from the relationships for estimating the minimum visible droplet size, as well as the laser profile and depth of field information, an appropriate f# can be chosen using Equation 8 and Equation 14 (illustrated in Figure 5). This choice will be a compromise since the optimum estimated f# from equalizing the depth of field and beam width results in too little light reaching the camera film. Therefore, an f# of 5.6 was chosen for the measurements. The use of the f# of 8.0 was also investigated, but an f# of 5.6 provides a higher signal level, allowing for decreases in laser power due to degradation and detuning over time.

3.7 Effect of Beam Sheet Thickness and Fluorescence Intensity on Droplet Size and Velocity Measurements

3.7.1 Fluorescence vs. Scattering

While not discussed in depth in this thesis, it is useful to briefly examine the reasons why scattered light droplet images are troublesome for droplet sizing. Everest and Atreya (2003) compared the fluorescent and scattering signals from water droplets doped with Rhodamine WT dye. They used a dual Nd:YAG laser system to form 355 nm and 532 nm light sheets with roughly Gaussian sheet intensity profiles over the sheet thickness. The laser sheets had full widths at half maximum (FWHM) of approximately 4 mm. Drops of approximately 2.8 mm in diameter were produced with a 22 gauge hypodermic needle, and traversed in 1 mm increments from behind through the light sheets. Successive flashes of the lasers illuminate the same drop twice as it falls vertically as shown in Figure 30.

Fluorescence at 588 nm from 355 nm excitation is observed in the upper drop in each frame, while scattering and fluorescence from the 532 nm beam is observed in the lower drop. Filters were not used for taking these images. The scattering of the 532 nm laser beam by the forward edge of the drop is the first and last of the signals observed in the sequence. The largest source of this light is reflected light although signals from the rear and top of the drop indicate the effect of internal reflection. In the sequence of photographs from A to U, the fluorescence from 532 nm appears before the fluorescence from 355 nm due to both a slightly wider beam and the increased response of the dye to 532 nm excitation. Note that both sets of drops are the same yellow/green, and so the drops can not be easily differentiated by color alone. The important conclusion from this work, which is vividly illustrated by Figure 30, is that the size of the scattered light image is a function of position in the light sheet. At the edge of the sheet, it appears as a small, or multiple small droplets. Near the center of the sheet, it appears as an overly large drop with indistinct edges. For these reasons, scattered light signals are not used for droplet sizing, and two fluorescent dyes are used to provide for color differentiation in the current work.

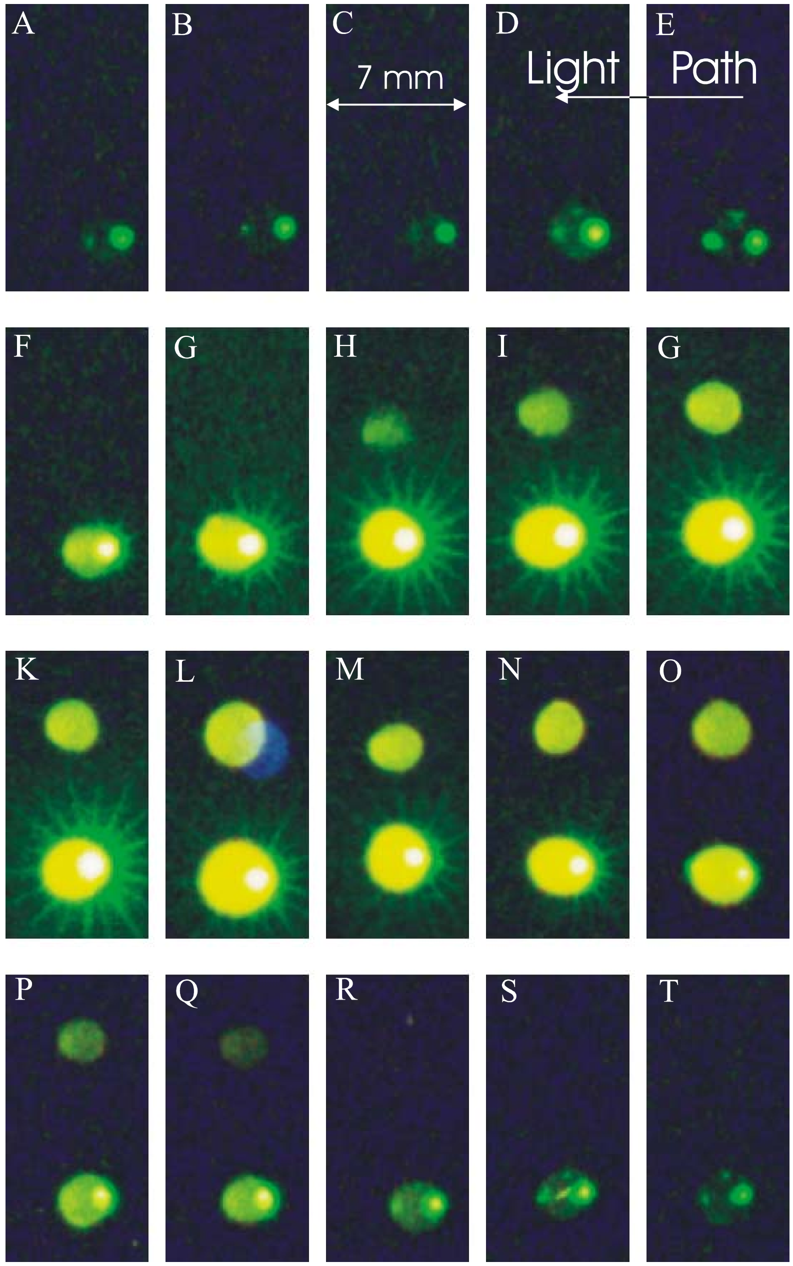

Figure 30. Images of 2.8 mm drop as it is moved forward from behind the laser sheet in 1 mm increments. The 532 nm laser sheet has FWHM of 4.4 mm and the 355 nm laser sheet has FWHM of 3.6 mm. Laser power for the 532 nm beam is 220 mJ/pulse and for the 355 nm beam is 130 mJ/pulse. Fluorescence at 588 nm from 355 nm excitation is observed from the upper drop in each frame, while scattering and fluorescence from 532 nm excitation is observed from the lower drop (Filters were not used in taking these images). When the drop is centered in the beam sheets, the drop size as measured by the 355 nm excitation is 2.7 mm, while the drop size as measured by 532 nm excitation and scattering is 3.3 mm.

3.7.2 Laser Beam Sheet

The laser beam incident intensity and the illuminated drop volume are important for determining the intensity of the signal collected from the drop. The incident intensity is a function of the location of the drop in the light sheet, both vertically and in the depth of the sheet. As stated earlier, a two-color fluorescence method was devised to improve the color differentiation, so the effect of droplet beam sheet position was further investigated for a 460 mm × 540 mm area with a medium format camera. This was done to explore the limits of the technique and develop a method for measurements in real sprinklers. The measurement system was assembled in the same configuration as used for the spray experiments. The laser power profiles were determined by projecting the laser sheet on a sheet of paper. The camera on the opposite side imaged the paper, and the scanned image analyzed. The exposure of the film (f#) was set so that the most intense portion of the sheet in the image did not saturate the film. Beam sheet profiles are shown at the vertical location of zero (where the unexpanded beam would hit) in Figure 31 and Figure 32. One set of beam sheet measurements was conducted using the original beam diameters from the lasers. In order to equalize and reduce the beam sheet widths, an 8 mm slit was installed after the sheet forming optic, resulting in the second set of power profiles. The laser power fluxes at the vertical location of zero (where the unexpanded beam would hit) are shown in Table 6. Based on the second set of sheet profiles (with slit installed) and depth of field calculation, the best aperture setting for a magnification of 0.13 would be f# of 9.5. Note that diffraction from the presence of the 8 mm slit was not significant, as can be seen in the laser sheet power profiles. Laser sheet profiles at vertical locations in the sheet ranging from 30 cm above vertical zero to 30 cm below vertical zero are shown in Appendix A, illustrating consistent power levels throughout the measurement region.

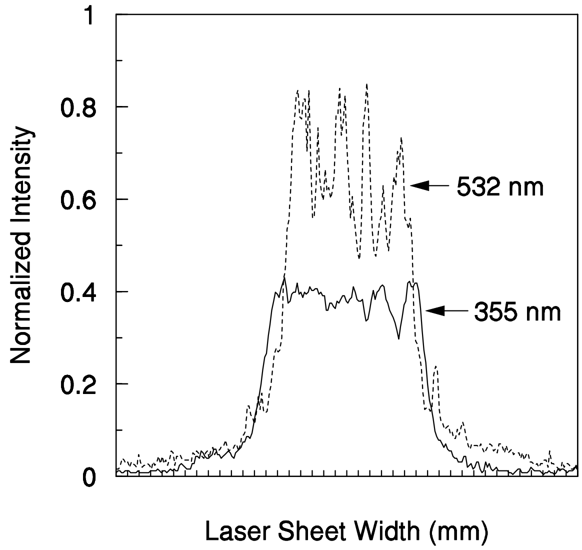

Figure 31. Laser sheet power profile measured at the near edge of the droplet measurement region. Laser power is 4.78 W at 355 nm, and 5.60 W at 532 nm. Beam sheet thickness is approximately 13.5 mm for the 355 nm sheet and approximately 10.0 mm for the 532 nm sheet over a vertical range of 0.6 m.

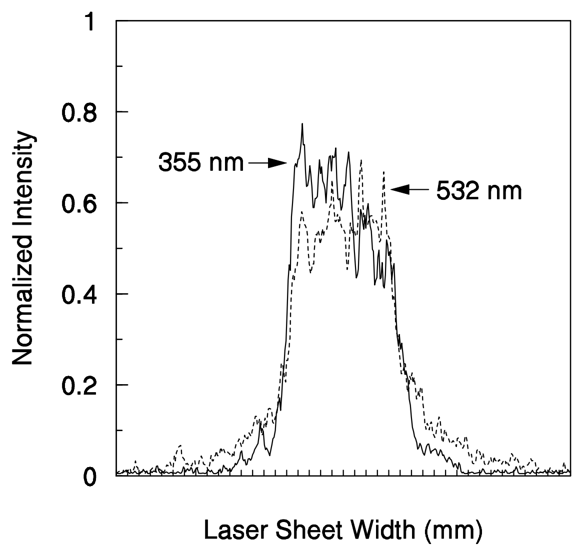

Figure 32. Laser sheet power profile measured at the near edge of the droplet measurement region. Laser power is 4.00 W at 355 nm and 7.20 at 532 nm. An 8 mm steel slit is installed after sheet forming optic. Beam sheet thickness is approximately 10.5 mm for the 355 nm sheet and approximately 10.0 mm for the 532 nm sheet over a vertical range of 0.6 m.

Table 6. Incident radiation flux at vertical center of laser sheet.

Wavelength (nm)	8 mm slit installed?	Nominal Beam Sheet Thickness (mm)	Incident Flux (W/m^2)
355	No	14	315
532	No	11	450
355	Yes	11	250
532	Yes	10	350

A plot showing the predicted depth of field for various f#s is shown in Figure 33. This graph illustrates one of the challenges of using two wavelengths of light. Given the depth of field relation in Equation 8, it is not possible to match the depth of field and laser sheet thickness while retaining the same measurement volume for both wavelengths. In addition, the graphs clearly demonstrate that the difference in DOF for the two wavelengths increases with f#. One possible solution would be to compromise between the two predicted DOFs for the two wavelengths. Another solution is to optimize for one wavelength, and use it for sizing the droplets. In this work, the measurement system was optimized for the 355 nm incident beam (439 nm emission) used for droplet sizing, but was ultimately driven by fluorescent signal levels. The signal levels indicated that f#s of 5.6 or 8.0 would provide enough fluorescent intensity for detection, but that f/8.0 was marginal. In order provide for a possible decrease in laser intensity over time due to aging flash lamps, the sprinkler experiments were conducted with an f# of 5.6. While the depth of field for f/5.6 (Figure 33) is less than the laser sheet thickness from Table 6, good results were obtained as shown in the calibration/verification images discussed later in this thesis. In addition, the calibration/verification images showed that the measurement region thickness for this work was clearly determined by the laser sheet intensity.

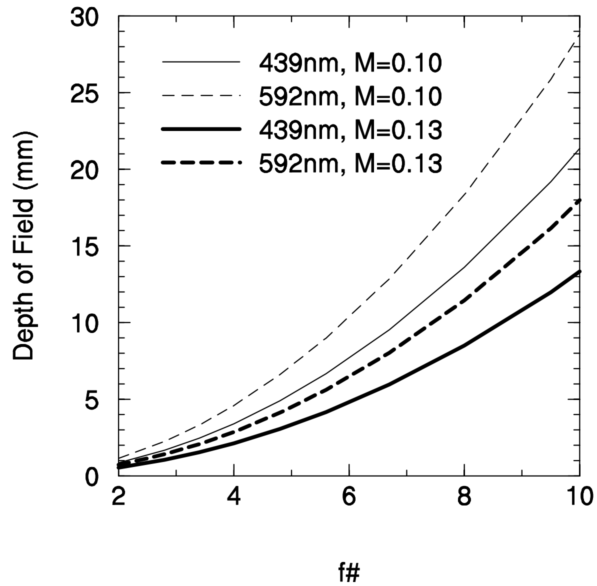

Figure 33. Predicted depth of field for various combinations of magnification, fluorescence emission wavelength, and f#. The plots are based on fluorescent emission wavelengths from a nominal solution of 3 mg/L of rhodamine and 10 mg/L of stilbene in water using the 532 nm notch filter. Note that 439 nm is the 50% cumulative emission intensity wavelength for 355 nm excitation (the wavelength above which and below which 50% of the integrated relative intensity versus wavelength function lies), and 592 nm is the 50% cumulative emission intensity wavelength for 532 nm excitation.

The relationship between the depth of field and the beam sheet thickness has been discussed, and it has been suggested that matching the depth of field and the beam sheet thickness should result in the best images. Another important consideration in determining the beam sheet thickness is the size of the particle that is to be measured. If the sheet is very thin relative to the particle, the probability of measuring the true diameter is small. The measured mean drop diameter is related to the beam sheet thickness by the following formula:

$$D_m = \frac{\left(\left(\frac{2}{3} \right)^{\frac{1}{2}} D_a^2 + D_a b \right)}{D_a + b} \tag{15}$$

Where 'D_m' is the measured mean drop diameter, 'D_a' is the actual drop diameter and 'b' is the beam sheet thickness. The relation is derived from the geometric probability of some portion of the laser sheet illuminating the true diameter of the droplet. If the beam sheet is infinitesimally thin, the measured diameter is 81.6% of the actual diameter. This means that if all the drops were uniformly the same diameter, the images would show a variety of sizes with a mean diameter that is 81.6% of the actual diameter. If the beam sheet is equal to the drop diameter, the measured drop diameter will be 90.8% of the actual diameter, whereas, if b is 10 times the diameter of the drop, the measured average drop diameter will be 98.3% of the true diameter for mono-dispersed drops. When a variety of drop sizes are to be measured instantaneously, it is important that the measured diameter be as nearly equal to the true diameter as possible. This would indicate that a wider beam sheet is better than a thin one.

Another reason for a thicker beam sheet is related to the size of the sampling region. Given a number of drops randomly distributed in a volume, such that the mean distance between drops is denoted 's', then there is a lower limit to the smallest volume that can be sampled and still return the correct number density, which is $1/s^3$. Sampling with a beam sheet dimension less than the mean distance between drops may result in underestimating the total number of drops. In the sprinkler experiments, the laser beam was expanded in only one direction, and reduced in width by the 8 mm slit, resulting in a sheet thickness of approximately 10 mm. The water flow rate was calculated from the measured drop diameters and the velocity of the drops. For axis-symmetrical sprays, the calculated water flow rate matched the flow rate of the sprinkler to within the measurement error.

Before moving on to the calibration/verification measurements, it will be useful to summarize the parameters of the measurement system discussed so far. Based on the estimates and measurements of system resolution, a magnification of 0.13 will be used, resulting in measurement region pixel sizes of 50 μm, and a measurement region 0.46 m × 0.54 m in size. The thickness of the measurement region is approximately 10 mm, which is thick enough to capture the velocity of the largest drops considered (3 mm) if there is an in-plane velocity component, and provides for low levels of statistical error in measuring the true diameter of the droplet.

The concentrations of stilbene and rhodamine in the water are set to approximately 10 mg/L and 3 mg/L respectively, which provides for a strong fluorescent response to 355 nm and 532 nm laser light, respectively. With the 532 nm notch filter installed, the drop images can be differentiated by color, with the stilbene producing a blue image, and the rhodamine producing a yellow image. The signal levels of images captured by Fuji NPZ800 medium format color film, using a camera lens f/5.6, are strong enough for detection of droplets approximately 200 μm in diameter. While the depth of field from f/5.6 is thinner than the laser sheet thickness, larger f#s do not produce sufficient signal levels for imaging 200 μm drops with a cushion for laser degradation over time.

3.7.3 Calibration/Verification Droplets

In order to provide measurements with low levels of error and documented levels of uncertainty, the measurement system is calibrated with droplet diameters that span the design range of 200 μm to 3000 μm. This size range was chosen based on previous research (Putorti, Belsinger, and Twilley 1999) that indicated approximately 98% of the water from typical fire sprinklers is contained in droplets larger than 200 μm in diameter. The droplet production device must be capable of delivering the monodisperse droplets through a known and consistent trajectory. Only in this way will it be possible to compare the size of the droplet image to the actual size of the droplet, and gauge the effect of particle location in the laser sheet on the measured droplet diameter. The 3000 μm water drops were produced by a 22 gauge hypodermic needle, carefully cut and honed to produce an opening perpendicular to the shaft of the needle. The needle is fed with an elevated reservoir, using the elevation head to cause flow out of the needle. The syringe is attached to a dial caliper traversing device, constructed to allow the needle to be moved through the thickness of the sheet in 1 mm increments. The apparatus allows the monodisperse droplets to fall with a given vertical trajectory, and the trajectory to be moved in a precise manner across the thickness of the laser sheet. The readability of the caliper is 0.001 in., and the uncertainty in the measurement is $\pm 2.54 \times 10^{-2}$ mm (0.001 in). The droplet size is determined by measuring the mass of the droplets. Rhodamine and stilbene dyes are added to the water prior to filling the elevated reservoir. The syringe apparatus is shown in Figure 34.

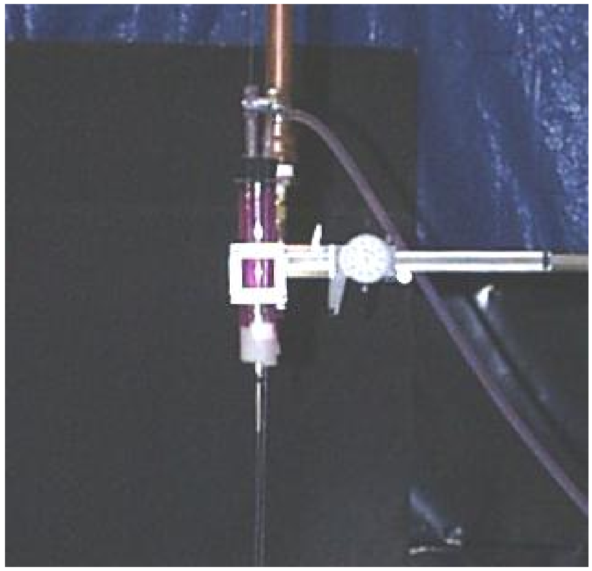

Figure 34. Photograph of the caliper and syringe apparatus used to produce a vertical stream of 3000 µm diameter water droplets.

A monodisperse stream of 200 µm droplets with consistent trajectory is formed using a vibrating orifice aerosol generator (VOAG) offered by TSI, Inc. This device operates by passing water through a vibrating piezoelectric section and out an orifice. The water exits the orifice as a stream, and breaks up into a monodisperse series of droplets, the size of which is governed by the vibration frequency, orifice size, and fluid flow rate. The device will produce droplets on the order of 20 µm to 400 µm in diameter depending on the operation parameters. For water, the maximum droplet size is approximately 200 µm in diameter. In order to produce the 200 µm droplets, the VOAG was operated with a 100 µm diameter orifice, a fluid flow rate of 2.2 cm^3/min, and driven by a sinusoidal square wave vibration frequency of 8.621 kHz with a magnitude of 4V trough to peak.

The VOAG was mounted on a traversing mechanism constructed to allow the droplet stream to traverse the sheet. The traversing mechanism provides 1 mm of movement per handle revolution, and a linear mm scale for reference. The uncertainty in the measurement is estimated at ±0.13 mm (0.005 in.) The device was found to be very repeatable during the experiments, with minimal lash in the mechanism. The results of the drop size calibration/validation are stated and discussed later in the drop sizing method section. The VOAG assembly is shown in Figure 35.

Figure 35. Assembly for producing a vertical stream of 200 μm droplets, and moving them through the thickness of the laser sheet.

3.8 Aperture and Scanner Effects

The final effect of the aperture size on qualitative image quality is shown in Figure 36. This figure shows 2410 μm ±20 μm droplets illuminated by a 355 nm laser sheet. The images were carefully scanned in order to provide the best possible focus from the scanner. It can be seen that the best image is provided at f=8.0, although higher image intensity and only slightly worse droplet boundaries are present at f=5.6 and f=4.0. The droplet clearly has more distortion at f=2.8. The affect of improper focusing by the scanner introduces much more distortion than aperture size, as shown in Figure 37. In this figure, two successive scans of the same image are compared. The scanner, which utilizes an auto focus mechanism, appears to have difficulty with photos having large dark areas. Images of actual sprinklers, with large brightly-lit areas, are less susceptible to focus errors. The scanner also has a multiple exposure negative holder, with one position that works much better than the others. The manufacturer suggested disabling the auto focus mechanism, but this did not improve the image quality as determined from the resolution charts and droplet images. Figure 37 also shows how the color differentiation is accomplished by the two-color fluorescence method.

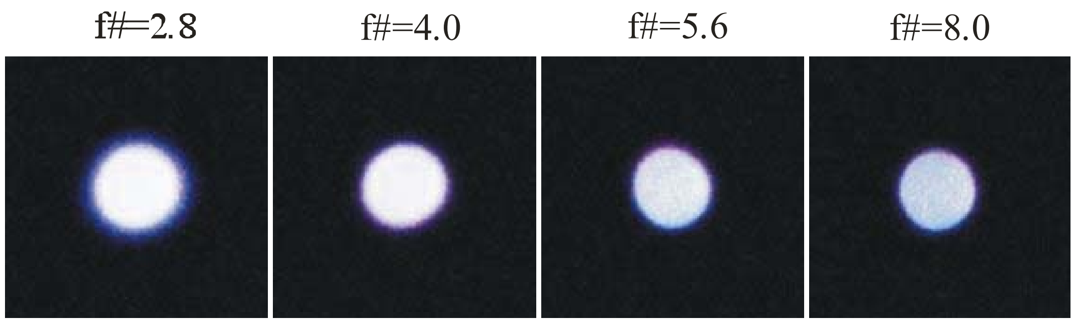

Figure 36. Effect of f# on droplet images. 2800 μm diameter water drops with approximately 3 mg/L of stilbene and 3.3 mg/L of rhodamine illuminated with 355 nm laser sheet. Image quality improves as f# is increased from 2.8 to 8.0 as evidenced by haze around droplet perimeter. Images taken at f#s of 5.6 and 8.0 are of nearly equal quality.

3.9 Droplet Intensity Profile

The intensity profiles across droplet images were measured in order to formulate a method for determining the droplet size. Other researchers have recently predicted and measured two-dimensional fluorescent intensities for spherical droplets, and suggested that droplet intensities are better predicted when the concentrations of fluorescent dye are within a certain range. (Domann and Hardalupas 2001a, 2001b) This range is expected to vary with droplet diameter, d, since droplet fluorescent intensity is proportional to d^3

when incident light rays are reflected within the droplet a number of times before being absorbed. Thus, if the dye concentration is too high, the incident light rays will be absorbed before they are allowed to bounce around the inside of the drop and induce fluorescence in all areas of the droplet volume, and the fluorescent intensity is predicted to approach proportionality with d^2.

Figure 37. Effect of scanner focus on droplet images. The images in this figure show nominally 3000 μm diameter droplets illuminated with 532 nm (upper drops) and 355 nm (lower drops) laser sheets. The images are two successive scans of the same film. Care must be taken to verify that the scanner is properly focused, a procedure that is important with small pixel sizes.

The droplet intensity measured along the horizontal centerline of the droplet image parallel with the incident light rays is shown in Figure 38 for a 2921 μm ±27 μm droplet illuminated with 532 nm and 355 nm light at a magnification of 0.10 and f/5.6. The droplets were located in the center of the beam sheet, and therefore were uniformly illuminated. The droplets were composed of distilled water doped with 3.3mg/L (5.7×10^{-6} M) of Rhodamine WT and 3.0 mg/L (5.4×10^{-6} M) of stilbene. The plots indicate slightly different droplet diameters as measured by the width at half maximum, with the diameter of the blue image nearly equal to the actual droplet diameter, and the yellow image slightly larger. The phenomenon leading to the difference in image diameter as a function of wavelength has not been determined, but was originally thought to be partially caused by the inability to match the laser profile and camera depth of field for both wavelengths simultaneously. However, the depth of field effect would be expected to favor the yellow drop since the DOF is approximately equal to the sheet thickness for the yellow emission, while the DOF is less than half of the beam sheet thickness for the blue emission. (See Figure 33 and Table 6) In addition, the droplet is in the center of the sheet, and within the DOF, for both cases.

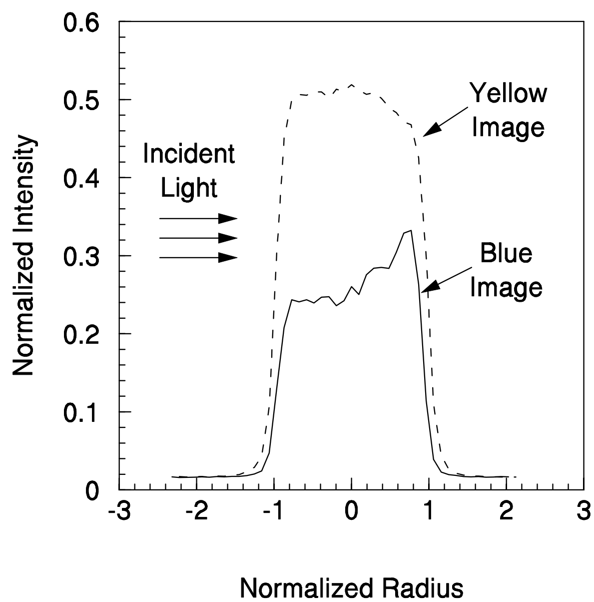

Figure 38. Horizontal intensity profile of 3 mm nominal diameter water droplet conducted through the centerline. Droplet was illuminated with 532 nm and 355 nm laser sheets. The intensity is normalized by the maximum film/scanner intensity of 2^{16}, and plotted against distance, normalized by the actual drop radius.

Normalized emission profiles for the 3 mm nominal diameter drops doped with Rhodamine WT and stilbene are compared to those predicted by Domann and Hardalupas (2001a) for 200 μm drops doped with Rhodamine 6G in Figure 39 and Figure 40. The intensities and diameters of the data and predictions have been normalized in order to compare the intensity profiles, not the actual intensities. In addition, the mass and molar concentrations of dye are noted, since the concentrations of different dyes are best compared on a molecular number concentration basis. Note that the fluorescent emission profile from Rhodamine WT is a top hat and doesn't match the shape of the predicted profiles. The measured stilbene emission profile, however, is qualitatively similar to the predicted high concentration profile for Rhodamine 6G, but with a 200× lower concentration of stilbene. In this case, the 500 mg/L Rhodamine 6G prediction is in reasonable agreement with the 3.0 mg/L stilbene data. This is unexpected since there is greater than a two order of magnitude difference in the molar concentrations, but only one order of magnitude difference in diameter between the two. An increase in the distance between fluorescent molecules of a factor of 10 would result in a decrease in concentration of 10^3, or a factor of 1000. The difference in droplet diameter will have some effect, but does not fully account for the agreement given the predicted (Domann and Hardalupas 2001b) effect of increasing droplet diameter. While the predictions do not agree with the data, they show that internal reflections can cause intensity peaks at either side, near or far from the light source, depending on concentration. Most of the images for the current work are symmetric, but many have peaks. The presence of peaks in the intensity profiles is one reason to use the slope of the droplet intensity for sizing, rather than a cutoff intensity. For a droplet with intensity peaks at the edge, the slope of the intensity will correctly identify the edges of the droplet, but the use of an intensity threshold could result in a measured drop size much smaller than the actual size. The use of intensity gradient is discussed fully in the droplet sizing section.

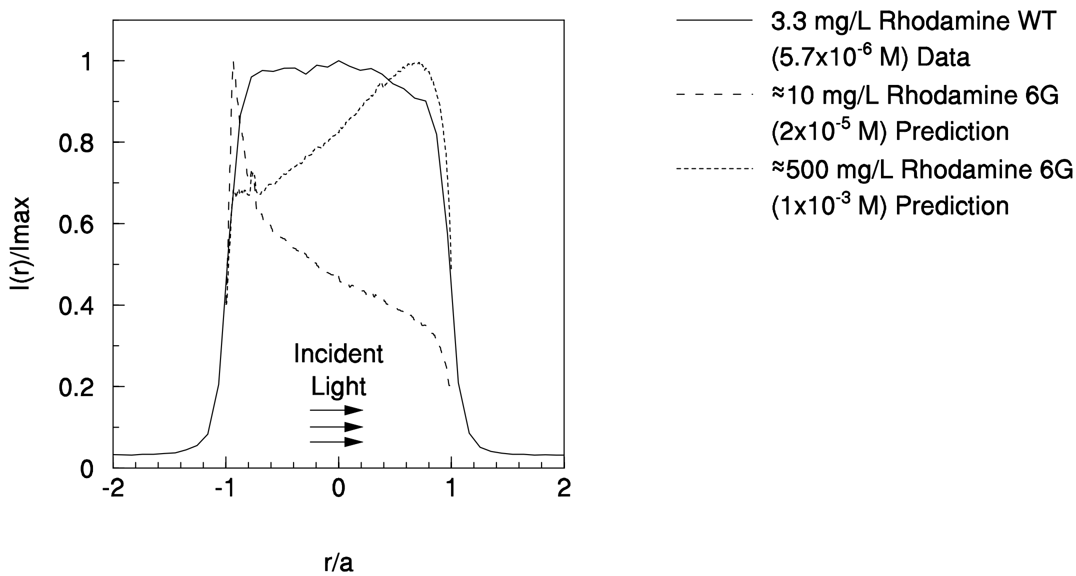

Figure 39. Horizontal intensity profile through the centerline of a 3 mm nominal diameter water drop illuminated by 532 nm light compared to profiles predicted by others. Intensity is normalized by the maximum film/scanner intensity, and the horizontal dimension is normalized by the droplet radius.

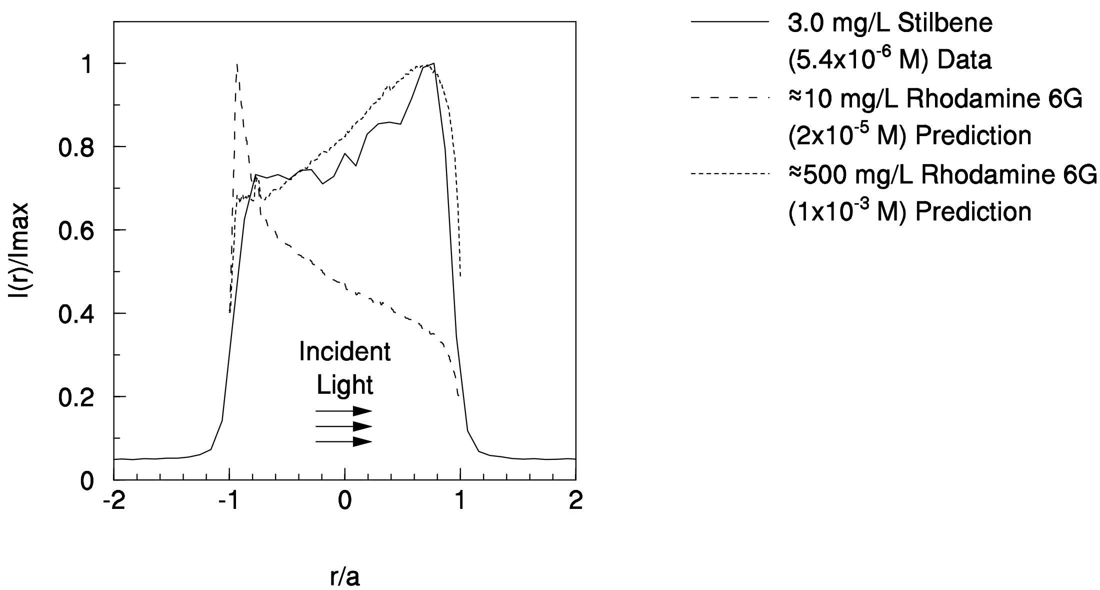

Figure 40. Horizontal intensity profile through the centerline of a 3 mm nominal diameter water drop illuminated with 355 nm light compared to profiles predicted by others. Intensity is normalized by the maximum film/scanner intensity, and the horizontal dimension is normalized by the droplet radius.

The 3 mm nominal diameter droplet images previously discussed do not saturate the photographic film. However, in application of the measurement method, saturation of the film with the signals from large droplets is necessary in order to have sufficient intensity above the background and noise to image the 200 μm nominal diameter droplets. The profiles for two different 201 μm ± 1.34 μm droplets illuminated with 355 nm light are shown in Figure 41, which are typical of these droplets. Note that the concentration of stilbene was increased to approximately 10 mg/L for the measurements of small droplets since the lower concentration of approximately 3 mg/L was not sufficient for imaging. The intensity profiles are qualitatively normal shaped, and absent of any peaks in intensity at the droplet edges. These droplets, however, are imaged with a 4 × 4 pixel array, which will lead to averaging of intensity over the droplet edges.

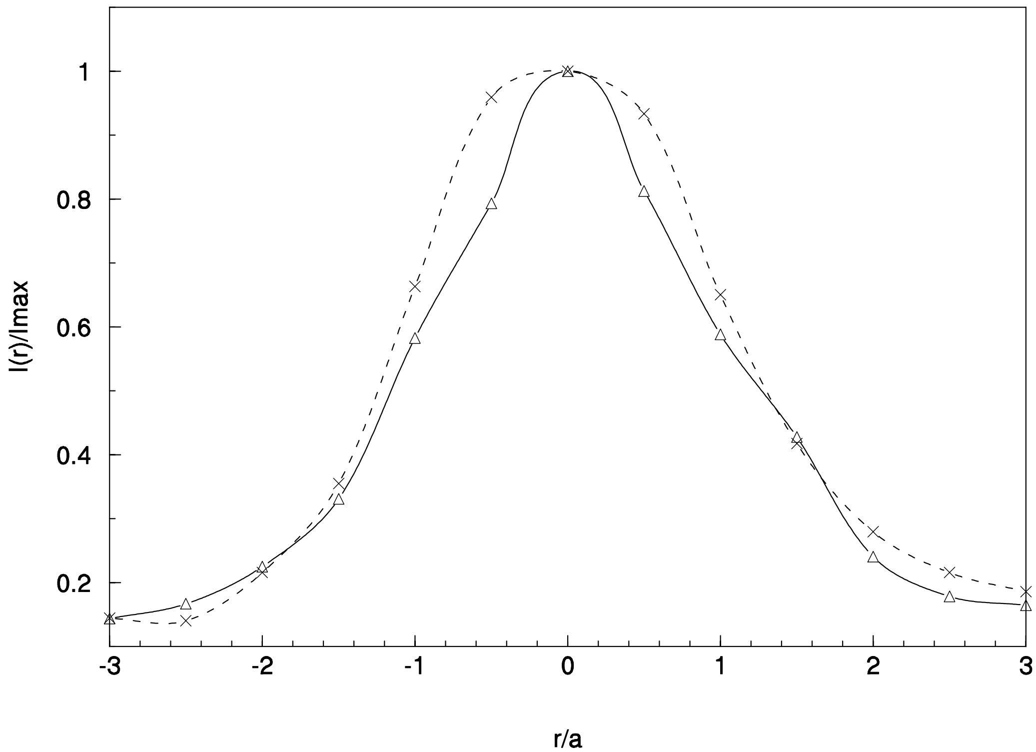

Figure 41. Horizontal intensity profiles through the centerline of 200 μm nominal diameter water drops illuminated with 355 nm light. Drops are doped with 9.65 mg/L of stilbene and 3.33 mg/L of Rhodamine WT. Intensity is normalized by the maximum film/scanner intensity, and the horizontal dimension is normalized by the droplet radius.

3.10 Droplet Sizing Method

The droplet sizes were determined by the following method:

1. First, verify the thickness of the measurement region. The intensities of 200 μm calibration droplet images were used to determine the background intensity and to separate droplets within the laser sheet from those outside the sheet. The 200 μm droplets were used for this determination since they produce the lowest intensity droplets within our measurement range. The width of the beam sheet was estimated from the imaged intensity profiles of the sheet projected on paper, as discussed previously. It was found that the

signal intensities from the 200 μm and 3000 μm droplets fell sharply as they neared the edge of the sheet, at a location that coincided with the previous determination of the beam sheet edges. The intensities of the 200 μm droplets located just outside the sheet (+1 mm uncertainty) were taken as the intensity cutoff for droplets to be included in the measurements. Their intensity was determined to be approximately 20,000 units on a scale of 0 to 65535 for a 16 bit/channel image using an HSI color model representation. (ie., $2^{16} = 65536$) This value was normalized to 0.305, allowing its application to other bit/channel settings and images. It was assumed that the background was totally dark (I=0) which is a good assumption for these images. The resulting minimum detectable droplet image diameter is 166 μm, as computed using the 0.305 cutoff intensity, f/5.6, M=0.13, and γ from 200 μm dye-in-water drops in Equation 14. This cutoff intensity defines the measurement volume.

2. Next, apply a 2-D Sobel edge enhancing filter (Media Cybernetics 2001) to the image. The sobel filter replaces the intensities within the image with scaled values representing intensity gradients. The algorithm is shown in Figure 42. The values of the intensity gradients range from 0 to 2^{16} for a 16 bit/channel image, and 0 to 2^{8} for an 8 bit/channel image. Therefore, the intensity of a sobel filtered image is equivalent to the intensity gradient of the unfiltered image. Application of the sobel filter to an image has the visual effect of converting a droplet image to a doughnut looking image. It was found that the diameters of large and small droplets are accurately determined by measuring the diameter midway between the inner and outer edges of the

doughnut at a normalized intensity gradient of 0.305. Note that the value of the normalized intensity gradient used to measure the drop diameter happens to be the same as the normalized value of the background intensity cutoff used above, but the two are not related. The Normalized intensity gradient value for drop sizing, 0.305, was derived from examining the gradients of drop images of various drop sizes. A value was determined that was above the background and noise, but low enough to not miss the peaks from a range of drop sizes. The measurement of drop diameter using the normalized intensity gradient is illustrated for an ideal droplet in Figure 43. Determining the droplet diameter by way of an intensity profile on an unfiltered image was found to cause greater errors on large and small droplet sizes than by using the intensity gradients of the sobel filtered images. The image dimensions were calibrated by photographing a steel ruler at the start of each roll of film.

A	B	C
D	E	F
G	H	I

$$E=(X^2+Y^2)^{0.5}$$
$$X=(C+2F+I)-(A+2D+G)$$
$$Y=(A+2B+C)-(G+2H+I)$$

Figure 42. The Sobel filter algorithm is demonstrated by considering a 3×3 pixel matrix. The intensity value of pixel "E" in the filtered image (intensity gradient) is calculated by the above equations, using the intensity values of the surrounding pixels in the pre-filtered image.

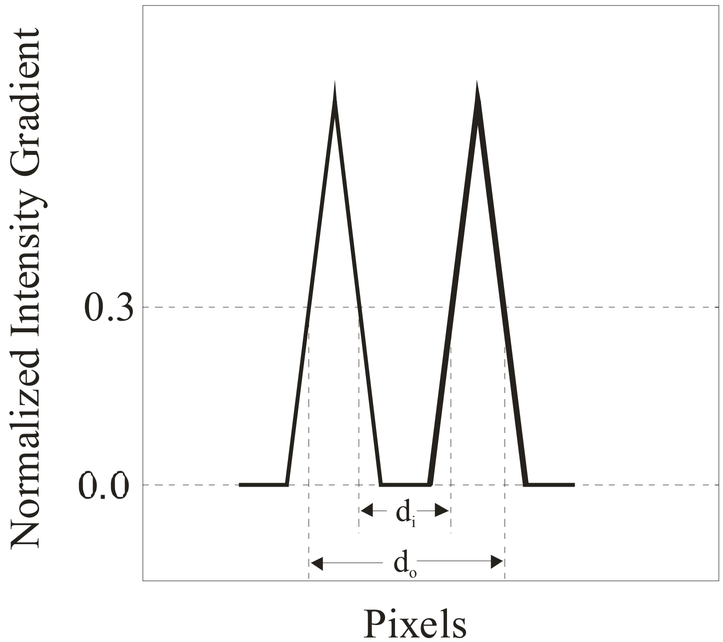

Figure 43. An intensity profile of an ideal sobel filtered droplet image. The intensity profile of a sobel filtered image is equivalent to the intensity gradient profile of the original image. The intensity gradient is normalized by the maximum pixel intensity. The average of the inner and outer doughnut diameters, $(d_i + d_o)/2$, at an intensity gradient of 0.305 is the equivalent diameter of the droplet.

Examples of small droplets, nominally 200 μm in diameter, are shown in Figure 44. These droplets are shown in their unfiltered form and after the application of the sobel filter. Figure 45 and Figure 46 show the normalized intensities of the images before and after the application of the sobel filter. These profiles were measured along a horizontal line cutting through the center of the droplet. The plots illustrate that it is difficult to determine the diameter of the drops by looking at the droplet intensity alone. In addition, the graphs show that it is also difficult to determine the drop diameter from the peaks of the intensity gradient. For small drops, the pixel size is relatively large, and the pixels may not be perfectly aligned with the peak in the intensity gradient. Therefore, the normalized cutoff value of 0.305 in the intensity gradient was empirically determined for use in sizing the droplets.

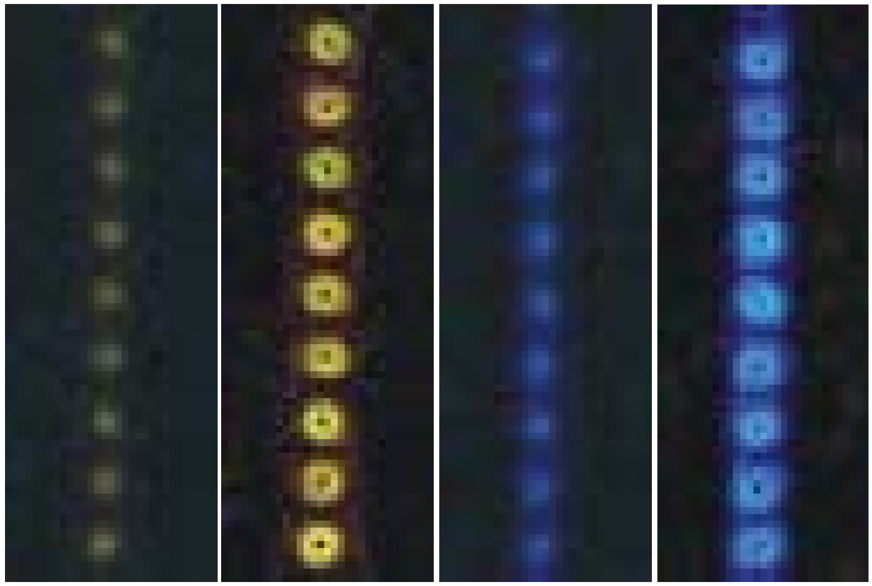

A B C D

Figure 44. Examples of 200 μm nominal diameter droplets. Here, 'A' and 'B' are illuminated with 532 nm light, while 'C' and 'D' are illuminated with 355 nm light. Also, 'A' and 'C' are raw images of droplets. The result of applying the sobel filter to these images is shown in 'B' and 'D'. Note that the images here are limited in quality by the electronic file size limitations of publication.

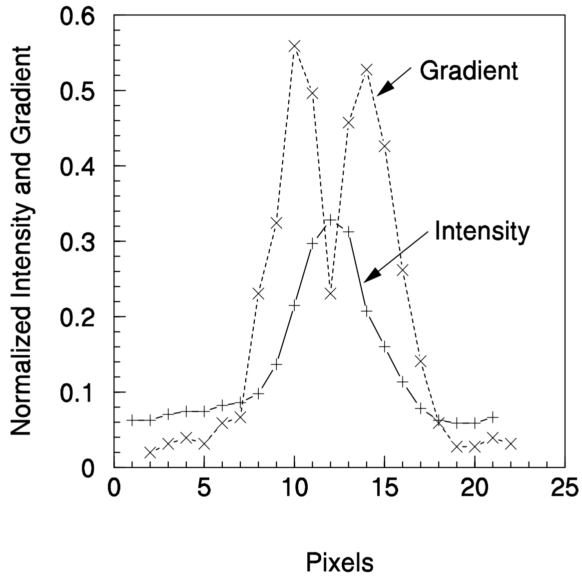

Figure 45. Normalized profiles of 200 μm nominal diameter water droplet conducted through the image centerline before (intensity profile) and after (gradient profile) application of the sobel filter. The droplet was illuminated with a 355 nm laser sheet, and contained 9.65 mg/L of stilbene and 3.33 mg/L of rhodamine dye. A magnification of 0.13 and f/8.0 were used. The intensity and intensity gradient are normalized by the maximum pixel intensity (2^8), and plotted against distance in pixels.

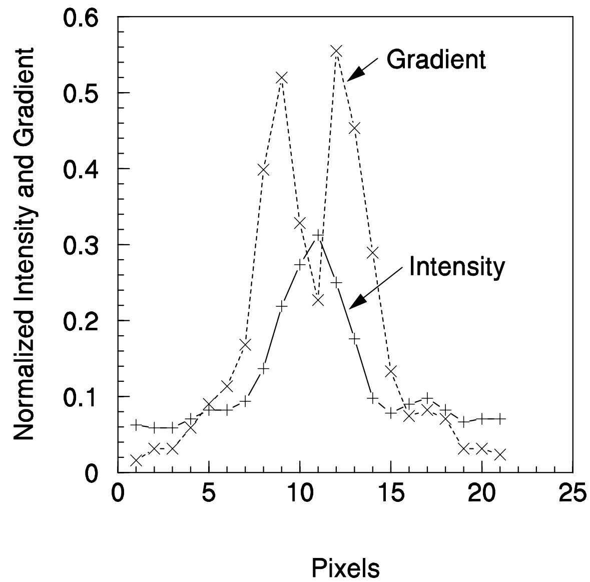

Figure 46. Normalized profiles of 200 μm nominal diameter water droplet conducted through the image centerline before (intensity profile) and after (gradient profile) application of the sobel filter. The droplet was illuminated with a 532 nm laser sheet, and contained 9.65 mg/L of stilbene and 3.33 mg/L of rhodamine dye. A magnification of 0.13 and f/8.0 were used. The intensity is normalized by the maximum pixel intensity (2^8), and plotted against distance in pixels.

To account for the eccentricity of the droplet images, the areas of the inner and outer doughnuts are used to calculate an equivalent diameter for each droplet. The sizing algorithm accomplishes this task by defining two areas on each drop image. These two areas are defined by pixels with a normalized intensity gradient value of 0.305; an inner area smaller than the drop, and an outer area larger than the drop. Each of the two areas is measured (m^2), and the diameters of circles with the same areas are calculated as the inner and outer equivalent diameters. The equivalent diameter of the drop is reported as the average of the inner and outer equivalent diameters. By using the doughnut method on the intensity gradient data, the diameter can be measured to an uncertainty within one pixel width. This will be demonstrated later.

Similar examples of large droplets are shown in Figure 47. This figure shows a single droplet of approximately 3 mm diameter falling through the air. The images are presented before and after the application of the sobel filter. In this case the doughnut can be seen more clearly due to the larger number of pixels covering the drops. Notice that the droplet is not perfectly spherical in nature. Plots of the droplet image intensity profiles are shown in Figure 48 and Figure 49. As in the case of the small droplets, the diameters are measured using the inner and outer areas of the doughnuts, accounting for the eccentricity of the droplet in two dimensions.

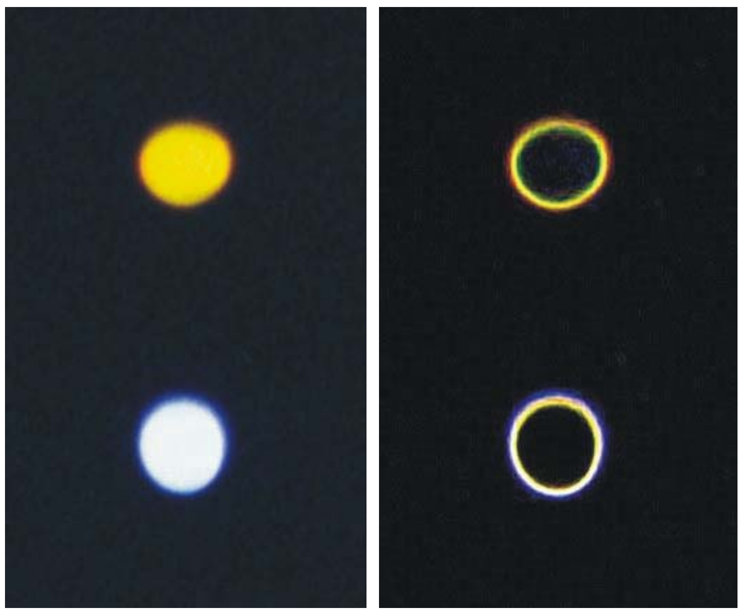

Figure 47. Examples of a 3 mm nominal diameter falling drop. The uppermost droplet images in both panes are the result of illumination with 532 nm light, while the lower droplet images are from 355 nm light. The left pane contains raw images of the drop, while the results of applying the sobel filter to these images are shown in the right pane. Note that the images here are limited in quality by the electronic file size limitations of publication.

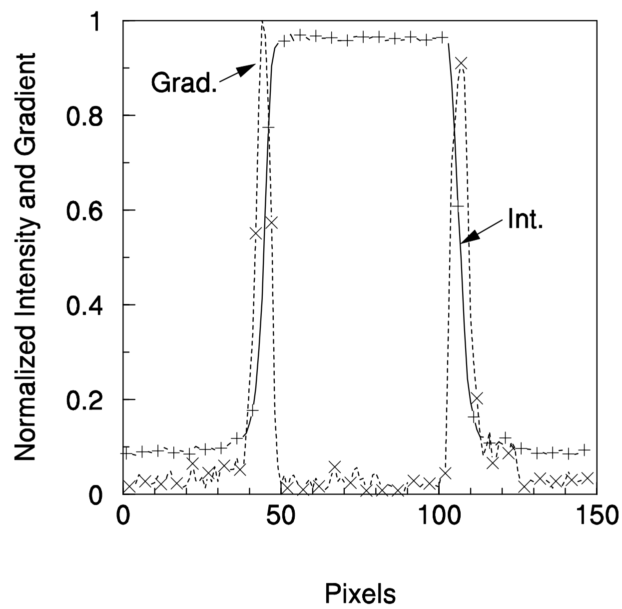

Figure 48. Horizontal intensity profile of 3 mm nominal diameter water droplet conducted through the image centerline before and after application of the sobel filter. Droplet was illuminated with a 355 nm laser sheet. The intensity is normalized by the maximum intensity (2^{16}), and plotted against distance in pixels. One out of every five data points are shown for clarity.

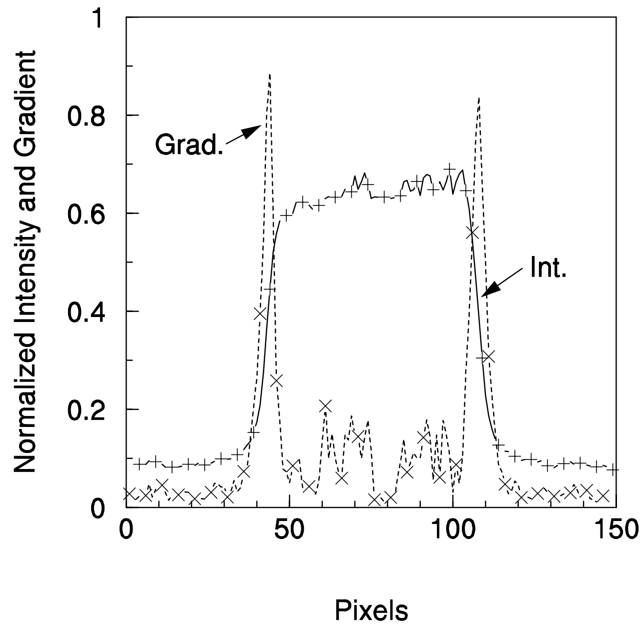

Figure 49. Horizontal intensity profile of 3 mm nominal diameter water droplet conducted through the image centerline before and after application of the sobel filter. Droplet was illuminated with a 532 nm laser sheet. The intensity is normalized by the maximum intensity(2^{16}), and plotted against distance in pixels. One out of every five data points are shown for clarity.

Using the above methodology, images containing vertical streams of calibration droplets were analyzed. Due to the slight curvature of the vertical iso-intensity profile of the laser sheet, the images of the droplet stream located very close to the edge of the sheet contain less droplets than those near the center. Images from droplets close to the sheet edge are also susceptible to small positional errors, since small changes in horizontal position are associated with steep changes in laser sheet intensity. The fractions of droplets measured by the analysis algorithm at various sheet positions are shown in Figure 50 and Figure 51. As discussed previously, despite some intensity profile curvature near the edge of the laser sheet, the droplet image drop off is steep at the edge of the sheet thickness. In addition, the plot shows similar results for analyses using 8 bit/channel and 16 bit/channel images. The use of 8 bits/channel cuts the size of the raw image files substantially compared to 16 bits/channel. For a 60 mm × 70 mm film negative scanned at 4000 dpi, this relates to a 250 MB image versus a 500 MB image. Note that the beam sheet was approximately 14 mm thick during the small drop experiments, but was limited to approximately 11 mm for the large drop experiments by the installation of the 8 mm slit. This explains why the steep decrease in drop fraction occurs at different distances from the center for large and small drops. In both cases, this steep decrease corresponds with the edge of the laser sheet.

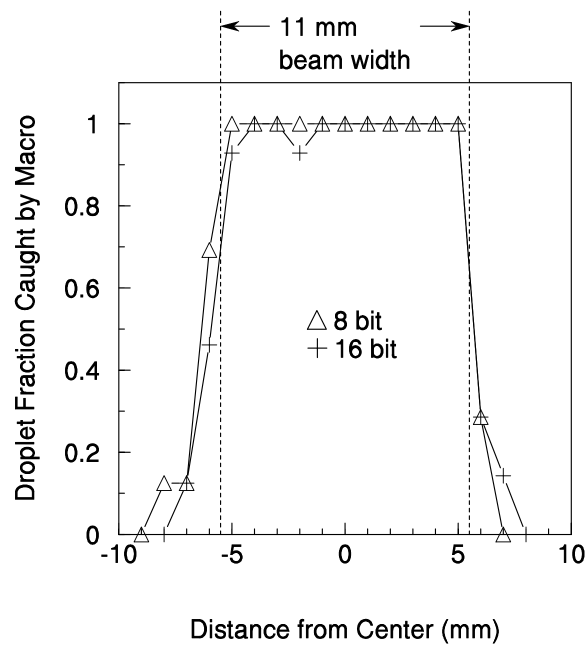

Figure 50. Fraction of 3000 µm nominal diameter droplets, illuminated by 355 nm sheet, caught by the image analysis macro versus the distance from the centerline of the laser sheet thickness.

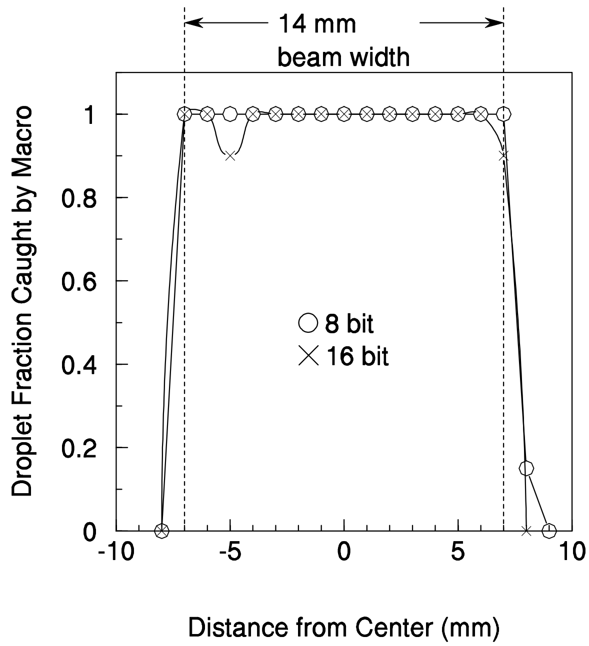

Figure 51. Fraction of 200 µm nominal diameter droplets, illuminated by 355 nm sheet, caught by the image analysis macro versus the distance from the centerline of the laser sheet thickness.

Due to the smaller number of droplets that will be imaged by the edge of the sheet, the statistics used to determine the uncertainty of the droplet size measurement are based on the total number of calibration droplets within the sheet. Therefore, the average droplet size at any particular location in the sheet is the average of the droplets measured at that horizontal position, but the droplet size average within the sheet is the average of all droplets images within the sheet, not the average of the average values determined at each horizontal location. The results of the calibration are summarized in Table 7, and illustrated in Figure 52 through Figure 55. Note that the measurement system has not been calibrated, per se, the PTVI diameters shown in the figures and in the table are the measured size of the droplet images. The error in sizing is less than 6% for both drop diameters.

Table 7. Summary of Droplet Uncertainties and Errors from Calibration/Verification

Nominal Drop Diameter (μm)	Actual Drop Diameter (μm)	Average PTVI Diameter (μm)	Diameter Error (%)	Nominal Laser Sheet Thickness (mm)	Scanner Bits/Channel
200	201 μm ± 1.34 μm	206 μm ± 46 μm	2.5	14	8
200	201 μm ± 1.34 μm	208 μm ±35 μm	3.5	14	16
3000	2917 μm ± 16 μm	3090. μm ± 227 μm	5.9	11	8
3000	2917 μm ± 16 μm	3078 μm ± 214 μm	5.5	11	16

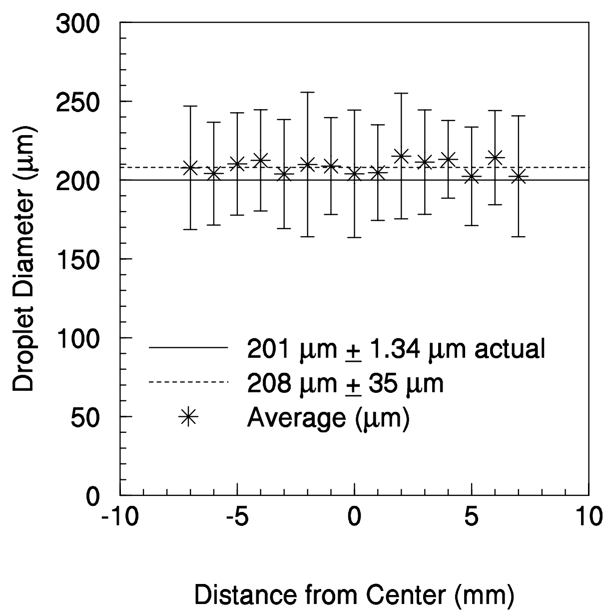

Figure 52. Comparison of calibration droplet diameter and image diameter as reported by the imaging analysis macro. The nominally 200 μm diameter droplets were illuminated by a 355 nm laser sheet. The photographs were scanned using 16 bits/channel. The solid line represents the actual drop size, while the dotted line represents the average drop size over the entire laser sheet as reported by the macro. The error bars represent the uncertainty in the average droplet size reported by the macro for each sheet location (Type A uncertainty).

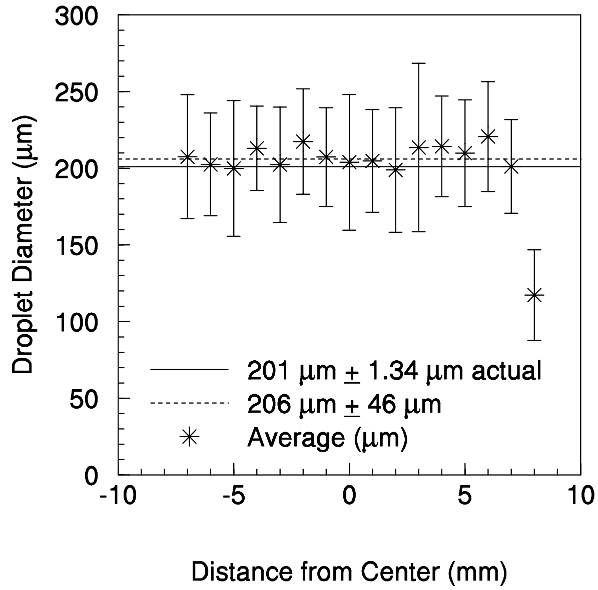

Figure 53. Comparison of calibration droplet diameter and image diameter as reported by the imaging analysis macro. The nominally 200 μm diameter droplets were illuminated by a 355 nm laser sheet. The photographs were scanned using 8 bits/channel. The solid line represents the actual drop size, while the dotted line represents the average drop size over the entire laser sheet as reported by the macro. The error bars represent the uncertainty in the average droplet size reported by the macro for each sheet location (Type A uncertainty).

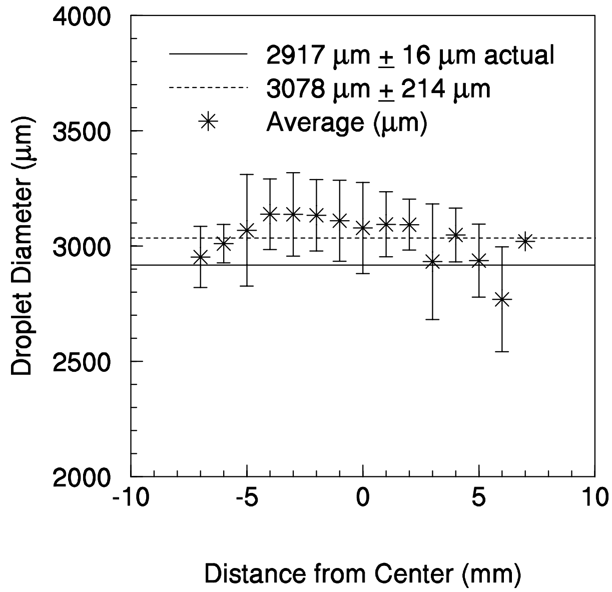

Figure 54. Comparison of calibration droplet diameter and image diameter as reported by the imaging analysis macro. The nominally 3 mm diameter droplets were illuminated by a 355 nm laser sheet. The photographs were scanned using 16 bits/channel. The solid line represents the actual drop size, while the dotted line represents the average drop size over the entire laser sheet as reported by the macro. The error bars represent the uncertainty in the average droplet size reported by the macro for each sheet location (Type A uncertainty).

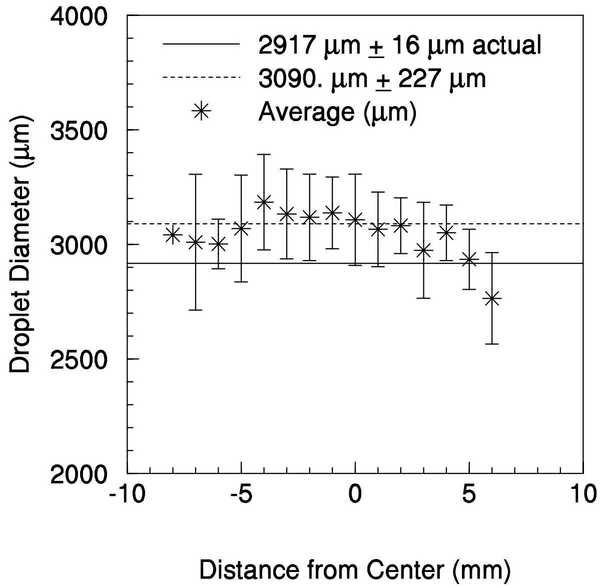

Figure 55. Comparison of calibration droplet diameter and image diameter as reported by the imaging analysis macro. The nominally 3 mm diameter droplets were illuminated by a 355 nm laser sheet. The photographs were scanned using 8 bits/channel. The solid line represents the actual drop size, while the dotted line represents the average drop size over the entire laser sheet as reported by the macro. The error bars represent the uncertainty in the average droplet size reported by the macro for each sheet location (Type A uncertainty).

In summary, the calibration/verification experiments showed that the laser energy profile determined the thickness of the measurement volume, even though the predicted depth of field was approximately half that of the sheet thickness. In addition, the measured droplet diameters at the edge of the sheet were consistent with those at the center of the sheet, indicating that having the DOF smaller than the light sheet by a factor of 2 did not have a strong effect on the results. It has been demonstrated that using the signal from stilbene in water, fluorescing in response to a 355 nm laser sheet of approximately 11 mm in thickness, with a magnification of 0.13 and f/5.6, provides measurement of 200 µm to 3000 µm diameter droplets with low levels of uncertainty. In addition, using images that were scanned at 8 bits/channel does not result in a significantly larger uncertainty than using 16 bits/channel. This is an important point because 8 bit/channel image file sizes are approximately half that of 16 bit/channel images. For experiments in sprinkler sprays, the stilbene signal will be used for droplet sizing, and used in conjunction with the rhodamine signal for velocity measurement.

CHAPTER 4

MEASUREMENTS IN SPRINKLER SPRAYS

4.1 Experimental Setup

The PTVI technique developed in the previous chapter is applied to the measurement of droplet size and velocity in sprinkler sprays. The experimental setup for the sprinkler measurements is the same as used for the calibration/verification measurements, except the syringe/needle and VOAG are replaced by an axis-symmetric sprinkler. The sprinkler is composed of a circular orifice, with a smooth angled strike plate that transforms the water jet from the orifice into a symmetrical water sheet. The water sheet breaks up at or near the sprinkler, forming a symmetrical umbrella or hollow cone shaped water spray. The sprinkler is shown in Figure 56. It features a removable strike plate, attached to a threaded rod running through the center of the orifice. The sprinkler orifice sizes are referred to by the equivalent diameter of the opening, defined as $[(4/\pi)(A_{orifice}-A_{rod})]^{1/2}$, where A is defined as the area of the orifice and of the rod. The axis of symmetry of the sprinkler and sprinkler spray passes through the length of the rod to the surface of the water collection platform. The rod allows for various strike plates to be attached to different orifices, and provides for variation in the distance between the orifice and the strike plate. The distance from the apex of the strike plate to the orifice was approximately 4.45 mm (0.175 in) for all experiments except for the 0.757 L/s

(12 gpm), 8.5 mm nozzle, 90 degree strike plate experiment where a 1.91 mm (0.075 in) distance was needed to stabilize the flow. This distance is shown as ‘a’ in Figure 56.

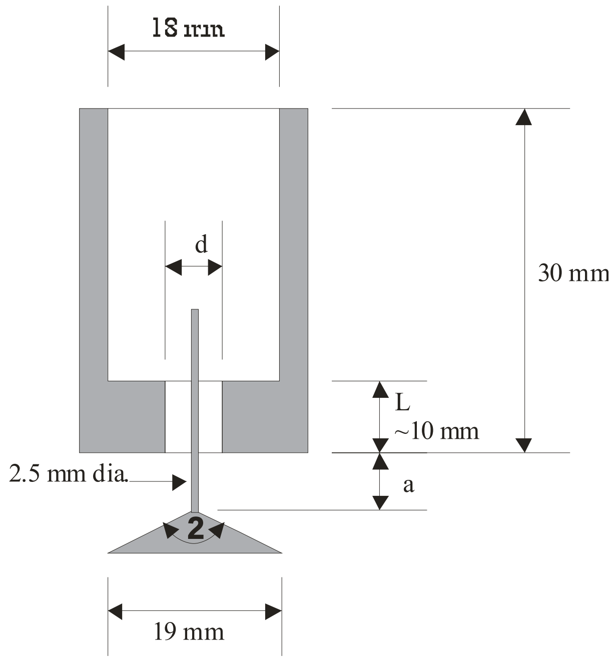

Figure 56. Diagram of the axis-symmetric sprinkler.

The sprinklers were operated at a number of water flow rates to provide a wide range of droplet sizes and velocities. The Reynolds and Weber numbers of the flows encompass those present in typical commercial sprinklers. The range of flow rates also provide a similar range of Re and We for the different orifice sizes. Strike plate angles, θ, consisted of 60°, 90°, and 120° in order to control the initial trajectory of the drops. These three strike plate angles were used with each of the flow rate and orifice combinations shown in Table 8. The matrix of orifice sizes, flow rates, and strike plate angles results in a total of 27 combinations for testing.

Table 8. Sprinkler operating conditions.

	Effective Sprinkler Nozzle Diameter		
Flow Rate	4.07 mm	6.04 mm	8.48 mm
0.189 L/s (3 gpm)	X		
0.315 L/s (5 gpm)	X		
0.379 L/s (6 gpm)	X	X	X
0.568 L/s (9 gpm)		X	
0.631 L/s (10 gpm)		X	X
0.757 L/s (12 gpm)			X

The water is provided by a 0.75 kW (1 hp) mechanical, 14 stage centrifugal pump, capable of providing 0.757 L/s (12 gpm) at 689 KPa (100 psig), and 1.28 MPa (185 psig) maximum pressure. Due to the pressure/flow limitations of the pump, the same flow rates could not be used for all of the sprinkler orifice sizes. The pump drafts from a holding tank containing the dye/water solution through a filter. After leaving the pump, the solution passes through a turbine flow meter, a globe valve for throttling the flow, past a pressure gauge, and out through the sprinkler. The elevated platform under the sprinkler routes the solution to a sump, where it is pumped, filtered, and sent back to the holding tank for recirculation. The water supply system is shown in Figure 57.

For the sprinkler experiments, the laser sheets are oriented to cut through the spray vertically, with the sprinkler axis of symmetry in the centerline plane of the sheet thickness. The camera is situated perpendicular to the centerline plane, and the camera lens finely focused on this plane. The laser sheets, camera focus, and sprinkler axis are aligned using nylon monofilament which fluoresces in response to the laser light, and provides a good vertical line for the camera focusing screen.

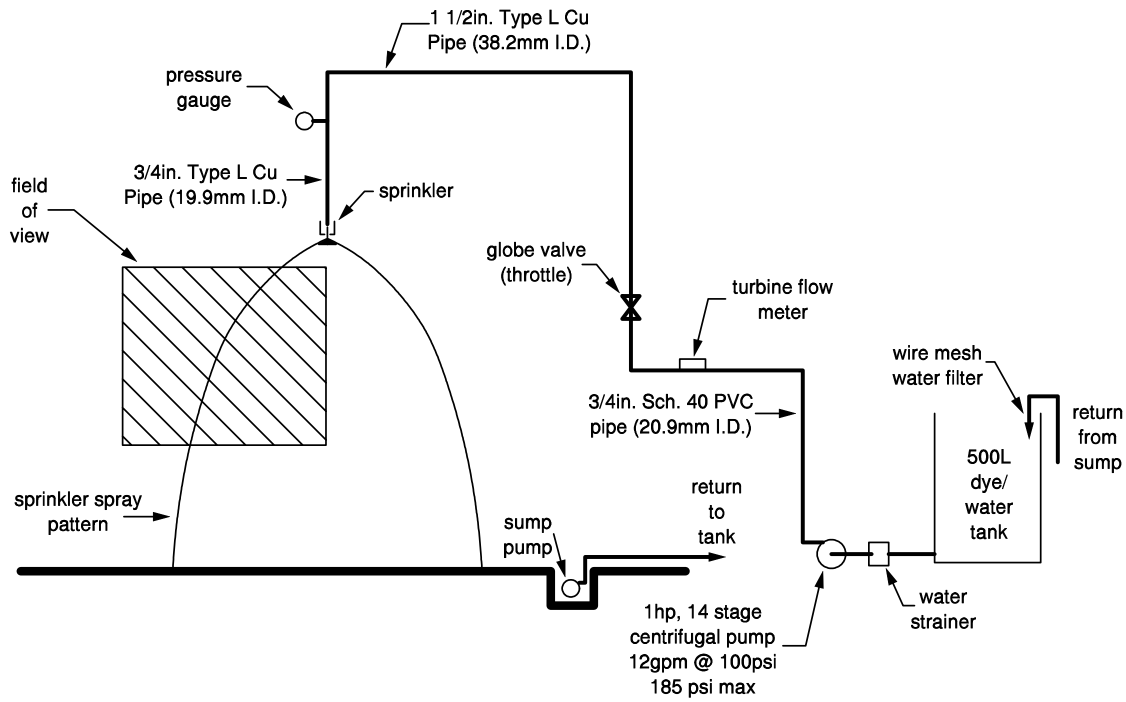

Figure 57. Sprinkler water supply and PTVI field of view.

The initial Δt between the two laser sheet pulses is estimated using the velocity of the water jet emerging from the sprinkler orifice. Assuming a simple flow of incompressible fluid and no friction or breakup losses, the Bernoulli equation is applied, and the initial velocities of the droplets should be the same as the orifice velocity. The initial Δt is the time needed for a large droplet (≈3 mm diameter) to move approximately 3 diameters in the spray field, or approximately 9 mm. This distance was not chosen arbitrarily, but is based on the fact that there is a distribution of drop sizes and velocities. While the droplet velocity will not exceed that at the orifice, there will be slower drops in the measurement region. The Δt is chosen to provide enough distance between the drop images for differentiation, ie. at least one drop diameter apart, and a small enough distance for image matching. Since experimental setup is time consuming, the film must be sent out for development, and the droplets may change speed during their travel, several values of Δt were used for each experiment which bracket the estimated time. In the sprinkler experiments, it was found that the drops slowed significantly over the measurement region, requiring 3× the calculated Δt for measurement of large drops.

The same basic experimental setup and operation parameters were used in all of the sprinkler experiments. These consisted of Fuji NPZ800 medium format color film, a 210 mm camera lens set to f/5.6 with 532 nm notch filter, an exposure of 1/60 s, an 8 mm slit to limit the laser sheet thickness, and scanning at 8 bits/channel. In addition, the fluorescent dye concentrations for all of the sprinkler experiments were approximately 3.3 mg/L of Rhodamine WT and approximately 10. mg/L of stilbene.

4.2 Sprinkler Spray Images

Images from the PTVI method are shown for two sprinklers operating at approximately 0.379 L/s (6 gpm) in Figure 58 and Figure 59. Due to the symmetry of the sprinkler and the digital pixel array in the film scanner, the Cartesian coordinate system is used to identify points within the measurement area. Additionally, the flow from the sprinkler can be defined in terms of a radial distance from the axis of symmetry, and an axial distance from the sprinkler along the axis of symmetry. In both cases, the origin is defined as the center of the sprinkler orifice. Given these definitions, the sheet breakup in the 6 mm orifice case can be clearly seen, and occurs approximately 0.10 m radially and 0.11 m axially from the orifice. The breakup in the 4 mm orifice case occurs closer to the strike plate, and continues as the ligaments also break up into droplets. In order to optimize the data gathered for each sprinkler, the measurement region is shifted radially and axially from the strike plate in order to allow the droplet density to decrease, and so that primary breakup occurs prior to the water entering the field of view of the camera.

The measurement regions used for analysis are shown in Figure 60 and Figure 61.

Magnified sections of the measurement regions are shown in Figure 62 and Figure 63.

Droplet pairs of various sizes can be clearly seen in these photos.

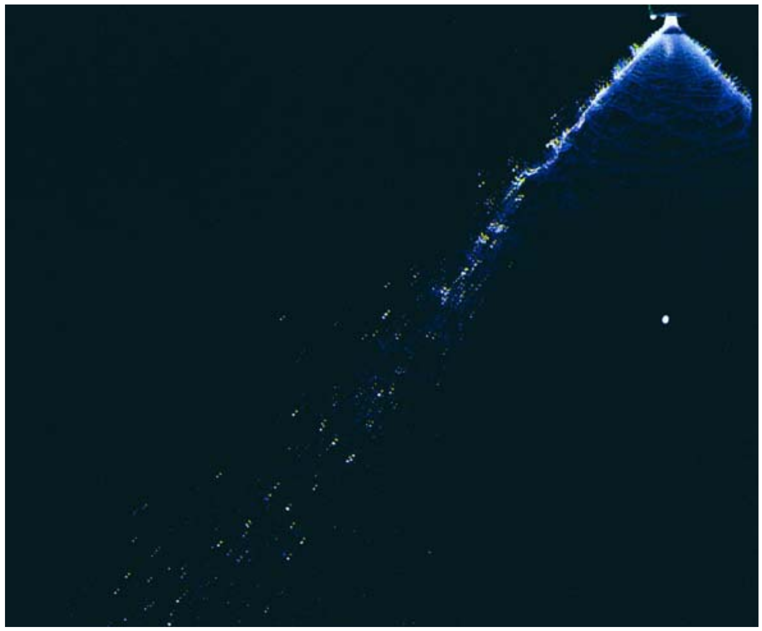

Figure 58. Axis-symmetrical sprinkler with 6 mm nominal diameter orifice and 90 degree strike plate operating at approximately 0.379 L/s (6 gpm). Image area is approximately 0.54 m (21 in.) wide by 0.43 m (17 in.) high. A large droplet can be seen falling from the strike plate support rod.

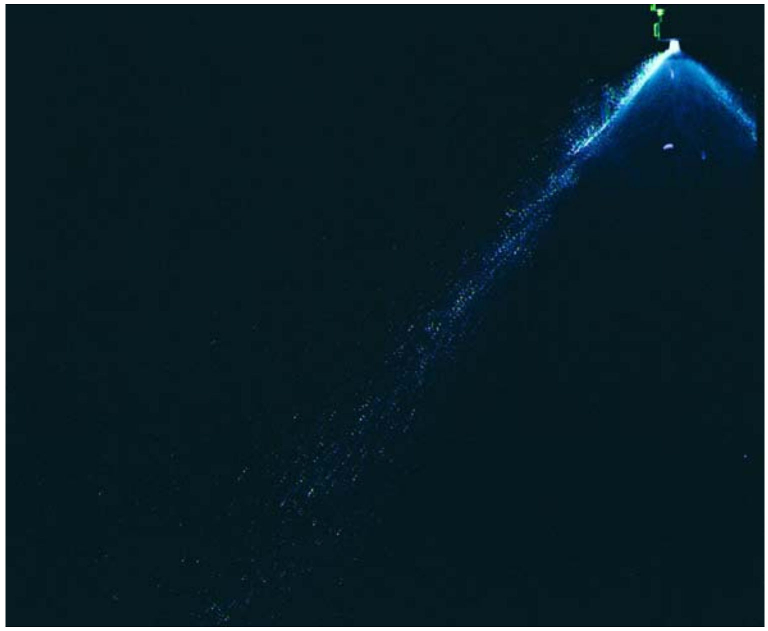

Figure 59. Axis-symmetrical sprinkler with 4 mm nominal diameter orifice and 90 degree strike plate operating at approximately 0.379 L/s (6 gpm). Image area is approximately 0.54m (21 in.) wide by 0.43 m (17 in.) high. A large droplet can be seen falling from the strike plate support rod.

Figure 60. Axis-symmetrical sprinkler with 6 mm nominal diameter orifice and 90 degree strike plate operating at approximately 0.379 L/s (6 gpm). Image area is approximately 0.54 m (21 in.) wide by 0.43 m (17 in.) high. The upper right hand corner of the image area is located approximately 0.216 m (8.5 in.) vertically down from the orifice, and 0.140 m (5.5 in.) horizontally from the symmetric centerline of the orifice. The large orange circle in the upper left of the image is a light emitting diode used as a reference location.

Figure 61. Axis-symmetrical sprinkler with 4 mm nominal diameter orifice and 90 degree strike plate operating at approximately 0.379 L/s (6 gpm). Image area is approximately 0.54 m (21 in.) wide by 0.43 m (17 in.) high. The upper right hand corner of the image area is located approximately 0.152 m (6 in.) vertically down from the orifice, and 0.127 m (5 in.) horizontally from the symmetric centerline of the orifice. The large orange circle in the upper left of the image is a light emitting diode used as a reference location.

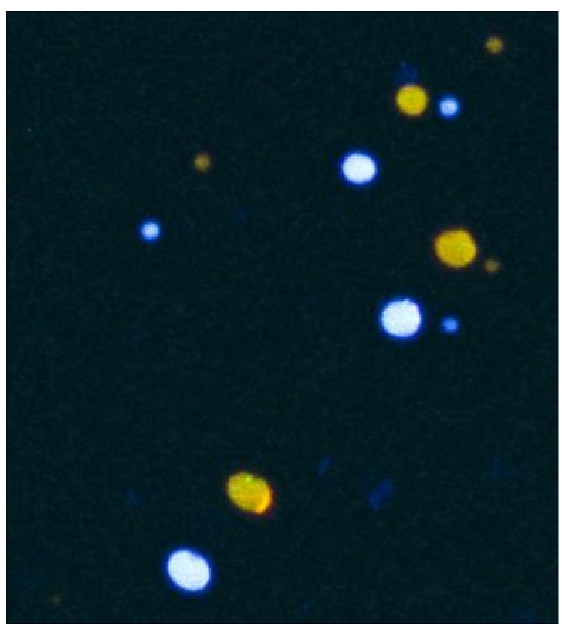

Figure 62. Magnified portion of the measurement area, measuring approximately 20 mm × 20 mm, from the 6 mm nominal orifice diameter sprinkler operating at approximately 0.379 L/s (6 gpm).

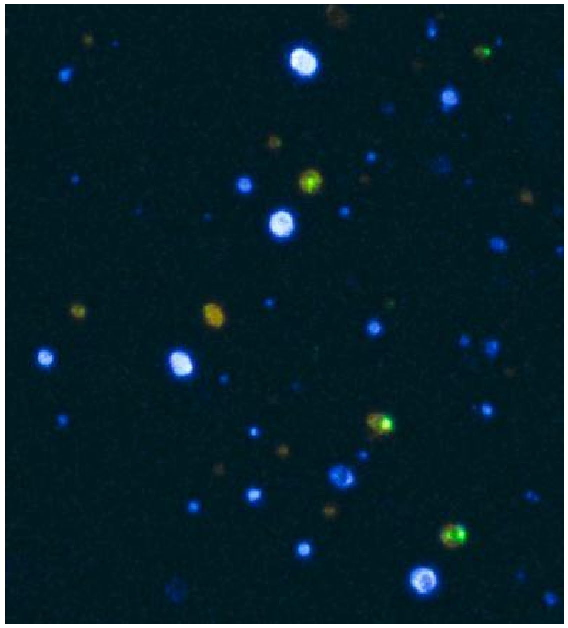

Figure 63. Magnified portion of the measurement area, measuring approximately 20 mm × 20 mm, from the 4 mm nominal orifice diameter sprinkler operating at approximately 0.379 L/s (6 gpm).

Photographs were taken for all of the operating conditions listed in Table 8 with the sprinkler located in the upper right hand corner of the FOV. The photos were digitized and analyzed with the droplet size and velocity algorithms. From these photos, the appropriate Δt between laser pulses was verified, and the location of the breakup region determined. Near the breakup region, the drop concentration is too high for measurements of individual drops. In order to make full use of the FOV, the distance at which individual droplets can be imaged is determined and the upper right hand corner of the FOV is located at this distance. Since the location is approximate, the same FOV location can be used for a number of sprinkler operating conditions. For spatial reference, a light emitting diode of known distance from the sprinkler is placed near the upper left hand corner of the FOV during the experiments. The LED is out of the spray, and provides a visible reference point in the image. The coordinates of the FOV during the experiments are shown in Figure 64 and Table 9.

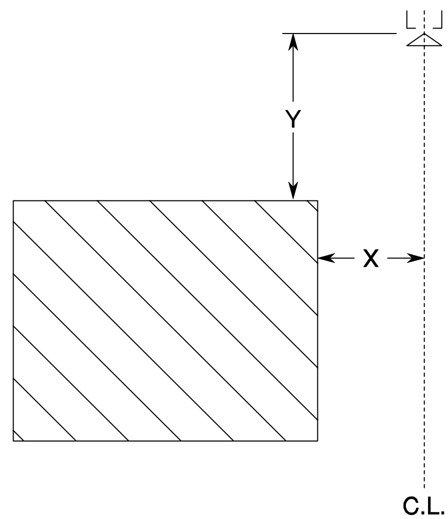

Figure 64. Location of measurement region.

Table 9. Location of measurement region.

Orifice Diameters (mm)	Strike Plate Angle (deg)	Horizontal Position, X (m)	Vertical Position, Y (m)
4.07, 6.04, 8.49	120	0.210	0.133
6.04, 8.49	90	0.140	0.216
4.07	90	0.127	0.152
4.07, 6.04, 8.49	60	0.000	0.406

4.3 Image Analysis Algorithms

Once the film has been developed, it is digitized at 4000 dpi and 8 bits/channel (24 bit image) with a film scanner. The images scanned in this manner are on the order of 260 MB in size, therefore efficiency of the analysis methods is important. A custom macro written in Microsoft Visual Basic, and executed within ImagePro Plus V4.5, analyzes the images. At the start of this investigation, each image was split up into 9 images for analysis, and then recombined. Alternative methods were found, however, that allowed for the analysis of the whole images, simplifying the process. The computer used to analyze the images is equipped with a 1.8 GHz Pentium 4 processor, 1 GB of RAM, and Windows 2000.

The macro automates the analysis of each image, conducting the following general steps. Brief user's and reference guides for the macro are given in Appendix B and Appendix C, with the text of the macro listed in Appendix D.

1. Measure the size of the droplets and their locations. This is done by examining the intensity gradients to find the droplet edges. This is discussed in detail in Chapter 3.
2. Reject drops with an aspect ratio >2, where the aspect ratio is defined as the major diameter/ minor diameter. This gets rid of image defects such as lint and dust on the film, as well as portions of irregular drops that are outside the measurement volume.
3. Get the locations of the yellow images, and make separate lists of the sizes and locations of the yellow and blue images.
4. Match the yellow and blue image pairs, and determine the velocity of the drop associated with the image pair. This is done by examining the following 3 relationships, and repeating the process 3 times so that the images are matched with their best mate.
    a. The distance between the droplet images must be reasonable compared to the distances between the other drop pairs. (The distance between a pair of drop images must be between 0.25× to 1.75× the average distance between drop image pairs)

b. The size of the yellow and blue images must match. (The diameter of the blue drop must be >2× the yellow drop diameter. The process of size matching is iterated, so the diameter differences decrease with further iteration as older tentative pairings are abandoned for new pairings between drop images closer in size.)

c. The angle between the drop images (velocity unit vector) must be reasonable compared to the initial angle of the strike plate. (The velocity angle must be ±30° from the strike plate angle)

5. Report the results of the analysis. Locations and sizes of the drops are determined from the blue images, and droplet velocity determined from the blue and yellow pairs.

The sizing algorithm is quite general in scope, and is applicable to general flow streams. The velocity algorithm, however, was developed specifically for sprinklers where the approximate direction of the water droplets is known beforehand. It should work well if the directions are within a quadrant, but is expected to have limited success where droplets are subject to flow reversals or turbulence. Such a case would be the examination of flows in a fire environment, where flow reversals are expected. Under such conditions, the methodology used in the velocity algorithm would need to be reconsidered, but the two-color imaging would still be valuable in resolving flow direction.

CHAPTER 5

SPRINKLER DROP SIZE AND VELOCITY

The image analysis macro produces two data files for each image. One file contains droplet size data consisting of droplet location and equivalent drop diameter. The second file contains droplet velocity data consisting of droplet location, equivalent drop diameter, speed, and direction. Since droplets could not always be paired, the velocity data file is a subset of the droplet diameter file.

In order to calculate statistics for the droplets, droplet sizes were categorized using size bins. Each bin is 100 μm wide, and is identified by the upper bound of the size bin. Therefore, drops smaller than 100 μm are in the 100 μm bin, droplets with diameters between 100 μm and 200 μm are counted in the 200 μm bin, and so on up to 3000 μm. This methodology was chosen since it is the most compatible with viewing the cumulative distribution functions of drop size. The same methodology was used to determine the droplet velocity distribution as a function of drop size. Since approximately 10 film exposures exist for each sprinkler operating condition, the results were averaged over the exposures. The number and volume fractions of drops as a function of drop diameter are listed in Appendix E for all operating conditions. The number fraction is defined as the number of drops within a bin, divided by the total number of drops in all size bins, as shown in Equation 16. The volume fraction is defined as the volume of the drops within a bin, divided by the total volume of the drops within all of the bins, as shown in Equation 17.

$$NF(bin) = \frac{N_{bin}}{\sum_{i=bin1}^{bin30} N_i} \qquad (16)$$

$$VF(bin) = \frac{V_{bin}}{\sum_{i=bin1}^{bin30} V_i} \qquad (17)$$

where: NF(bin)=number fraction of drops within the size bin
VF(bin)=volume fraction of drops within the size bin
N_{bin}=number of drops within the size bin
V_{bin}=volume of drops within the size bin
bin1=bin containing drops from 0 μm to 100 μm in diameter.
bin30=bin containing drops from 2900 μm to 3000 μm in diameter.

Given the above definitions, $\sum_{i=1}^{30} NF(i) = 1$ and $\sum_{i=1}^{30} VF(i) = 1$.

The volume fraction is more useful than the number fraction due to the greater uncertainty in the total number of drops present in the measurement volume. Since the experimental setup is limited to measuring drops greater than approximately 150 μm in diameter, and there are potentially a large number of drops below this size, the number fraction is expected to be skewed toward larger drop diameters. This limitation has a much smaller effect on the volume fraction data, since the potentially large numbers of small drops contain a very small volume of water.

Cumulative number fraction and cumulative volume fraction data for all operating conditions is also given in Appendix E. The cumulative fraction data represents the number or volume fraction of droplets with diameters equal to or less than a given size.

This is calculated by summing the number or volume of the drops in all bins smaller than the diameter of interest, and dividing by the total number or total volume of all drops measured, as shown in Equation 18 and Equation 19. Given these definitions, CNF(30)=CNF(3000 μm)=1 and CVF(30)=CVF(3000 μm)=1. As with the number fraction data, the cumulative number fraction data is limited by the potentially large number of drops too small to be detected. The cumulative volume fraction data does not have this limitation, and is quite valuable for sprinkler studies. In both cases, the median drop sizes are also listed in tables within Appendix E.

$$CNF(bin) = \frac{\sum_{i=bin1}^{bin} NF(i)}{\sum_{j=bin1}^{bin30} NF(j)} \tag{18}$$

$$CVF(bin) = \frac{\sum_{i=bin1}^{bin} VF(i)}{\sum_{j=bin1}^{bin30} VF(j)} \tag{19}$$

where: CNF(bin)=cumulative number fraction of drops with diameters ≤ the upper size range of the bin
CVF(bin)=cumulative volume fraction of drops with diameters ≤ the upper size range of the bin

Droplet velocity data is also compiled, but is more difficult to present. Velocities have magnitude and direction, and it is conceivable that droplet velocity components are functions of droplet size as well position in the spray field. Despite these challenges, the average velocity magnitudes (m/s) of drops within the measurement region are presented as a function of drop size in Appendix E for all operating conditions. In this table, a velocity of zero is the result of no droplet velocities being measured in the size range. Droplet velocities are discussed in depth later in this chapter.

5.1 Drop Size Distribution

The drop size distribution is an important characteristic of the sprinkler spray that describes the number, surface area, or volume of water contained in various droplet size ranges. Plots of the cumulative volume fraction for all of the operating conditions are presented in Appendix E, and illustrate that the sprinkler operating conditions have a large effect on the drop size distribution. One measure of this effect is the volume median drop size, which corresponds to the drop size at 50% cumulative volume fraction.

In order to make the most out of the droplet size data, it would be useful to find an analytical function that fits the number and volume fraction data. One function that commonly fits droplet size data well is the log-normal function. The log-normal function is convenient for many reasons, including widely available conversion equations between count, surface area, and mass fractions (Hinds 1999). The function is also useful in that the data of this form will produce a Gaussian shaped symmetric plot. The log-normal distribution (number fraction) is given in Equation 20 (Babinsky and Sojka 2002). For the drop size functions discussed in this section, there are notation conventions used for easily determining the character of the function. Lowercase “f ”, for example denotes a fraction, while uppercase “F” denotes a cumulative fraction. The subscript “0” denotes a function based on count or number, while a subscript of “3” denotes a volume based function.

$$f_0(d) = \frac{1}{d\left(\ln[\sigma_{LN}]\right)\sqrt{2\pi}} \exp\left[-\frac{1}{2}\left(\frac{\ln[d/\bar{d}]}{\ln[\sigma_{LN}]}\right)^2\right] \quad (20)$$

where: $f_0(d)$=number fraction
$\bar{d}$ =logarithmic mean size of distribution
σ_{LN}=width of distribution
d=drop diameter

Assuming that the data is fit by a log-normal function, two data sets are chosen that represent the range of operating conditions considered in this study. By using the symmetry of log-normal plots, an indication will be given as to the ability of the measurement technique to capture the entire droplet size range produced by the sprinklers. The two operating conditions considered are 4 mm and 6 mm orifice sprinklers, both operated at 0.379 L/s (6 gpm) and having 90 degree strike plates. The Weber numbers of the flows, defined at the orifice, are 4.72×10^4 and 1.44×10^4 respectively, out of a range of 5.20×10^3 to 4.72×10^4 for all of the experiments.

The drop size number fractions for the two operating conditions are first plotted in Figure 65 on linear axis. From this plot it can be seen that there is a steep drop in number fraction at diameters smaller than the median, but a long tail at diameters larger than the median. The median droplet size based on count is approximately 220 μm for both sprinkler operating conditions, but it is estimated that 4.6% of the 6mm orifice drops and 41% of the 4 mm orifice drops were less than 200 μm. The data is plotted in log-normal format in Figure 66, a process that compresses the tail at large diameters, and expands the data at small diameters. The data was converted to log-normal format by dividing the number fraction in each bin by the difference in the natural logs of the upper and lower bounds of the bin. (Hinds 1999) If the data is fit by a log-normal distribution, the plot will be symmetric. In this case, the plot illustrates that the diameter of peak number fraction has been captured, but that many droplets under 100 μm in size have probably been missed by the measurement technique. This is not surprising since at the onset of this study the decision was made to concentrate on measuring drop sizes larger than 200 μm with a low level of uncertainty, which in the past was found to contribute most to the overall water volume. Note that the smallest size bin, 0 μm to 100 μm, is excluded due to the logarithm of the lower limit being undefined. The number fraction plotted in log-normal format suggests that the number median is between 200 μm and 300 μm, which agrees with the cumulative number fraction plot. Since the number fraction peak has been captured, the plots suggest that the droplet measurement technique did not miss a large number of small droplets below the detection limit.

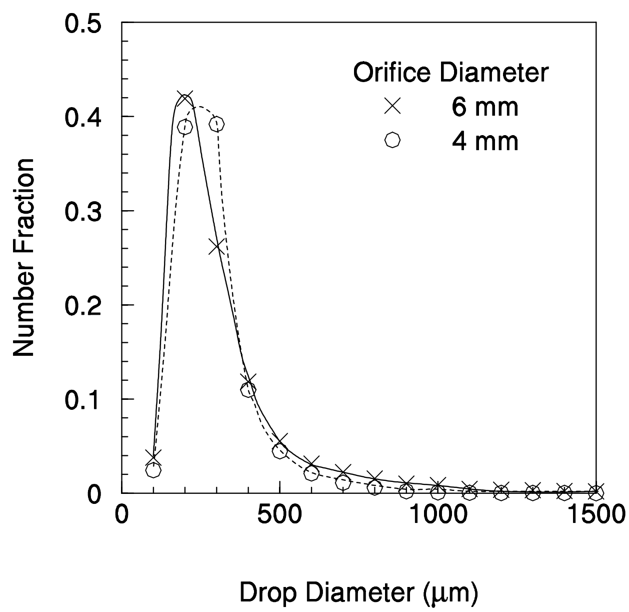

Figure 65. Drop size number fraction distribution is compared for the 6 mm and 4 mm nominal diameter orifice sprinklers operating at 0.379 L/s (6 gpm).

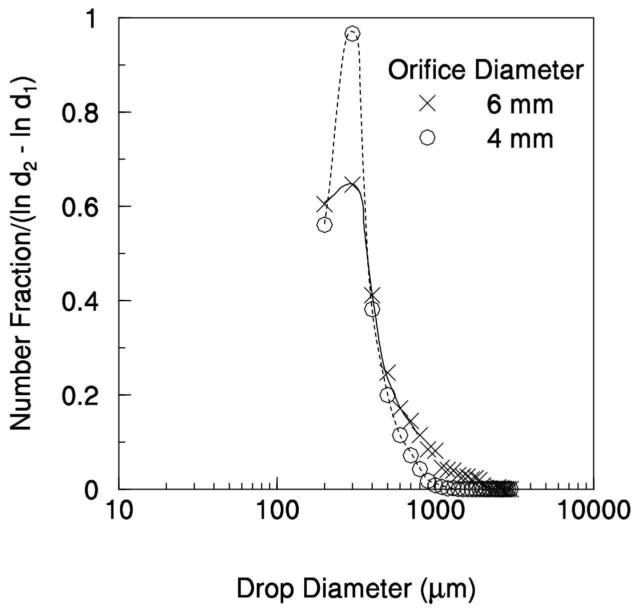

Figure 66. Drop size number fraction distribution plotted in logarithmic format. The diameter of peak number fraction has been captured, but as expected, there are many droplets less than 200 μm that have been missed by the measurement technique. A log-normal drop size distribution would form a normal shaped curve on this plot. The values of d_1 and d_2 used to calculate the ordinate are the lower and upper bounds of each droplet size bin.

Linear plots of the droplet volume fractions are found in Figure 67. These plots show that for the 4 mm sprinkler, the peak water volume fraction is at approximately 300 μm, and decreases rapidly at larger drop sizes. For the 6 mm orifice, the water volume is distributed similarly for drop sizes from approximately 500 μm to 2000 μm. The droplet volume fraction distribution is graphed using logarithmic plots in Figure 68. If the drop distribution is log-normal in nature, then the drop volume distribution should be symmetric, of the same shape as the number distribution, but shifted to the right. It appears that the volume distribution does not fit the log-normal distribution well, especially for the 6 mm orifice size, which is true for most of the sprinkler data examined in this research. The distribution does seem to indicate, however, that the measurements did a good job of capturing the droplets containing most of the water from the sprinkler.

This is also illustrated by examining the cumulative water volume fraction shown in Figure 69. This graph shows that the original premise of the measurement design holds true, that droplets greater than 200 μm in diameter contain more than 95% of the water ejected by the sprinkler (98.7% for the 6 mm orifice and 95.1% for the 4 mm orifice). This condition holds true for sprinklers producing a wide range of droplet sizes and operating conditions. The cumulative volume distribution also shows that the 4 mm orifice sprinkler provides 50% of the water volume (volume median) at drop sizes greater than approximately 450 μm, while the 6 mm sprinkler provides 50% of the water volume at drop sizes greater than approximately 1140 μm. While the number median drop sizes are similar, at approximately 220 μm, there is a substantial difference in the volume median drop sizes due to the d^3 relationship. Since fire suppression is dependent on the volume (mass) of water available for cooling, the volume distributions provide more insight into the effectiveness of the sprinkler.

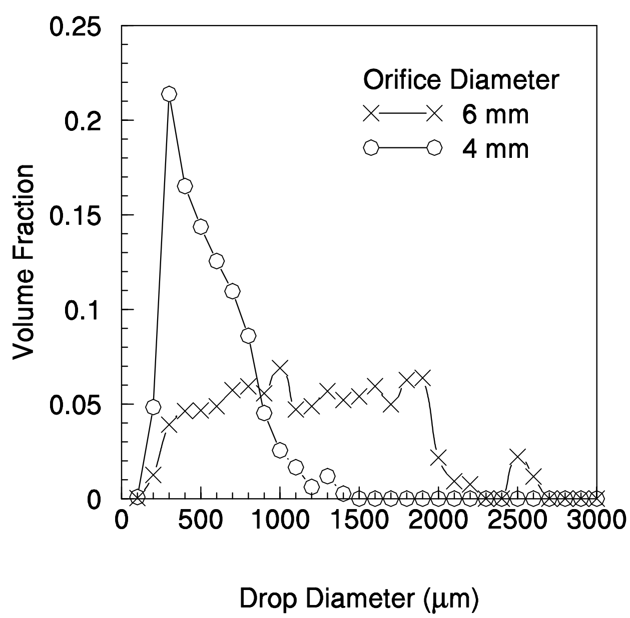

Figure 67. Drop size volume fraction distribution is compared for the 6 mm and 4 mm nominal diameter orifice sprinklers operating at 0.379 L/s (6 gpm).

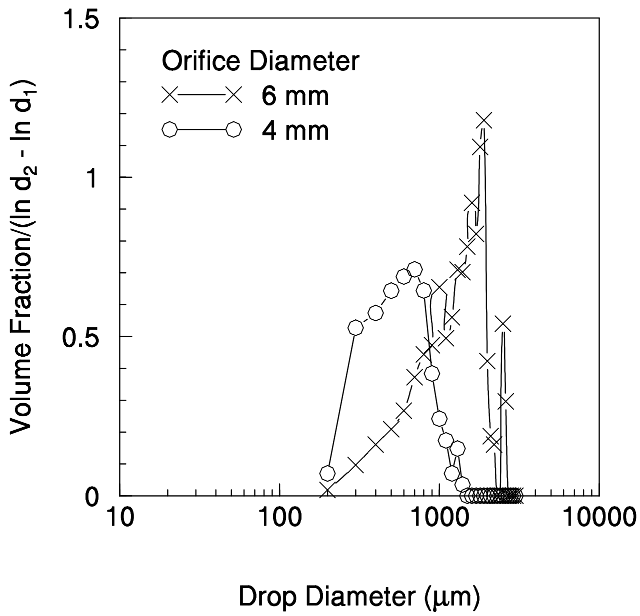

Figure 68. Drop size volume fraction distribution plotted in logarithmic format. The diameter of peak volume fraction has been captured, along with the slopes down to nearly zero on each side of the peak. This indicates that the measurement has captured most of the volume flow. A log-normal drop size distribution would form a normal shaped curve on this plot. The values of d_1 and d_2 used to calculate the ordinate are the lower and upper bounds of each droplet size bin.

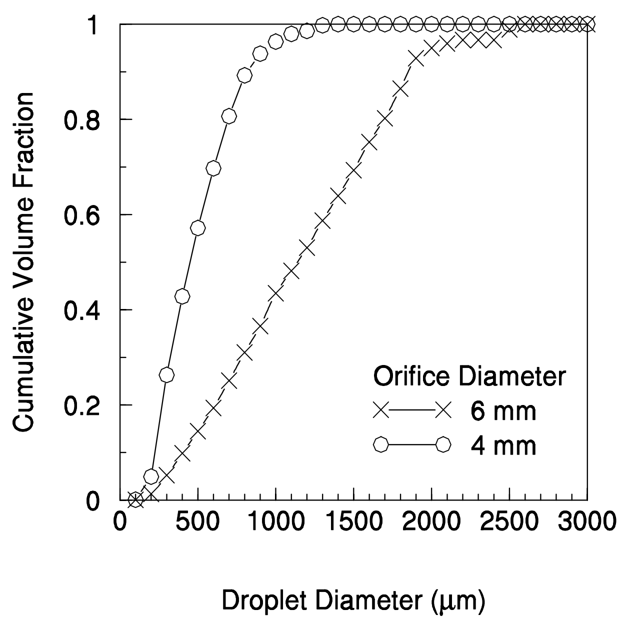

Figure 69. Cumulative volume fraction distribution. The 6 mm nominal orifice sprinkler produces droplets containing a higher fraction of water at larger drop sizes than the 4 mm orifice sprinkler.

The above results for the 4 mm and 6 mm orifice sprinklers operated at 0.379 L/s (6 gpm) were derived from averaging the results of 8 film exposures. One of the questions to be answered is how many images are necessary to suitably characterize the flow from the sprinkler. For the axis-symmetric sprinklers studied here, the results are summarized in Figure 70 and Figure 71. In these figures, the results from one exposure and from averaging the results from 4 and 8 exposures are plotted for comparison. For the 4 mm orifice sprinkler, the results from 4 and 8 exposures are nearly identical, while the results from 1 exposure are within approximately 10% of the 4 and 8 exposure values over the entire droplet diameter range. For the 6 mm orifice, the 4 and 8 exposure results were within approximately 2% of each other, while the 1 exposure result was within approximately 15% of the 4 and 8 exposure values over the entire droplet diameter range. These results indicate that for the sprinklers studied here, approximately 4 exposures would be sufficient for determining droplet size statistics, and less than 4 exposures are acceptable if a higher level of uncertainty can be tolerated or if time varying behavior is to be captured.

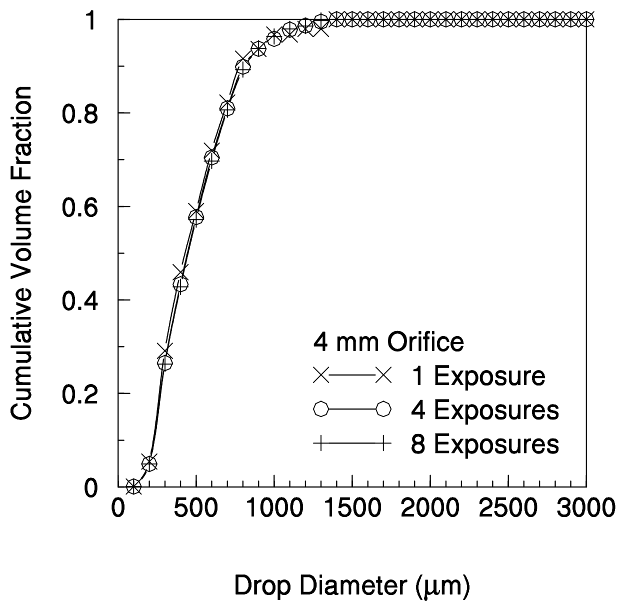

Figure 70. Cumulative volume fraction for the 4 mm nominal diameter orifice, comparing the results of averaging 1, 4, and 8 film exposures.

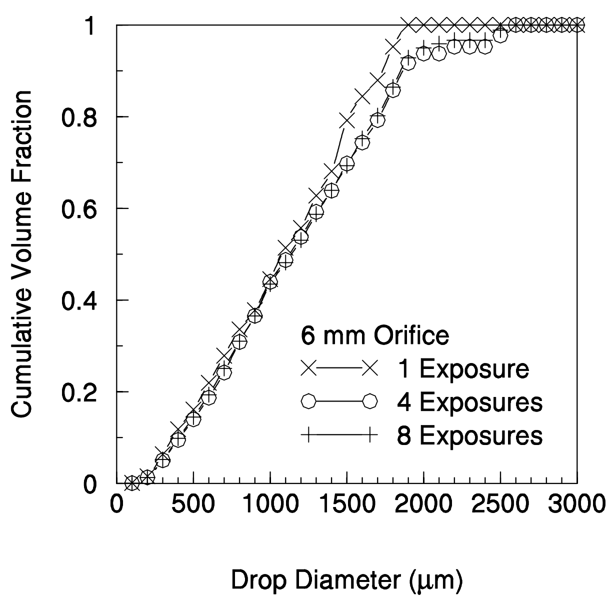

Figure 71. Cumulative volume fraction for the 6 mm nominal diameter orifice, comparing the results of averaging 1, 4, and 8 film exposures.

It has been demonstrated that the log-normal distribution is not effective for characterizing the droplet size distributions. The most useful function would be one that fits all of the sprinkler data. In an effort to find such a function, several other functions commonly used to characterize droplet sprays were applied to the droplet size data. These functions consisted of the normal distribution, root-normal distribution, log-hyperbolic distribution, the Nukiyama-Tanasawa distribution, and the Rosin-Rammler distribution (Babinsky and Sojka 2002). Of these functions, it was found that the log-normal function fit a portion of the data at small drop sizes, and the Rosin-Rammler function fit the larger droplet sizes.

This agrees with the work of both You (1986) and Dundas (1974), who found that the cumulative volume fraction distributions of commercial sprinklers could be represented by a combination of log-normal and Rosin-Rammler distributions. In their studies, the log-normal distribution was fitted to drop diameters less than the median size, and the Rosin-Rammler distribution was fitted to droplet diameters greater than the median. (McGrattan, Forney, et al. (2002) give a procedure for assuring a smooth transition between the two functions for use with fire models.) The data from the current study was plotted in different ways to look for a similar correlation. Plotting the data on a graph with a logarithmic axis for the drop diameter, and a probability axis for the cumulative volume fraction should show a straight line for the data following a log-normal distribution. This was done for all of the droplet size data, and it was found that most of the operating conditions had some data, all at small drop diameters, fitting the log-normal distribution. In addition, the Rosin-Rammler distribution fit the data at larger drop sizes for most of the sprinkler operating conditions. The transition from log-normal to Rosin-Rammler, however, did not occur at the same cumulative volume fraction for all of the operating conditions and was frequently much different than the volume median drop diameter. Large portions of some cumulative volume distributions fit normal distributions.

For characterization of the sprinkler drop size distributions, general rules for fitting functions to the droplet size data were not found. For calculations of sprinkler sprays, and for gauging their effectiveness, the most important droplets are those containing most of the water. Therefore it may be possible to fit a function to the most important parts of the cumulative volume fraction function. This is investigated for the 4 mm and 6 mm sprinklers discussed in previous paragraphs, and illustrated in Figure 72. Figure 72 shows a Rosin-Rammler fit to the data, concentrating on matching the areas containing most of the water volume. The Rosin-Rammler function is defined as (You 1986):

$$F_3(d) = 1 - \exp\left[-\phi\left(\frac{d}{d_m}\right)^{\gamma}\right] \qquad (21)$$

where: $F_3(d)$=cumulative volume fraction
$\phi = kd_m^{\gamma}$
d_m=volume median drop diameter
d=drop diameter
k=adjustable parameter that scales $F_3(d)$ in the positive and negative directions
γ=adjustable parameter that changes the curvature of the function.

For these two cases, the Rosin-Rammler function provides good agreement for drop sizes ≥300μm, but agreement decreases at smaller drop sizes, especially for the 4 mm orifice. The distribution covers 74% of the water volume from the 4 mm orifice sprinkler, and 95% of the water volume from the 6 mm sprinkler at drop sizes ≥300 μm.

The data is also shown plotted on probability and logarithmic axes in Figure 73. This plot illustrates the limits of the log-normal distribution. Given the axes of the plot, data fitting a log-normal distribution would be a straight line. This region is limited to drop sizes ≤300μm for both orifice sizes.

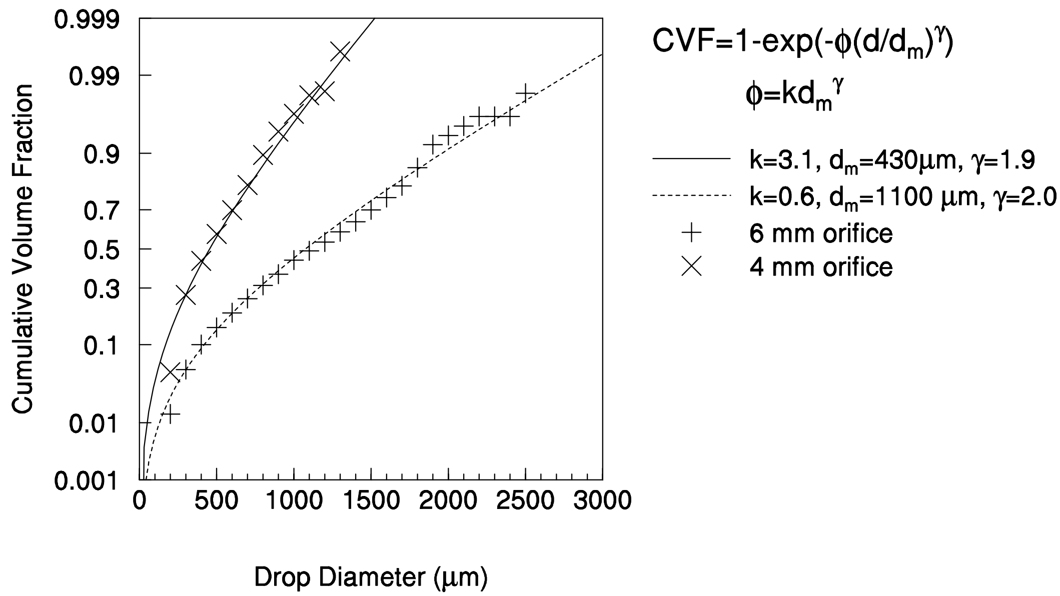

Figure 72. The Rosin-Rammler function is fit to the cumulative volume fraction data. The volume median drop size, d_m, is determined from the diameter at CVF=0.5. The values of k and γ are determined by inspection.

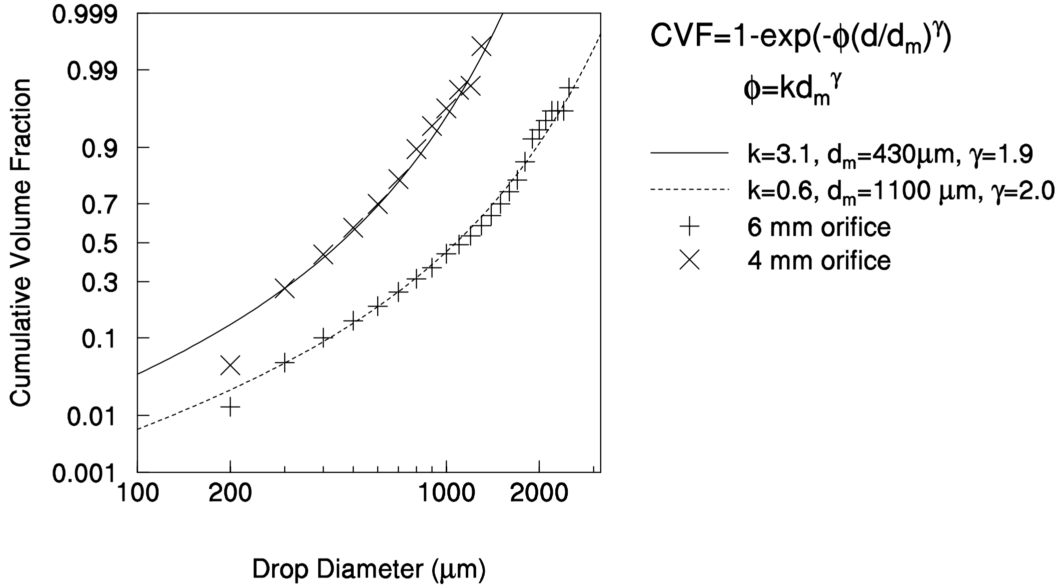

Figure 73. The Rosin-Rammler function is compared to the cumulative volume fraction data on log-probability axes. A log-normal function would be a straight line on these axes, and fits the data at drop sizes less than approximately 300 μm.

As discussed in Chapter 2, the drop size distribution is expected to be a function of the sprinkler Weber number, $We=\rho du^2/\sigma$, where ρ is water density, d is orifice diameter, u is orifice velocity, and σ is the droplet surface tension. The Weber and Reynolds numbers for the sprinkler flow conditions are shown in tabular format in Appendix E. It was observed that the drop size distributions for experiments with the same orifice diameter and flow rate were similar. There are two sets of experiments, however, with nearly identical orifice Weber numbers. The drop size distributions for these cases are plotted in Figure 74. Notice that the drop size distributions with the same Weber number have a similar shape. Since the only variable that affects the value of We in these experiments is the water velocity at the orifice, these plots illustrate that some collapse of the data occurs for similar orifice velocities. The plots also show that the volume fraction distributions differ in shape. This suggests that there is not a universal drop size distribution function for all of the experiments.

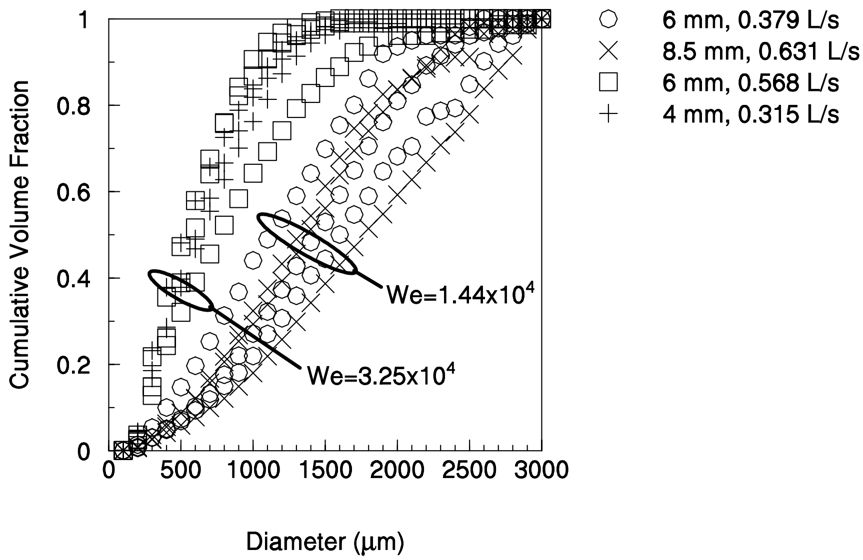

Figure 74. Cumulative drop size volume fraction distributions by Weber number. Note that there are only two Weber number conditions in the plot; 3.25×10^4 and 1.44×10^4.

Given the importance of the volume median drop size, it would be useful to be able to predict it given the characteristics of the sprinkler. As briefly discussed in the Chapter 2, previous researchers found that the drop size from sprinklers could be correlated by the following expression (Dundas 1974):

$$\frac{d_m}{d} = c\, We^{-\frac{1}{3}} \tag{22}$$

Where "d_m" is the volume median drop diameter, "d" is the orifice diameter, and "c" is a constant dependent on the sprinkler geometry. The exponent of the Weber number was the result of an analysis of the breakup of thin liquid sheets, which first disintegrated into liquid ligaments, then into drops.

The droplet size results from the current study, as well as the results from other researchers are shown in Figure 75. The data from other researchers consists of that from an idealized sprinkler, as well as from a spray nozzle offered by Spraying Systems Co. (Dundas 1976). The NIST data from this study is proportional to $We^{-2/3}$ rather than to the $We^{-1/3}$ relation that fits the Dundas idealized sprinkler data. In addition, the spray nozzle data has a range of slopes, varying from -1/3 for $We<10^4$ to -2/3 for $We>3\times10^4$, when transitioning over a large range of Weber numbers. Given the behavior of the NIST data as compared to the data from other researchers, it appears that the droplet breakup mechanism is different for the NIST sprinkler. This is not altogether unexpected due to the breakup regimes described by other researchers (Prahl and Wendt 1988, Villermaux and Clanet 2002) that describe sheet breakup without formation of the ligaments proposed by Dundas. While Villermax and Clanet (2002) have also published data investigating the drop size distributions as a function of Weber number, their data is correlated using the arithmetic mean droplet diameter (count), and does not include enough information for conversion to volume median droplet diameter. Therefore, their data could not be included in Figure 75.

An interesting phenomenon was also observed in the NIST data. The 5 outlying points on the plot are at $We=5.20\times10^3$, the lowest Weber number studied, and the result of 0.379 L/s (6 gpm) flowing through an 8.5 mm sprinkler nozzle. For all strike plate angles at this flow condition, the water sheet persisted long enough after leaving the strike plate to be significantly affected by surface tension and gravity forces. The result was similar to the “water bells” described by Taylor (1959). For the sprinklers studied, flows in this We regime did not fit the trends of the other data. The reason for this difference is not fully understood. The sprinkler Weber numbers of all the sprinkler operating conditions put the water flows within the flapping regime ($We \geq 10^3$) described by Villermax and Clanet (2002), so all of the data was expected to follow the same $We^{-2/3}$ relation. This will be discussed further in the sections on droplet velocity.

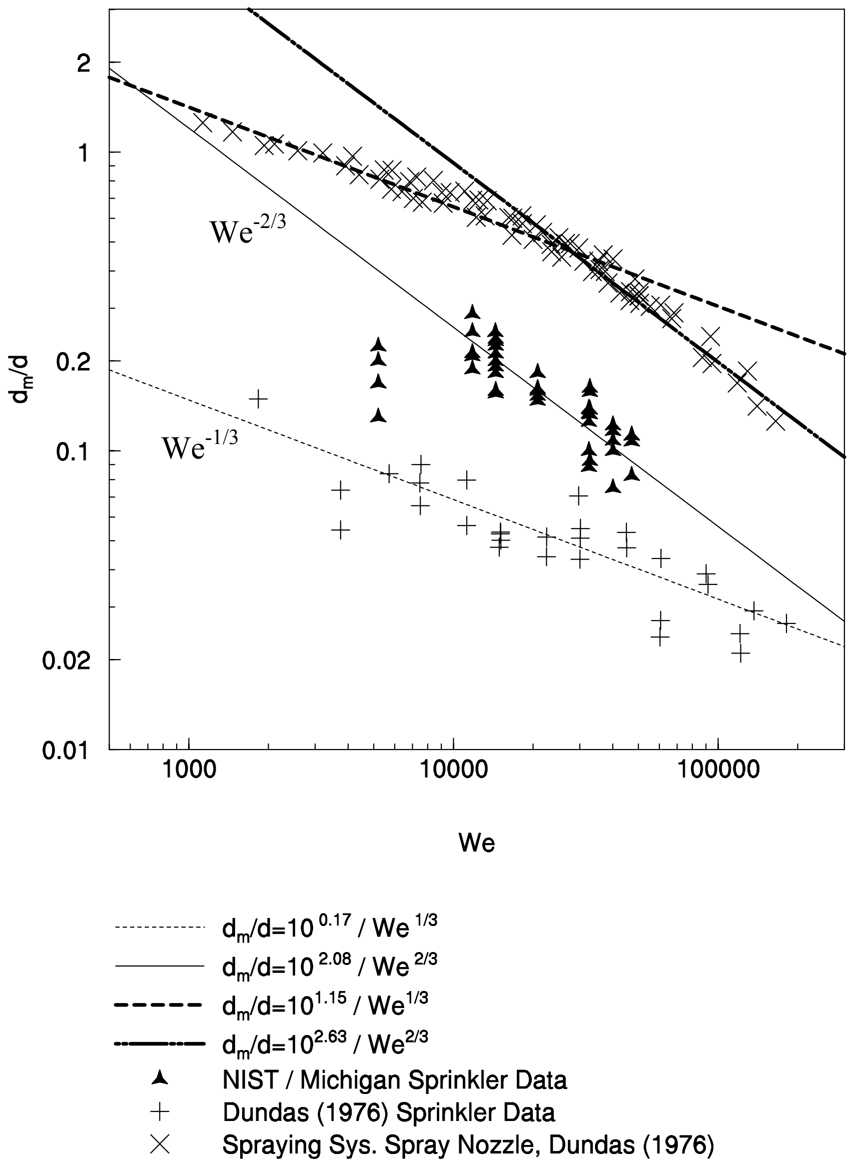

Figure 75. Normalized droplet size as a function of sprinkler Weber number. Drop size is expressed by normalizing the volume median droplet size, d_m, with the equivalent orifice diameter, d.

5.2 Measured Water Flux Distribution

The water flux distributions applied to the floor beneath the sprinklers were measured by a row of square pans. The polystyrene pans, each having interior dimensions of 147 mm ± 1 mm by 147 mm ± 1 mm by 149 mm ± 1 mm high, with a wall thickness of 2.54 mm ± 0.05 mm, were placed in a straight line under the sprinkler. The line of pans intersected the axis of symmetry of the sprinkler, so that the pans formed a complete diameter of the circular water pattern formed on the floor. (Figure 76) Sprinkler water fluxes were measured at the floor for most of the sprinkler operating conditions listed in Table 8, at 2.083 m ± 0.013 m below the sprinkler.

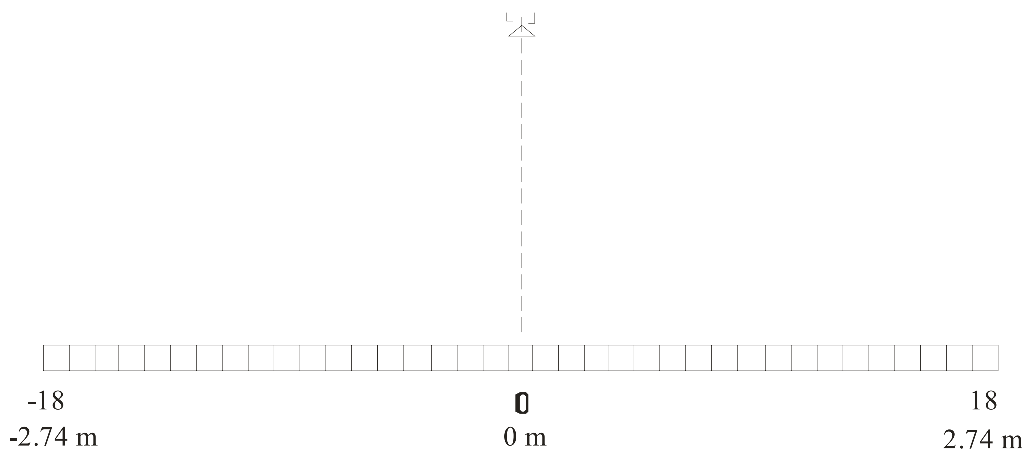

Figure 76. Water collection pans. The water collection pans are located under the sprinkler, and form a diameter of the roughly circular water pattern on the floor. The centerline of the sprinkler is located over the center of pan "0." The centers of the outermost pans are located approximately 2.74 m from the sprinkler centerline.

Prior to the flux measurements, the mass of each bucket was determined using an electronic balance. For each operating condition, the buckets were dried, aligned under the sprinkler, and covered with a sheet of plastic. The water flow was started, and once the flow rate and pressure were stabilized, the plastic cover was removed. When the fastest filling bucket(s) neared capacity, a pail was inserted over the sprinkler, halting the filling of the pans, while the water flow was stopped. The total filling time for the buckets was recorded.

At the end of the test, the outside surfaces of each pan were dried and the mass measured. Water fluxes were calculated by dividing the mass of water delivered by the filling time and the pan area. Due to the design of the sprinklers, axis-symmetric behavior was expected. In order to verify this, an entire diameter of the spray field was measured instead of a single radius.

The water fluxes for the sprinkler operating conditions are shown in Figure 77, Figure 78, and Figure 79, with an uncertainty of $\pm 2.0\times10^{-3}$ kg/(m^2s). Unfortunately, the symmetrically constructed sprinkler did not operate in a symmetric manner for all operating conditions. In some cases, this could be seen beforehand by observing the water pattern on the floor. In other cases, the delivered density measurement was necessary to uncover the asymmetric behavior. For some operating conditions, mostly those where high flow rates were exiting a small nozzle, the water sheet would adhere to the strike plate on one side, and to the orifice opening on the other. In some cases, this behavior was unsteady, and the flow would flip flop between the two. In other cases, ligaments of water would emerge from the orifice area instead of a smooth water sheet. Some of the asymmetrical behavior could be remedied by careful adjustment of the nozzle, or slight bending of sprinkler parts. During testing, if the sprinkler flow was not qualitatively steady, the test was abandoned, resulting in no data for some sprinkler and flow combinations. For future experiments, the sprinklers should be redesigned, constructed of stronger materials, and manufactured to higher tolerances.

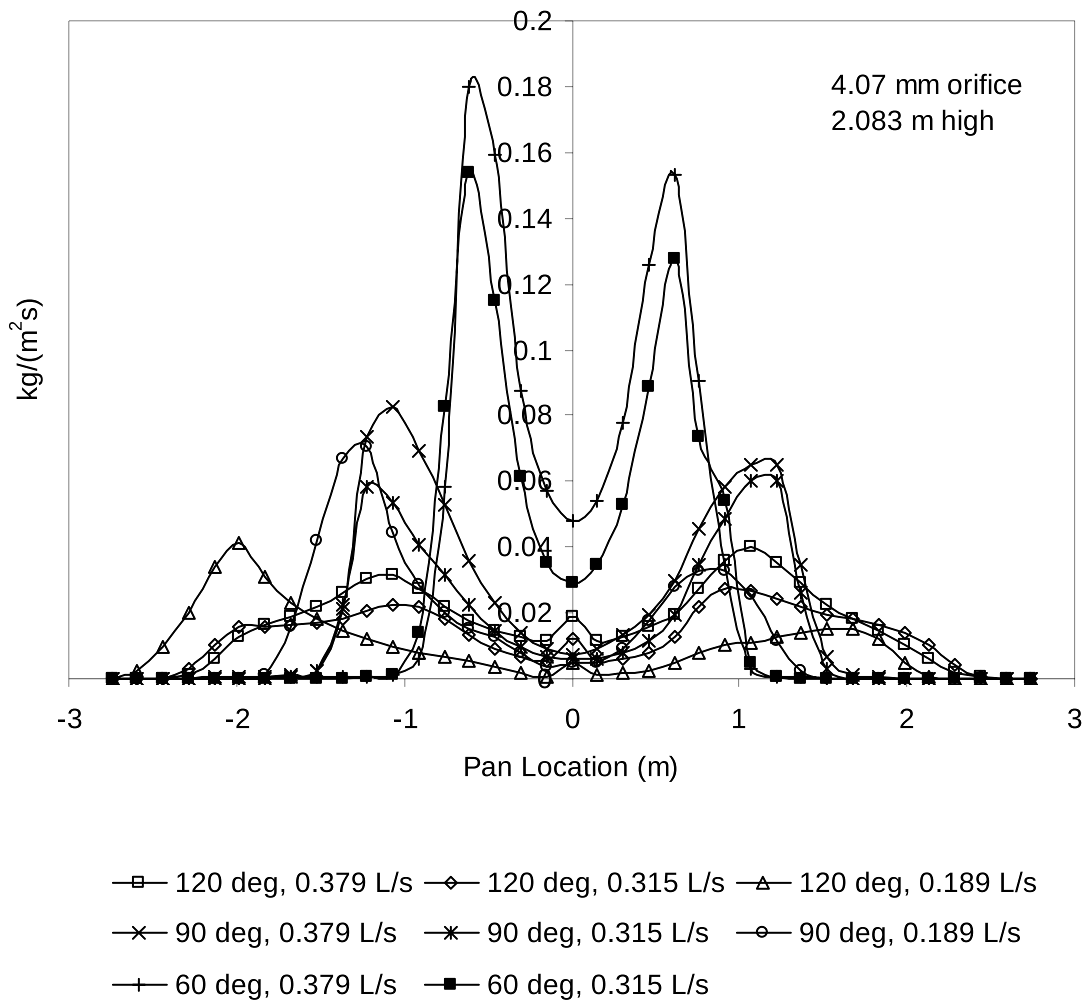

Figure 77. Water flux from a 4 mm nominal orifice diameter sprinkler approximately 2.08 m above the floor. Data is shown for various strike plate angles and flow rates.

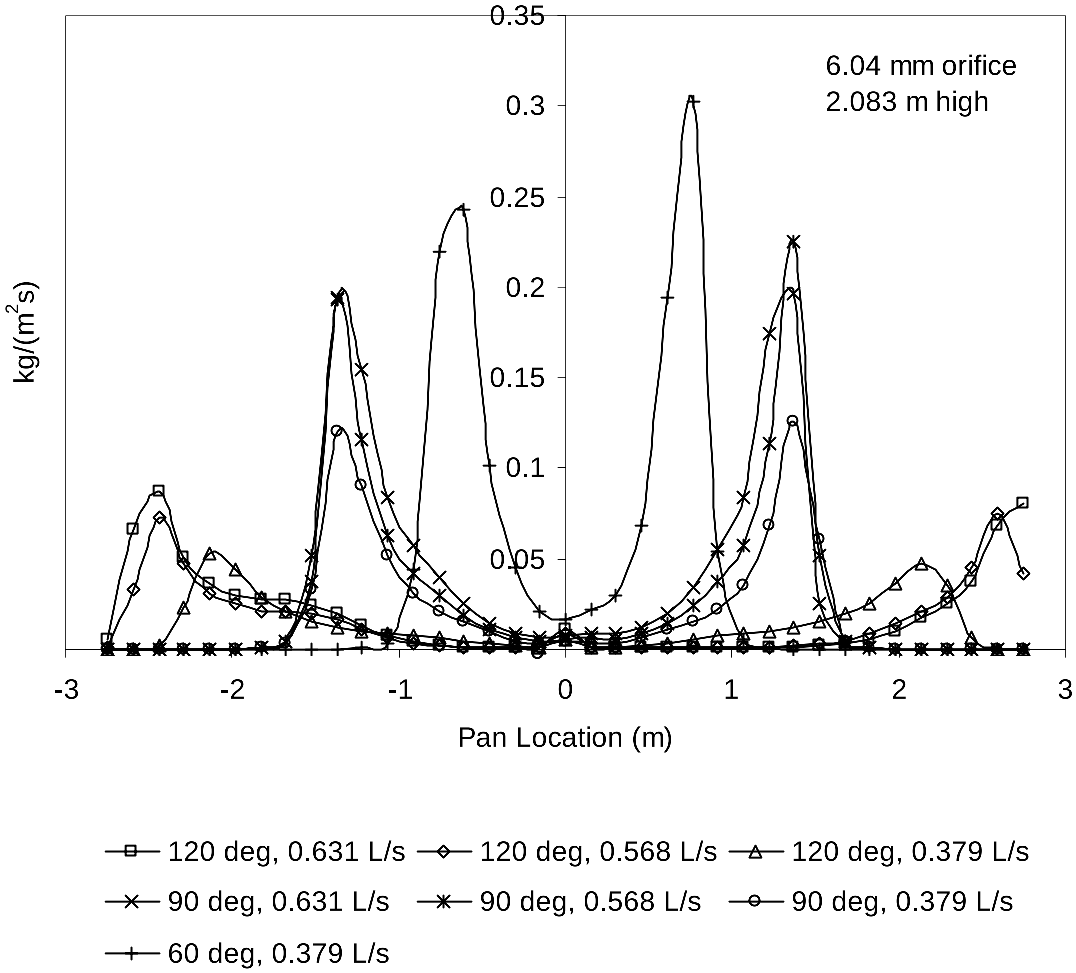

Figure 78. Water flux from a 6 mm nominal orifice diameter sprinkler approximately 2.08 m above the floor. Data is shown for various strike plate angles and flow rates.

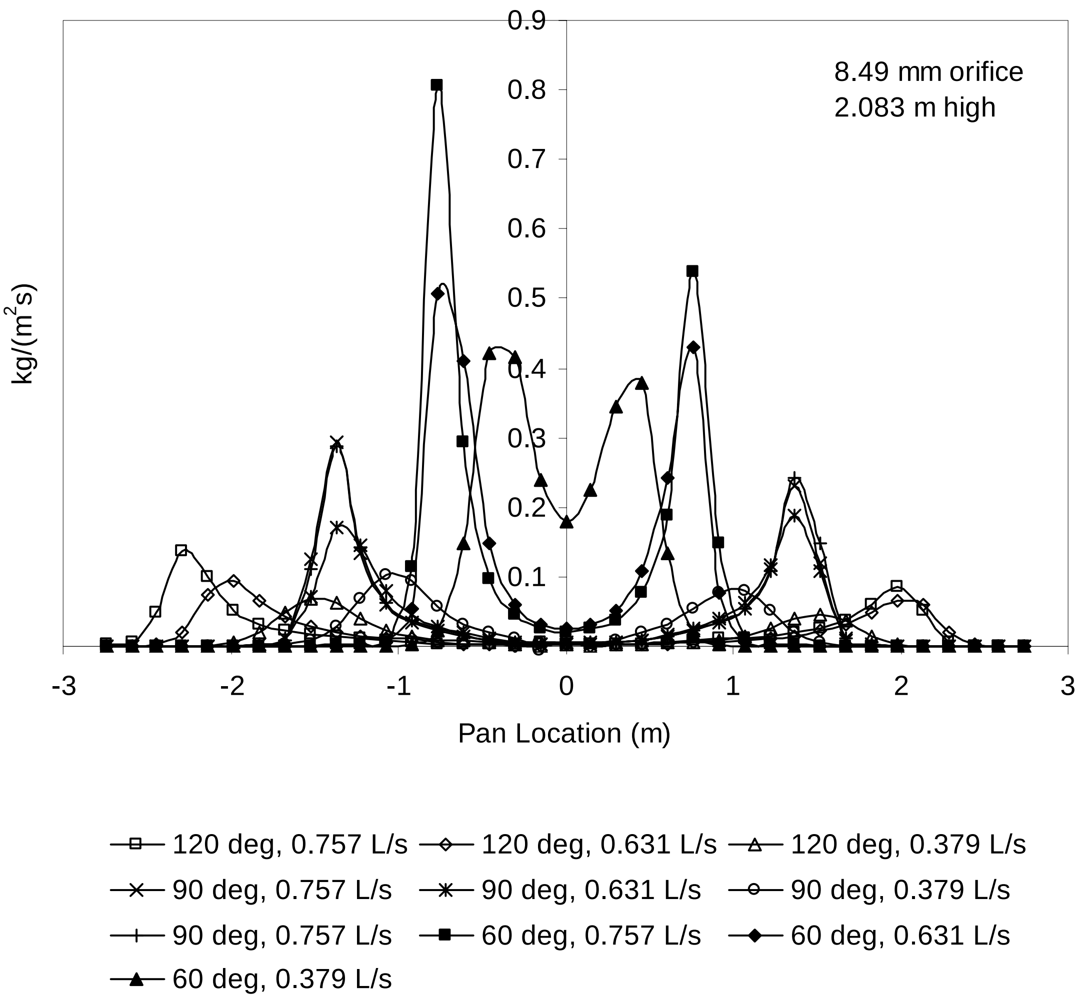

Figure 79. Water flux from a 8.5 mm nominal orifice diameter sprinkler approximately 2.08 m above the floor. Data is shown for various strike plate angles and flow rates.

Due to the asymmetrical nature of the water flux for some of the sprinkler operating conditions, only a subset will be used later for comparison to the predicted water flux. The cases that will be used for comparison are those where the two radii indicated symmetrical behavior. One difficulty in this method of choice is that the pan tests were conducted after the sprinkler drop size measurements were complete. The sprinklers had been assembled/disassembled many times between the droplet measurements and the pan tests. Therefore, it is possible that some of the operating conditions that were symmetrical for the pan tests were not symmetrical during the drop measurements.

5.3 Conservation of Mass

Due to the design of the sprinklers, they did not always produce an axis-symmetric water pattern. In order to find a set of symmetric data, the images are used to check for conservation of mass. A slice of the water spray field, represented by an image, is integrated over the entire field by rotation about the axis of symmetry. The water flux through the lower surface of the integrated volume, parallel to the floor, should equal the mass flow rate of water through the sprinkler. The measurement volume is shown in Figure 80. In order for the calculation to be accurate, all horizontal planes cutting through the measurement area must contain all of the water spray at that elevation. Notice that at $y < y_1$ and $y > y_2$ some portion of the water spray is out of the measurement region. For accurate results, droplets within the area defined by r_1, r_2, y_1, and y_2 are included in the calculation. In addition, the lower surface, through which the flux passes, is defined by y_2.

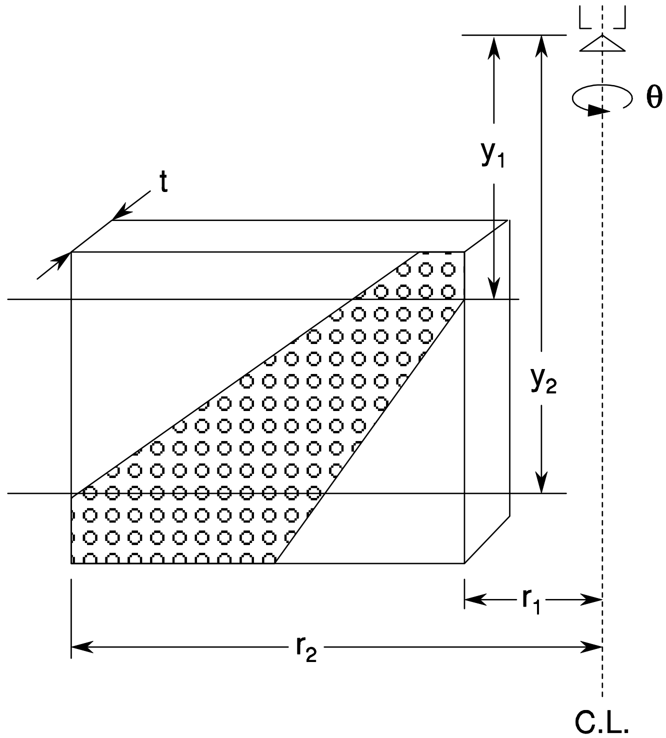

Figure 80. Sprinkler measurement volume.

To begin the calculation, the drop size number distribution is derived from the image data. The number distribution, $N(d)^*$, is defined as the number of drops within a size interval, divided by the width of the size interval. Therefore, the total number of drops, N_{total}, is:

$$N_{total} = \int_{d_{\min}}^{d_{\max}} N(d)^* \, dd \tag{23}$$

and the total water volume is:

$$V_{\substack{total \\ water}} = \int_{0}^{\infty} \frac{\pi d^3}{6} N(d)^* \, dd \tag{24}$$

An expression can be defined for the droplet number concentration, $N(d)^{**}$, as the number of drops per unit measurement volume between d and d+dd. The total number of drops per unit volume is:

$$N'''_{total} = \int_0^\infty N(d)^{**}\, dd \tag{25}$$

The vertical velocity distribution is also needed, and is derived from the image data. As with the size distribution, the droplet velocity distribution, v(d), is also stated as a function of droplet diameter. Since $N(d)^{*}$ and v(d) are calculated from the entire image, we have averaged over the entire measurement volume. This assumes an axis-symmetric sprinkler spray with a homogeneous measurement volume where N and v are not functions of r, θ, or z.

The water flow rate passing through a horizontal plane cutting the entire sprinkler spray is:

$$\dot{V} = \int_{r_1}^{r_2} \int_{d=0}^{\infty} \frac{\pi d^3}{6} N(d)^{**} v(d) 2\pi r\, dd\, dr \tag{26}$$

In this expression, the first three terms of the integrand represent the water flux, and the fourth term is the area over which the flux is applied. For incorporation into a calculation algorithm, the expression is better shown in summation notation, with the same result:

$$\dot{V} = \pi\left(r_2^2 - r_1^2\right)\sum_{i=d_{\min}}^{d_{\max}}\left(\frac{V_{water}}{V_{\substack{measurement\\ region}}}\right)_i \left(v_{drop}\right)_i \tag{27}$$

The terms inside the summation are calculated for each droplet size bin. It is important to note that the two radii, r_1 and r_2, correspond to the inner and outer edges of the measurement volume. This assures that the average droplet density is consistent with the area of applied water flux. The area over which the flux is applied is shown in plan view in Figure 81.

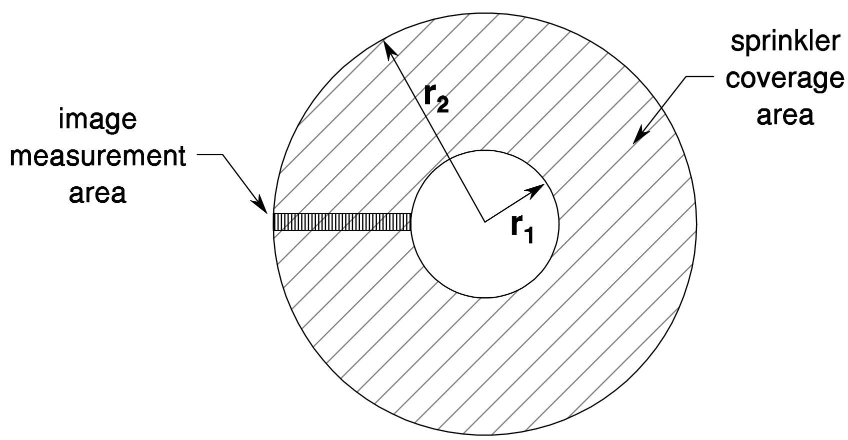

Figure 81. Sprinkler coverage area, plan view.

The water flow rates were calculated using Equation 27, and the results averaged for the approximately 10 film exposures taken for each operating condition. The average calculated water flow rates were compared to the measured water flow rate through the sprinkler. Errors ranged from a low of 2% to a high of 94%, with the frequency of occurrence of each error illustrated in Figure 82. It can be seen that 2/3 of the operating conditions resulted in less than 30% error. The cases with large errors appear to be a result of asymmetrical operation of the sprinklers, as discussed in the previously section on measured water flux distribution. For the 6 mm orifice sprinkler with a 90 degree strike plate operating at 0.379 L/s (6 gpm), the error was 2.5%. For the 4 mm orifice sprinkler with a 90 degree strike plate operating at 0.379 L/s (6 gpm), the error was 7.4%. A table showing the estimated error for each operating condition can be found in Appendix E.

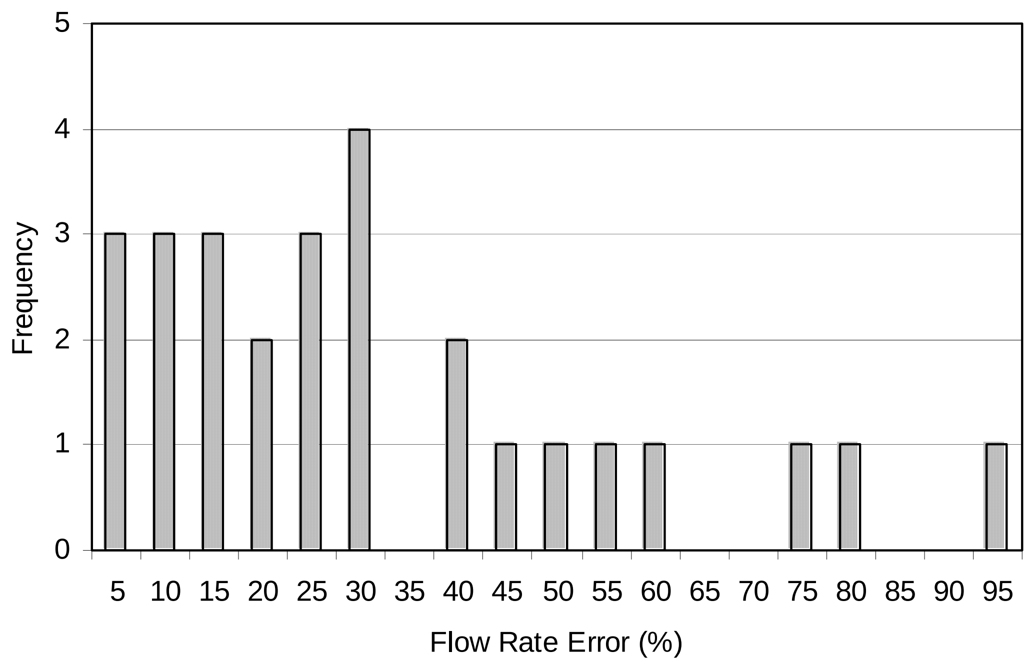

Figure 82. Flow Rate Errors.

Due to the asymmetrical behavior of some of the sprinklers and sprinkler operating conditions, it was necessary to identify sets of data for in-depth examination, and for later modeling. Several criteria were developed, and used to choose sets of data. The first criterion was that the pan test data for the sprinkler needed to be symmetric. The second criterion was that the result of the conservation of mass calculation should have a low level of error, preferably less than 10%. A list of candidates that fit the two criteria was compiled. From this list, two sprinkler combinations were chosen that represented the range of sprinkler operating conditions. One sprinkler will produce small droplets traveling at high velocity, and the other will produce larger droplets traveling at lower velocities. The chosen combinations were: 6 mm orifice sprinkler with a 90 degree strike plate operating at 0.379 L/s (6 gpm), and a 4 mm orifice sprinkler with a 90 degree strike plate operating at 0.379 L/s (6 gpm.)

5.4 Drop Velocity

Droplet velocity vectors from two sprinkler operating conditions are shown in Figure 83 and Figure 84. These graphs show the vectors measured from one film exposure, which include approximately 400 vectors each. Since the position and velocity of each droplet pair is available, the vector data was plotted on a single graph for each sprinkler, with the sprinkler located at the origin. A reference vector is shown, the magnitude of which is the same as the velocity of the water jet as it exits the sprinkler orifice. The plots are cluttered, but are included to show the density at which measurements were taken. In contrast to PIV results, the velocities were not averaged and plotted for interrogation regions since this would disregard the velocity differences between droplet sizes within each region. The full data set is used to validate trajectory predictions in later chapters.

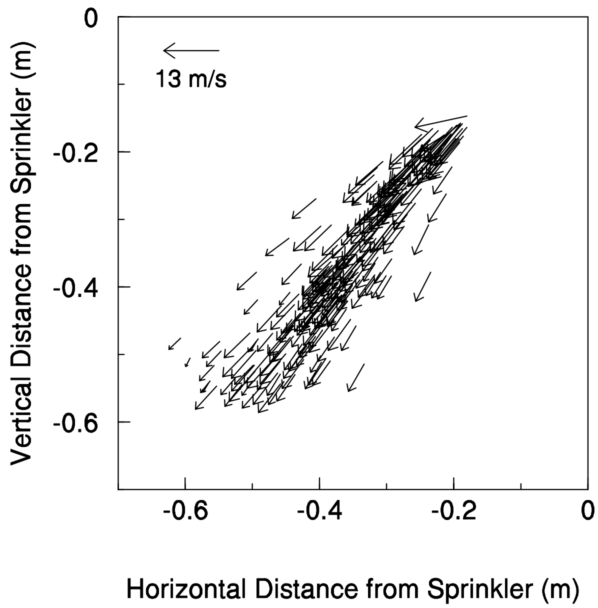

Figure 83. Droplet velocities are shown for one image exposure from the 6 mm nominal orifice sprinkler with a 90 degree strike plate operating at 0.379 L/s (6 gpm).

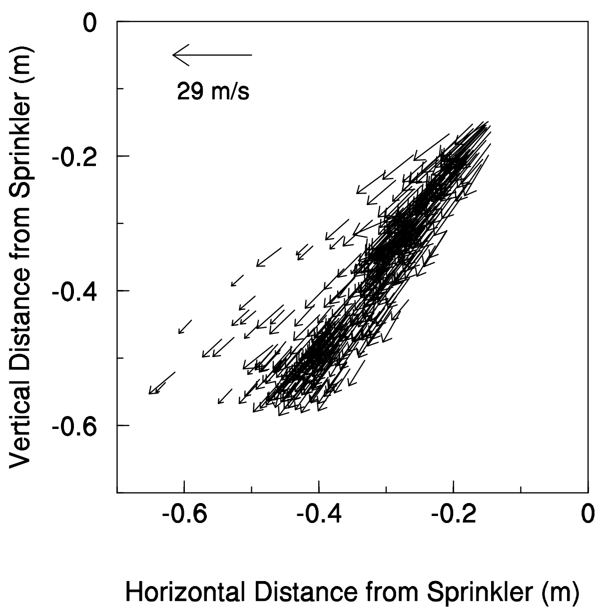

Figure 84. Droplet velocities are shown for one image exposure from the 4 mm nominal orifice sprinkler with a 90 degree strike plate operating at 0.379 L/s (6 gpm).

The speed of the droplets is given by the magnitude of the measured velocity vectors. The average speeds of the droplets within each size bin are listed in Appendix E.

The droplet speeds for the 4 mm and 6 mm orifice diameter sprinklers with 90 degree strike plates operating at 0.379 L/s (6 gpm) are shown in Figure 85. The graph shows that the average droplet speed is a function of diameter, and it is encouraging that the function is single valued so that there is a single drop speed for a given drop size. For comparison, the velocities of the water jets exiting the nozzles of the sprinklers are 29.1 m/s and 13.2 m/s respectively. Given the assumption of no energy loss during sheet breakup, there is a significant loss of velocity due to drag for most droplet sizes between sheet breakup and the location that the drop velocity is measured. The velocity loss is inversely related to the droplet diameter.

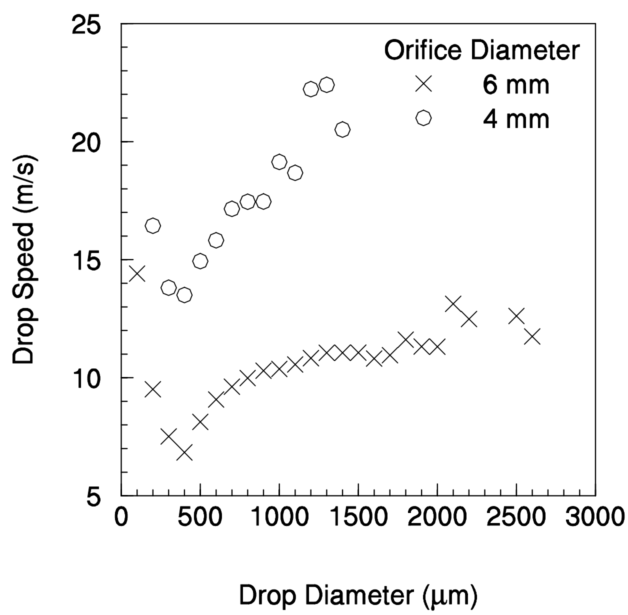

Figure 85. Droplet speed for 4 mm and 6 mm orifice sprinklers with 90 degree strike plates operating at 0.379 L/s (6 gpm). The data is averaged over the measurement region.

In this study, the direction of a droplet is defined by the angle of the vector with respect to the South Pole as shown in Figure 86. To generalize the results for all strike plate angles, the droplet angles can be expressed by their deviation from the strike plate angle. Using this convention, deviation angles toward the North Pole are positive, and deviation angles toward the South Pole are negative. As an example, a droplet leaving a 90 degree strike plate sprinkler with a vector direction angle of 40 degrees would have a deviation angle of -5 degrees ($40-0.5\times90$).

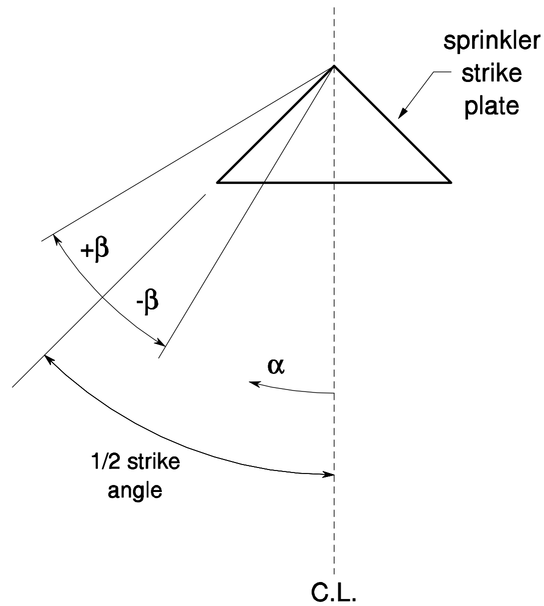

Figure 86. Sign conventions for velocity vectors. The direction of the velocity vector is shown as α, and expressed as a deviation angle, β.

The angle of the velocity was found to be a weak function of drop size. This is illustrated for two sprinklers in Figure 87. For these operating conditions, the deviation angle for most drop sizes gradually increases from approximately -10 degrees for 500 µm drops to -5 degrees for 2500 µm drops. Further investigation showed little to no effect of flow rate on the deviation angle of the drops for a given orifice and strike plate, as shown in Figure 88 through Figure 90. These plots do show, however, a relationship between the strike plate angle and the droplet deviation angle, with the deviation decreasing as the strike plate angle increases. The data shows an increase in the absolute value of the deviation angle, from approximately -5 degrees to approximately -10 degrees as the strike plate angle changes from 120 degrees to 60 degrees, suggesting that there may be an average deviation angle for each strike plate angle. It is suspected that the dependence of the deviation angle on strike plate angle is caused by entrainment forces on the sprinkler flow.

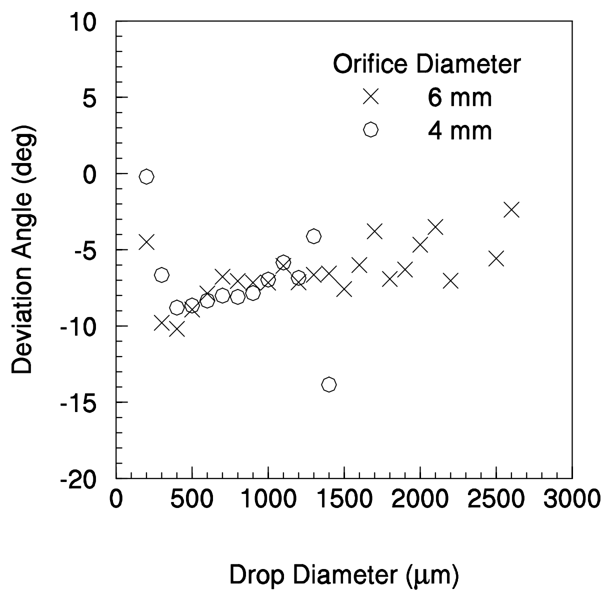

Figure 87. Average droplet trajectory deviation from strike plate angle. The cone angle of the strike plate is 90 degrees, so the strike plate surface is located 45 degrees clockwise from the vertical axis of symmetry (South Pole defined as 0 degrees). All of the deviations are negative, indicating that the droplet paths are displaced from the 45 degree reference angle toward the South Pole.

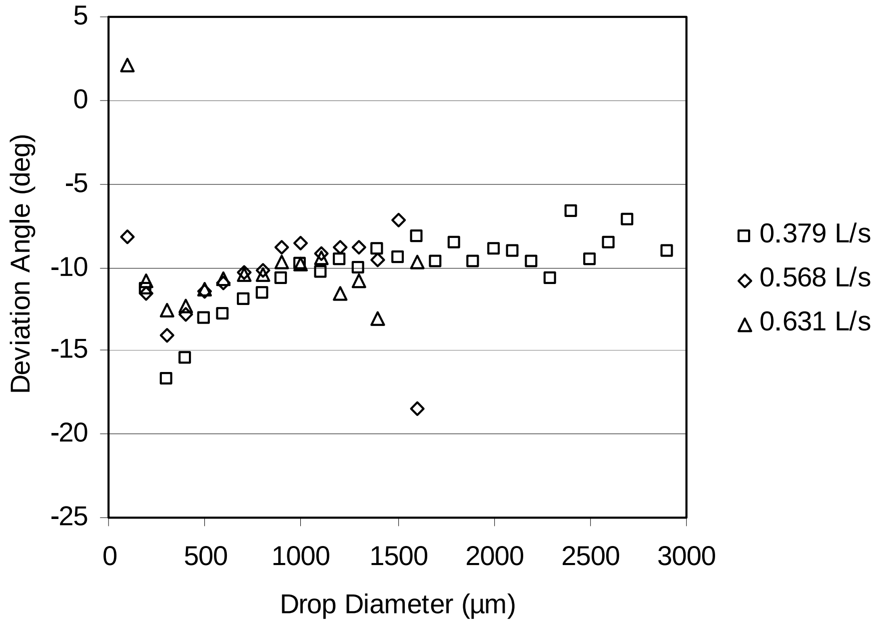

Figure 88. Velocity deviation from strike plate angle as a function of drop diameter for a 6 mm orifice sprinkler with a 60 degree strike plate. Deviation angles are similar for various flow rates.

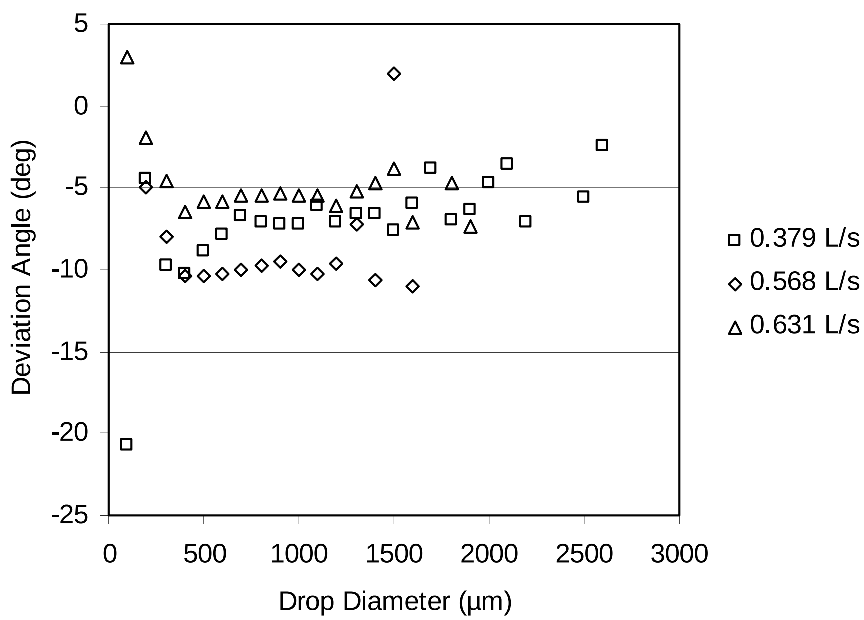

Figure 89. Velocity deviation from strike plate angle as a function of drop diameter for a 6 mm orifice sprinkler with a 90 degree strike plate. Deviation angles are similar for various flow rates.

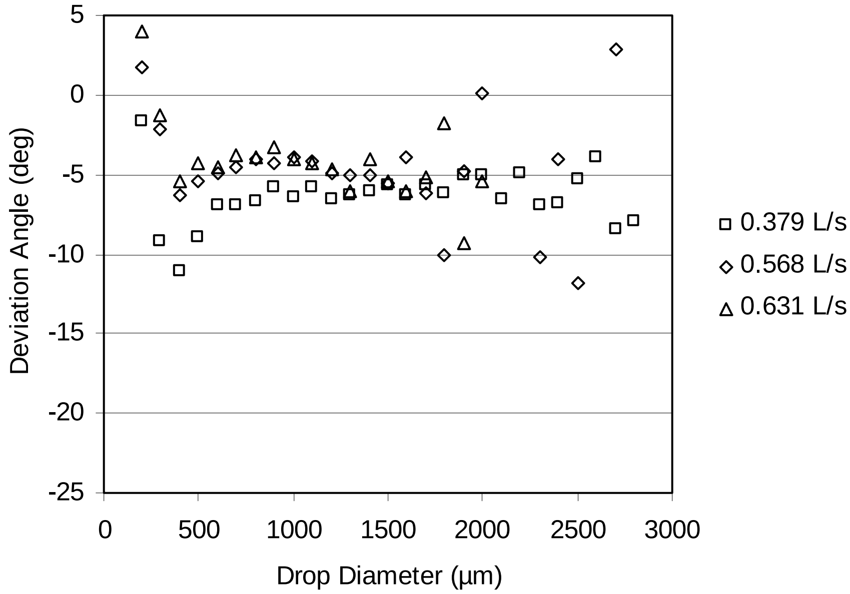

Figure 90. Velocity deviation from strike plate angle as a function of drop diameter for a 6 mm orifice sprinkler with a 120 degree strike plate. Deviation angles are similar for various flow rates.

If the average deviation angle for droplets is known as a function of strike plate angle, a distribution about this average is needed to characterize the spread of the data. The deviation angle as a function of droplet size is investigated in Figure 91 and Figure 92. The number fraction of drops as a function of deviation angle is shown for a range of droplet sizes. The graphs show that for two representative sprinkler operating conditions, the drop deviation angles are qualitatively normally distributed about a mean deviation angle. The mean and spread of the distributions are similar over the entire drop size range. Since the water distribution is tied more to volume distributions than to number distributions, this behavior is investigated in Figure 93 and Figure 94. The volume distributions are similarly shaped, but the mean is shifted slightly toward smaller deviations. Comparison of the number and volume distributions strongly suggest a normal distribution since they are of the same shape but shifted along the horizontal axis, a characteristic of normal distributions.

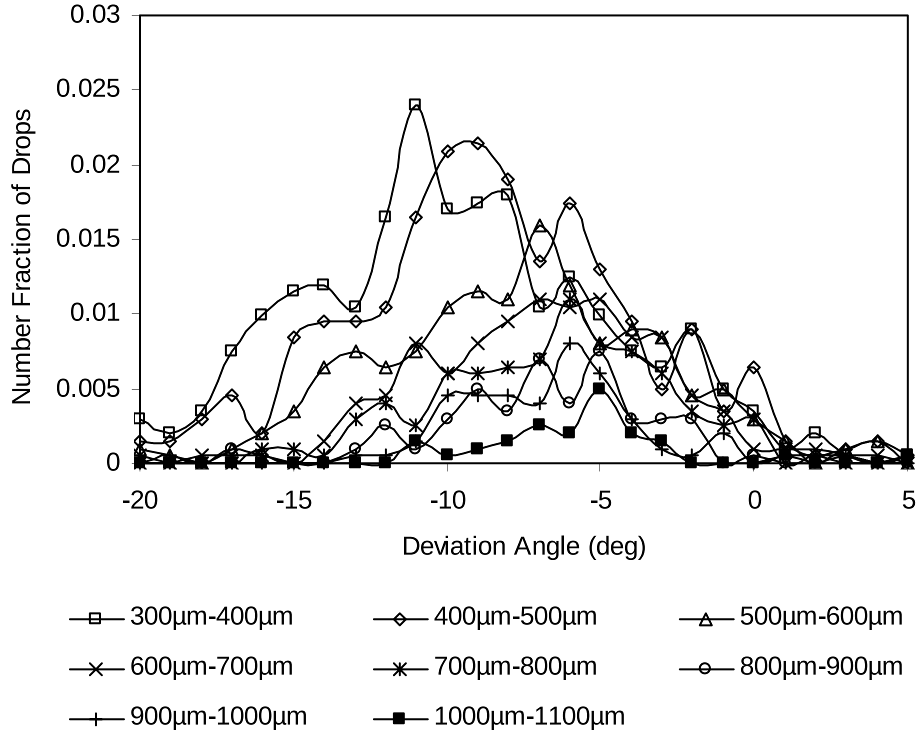

Figure 91. Number fraction of drops as a function of deviation angle for various drop size ranges. Sprinkler with 6 mm orifice, 90 degree strike plate, operated at 0.379 L/s (6 gpm).

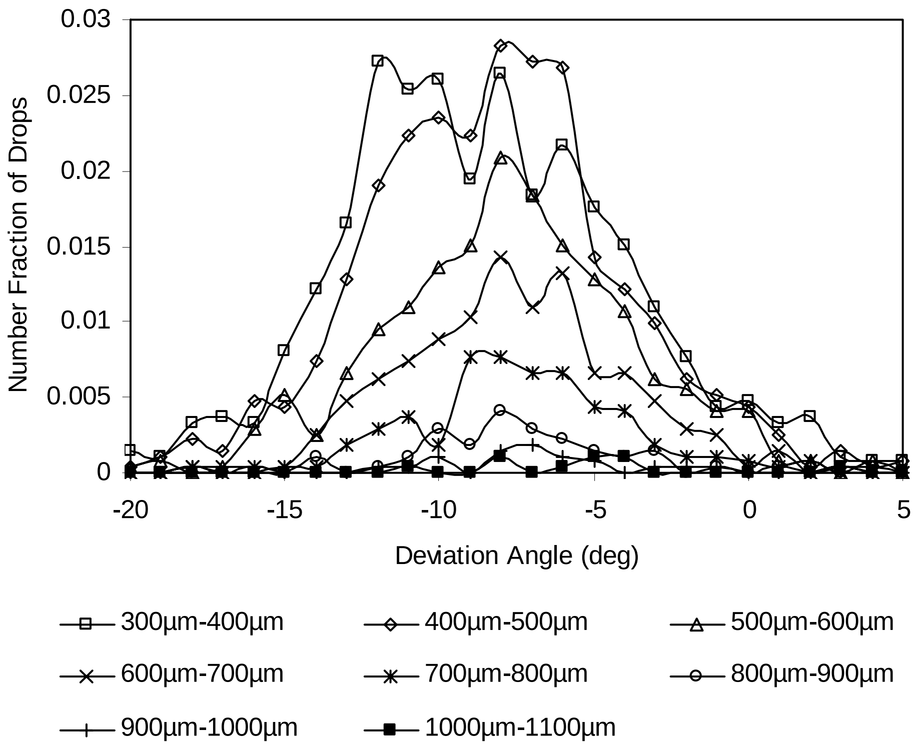

Figure 92. Number fraction of drops as a function of deviation angle for various drop size ranges. Sprinkler with 4 mm orifice, 90 degree strike plate, operated at 0.379 L/s (6 gpm).

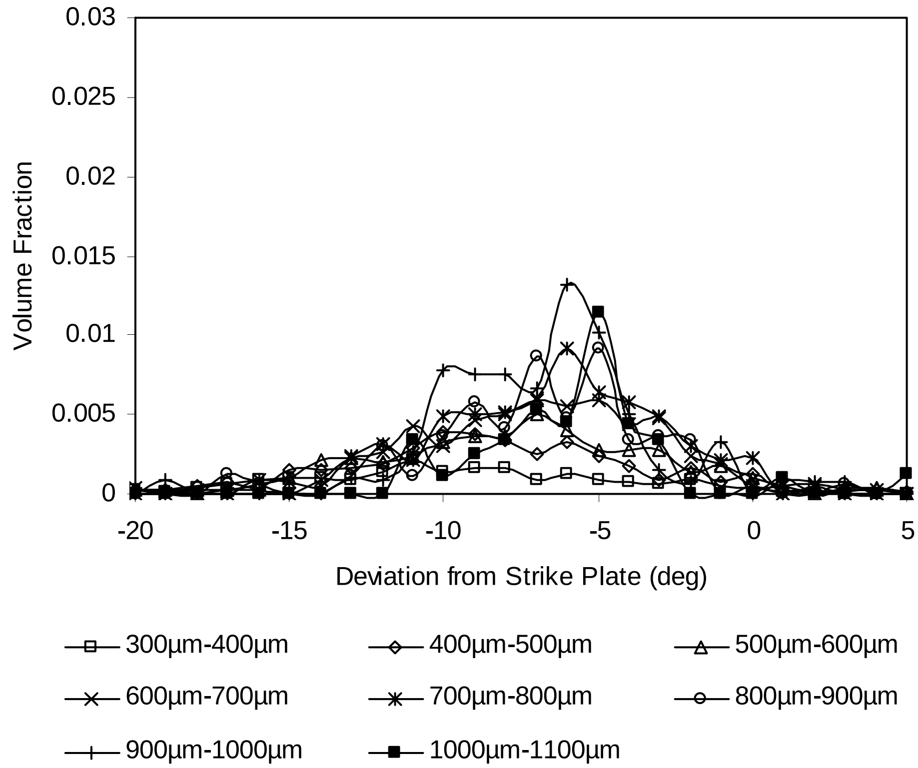

Figure 93. Volume fraction of drops as a function of deviation angle for various drop size ranges. Sprinkler with 6 mm orifice, 90 degree strike plate, operated at 0.379 L/s (6 gpm).

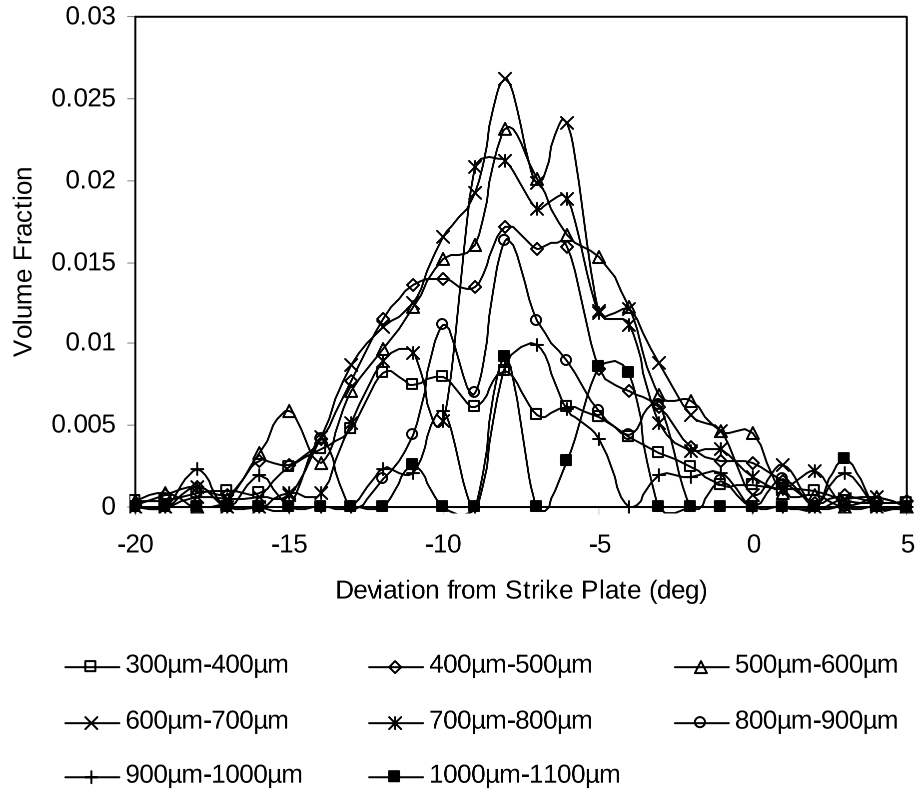

Figure 94. Volume fraction of drops as a function of deviation angle for various drop size ranges. Sprinkler with 4 mm orifice, 90 degree strike plate, operated at 0.379 L/s (6 gpm).

The distribution of drop deviation angles is further investigated in Figure 95 and Figure 96 for two sprinkler operating conditions. In these plots, the deviation angles are averaged over all drop sizes. The number and volume fractions of drops as a function of velocity deviation angle are similar for both operating conditions. In order to facilitate modeling of the drop trajectories, it would be useful to have a distribution function for the drop deviation angle. While our data suggests a normal distribution, predictions of angle distribution have been made in the literature, and suggest a cosine function based on the sinusoidal disturbances within a water sheet (Wendt and Prahl 1986).

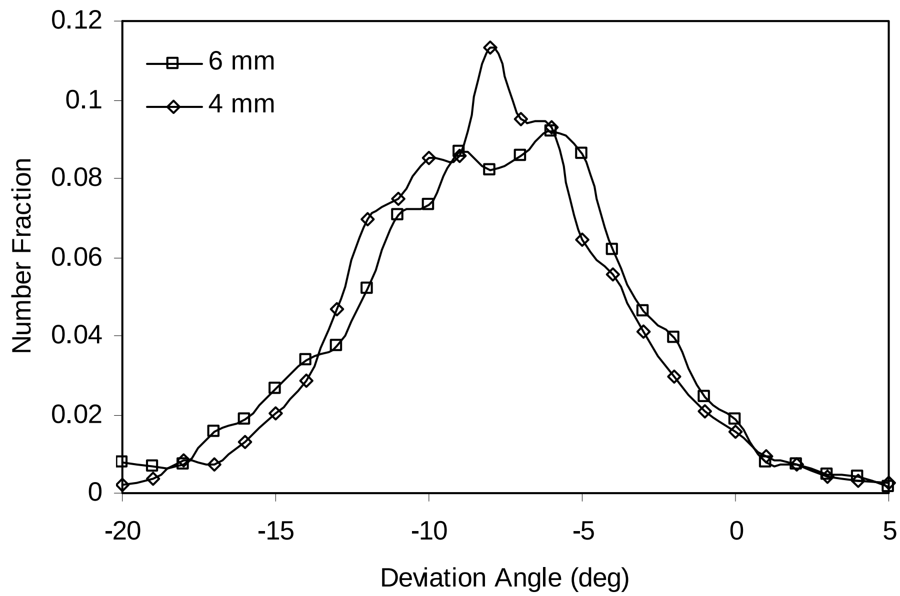

Figure 95. Droplet number fraction as a function of deviation angle for 4 mm and 6 mm orifice sprinklers with 90 degree strike plates operating at 0.379 L/s (6 gpm). The data is averaged over all droplet sizes.

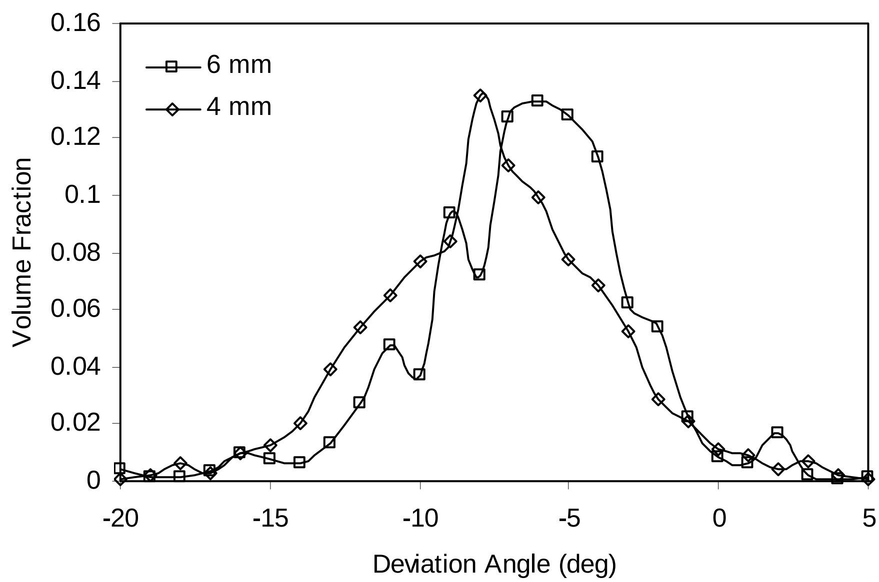

Figure 96. Droplet volume fraction as a function of deviation angle for 4 mm and 6 mm orifice sprinklers with 90 degree strike plates operating at 0.379 L/s (6 gpm). The data is averaged over all droplet sizes.

The normal distribution is given by Equation 28 (Holman 1989):

$$P_n(x) = \frac{1}{\sigma\sqrt{2\pi}} \exp\left(-\frac{[x - x_m]^2}{2\sigma^2} \right) \quad and \quad P_n(x_m) = \frac{1}{\sigma\sqrt{2\pi}} \qquad (28)$$

where: $P_n(x)$=probability of x
$P_n(x_m)$=probability of the mean value, the maximum probability
x_m=mean
σ=standard deviation

And the cosine function is given by Equation 29:

$$P_C(x) = \frac{A}{2} + \frac{A}{2} \cos\left(\frac{2\pi}{2\phi}\theta - \left[\frac{2\pi}{2\phi}\theta_{peak} \right] \right) \qquad (29)$$

where: $P_C(x)$=probability of x
A=amplitude
θ=deviation angle
θ_{peak}=mean deviation angle where peak probability occurs
φ=half distribution width

The first term of $P_C(x)$ shifts the distribution vertically. The second A/2 term scales the amplitude of the function. The first term within the cosine provides the cycle width, while the second term shifts the function horizontally.

The normal and cosine functions given in Equation 28 and Equation 29 are fitted to sprinkler data in Figure 97. The graph shows that for the two combinations tested, good agreement is seen between the data and the normal distribution function with d_m=-8 degrees, and σ=4. The mean drop diameter used in the fit was determined from the median of the data, while the standard deviation determined from inspection. The normal distribution function was also fit to a wide variety of data in Figure 98 to Figure 100. To test the fit of the normal distribution, the data from each strike plate angle is plotted separately. Note that there is good agreement with the normal distribution, and that the standard deviation in all cases is 4, indicating that the spread is similar for all the data. The average or median of the distribution is derived from the count average of the droplet deviations for each particular strike plate angle. This average is different for each of the strike plate angles. While the normal distribution is a reasonably good fit for the 60 degree strike plate angle, a cosine function does fit better, and has good agreement.

The drop angle data does lend credence to the cosine distribution and the sinusoidal water sheet disturbance theory; however the data can be better represented by a normal distribution. This distribution arises when a multitude of random factors influence the droplet velocity angle that would otherwise have a single value. This random distribution will be used later to develop predictions of water distributions from a sprinkler to the floor.

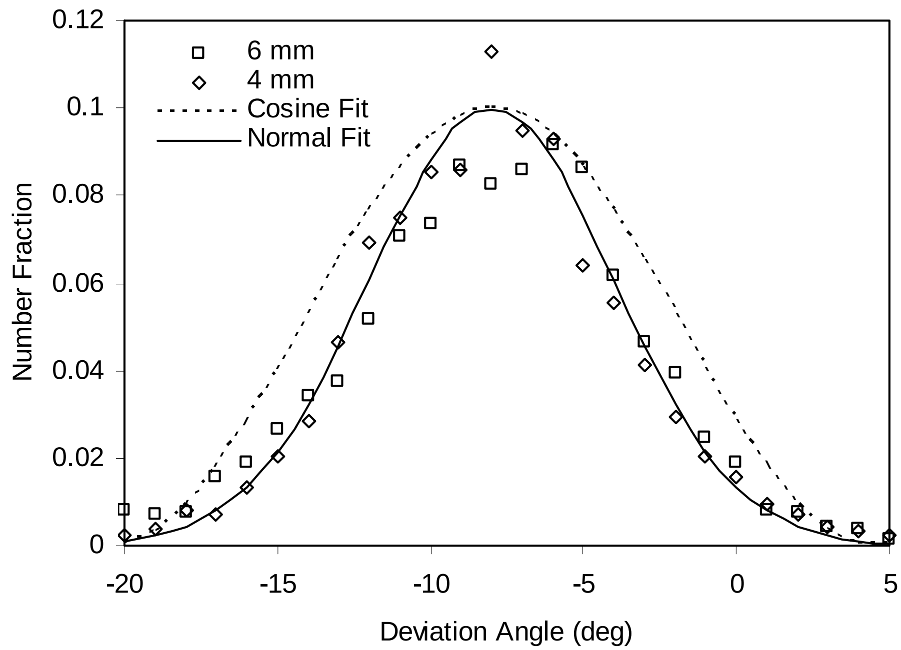

Cosine Fit: NF=0.05+0.05*cos(angledeg*360/25+115)
Normal Fit: Mean=-8 deg, Stdev=4

Figure 97. Droplet number fraction as a function of deviation angle for 4 mm and 6 mm orifice sprinklers with 90 degree strike plates operating at 0.379 L/s (6 gpm). The data is averaged over all droplet sizes. Normal and cosine functions are fit to the data.

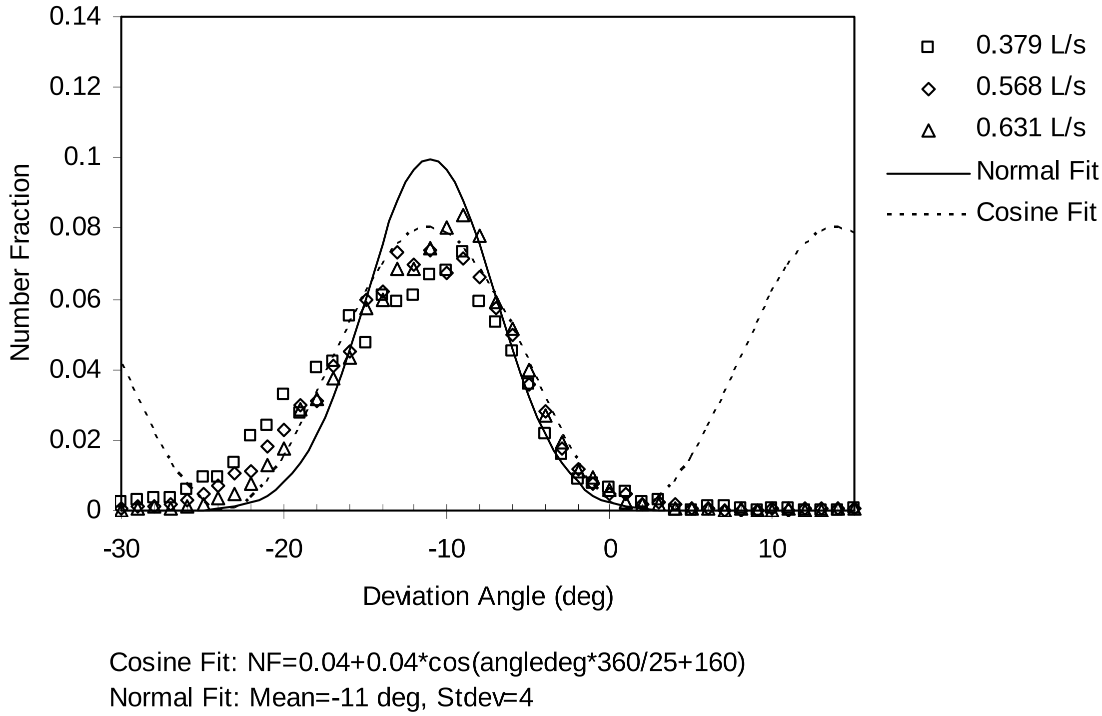

Figure 98. Droplet number fraction as a function of deviation angle for sprinklers with 6 mm orifices and 60 degree strike plates. Normal and cosine functions are fit to the data. The normal distribution has a mean of -11 degrees, and a standard deviation of 4.

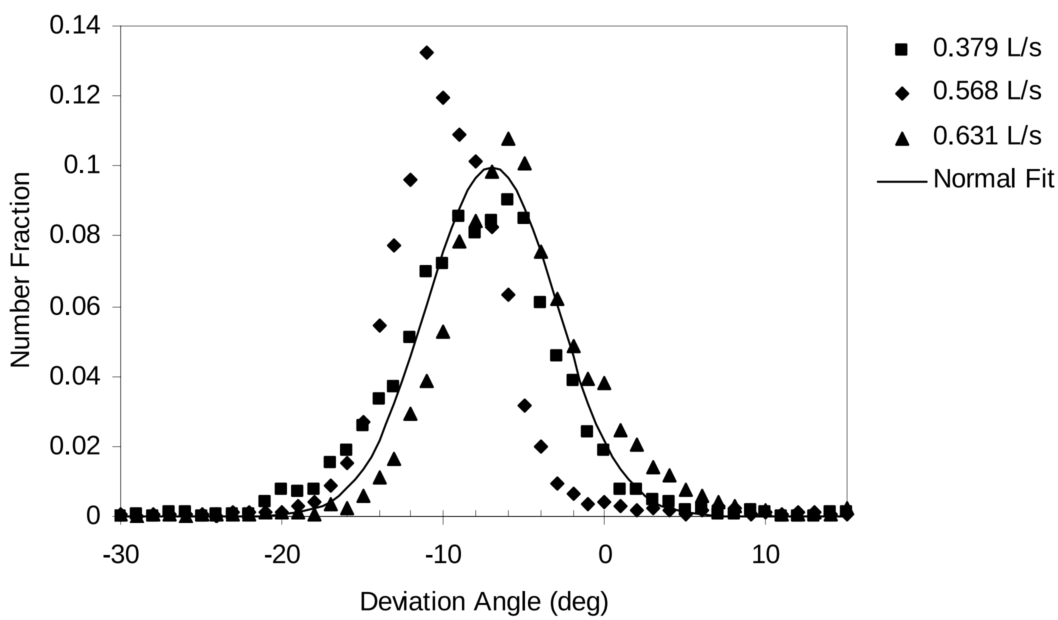

Figure 99. Droplet number fraction as a function of deviation angle for sprinklers with 6 mm orifices and 90 degree strike plates. The normal function is fit to the data. The normal distribution has a mean of -7 degrees, and a standard deviation of 4.

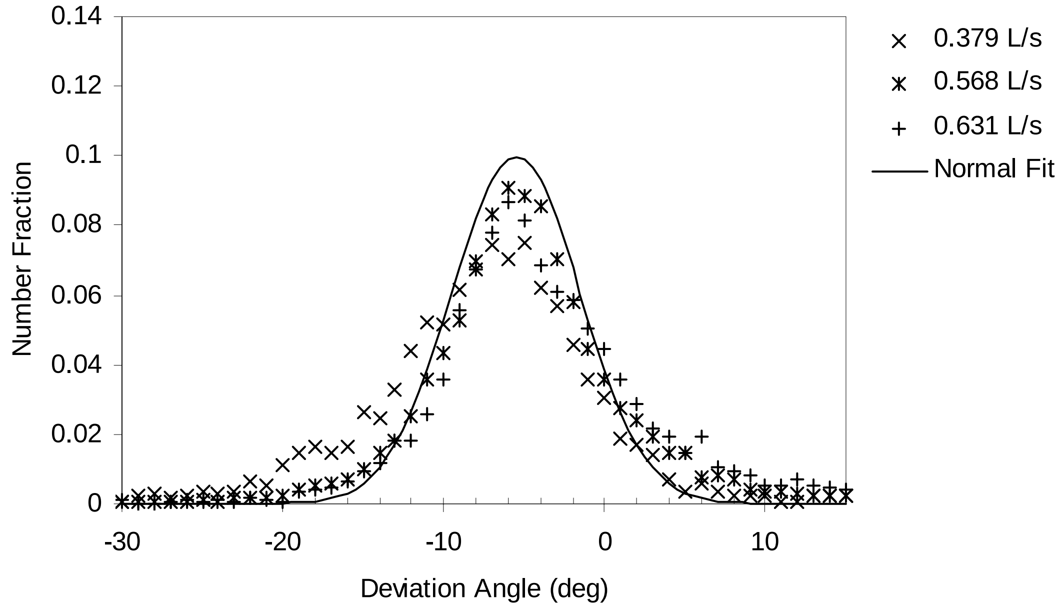

Figure 100. Droplet number fraction as a function of deviation angle for sprinklers with 6 mm orifices and 120 degree strike plates. The normal function if fit to the data. The normal distribution has a mean of -5.5 degrees, and a standard deviation of 4.

As discussed briefly in the drop size section, sprinklers with We=5.20×10^3, the lowest Weber number studied, appeared to be operating in a different flow regime than the other sprinkler conditions. This had an effect on the drop size distribution, and also has an effect on the initial drop angle. It appears that at We<1.44×10^4, the water sheet is affected by gravity and surface tension significantly prior to breakup, causing the drops to have greater angular deviations from the strike plate. While gravity forces may be negligible for flows in the flapping regime (We>1000) with respect to average drop size (Villermaux and Clanet 2002), it appears to be a factor in the initial drop angle.

The effect of We on the mean droplet deviation angle is shown in Figure 101. There is significant scatter in the data caused by uncertainties in the strike plate angle due to the aforementioned manufacturing tolerances, and the instability of some sprinkler operating conditions. The figure, however, does not include data from two operating conditions that were known to be unstable (0.315 L/s and 0.379 L/s through the 4.07 mm orifice). From the figure, it can be seen that the droplets from sprinklers operating at We=5.20×10^3 have significantly greater angular deviations from the strike plate than the other operating conditions. As the value of the Weber number increases from 5.20×10^3 to 1.44×10^4, a rapid decrease in the droplet deviations from the strike plate occurs, where inertial forces overwhelm gravity and surface tension forces. Water issuing from an 8.5 mm orifice sprinkler with a 120 degree strike plate operating at 0.379 L/s (We=5.20×10^3) is shown in Figure 102, illustrating a large deviation from the strike plate angle. Sheet breakup occurs approximately 0.275 m from this sprinkler.

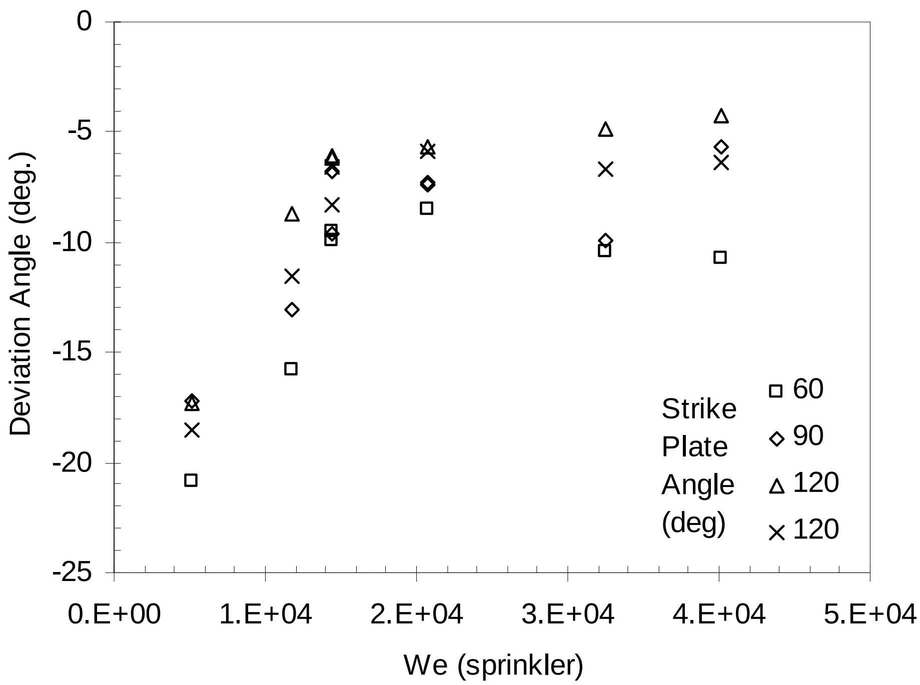

Figure 101. Droplet velocity deviation angle as a function of Weber number for all sprinkler operating conditions. Data from the 4 mm orifice operating at 0.315 L/s (5 gpm) and 0.379 L/s (6 gpm) is not included due to instability.

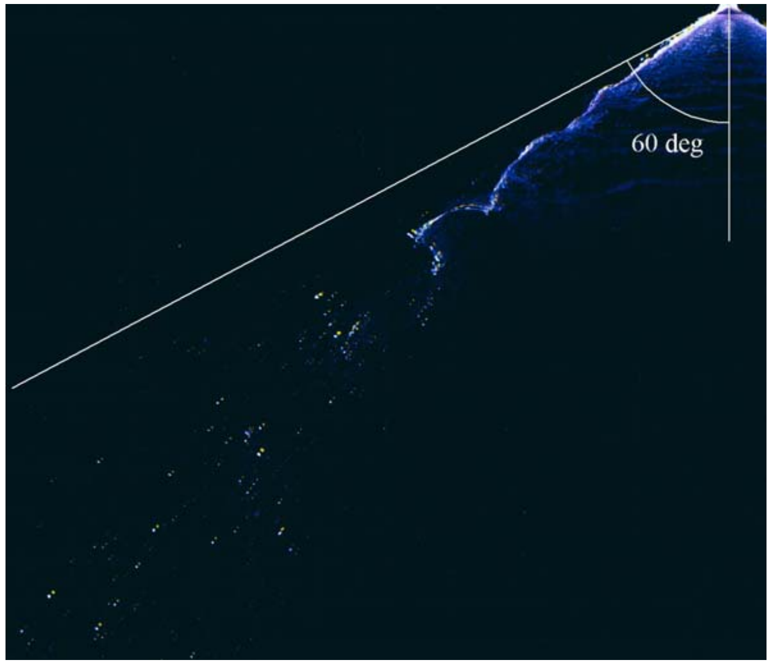

Figure 102. Image of water from an 8.5 mm orifice sprinkler with a 120 degree strike plate operating at 0.379 L/s (6 gpm.) Water sheet breakup occurs approximately 0.275 m from the sprinkler.

A cursory exploration was conducted by observing low Weber number flows from a 6 mm orifice sprinkler with a 120 degree strike plate. Plain water and water with detergent were passed through the sprinkler in order to qualitatively investigate the affect of surface tension on deviation angle. The detergent serves to lower the surface tension of the mixture, thereby raising the Weber number of the flow given the same flow rate. Since the surface tension of water with detergent was not measured, only the We of the plain water flows are reported.

Water and water/detergent mixture flows of 0.126 L/s (2 gpm) are compared in Figure 103, with $We=1.6\times10^3$ for the water flow. The comparison shows some difference in the breakup of the water into droplets. Flows of approximately 0.095 L/s (1.5 gpm) are shown in Figure 104, with $We\approx900$ for the plain water. It can be seen that the sheet is smooth, and water drops break off from the sheet with an angle of approximately 0 degrees from the South Pole. Note that this is approximately the critical We as defined by Huang (1970) and Clanet and Villermaux (2002) for the transition from a smooth to a flapping water sheet. It can be seen that the deviation angle of the water sheet is less for the water/detergent mixture compared to the plain water flow, although the drops in both cases fall nearly straight down. The water sheet with detergent travels farther from the orifice than the plain water before breakup. This suggests that the surfactant allows the water sheet to remain stable at smaller thicknesses. As the sheet gets thinner, the effects of surface tension should increase, since the other forces on small fixed volume elements within the sheet, ie. inertia and gravity, are tied to the mass which is decreasing. Surface tension, however, is a function of the area of the element, which is constant.

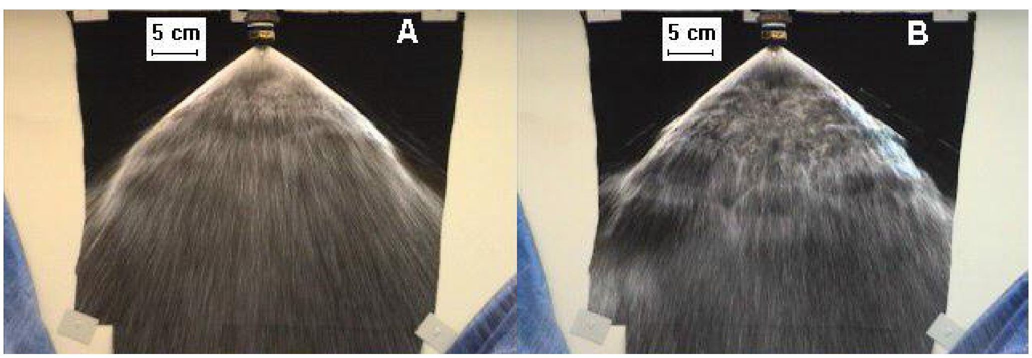

Figure 103. Comparison of 0.126 L/s (2 gpm) flows through a 6 mm orifice sprinkler with a 120 degree strike plate. Photo "A" is plain water, while photo "B" is water with detergent added.

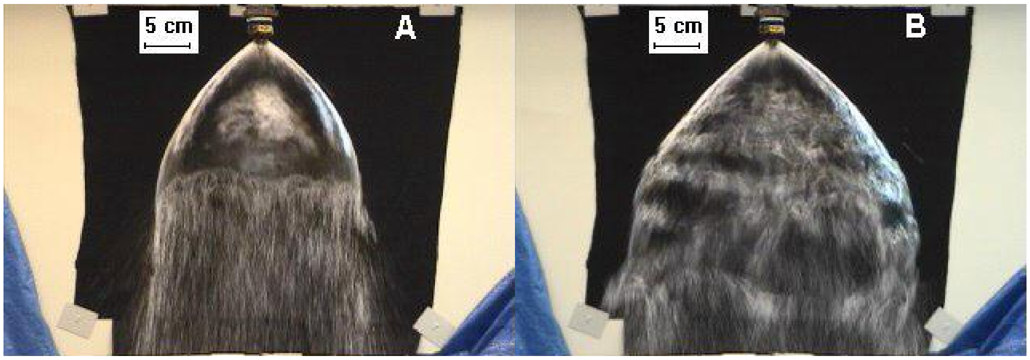

Figure 104. Comparison of approximately 0.095 L/s (1.5 gpm) flows through a 6 mm orifice sprinkler with a 120 degree strike plate. Photo "A" is plain water, while photo "B" is water with detergent added.

The next set of photos, Figure 105, compare the water and water/detergent mixtures at a flow rate of 0.063 L/s (1 gpm.) The plain water flow has We=400. The plain water sheet curves inward before breakup, while the water/detergent flow forms a nearly closed cavity. This is further illustrated in Figure 106, where the sprinkler operates at 0.032 L/s (0.5 gpm), with plain water We=100. In this case the plain water forms a nearly closed cavity, with the droplet paths intersecting below the cavity. The water/detergent flow forms a closed cavity. At flow rates too low to measure with the current experimental setup, <≈0.3 gpm, the plain water flow also forms a closed cavity, as shown in Figure 107a. If the cavity is disturbed with a rod, Figure 107b, it reforms with the same size and shape, illustrating that the cavity condition is stable. Bubbles trapped in the cavity of a water/detergent flow, Figure 107c, illustrate that there were recirculating air flows within the cavity.

It appears that at lower surface tensions, the sheet can be thinner, and at low values of We the sheet travels farther before breakup occurs. The curving inward of the sheet forming the cavity may be the result of a pressure difference, made possible by the surface tension that is supporting the film of water. Qualitatively, this may be similar to free stream line flows encountering obstacles, as discussed by Bachelor (1967.)

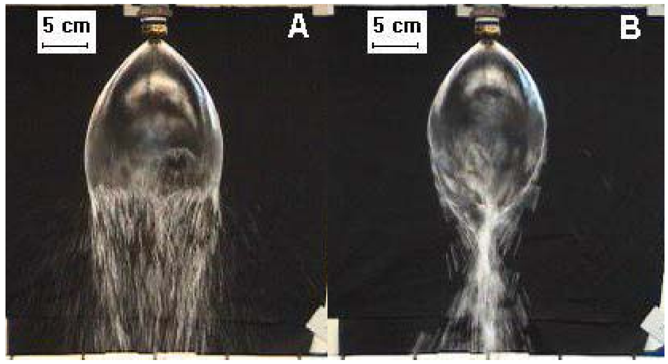

Figure 105. Comparison of 0.063 L/s (1 gpm) flows through a 6 mm orifice sprinkler with a 120 degree strike plate. Photo "A" is plain water, while photo "B" is water with detergent added.

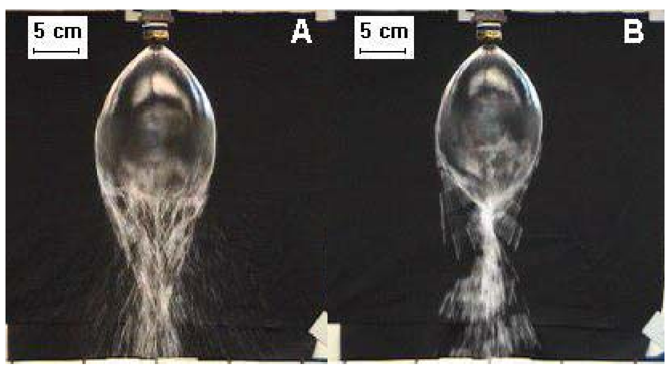

Figure 106. Comparison of 0.032 L/s (0.5 gpm) flows through a 6 mm orifice sprinkler with a 120 degree strike plate. Photo "A" is plain water, while photo "B" is water with detergent added.

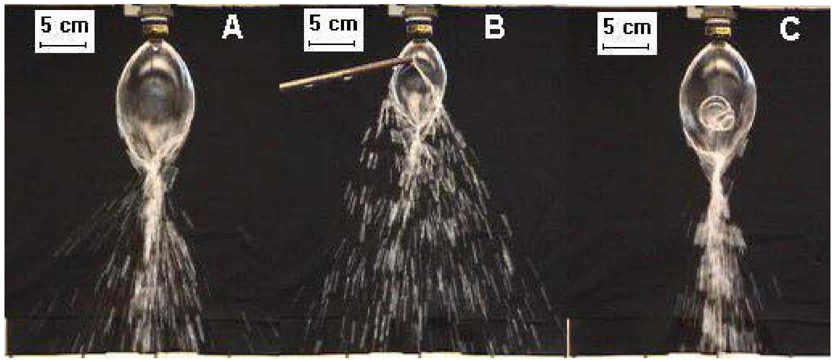

Figure 107. Comparison of flow rates less than 0.032 L/s (0.5 gpm) through a 6 mm orifice sprinkler with a 120 degree strike plate. Photo "A" is plain water, which has formed a stable closed cavity. Photo "B" is a plain water cavity disturbed and opened by insertion of a metal rod. The cavity reforms to the same size and shape upon removal of the rod. Photo "C" is a water/detergent flow cavity with bubbles trapped inside. These bubbles moved about the cavity illustrating air circulation.

Reducing the surface tension can have two opposite effects. One effect is the reduction of the forces causing the water sheet to constrict and form a cavity. The second effect is allowing the sheet to become thinner, and travel farther from the sprinkler before breakup. The latter appears to be the dominant effect in the low flow experiments where We<1000. In the flows where We>1000, however, lowering the surface tension had little effect on the deviation angle of the sheet with respect to the strike plate. This suggests that gravity is the dominant factor in the increased deviation from the strike plate angle of the droplets experienced at $1.60\times10^3<We<1.44\times10^4$.

5.5 Random Angle Generator

The discovery that the normal function fits the droplet velocity angular distribution suggests that a random generator could reproduce the data. The random angle generator will be useful for modeling the water drop trajectories in later chapters.

A computer subroutine was written to randomly choose a trajectory angle for each drop, given the strike plate angle. The mean and standard deviations previously determined from data fits are used to define the deviation angle cumulative number fraction function. This function will have a value between 0 and 1. The macro randomly chooses a value (probability) between 0 and 1, and calculates the deviation angle associated with this probability. A table is created, which is a list of randomly chosen drop velocity angles consistent with the distribution function. The routine was tested by randomly creating a list of velocity angles, determining the cumulative number fraction function, and comparing it to the normal function. Excellent agreement was found, verifying that the algorithm was working correctly. The comparison is shown in Figure 108.

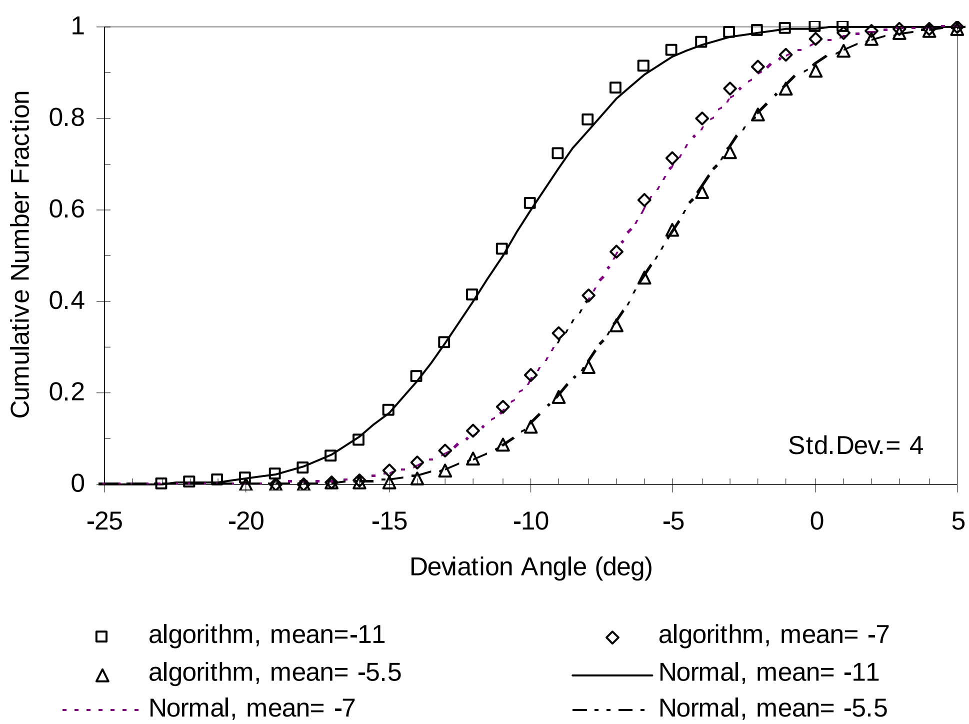

Figure 108. Verification of randomly generated droplet velocity angles by comparison to the normal cumulative number fraction distribution function.

When used in conjunction with the random drop size generator discussed in the next section, it will be possible to randomly choose the initial size and velocity of a droplet. In future sections of this study, the trajectories of the randomly chosen drops will be predicted. The use of the random drop generator will allow the trajectory routines to operate over tens of thousands of drops; much greater numbers than are available from the experimental data.

5.6 Random Drop Size Generator

A drop size generation routine was developed to randomly generate drop sizes that are consistent with a given drop size distribution. In previous sections, it was shown that the Rosin-Rammler function can be used to fit the drop size data in this study. The first step in the generation process is to determine the adjustable parameters of the Rosin-Rammler function for the data set of interest. Since correlations between different sprinkler operating conditions were not found, the values of k and γ must be determined for each operating condition. In addition to the cumulative volume fraction expression, $F_3(d)$, shown in Equation 21, an expression is needed for the volume fraction distribution, $f_3(d)$. The volume fraction expression is derived from analytical differentiation of the cumulative volume fraction, and is shown in Equation 30.

$$f_3(d) = k\gamma d^{\gamma-1} \exp\left(-kd^{\gamma}\right) \tag{30}$$

$$\int f_3(d) = 1 \tag{31}$$

Given the values of k and γ from the cumulative volume function, the volume fraction function is compared with experimental data in Figure 109. In the macro, a lookup table is created from this function, stating the value $f_3(d)$ at 25 µm increments. After creation of the lookup table, a checksum is conducted to verify that Equation 31 is true. The volume fraction function for a log-normal distribution, given in Equation 32, is also plotted for comparison with the data. From these plots, the Rosin-Rammler distribution shows reasonable agreement with the data, especially at larger drop sizes. The log-normal function shows better agreement at drop sizes below 500 μm for the 4 mm orifice sprinkler data, but is inferior overall to the Rosin-Rammler fit.

$$f_3(d)_{L-N} = \frac{1}{\sqrt{2\pi}} \frac{1}{\sigma d} \exp\left[\frac{-\left(\ln\left[d/d_m \right] \right)^2}{2\sigma^2} \right] \tag{32}$$

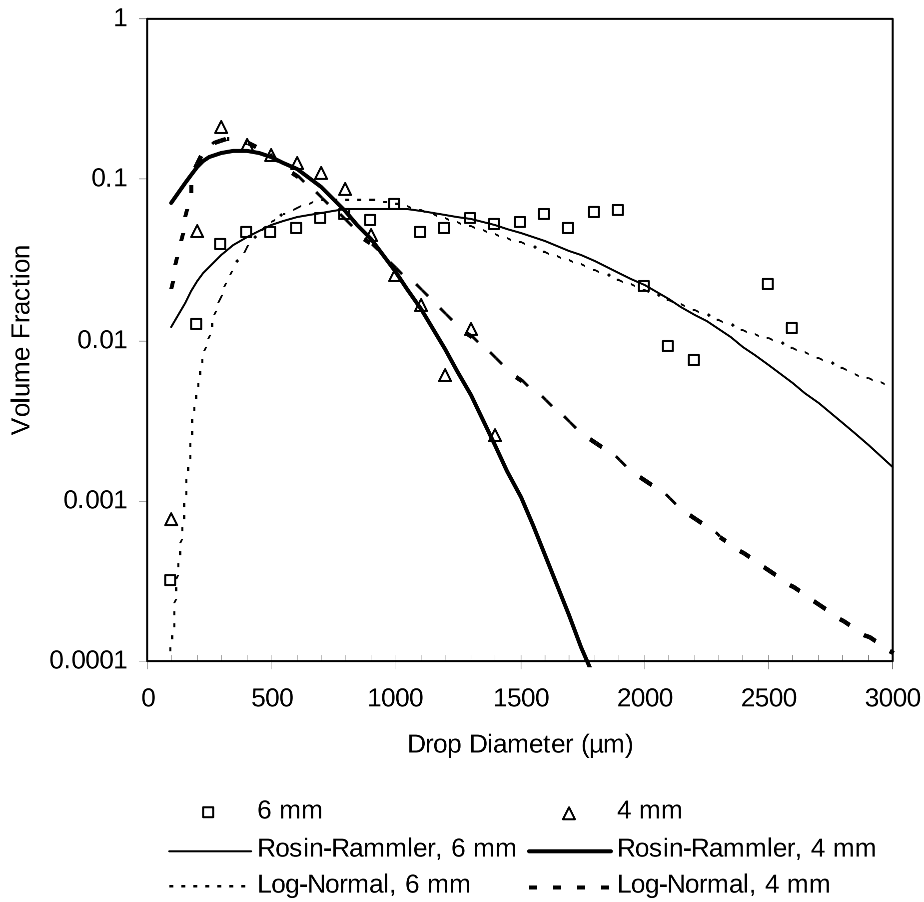

Figure 109. Comparison of Rosin-Rammler and log-normal fits to volume fraction droplet size data. Data shown is for 4 mm and 6 mm orifice sprinklers with a 90 degree strike plate operated at 0.379 L/s (6 gpm).

The next step in the process is to generate a function for the number fraction of drops as a function of drop diameter. This process is done numerically, according to Equation 33, for drop size increments of 25 μm in diameter. After the table is created, a checksum is conducted to verify agreement with Equation 34. Note that since the creation of the number fraction function is done numerically, further portions of the random drop size algorithm need not be changed if the form of the original volume fraction function is changed.

$$f_0(d) = \frac{f_3(d)/d^3}{\sum f_3(d)/d^3} \tag{33}$$

$$\sum f_0(d) = 1 \tag{34}$$

The numerically determined number fraction distribution is compared to the experimental data in Figure 110. Included in this figure are the Rosin-Rammler and log-normal functions. There is satisfactory agreement between the Rosin-Rammler function and the experimental data at large drop sizes, but poor agreement at drop sizes less than 500 μm. The primary limitation of the Rosin-Rammler distribution is illustrated in this plot, which is the tendency of $f_0(d) \rightarrow \infty$ as $d \rightarrow 0$. The log-normal distribution excels under these conditions, and matches the data well at drop sizes less than 500 μm. Despite the limitations of the Rosin-Rammler distribution, it does provide suitable results for characterizing the drop size distribution of the two sprinkler operating conditions, especially in accounting for the volume distributions. For this reason, the Rosin-Rammler distribution will be used to create the random drop size distributions.

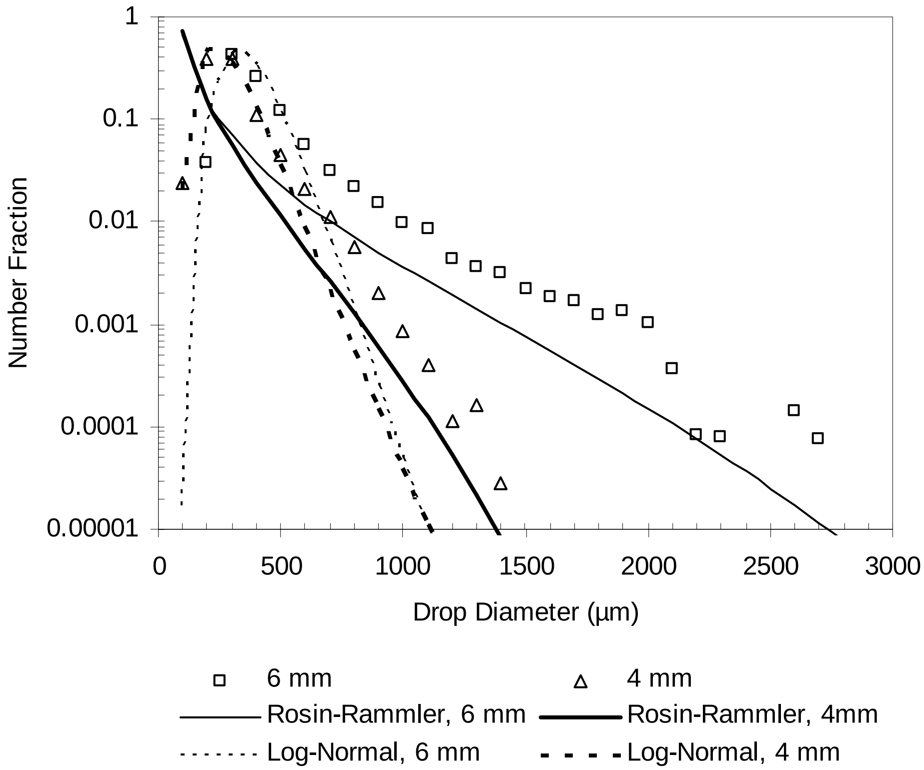

Figure 110. Comparison of the numerically calculated Rosin-Rammler number fraction distribution and the log-normal number fraction distribution to experimental data. Data is for 4 mm and 6 mm orifice sprinklers with 90 degree strike plates operating at 0.379 L/s (6 gpm).

A table of values, representing the cumulative number fraction is now created according to Equation 35. From the definition of cumulative number fraction, the cumulative probability of drop sizes up to 3000 µm in diameter is 1, and this is used to help verify that the algorithm is working properly.

$$F_0(d_i) = \sum_{n=0}^{i} f_0(d_n) \tag{35}$$

The cumulative number fraction function is now used to create a list of random drop sizes. A random number is chosen between 0 and 1, and the drop size corresponding to this probability is found from the lookup table and reported as the random drop size. In this way, a list of random drop sizes is created that is consistent with the drop size distribution. These lists of randomly generated data are referred to as pseudo data files in this study. A flow chart summarizing the process for generating random drop sizes based on experimental data is shown in Figure 111.

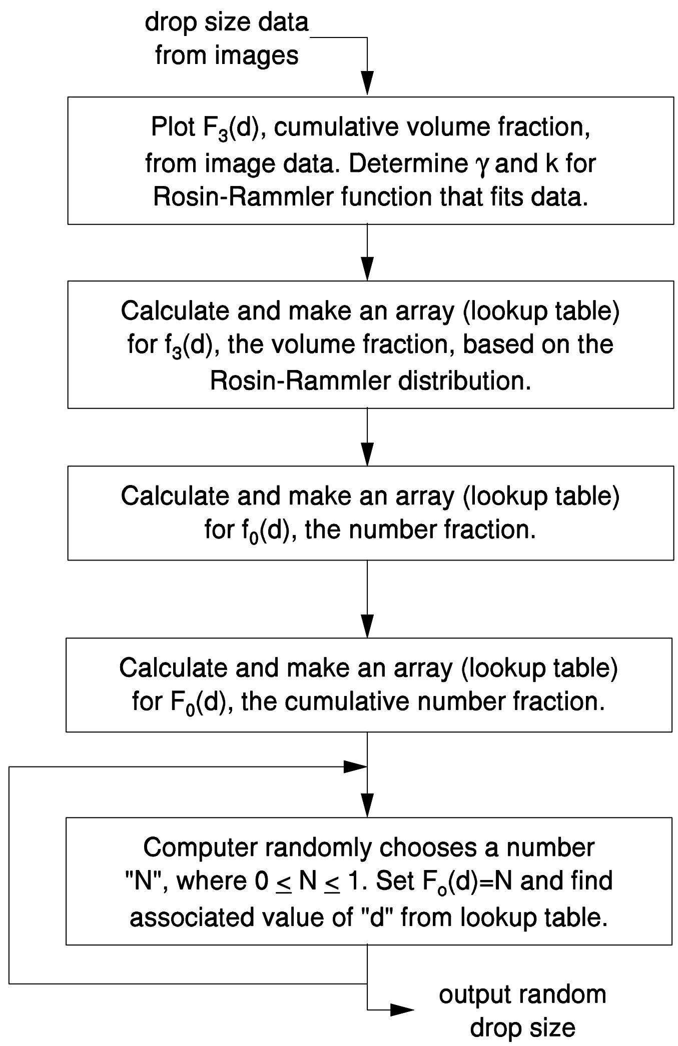

Figure 111. Flow chart illustrating the random droplet generation process.

A pseudo data file consisting of several thousand drops was analyzed as if it was a real data file, and plotted against the experimental cumulative volume fraction data in Figure 112. The figure compares the results of the random algorithm (pseudo data) from the Rosin-Rammler distribution to data from the 4 mm and 6 mm orifice sprinklers. The figure shows that the Rosin-Rammler function used to represent the experimental data is appropriate, and that the algorithm used for creating the pseudo data files is operating properly. Excellent agreement is seen for the 4 mm sprinkler, and good agreement is seen for the 6 mm sprinkler.

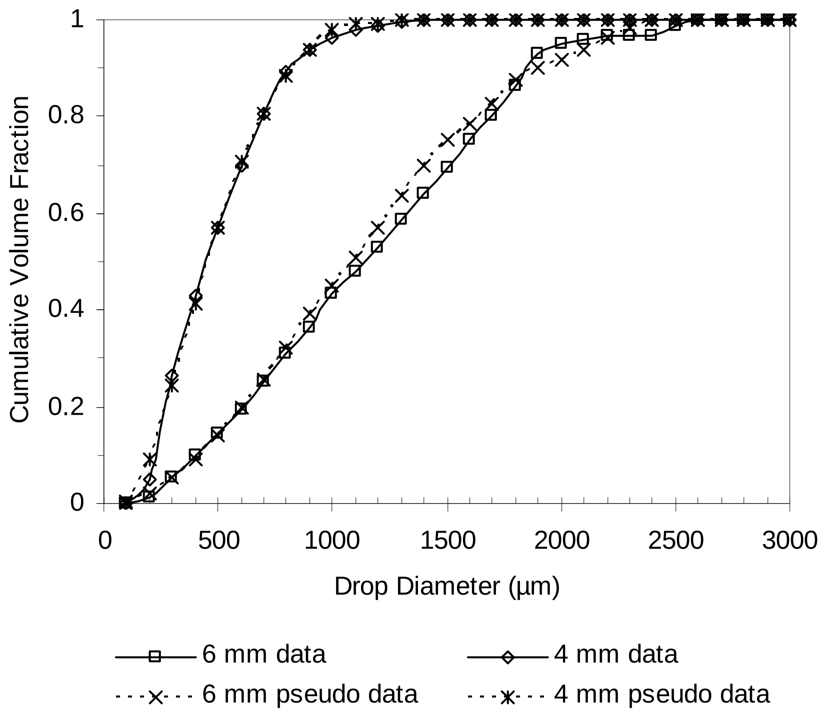

Figure 112. Comparison of cumulative volume fraction plots from random drop size algorithm (pseudo data) and experimental data. The comparison is for 4 mm and 6 mm orifice sprinklers with 90 degree strike plates operated at 0.379 L/s (6 gpm). Experimental data is the average of 8 film exposures.

The randomly generated droplet statistics are further investigated by comparing the number fraction distributions of the pseudo data to the experimental data. The number fraction distributions of the 4 mm and 6 mm sprinklers are shown in Figure 113 and Figure 114. For the 4 mm sprinkler, there is good agreement between the randomly generated pseudo data and the experimental data at drop diameters greater than approximately 400 μm. At smaller drop sizes, the random generation algorithm produces a higher fraction of drops than is seen in the experimental data. In the case of the 6 mm sprinkler, there is good overall agreement, but there is some disagreement at drop sizes less than approximately 400μm. Note that in order to rectify the poor behavior of the Rosin-Rammler distribution at small drop sizes (recall that $f_0(d)\rightarrow\infty$ as $d\rightarrow 0$), and to solve convergence problems in the trajectory program for very small drops that have velocities approaching zero, drop sizes below 150 μm are discarded. Also note that the PTVI technique used in the drop size measurements was also limited to detecting drops larger than approximately 150 μm in diameter.

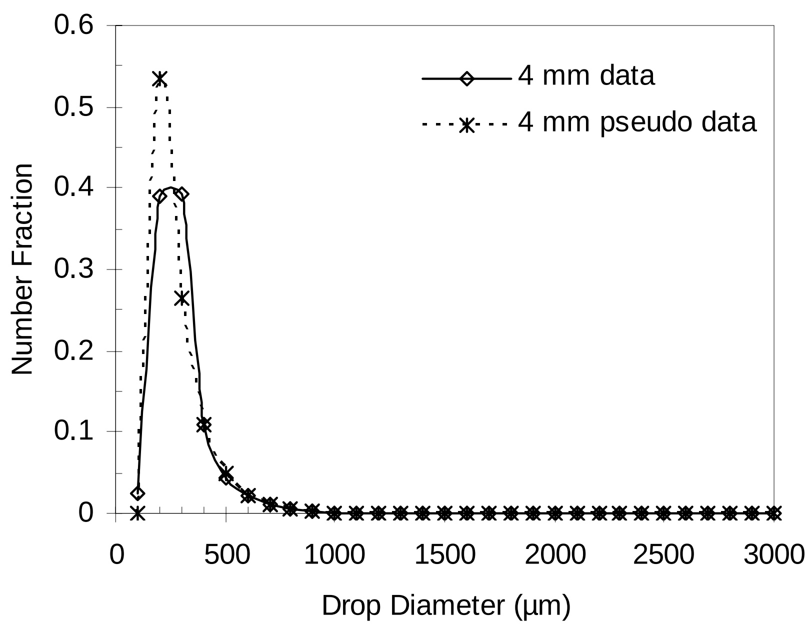

Figure 113. Comparison of randomly generated droplet number fraction pseudo data to experimental data. The comparison is for the 4 mm orifice sprinkler with 90 degree strike plate operated at 0.379 L/s (6 gpm).

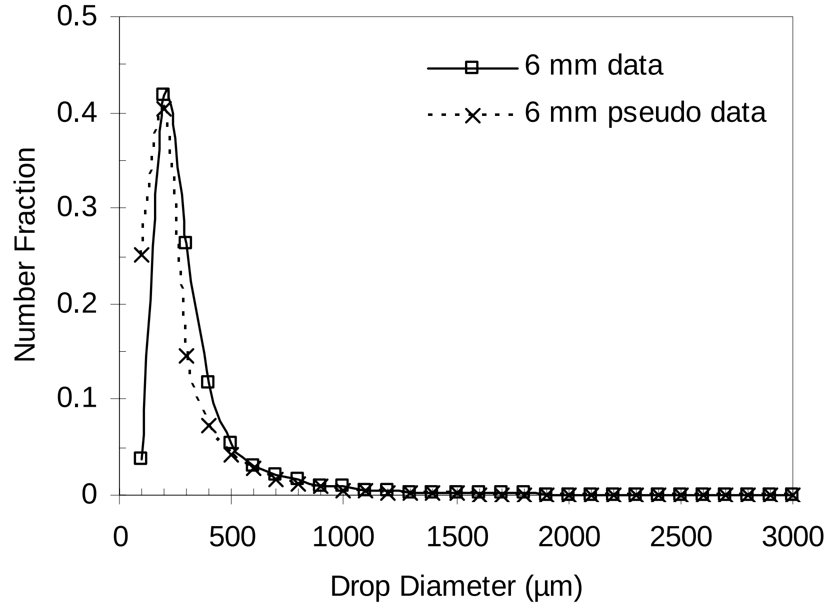

Figure 114. Comparison of randomly generated droplet number fraction pseudo data to experimental data. The comparison is for the 6 mm orifice sprinkler with 90 degree strike plate operated at 0.379 L/s (6 gpm).

As a result of the work in this section, a computer routine is available for producing sets of randomly chosen droplet sizes that match experimental data. In later chapters, the routine will be used in conjunction with the random drop angle generator to provide sets of droplets with random drop sizes and velocities.

CHAPTER 6

DROPLET TRAJECTORY AND WATER DISTRIBUTION

6.1 Droplet Trajectory Scaling

As stated in the background, previous researchers have applied simple trajectory models to sprinkler sprays in order to predict droplet paths and applied floor water density patterns. The researchers reported varying levels of agreement between the predicted and measured water application densities. In these computations, the droplets are treated as single, non-evaporating, spherical particles. While the authors either calculated or measured initial droplet velocities via PIV, they assumed droplet size distributions, measured them at various individual points in the spray, or back calculated them in their computations. In order to determine the relevance of using the simple trajectory models, it would be useful to have the initial sprinkler droplet size and velocity distributions as model inputs, then compare the computations of applied water density to the measured results.

The PTVI technique has the ability to provide droplet size and velocity information for the sprinklers to be studied. The empirical data gathered in the sprinkler droplet measurement portion of this work was entered into a simple trajectory model. This process entails using the droplet size and velocity data near the sprinkler as an input condition, and calculating the droplet trajectory and delivered water distribution at various heights.

In order to calculate the trajectory of a droplet after it has exited the breakup region, we begin with a free body diagram of a droplet, which can be seen in Figure 115. Once the droplet has been formed by the breakup of the water sheet near the sprinkler, we assume that the droplet remains spherical and is not evaporating. The only forces acting on this lone droplet are drag (friction and form) and gravity (corrected for buoyancy) which will govern its trajectory. In order to calculate the drag forces for sprinkler drops which reside within the range of $1<Re<500$, the coefficient of drag, C_D, can be approximated by $C_D=k/Re^a$ (Lapple and Shepherd 1940). Within this range of Re, the constants k=15.92 and a=0.584 were derived from a fit of the drag curve for spheres, which is shown in Figure 116. While some evaporation will occur, recall that the research in the literature has demonstrated that evaporation will have a negligible effect on drag for the conditions present in our experiments.

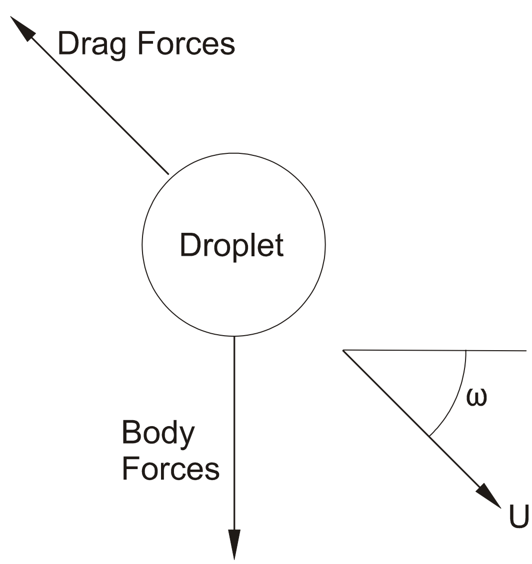

Figure 115. Forces acting on droplet.

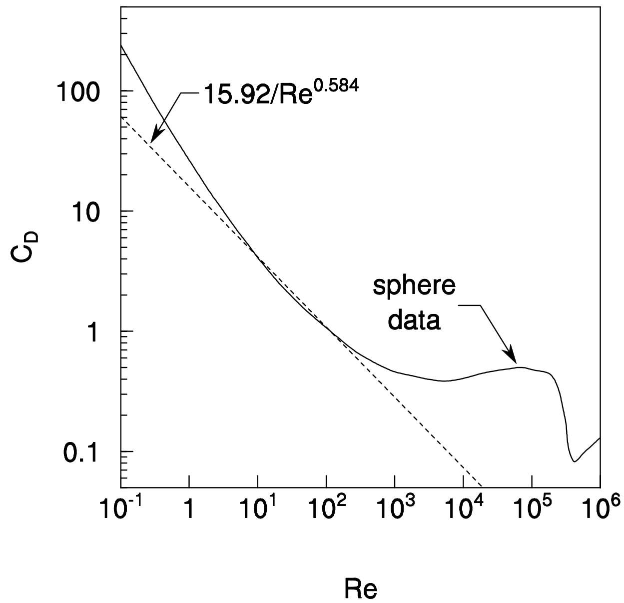

Figure 116. Coefficient of drag curve for solid spheres.

Newton's law of motion for the droplet, ∑F=d/dt (mu), can be split up into the two orthogonal scalar equations shown in Equation 36 and Equation 37.

$$\frac{du_x}{dt} = -\frac{3}{4} C_D \frac{\rho}{\rho_w} \frac{1}{d} U^2 \cos\omega \tag{36}$$

$$\frac{du_y}{dt} = g - \frac{3}{4} C_D \frac{\rho}{\rho_w} \frac{1}{d} U^2 \sin\omega \tag{37}$$

where: u_x=horizontal velocity
u_y=vertical velocity
C_D=coefficient of drag
ρ=air density
ρ_w=water density
d=drop diameter
U=magnitude of velocity
ω=angle of velocity
m=droplet mass

These expressions are similar to those used by Prahl and Wendt (1988).

The trajectory equations can be non-dimensionalized using the Reynolds number to represent velocity:

$$\frac{d(\mathrm{Re}\cos\omega)}{d\tau} = -\left(\mathrm{Re}^{2-a}\ \cos\omega\right) \tag{38}$$

$$\frac{d(\mathrm{Re}\sin\omega)}{d\tau} = \phi - \left(\mathrm{Re}^{2-a}\ \sin\omega\right) \tag{39}$$

where:

$$\mathrm{Re} = \frac{\rho u d}{\mu}; \quad C_D = \frac{k}{\mathrm{Re}^a}; \quad \tau = \frac{t}{t^*}; \quad t^* = \frac{4\rho_w d^2}{3k\mu}; \quad \phi = \left(\frac{8m\rho g}{k\pi\mu^2}\right)\left(\frac{\rho_w - \rho}{\rho_w}\right)$$

The equations of motion were non-dimensionalized by first choosing Re to represent velocity, and the t^* term formed using the dynamic viscosity for the units of time. The value of ϕ, which represents the body force term, was then determined from Newton's law in the vertical direction. Note that the $(\rho_w - \rho)/\rho_w$ term is the buoyancy correction. In the above equations μ is the air viscosity, and m is the mass of the droplet. The non-dimensionalized equations can be simplified to:

$$\frac{d\,\mathrm{Re}}{d\tau} = \phi \sin\omega - \mathrm{Re}^{2-a} \tag{40}$$

$$\frac{d\omega}{d\tau} = \frac{\phi \cos\omega}{\mathrm{Re}} \tag{41}$$

The equations of motion are formulated in this manner since the distance traveled by the droplet is a function of velocity and angle, both of which are changing with time. For negligible evaporation, ϕ is constant for the entire flight of the droplet.

In order to predict the delivered density below the discharging sprinkler, we must calculate the distances traveled by the droplets over time. The horizontal travel of the droplet, S_h=f(u, ω), is determined by integrating the velocity equation resulting in:

$$S_h = \left(\frac{4d\rho_w}{3\rho k}\right)\int_0^{\tau_f} \mathrm{Re}\cos\omega \, d\tau \tag{42}$$

Likewise, the vertical flight of the droplet, S_v=f(u, ω), is determined by integrating the velocity equation resulting in:

$$S_v = \left(\frac{4d\rho_w}{3\rho k}\right)\int_0^{\tau_f} \mathrm{Re}\sin\omega \, d\tau \tag{43}$$

Where the boundaries of the integrals are the initial time at which the droplet begins its travel, and τ_f is the non-dimensional time of flight of the droplet from the sprinkler to the floor. The travel distances can be non-dimensionalized resulting in:

$$S_h^* = \frac{S_h}{\left(\frac{4d\,\mathrm{Re}(0)\rho_w \cos\omega_0}{3\rho k}\right)} \tag{44}$$

$$S_v^* = \frac{S_v}{H} \tag{45}$$

Where S_h has been normalized by the invicid horizontal flight distance, $t^*U_0\cos\omega_0$, and S_v is normalized by the height of the sprinkler off of the floor, H. S_v could also have been normalized by the distance at which the horizontal velocity approaches zero, indicating that the water flux distribution would no longer change with increasing values of S_v. The equations for the location of the droplet as a function of time can be solved numerically.

Since the goal of the work is to predict the water flux on the floor, the time necessary for the droplet to hit the floor is not of interest. Therefore, the simplified trajectory equations, Equation 40 and Equation 41, can be further simplified by eliminating the time scale and assuming steady state:

$$\frac{dV}{V^{\frac{5}{2}}} = -\frac{1}{\phi}\frac{d\omega}{(\cos\omega)^{\frac{5}{2}}} \tag{46}$$

where:

$$V = \mathrm{Re}\cos\omega \tag{47}$$

which can be integrated to yield:

$$\frac{1}{V^{\frac{3}{2}}} = \frac{1}{V_0^{\frac{3}{2}}} + \frac{3}{2\phi}\left[f(\omega) - f(\omega_0)\right] \tag{48}$$

where:

$$f(\omega) = \int_0^{\omega} \frac{d\omega}{(\cos\omega)^{\frac{5}{2}}} \tag{49}$$

is an analytically known function that can be solved for a range of ω beforehand. Thus:

$$\mathrm{Re} = \frac{\mathrm{Re}(0)\cos\omega_0}{\cos\omega}\left(1 + \frac{3V_0^{\frac{3}{2}}}{2\phi}\left[f(\omega) - f(\omega_0)\right]\right)^{-\frac{2}{3}} \tag{50}$$

$$\frac{dS_h}{d\omega} = \frac{4d\rho_w}{3\rho k}\frac{\mathrm{Re}^2\ \cos\omega}{\phi\cos\omega} \tag{51}$$

$$\frac{S_h}{H} = \frac{S_h(0)}{H} + \frac{4d\rho_w}{3Hk\rho\phi}\int_{\omega_0}^{\omega}\mathrm{Re}^2\, d\omega \tag{52}$$

$$\frac{S_v}{H} = \frac{S_v(0)}{H} + \frac{4d\rho_w}{3Hk\rho\phi}\int_{\omega_0}^{\omega}\mathrm{Re}^2(\tan\omega)\, d\omega \tag{53}$$

with the following groups of non-dimensionalized parameters that govern the trajectories of the droplets:

$$\omega_0 \ ; \quad \frac{V_0^{\frac{3}{2}}}{\phi} ; \quad \frac{d}{H}\frac{\rho_w}{\rho}\frac{1}{\phi}$$

Therefore, if the above groups are preserved, the experiments can be conducted at reduced scale.

The distribution of droplets hitting the floor results in the delivered density at the floor. Recall that the delivered density at the floor was measured using collection pans, which were weighed at the end of each experiment. The distribution of water at the floor will be compared to the water distribution predicted by the trajectory model later in this chapter. The results of this portion of the study will indicate whether or not the simple trajectory models, which ignore the possible interactions of droplet induced flows, are a good approximation.

6.2 Droplet Trajectory Calculation

A computer algorithm was written to solve Equation 36 and Equation 37, providing the location of a droplet as it travels from the sprinkler to the floor. The algorithm solves the equations numerically using a 4^{th} order Runge-Kutta scheme. The trajectory calculation core, or subroutine, takes the initial drop size, velocity, and position as inputs, and outputs a new velocity and position after a given interval of time. In order to test the core for proper operation, two special cases of droplet motion were investigated. The first case assumes that the drops are falling under the force of gravity, with the direction of the velocity vector in the vertical direction only. The terminal velocities of drops with diameters of 200μm to 3000 μm, with initial velocities of 5 m/s to 20 m/s were calculated. The calculated velocities were compared to terminal velocities of water droplets in the literature (Gunn and Kinzer 1949). The error in the terminal velocity calculation was < 7% for droplets with Re < 800. For droplets larger than approximately 2000 μm in diameter, where Re > 800, errors were up to 82%. This is not totally unexpected, since the drag force curve fit begins to lose validity at Re > 500. To remedy the situation, another term is added to the calculation, which sets C_D=0.44 for Re > 500. When the terminal velocity calculations were repeated, the maximum error was found to be < 10%.

The horizontal travel portion of the subroutine was checked by calculating the travel distance as a function of time for a droplet exposed only to a constant drag force. The numerical calculations were compared to the results of an analytical calculation given in Equation 54 (Lapple and Shepherd 1940):

$$s = \left(\frac{3.03 d \rho_w}{\rho} \right) \ln \left(\frac{0.33 \rho u_0 t}{\rho_w d} + 1 \right) \tag{54}$$

where: s=distance
ρ_w=drop density
ρ=air density
d=drop diameter
u_0=initial drop velocity
t=time

When s=f(t) was calculated for g=0, C_D=0.44, u_0=10 m/s, and d=1000 μm, the results of the numerical subroutine and the analytical calculation were within 1.5% for travel times of 2 s. This indicates that the numerical subroutine is working properly.

6.3 Water Flux Prediction

Using the drop size and velocity data, the trajectory algorithm can predict the horizontal location of drops when they reach floor level. A computer program was written to read the drop sizes, velocities, and locations from the experimental data files. Each droplet was passed into the trajectory subroutine, and its position calculated until it reached the floor. The volume of the drop was added to the virtual pan corresponding to its final horizontal position. The virtual pans are of the same dimensions as the actual pans used to measure the water flux from the sprinklers. During the analysis of the data, it was found that the expression for C_D needed to be modified further. For drops with Re<1, the drag coefficient caused numerical overflows in the trajectory algorithm. This was solved by adding a relation for 0<Re<1. In summary, the C_D expression used in the trajectory subroutine is:

$$
\begin{aligned}
C_D &= \frac{24}{\mathrm{Re}} \qquad \textit{for} \qquad 0 \le \mathrm{Re} \le 1 \\
C_D &= \frac{k}{\mathrm{Re}^a} \qquad \textit{for} \qquad 1 < \mathrm{Re} \le 500 \\
C_D &= 0.44 \qquad \textit{for} \qquad \mathrm{Re} > 500
\end{aligned}
\tag{55}
$$

After all of the drops for a given data file are deposited in the appropriate pan, the total volume of water is reported for each pan. Due to the unsteady behavior of the sprinkler, each image captures a different volume of water. In order to collapse the data, the volume fraction of water is calculated for each pan and reported. This gives the predicted relative water flux distribution for the sprinkler. Data for 6 mm and 4 mm orifice sprinklers, located 2.08 m above the floor (1.93 m above the pans) are shown in Figure 117 and Figure 118. The data from 8 exposures is compared for each operating condition. The horizontal distance, S_h, is normalized by the inviscid travel distance, $S_{h,i}$, of a drop with an initial speed equal to the speed of the water at the orifice, an initial angle equal to the strike plate angle, and a diameter equal to the volume median diameter. Even though the water flux is normalized by the total water volume in the image, there is some variability in the water distribution due to differences in the velocities of the drops in each image.

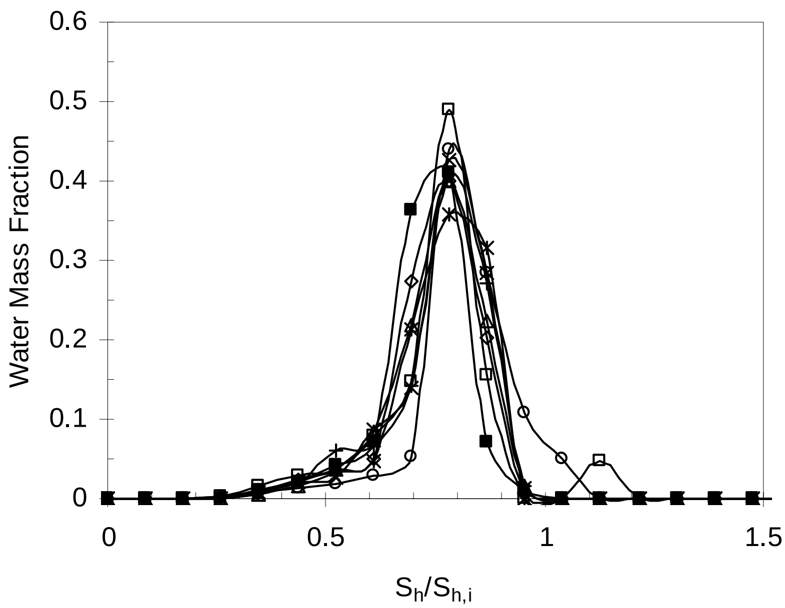

Figure 117. Predicted water distribution for 6 mm orifice sprinkler with 90 degree strike plate operating at 0.379 L/s (6 gpm).

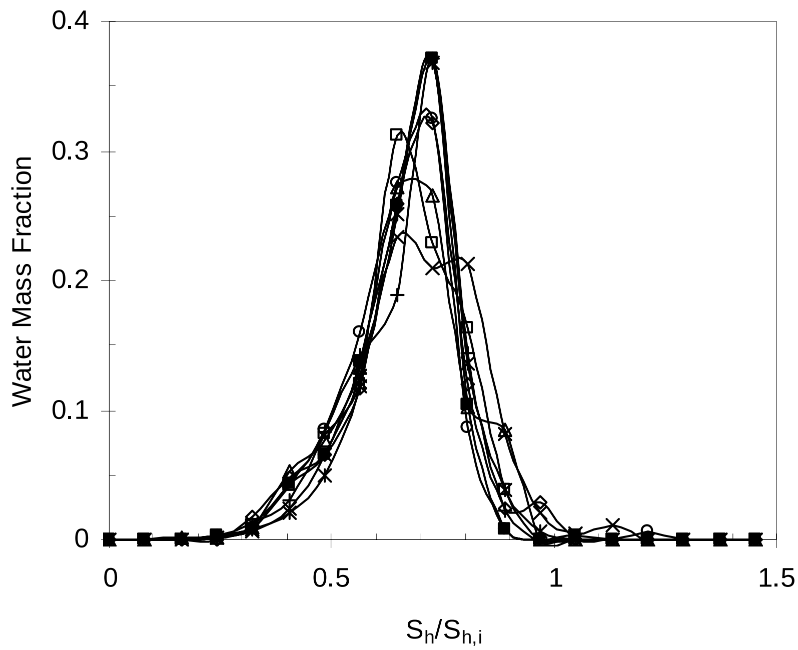

Figure 118. Predicted water distribution for 4 mm orifice sprinkler with 90 degree strike plate operating at 0.379 L/s (6 gpm).

The water distribution results for the 8 film exposures are averaged, and compared to the measured water distribution in Figure 119 and Figure 120. Since the water distributions were measured over a full diameter of the sprinkler spray, there are two radii of data for comparison. In contrast, since the sprinklers are assumed to be axis-symmetric, there is a single radius of predicted water distribution data. As shown in the figures and discussed previously, the sprinklers are not fully symmetric in operation, although there is good agreement between the two examples shown here for comparison with the predictions. Comparing the measured and predicted distributions, the figures indicate good agreement for the 6 mm orifice case, where the peak and width of the prediction agrees with the measured water distribution. Agreement is only fair for the 4 mm case, where the peak of the predicted water distribution is shifted away from the sprinkler axis by approximately 0.3 m. In addition, the predicted distribution is narrower, and shows no water in the pans close to the sprinkler. The measured distribution, however, indicates less water at the peak location, and water in the pans close to the sprinkler axis. This behavior is consistent with entrainment effects, which would be expected to shift water in towards the core of the spray. This behavior is expected to have more of an effect on the 4mm sprinkler, due to the larger fraction of small drops which are more susceptible to the effects of entrained air. Recall that the volume median drop diameter is approximately 1139 μm for the 6mm orifice and approximately 450 μm for the 4mm orifice with 90 degree strike plates at 0.379 L/s (6 gpm).

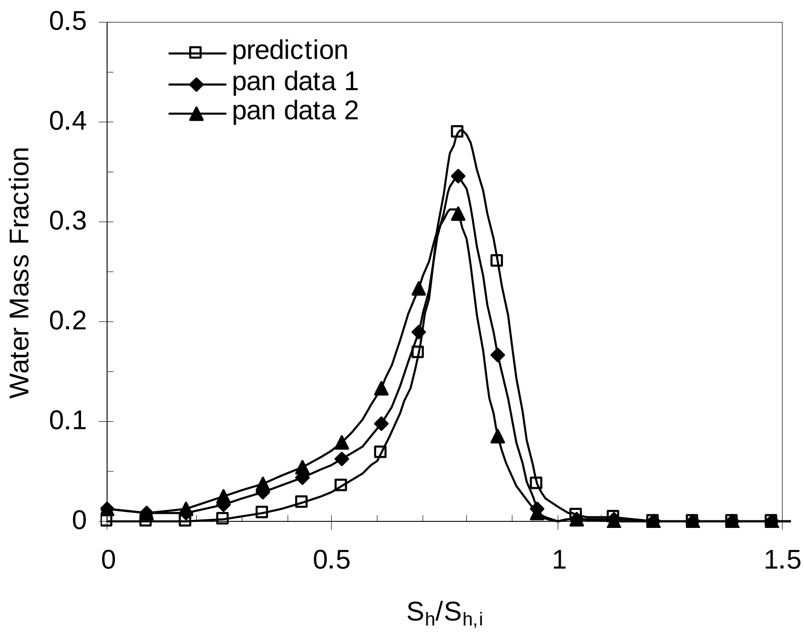

Figure 119. Comparison of measured and predicted water distribution for 6 mm orifice sprinkler with 90 degree strike plate operating at 0.379 L/s (6 gpm).

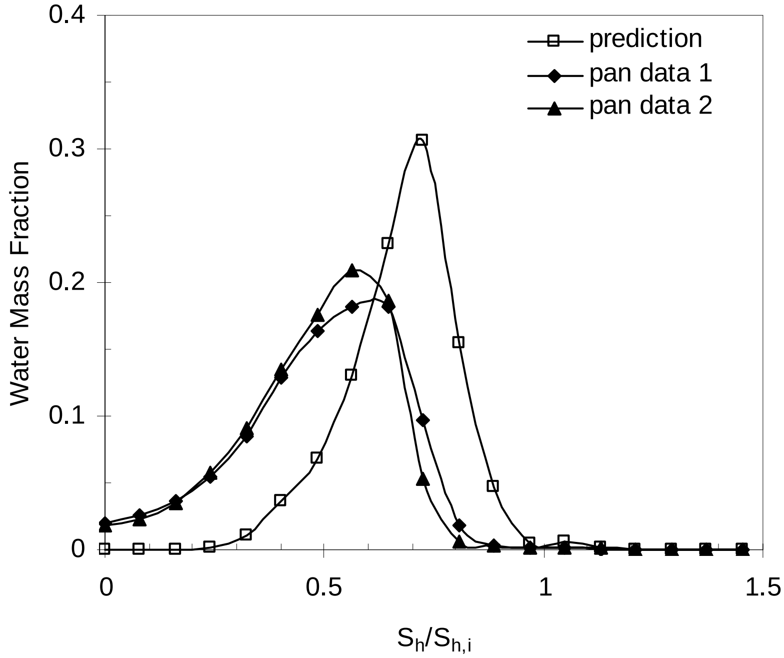

Figure 120. Comparison of measured and predicted water distribution for 4 mm orifice sprinkler with 90 degree strike plate operating at 0.379 L/s (6 gpm).

Due to the effects of drag, we expect the smaller drops to land closer to the centerline of the sprinkler than the larger drops, even without the effects of entrained air. This is illustrated in Figure 121 and Figure 122, where the drop size distribution is plotted for each pan. The data shown are the result of combining the trajectory predictions from 8 film exposures. Notice that as the distance from the sprinkler axis increases, the peak number fraction occurs at increasingly larger drop diameters. Due to the small number of drops measured at very large and very small drop sizes, the number of drops that were predicted to land in each pan is shown in Figure 123. As expected, the plot indicates that a very small number of drops are predicted to land in pans where $0 \leq S_h/S_{h,i} \leq 0.3$ and $0.9 \leq S_h/S_{h,i}$, but they all tend to be of the same size.

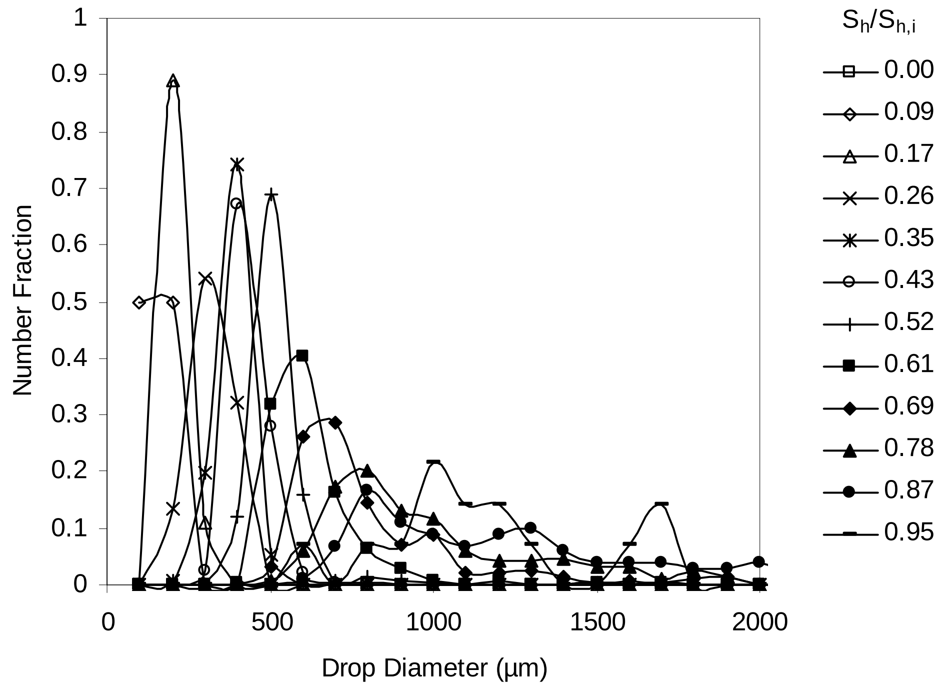

Figure 121. Drop diameter number fraction distribution as a function of location from the sprinkler axis. Results from water droplet trajectory predictions of a 6 mm orifice sprinkler.

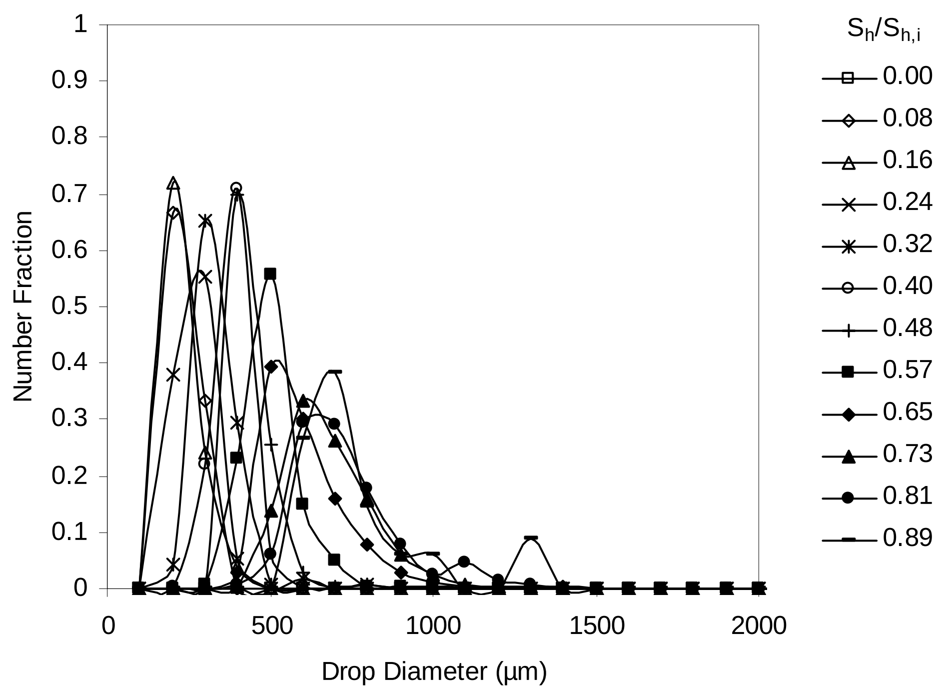

Figure 122. Drop diameter number fraction distribution as a function of location from the sprinkler axis. Results from water droplet trajectory predictions of a 4 mm orifice sprinkler.

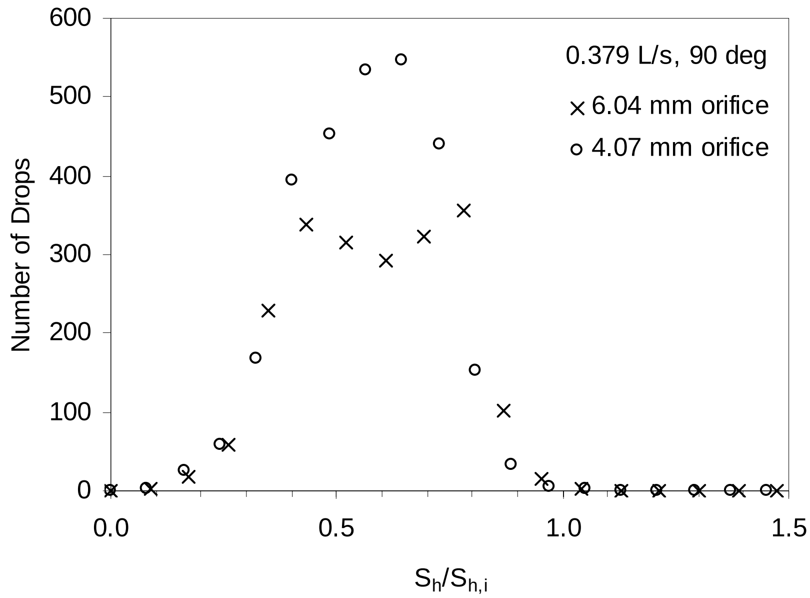

Figure 123. Number of drops predicted to land in each pan by the trajectory algorithm. Results for 4 mm and 6 mm orifice sprinklers.

When using the list of drops from the experimental images, there are two methods that can be used to average the data from multiple exposures. One method would be to run a prediction using the data from each image, and then average the results. A second method would be to combine the data from multiple images into one data file, then run the prediction using the combined data file. The second method is more convenient, and results in predictions nearly identical to the first method. The two methods are compared in Figure 124 and Figure 125. Given this comparison, a combination data file was constructed for each sprinkler operating condition for use in the water distribution calculations.

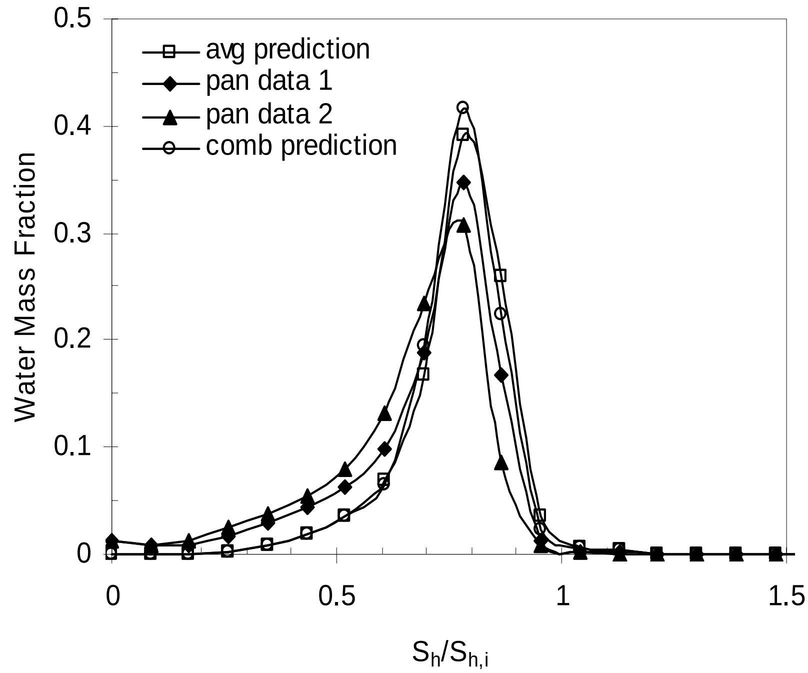

Figure 124. Comparison of averaging methods for experimental drop size and velocity data using predicted water distribution from 6 mm orifice sprinkler.

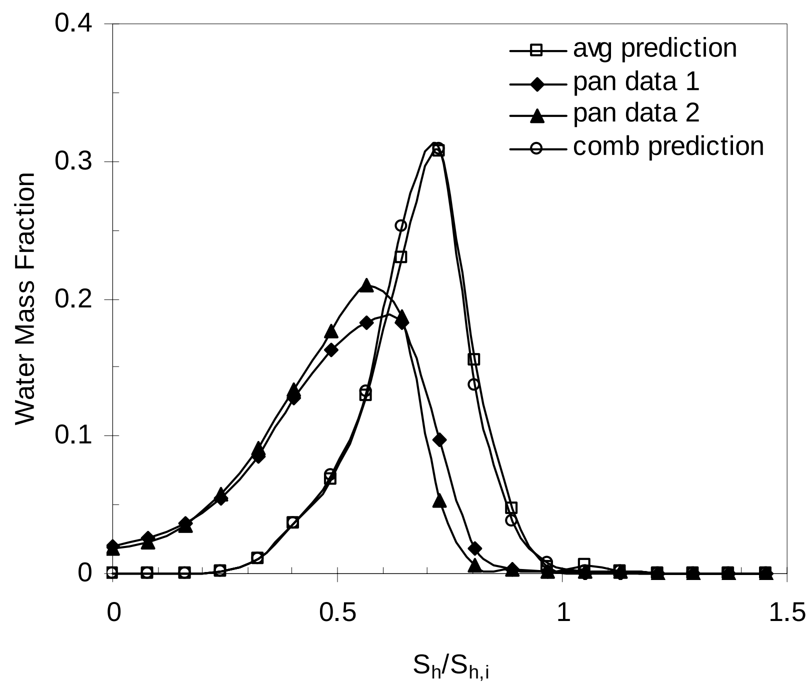

Figure 125. Comparison of averaging methods for experimental drop size and velocity data using predicted water distribution from 4 mm orifice sprinkler.

Given that satisfactory results were derived from the simple trajectory model using measured droplet size and velocity data, modifications to the input data are investigated. The measured sprinkler data derived from the images gives the characteristics of the water droplets at their respective locations in the spray field. It would be more useful to look at the conditions of these droplets at or very close to the sprinkler. By using the physical properties of the sprinkler, and assuming water sheet breakup occurs at the sprinkler, the spray can be modeled using several sets of initial conditions:

1. Use the drop size and velocity data measured from the images. Start all drops at the sprinkler (0,0).
2. Use the measured drop size distribution. Start all of the drops at the sprinkler (0,0). Use the speed of the water at the exit of the orifice as the initial drop speed, with the initial direction from the image data.
3. Use the measured drop size distribution. Start all of the drops at the sprinkler (0,0). Use the speed of the water at the exit of the orifice as the initial drop speed, with the initial direction the same as the angle of the strike plate.
4. Use the measured drop size distribution. Start all of the drops at the sprinkler (0,0). Use the measured speed from the image as the initial drop speed, with the initial direction the same as the angle of the strike plate.
5. Use the measured drop size distribution. Start all of the drops at the sprinkler (0,0). Use the speed of the water at the exit of the orifice as the initial drop speed, with the initial direction of all the drops from the volume average angle of all the drops as measured from the images.

The first two scenarios are compared to each other, a prediction using all of the image data, and to the measured water distribution, in Figure 126 and Figure 127. For both sprinkler operating conditions, scenario 1 illustrates that the velocity of the droplets has changed significantly from when they exit the sprinkler and where they were measured in the spray field. The result is a shifting of the water distribution toward the sprinkler axis. The plots from scenario 2 show good agreement with the predictions using all of the measured droplet data for both sprinkler operating conditions. This agreement suggests that all droplets may be assumed to start at the sprinkler (0,0) and at the speed of the water exiting the sprinkler. This greatly simplifies the modeling of the sprinkler spray.

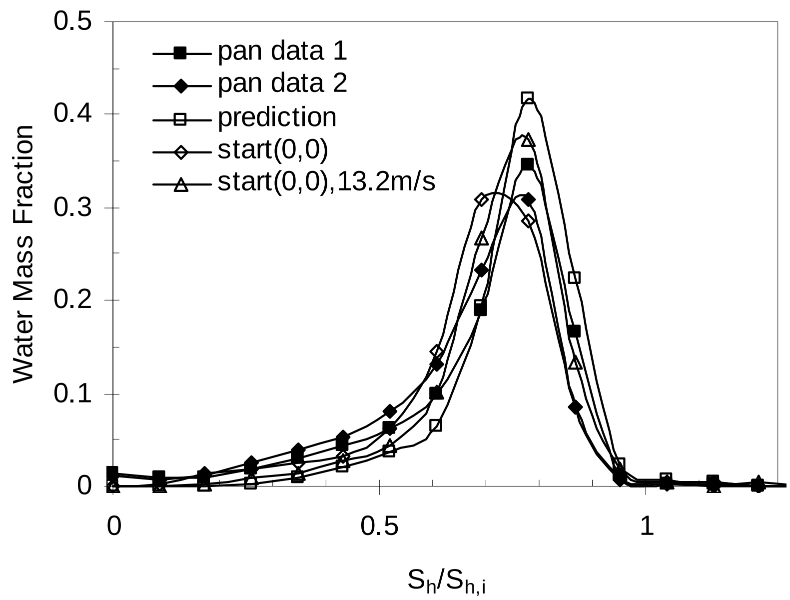

Figure 126. Comparison of sprinkler input data scenarios 1 and 2 to experimental water distributions for a 6 mm sprinkler with 90 degree strike plate operating at 0.379 L/s (6gpm). Note that the plot labeled "prediction" represents the water mass fraction calculated by the trajectory model using the drop velocities and drop locations from the sprinkler images.

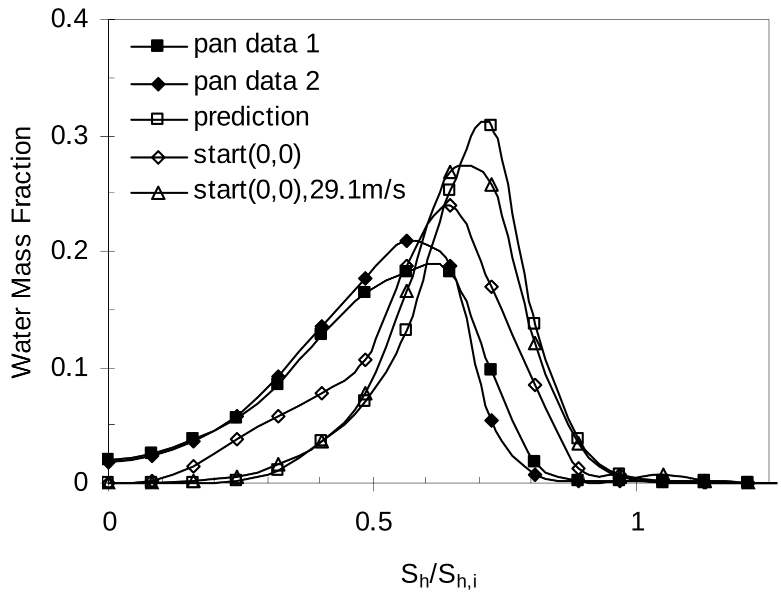

Figure 127. Comparison of sprinkler input data scenarios 1 and 2 to experimental water distributions for a 4 mm sprinkler with 90 degree strike plate operating at 0.379 L/s (6gpm).

Scenarios 3, 4, and 5 investigate the initial droplet angle. The results are compared to each other, a prediction using all of the image data, and to the measured water distribution, in Figure 128 and Figure 129. The predictions using scenarios 3 and 4 indicate a peak water mass fraction further from the sprinkler axis than the prediction using all of the experimental data as well as the measured water distribution. In addition, the water flux is spread over a much smaller area. This indicates that the median droplet angle of the data is not equal to that of the sprinkler strike plate (peak water mass fraction), and that there is a distribution of drop angles (spread of water mass fraction) that is important to the water distribution. The effect of the median drop angle on the distribution is verified by scenario 5, which has a peak water mass fraction at the same distance from the sprinkler axis as the prediction using all image data for 6 mm and 4 mm sprinklers, and the same as the peak in the measured water distribution for the 6 mm sprinkler.

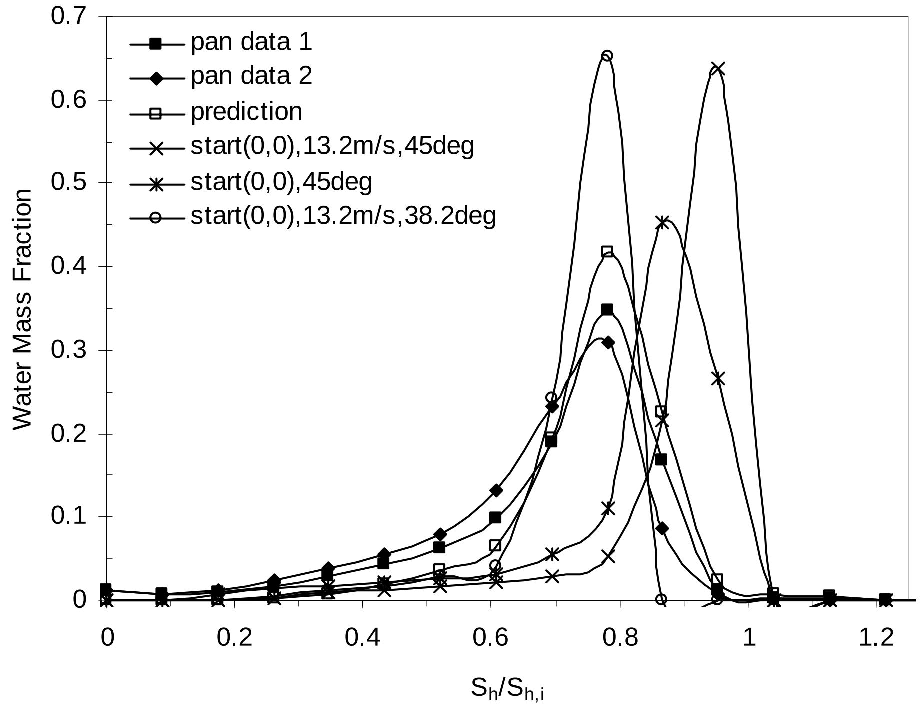

Figure 128. Comparison of sprinkler input data scenarios 3, 4, and 5 to experimental water distributions for a 6 mm sprinkler with 90 degree strike plate operating at 0.379 L/s (6gpm).

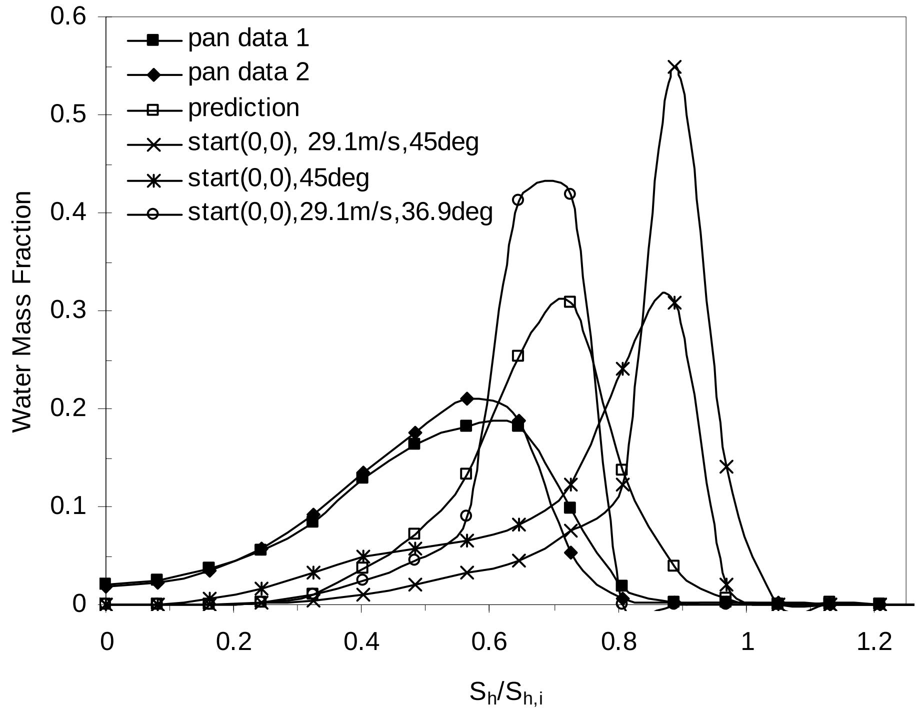

Figure 129. Comparison of sprinkler input data scenarios 3, 4, and 5 to experimental water distributions for a 4 mm sprinkler with 90 degree strike plate operating at 0.379 L/s (6gpm).

As a result of examining the above input data scenarios, it has been determined that modeling can be simplified by combining the initial velocity of the water jet exiting the sprinkler with an initial droplet location at the sprinkler. Relationships for the droplet size distribution, and initial droplet directions, however, are needed.

6.4 Water Distribution Predictions Using Size and Velocity Distribution Functions

The previous section illustrated that the prediction of water distributions can be simplified by assuming that all drops begin at the sprinkler, and that the magnitude of their initial velocities are that of the water jet. These two simplifications are combined with the random drop size generator, the random drop angle generator, and trajectory subroutine to predict water distributions. A pseudo data file is first created by inputting the parameters of the Rosin-Rammler distribution for drop size, and the mean/median drop angle for the normal distribution into a program that generates 20×10^3 pseudo drops. To construct the file, drop sizes are randomly chosen by the algorithm according to the Rosin-Rammler distribution in increments of 25 μm, from the range of 150 μm to 3000 μm in diameter. An associated initial drop angle is randomly chosen from the normal distribution. The height of the sprinkler and the initial velocity of the drop are then input in the water distribution program, along with the name of the pseudo data file. When executed, the water distribution program reads the first drop size and velocity from the pseudo data file, and the drop is sent on its way. The trajectory is calculated in steps using a numerical scheme, the final horizontal location is calculated, and the volume of the drop is added to the appropriate pan. The process is repeated within the water distribution program for the 20×10^3 drops, and the final water distribution is reported.

The resulting predictions of water distribution are shown in Figure 130 and Figure 131 for 4 mm and 6 mm sprinklers. The figures also compare the random drop predictions with predictions using the measured image data, as well as the measured water distribution data. The plots for the 6 mm sprinkler show good agreement between both types of predictions and the measured water distribution. There are some differences between the predictions using the random drops and the other plots, which are attributed to the curve fits used to define the droplet size and angle distributions.

The agreement between the predictions and between the randomized droplet data prediction and the measured water distribution for the 4 mm sprinkler are fair. The difference in the predictions is attributed to the curve fits used to define the droplet size and angle distributions. Agreement was expected to be less for the 4 mm case due to the larger numbers of small drops, which are not fit as well as the larger drops by the Rosin-

Rammler distribution. Recall that the distribution fit approximately 75% of the water volume well, as opposed to approximately 95% of the water volume for the 6 mm sprinkler. (See Figure 72 and Figure 73) The plateau region of the randomized data prediction is also explained by the fit of the drop size distribution. Recall the fit of the Rosin-Rammler distribution, which tends to predict a larger fraction of drops ≤200 μm than are actually present. These very small drops tend to be deposited very close to the sprinkler, which explains the plateau at $0 \leq S_h/S_{h,i} \leq 0.4$. As discussed earlier, entrainment effects are suspected of being the cause of the differences between the predictions and the measured water distributions.

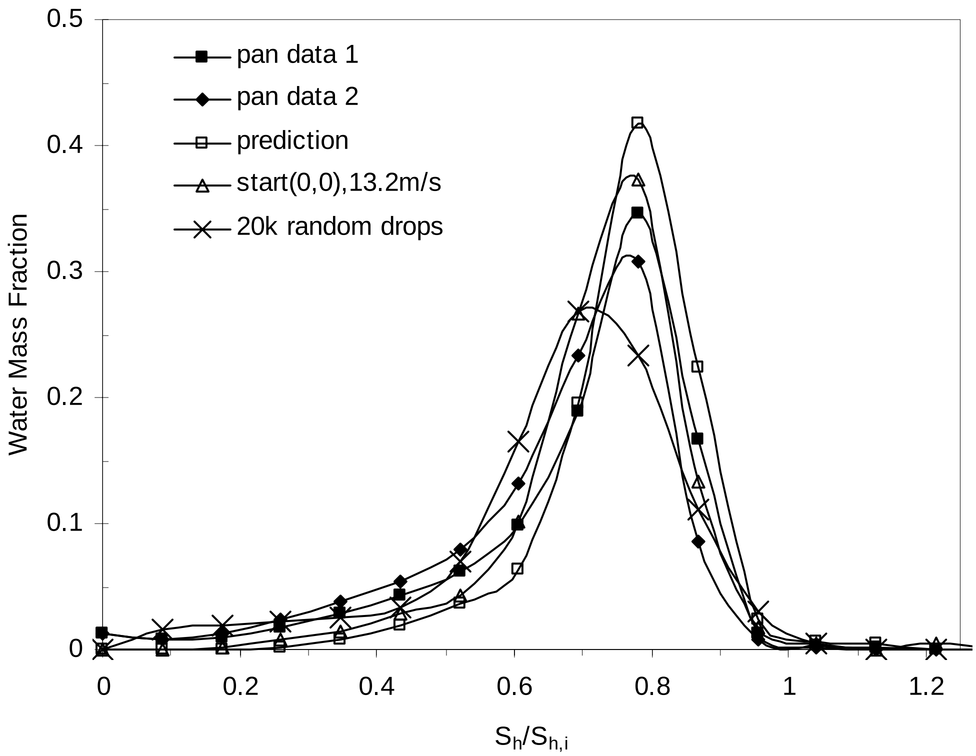

Figure 130. Comparison of water distributions predicted using randomly chosen droplets with those predicted using image droplet data, and with measured water distributions. Results shown for 6 mm orifice sprinkler with 90 degree strike plate operating at 0.379 L/s (6 gpm).

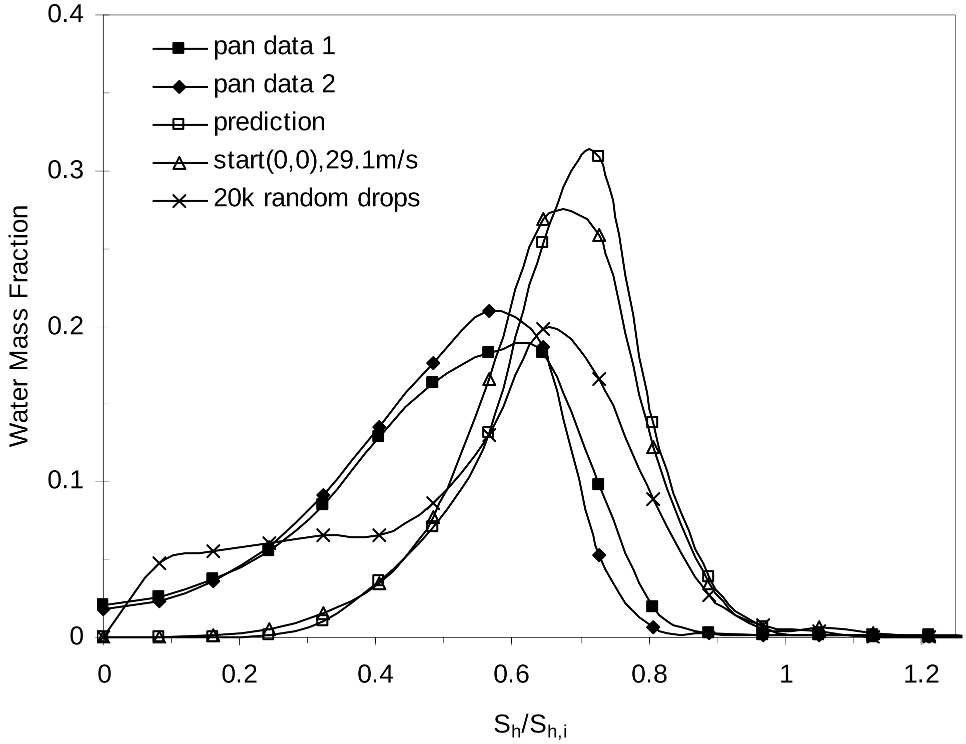

Figure 131. Comparison of water distributions predicted using randomly chosen droplets with those predicted using image droplet data, and with measured water distributions. Results shown for 4 mm orifice sprinkler with 90 degree strike plate operating at 0.379 L/s (6 gpm).

The water distributions predicted by the calculations using the random drop size and random velocity angle routines may change with the number of randomly chosen drops run through the calculation. In order to determine the number of drops needed to reach the point where the results no longer changed, calculations were run with 5×10^3, 10×10^3, 20×10^3, and 30×10^3 random drops. The results are shown in Figure 132, and indicate that the water distribution changes until the number of drops exceeds approximately 20×10^3. This is the number of drops used in the random drop investigations discussed earlier.

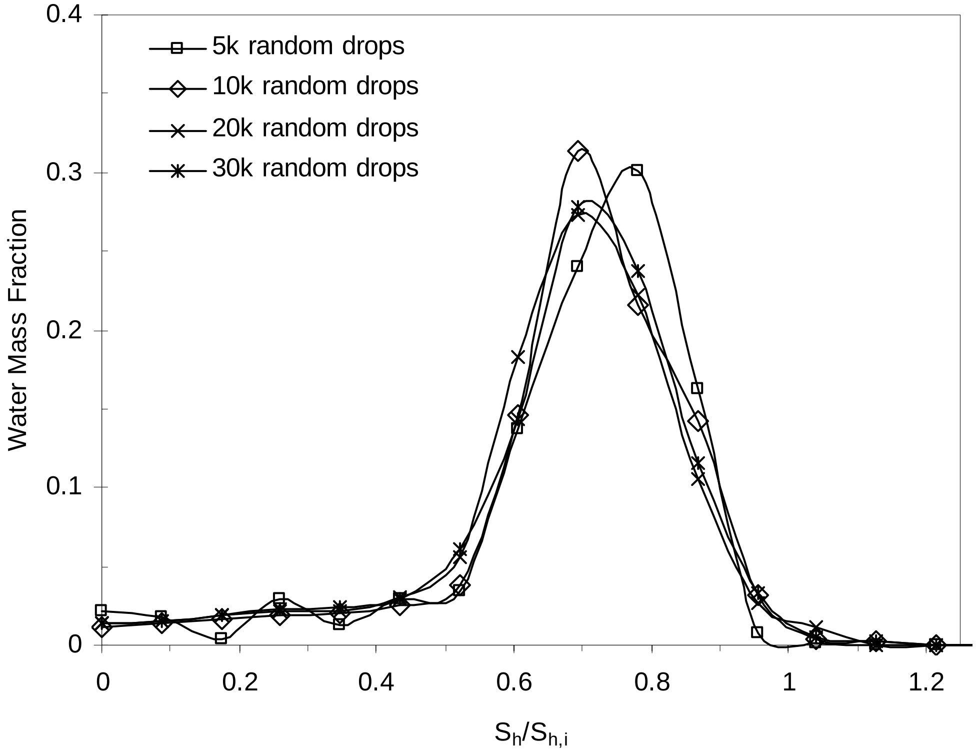

Figure 132. Comparison of predicted water distributions using various numbers of randomly generated drops. Results shown for 6 mm orifice with 90 degree strike plate operating at 0.379 L/s (6 gpm).

In summary, a simple trajectory model was used to predict the water flux from two representative sprinkler operating conditions (0.379 L/s of water through 4 mm and 6 mm diameter orifice sprinklers with 90 degree strike plates). There was good agreement between water flux predictions using actual drop data from the images, and those using randomly generated data from fits of the drop size and velocity distributions. For the sprinkler drop size distribution with a volume median diameter of approximately 1100 µm, there was good agreement between the predicted and measured water flux distributions. Fair agreement was found between the predicted and measured water flux distributions for the sprinkler drop size distribution with a volume median diameter of approximately 450 µm. The reduced agreement for small drop sizes appears to be caused by entrainment effects. For the two operating conditions investigated, a transition occurs between volume median drop sizes of approximately 450 μm to 1100 μm, where the effects of entrainment become small and may be neglected. This transition region may differ for sprinklers with other strike plate angles due to the change in entrainment as a function of strike plate angle.

Since the entrainment effects diminish as the strike plate angle increases, the trajectory calculations should yield better agreement for the water flux distributions from real sprinklers, where strike plate angles are typically >120 degrees. In addition, drop sizes from real sprinklers tend to be larger, so good agreement with the trajectory model is expected where the droplets are not interacting with a fire or fire plume. The results also suggest that for cases where entrainment may be neglected, the scaling concepts and three dimensionless parameters developed in the scaling section are valid, allowing sprinkler behavior to be investigated at reduced scale.

Good results were obtained when the droplets were assumed to start at the sprinkler (0,0) and at the speed of the water exiting the sprinkler, suggesting that the sheet breakup region and mechanism can be ignored. In addition, a simple trajectory model can provide valuable data if the drop sizes and velocities for the sprinkler are known. For a real sprinkler, the PTVI measurement technique could determine the droplet sizes and velocities with approximately 4 images of the sprinkler spray region.

CHAPTER 7

CONCLUSIONS

The work detailed in this thesis accomplished three main objectives, consisting of the development of the PTVI method, measuring the sizes and velocities of droplets from axis-symmetric sprinklers, and comparing predicted and measured sprinkler water distributions. The PTVI method developed in this work has the ability to simultaneously measure the drop size and velocity of a two phase water droplet in air flow within a region of approximately 0.5 m by 0.5 m by 10 mm thick. Drop sizes from 200 μm to 3000 μm in diameter were measured, with uncertainties of ±46 μm and ±227 μm respectively. The technique is general in nature and unobtrusive, allowing for its use in many disciplines where measurements of drop size and velocity are needed. In addition, the unobtrusive nature of the technique allows for measurements to be made in experiments where fires and sprays are interacting.

The PTVI technique was used to measure the droplet size distributions and velocity fields of axis-symmetric sprinklers with various orifice sizes and strike plate angles, operating at various flow rates. The range of operating conditions produced sprays with a wide range of droplet sizes and velocities. The resulting data from the experiments consists of droplet size, velocity, and position within the spray field. Having these three pieces of data for each droplet allows for the investigation of relationships between the size, velocity, and position of the drops. By integration of the drops within the spray field, and assuming symmetry, the total water flux within the spray was compared to the known flow rate of water through the sprinkler. For sprinklers operating in an axis-symmetric manner, there was good agreement between the calculated water flow rate and the measured water flow rate.

No single or combination of functions was found to characterize all of the drop size distributions, but the Rosin-Rammler distribution was useful for characterizing some of the sprinkler sprays. The distribution of droplet velocity angles, however, is well characterized by the normal distribution. It was found that the mean of the distribution is a function of the strike plate angle, but that the standard deviation of the distribution is constant for the sprinklers considered. In addition, the mean and standard deviation were not a function of sprinkler flow rate. The decrease in the mean deviation angle as the strike plate angle increases suggests that entrainment effects also decrease with increasing sprinkler strike plate angles.

The droplet data measured by the PTVI method, along with the distribution functions developed to represent the data, were input into a simple droplet trajectory model. This model assumes that the drops are solitary solid spheres subject to drag and gravity forces. Using the data from two representative sprinkler operating conditions (0.379 L/s of water through 4 mm and 6 mm diameter orifice sprinklers with 90 degree strike plates), the trajectory model predicts the water flux distribution on the floor below the sprinkler. For the sprinkler drop size distribution with a volume median diameter of approximately 1100 μm, there was good agreement between the predicted and measured water flux distributions. Fair agreement was found between the predicted and measured water flux distributions for the sprinkler drop size distribution with a volume median diameter of approximately 450 μm. The lower level of agreement for the smaller drops is a result of entrainment forcing the small droplets closer to the sprinkler axis of symmetry. For the two operating conditions investigated, a transition occurs between volume median drop sizes of approximately 450 μm to 1100 μm, where the effects of entrainment become small and may be neglected. This transition region may differ for sprinklers with other strike plate angles due to the change in entrainment as a function of strike plate angle.

It was found that the sprinkler water flux distributions can be modeled assuming the drops start at the sprinkler location, with initial speeds equal to that of the water exiting the sprinkler orifice. This is an important finding for fire modelers because it indicates that the virtual origin of the sprinkler spray is located at the sprinkler orifice. It also simplifies the modeling of the sprinkler since the initial speed can be calculated from the sprinkler flow rate, and the sprinkler can be treated as a point source thereby eliminating the need for considering sheet breakup mechanisms. In addition, the initial velocity angle of the sprinkler droplets can be derived from the normal distribution, and the initial drop size from the Rosin–Rammler distribution or a function known to represent the drop size distribution.

Since the entrainment effects diminish as the strike plate angle increases, the trajectory calculations should yield better agreement for the water flux distributions from real sprinklers, where strike plate angles are typically >120 degrees. In addition, drop sizes from real sprinklers tend to be larger, so good agreement with the trajectory model is expected where the droplets are not interacting with a fire or fire plume. For a real sprinkler, PTVI could be used to determine the necessary drop size and velocity distributions with as little as 4 photos.

The scaling analysis is partially confirmed by the sprinkler and water distribution measurements. Scaling is more accurate if a more detailed expression for C_D is included rather than a simple line fit for $1<Re<500$, as demonstrated by the trajectory model. The scaling of the sprinkler can be used along with the droplet angular distribution functions to change initial droplet conditions. The trajectory scaling can be used to determine the water distribution, with the input modified to get the desired water distribution. When combined, these two scaling methods can provide insight into improvements in sprinkler water distribution patterns, thereby improving the suppression efficiency of the sprinkler system.

APPENDICES

APPENDIX A

Laser Sheet Profiles

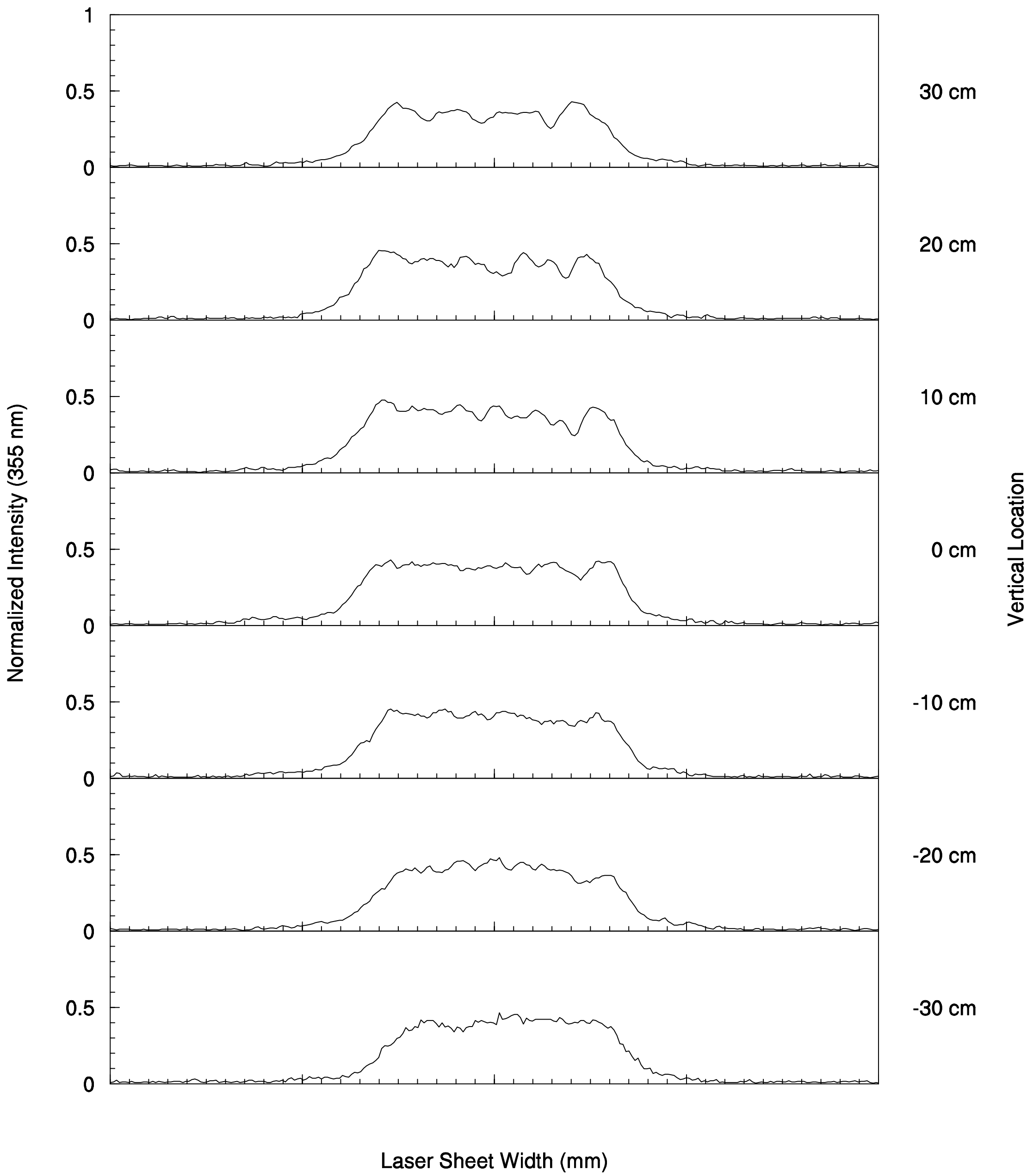

Figure A-1. Laser sheet power profile measured at the near edge of the droplet measurement region. Laser power is 4.78 W at 355 nm. Beam sheet thickness is approximately 13.5 mm over the vertical range of 0.6 m.

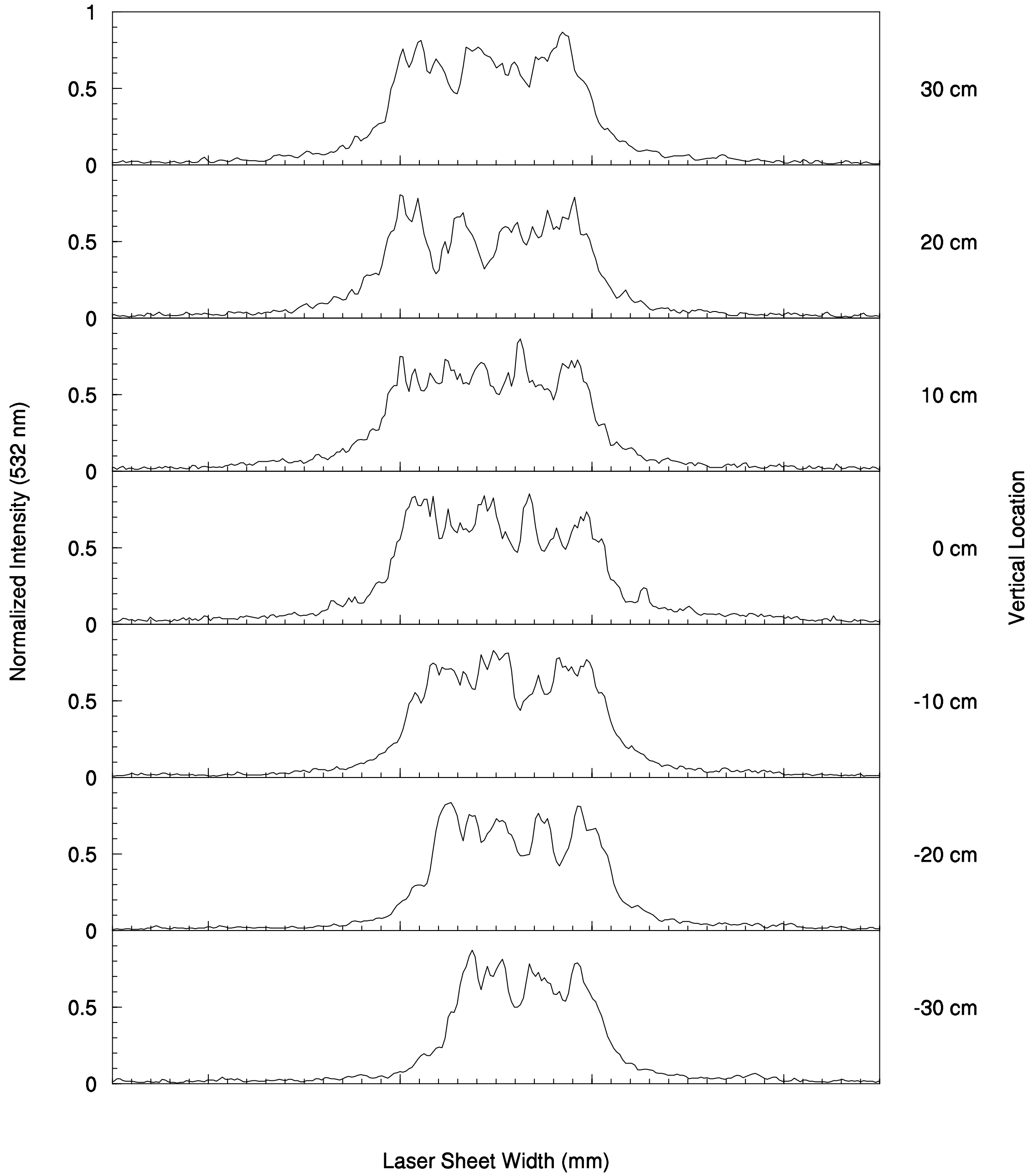

Figure A-2. Laser sheet power profile measured at the near edge of the droplet measurement region. Laser power is 5.60 W at 532 nm. Beam sheet thickness is approximately 10.0 mm over the vertical range of 0.6 m.

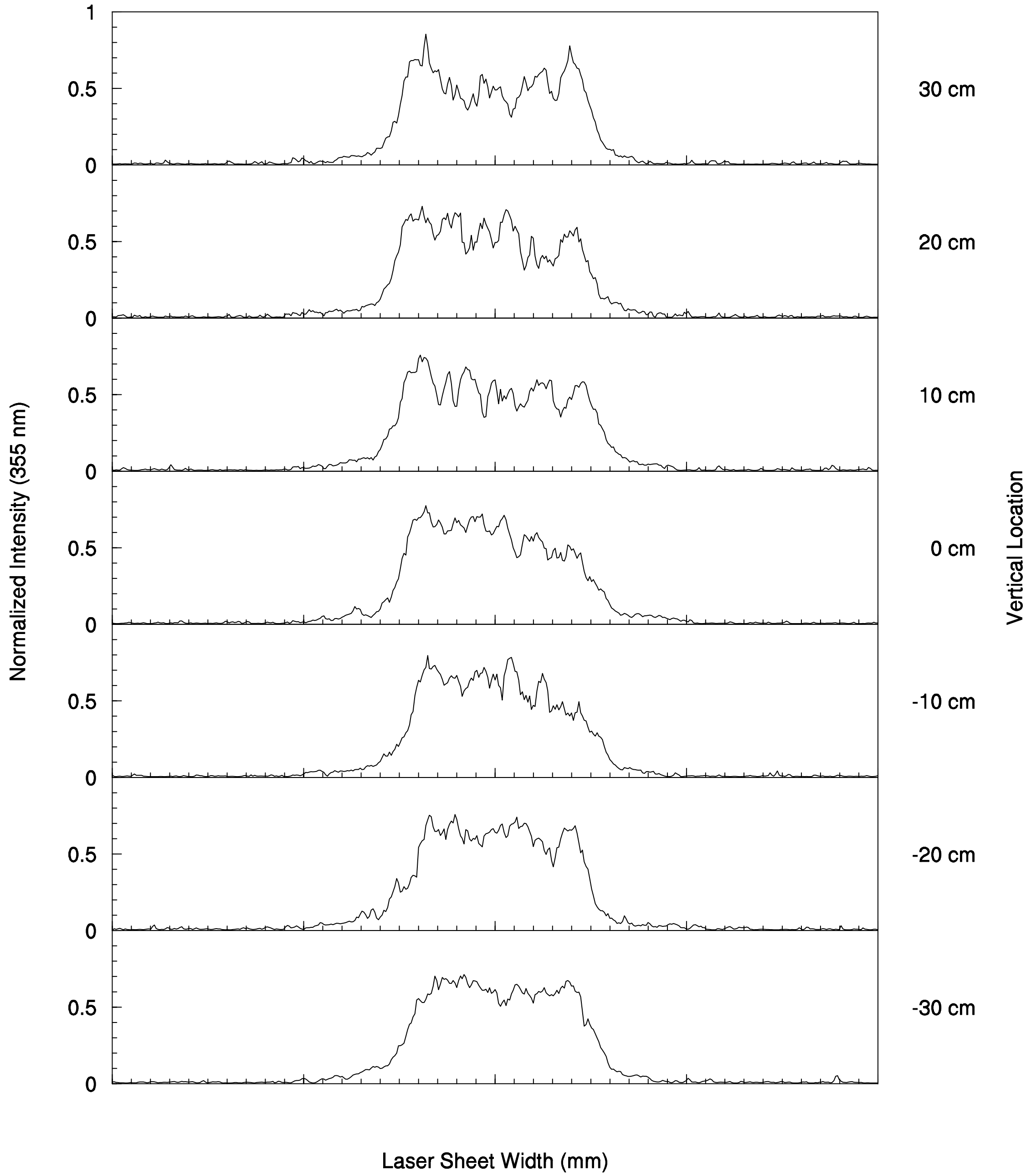

Figure A-3. Laser sheet power profile measured at the near edge of the droplet measurement region. Laser power is 4.00 W at 355 nm. 8 mm slit is installed after sheet forming optic. Beam sheet thickness is approximately 10.5 mm over the vertical range of 0.6 m.

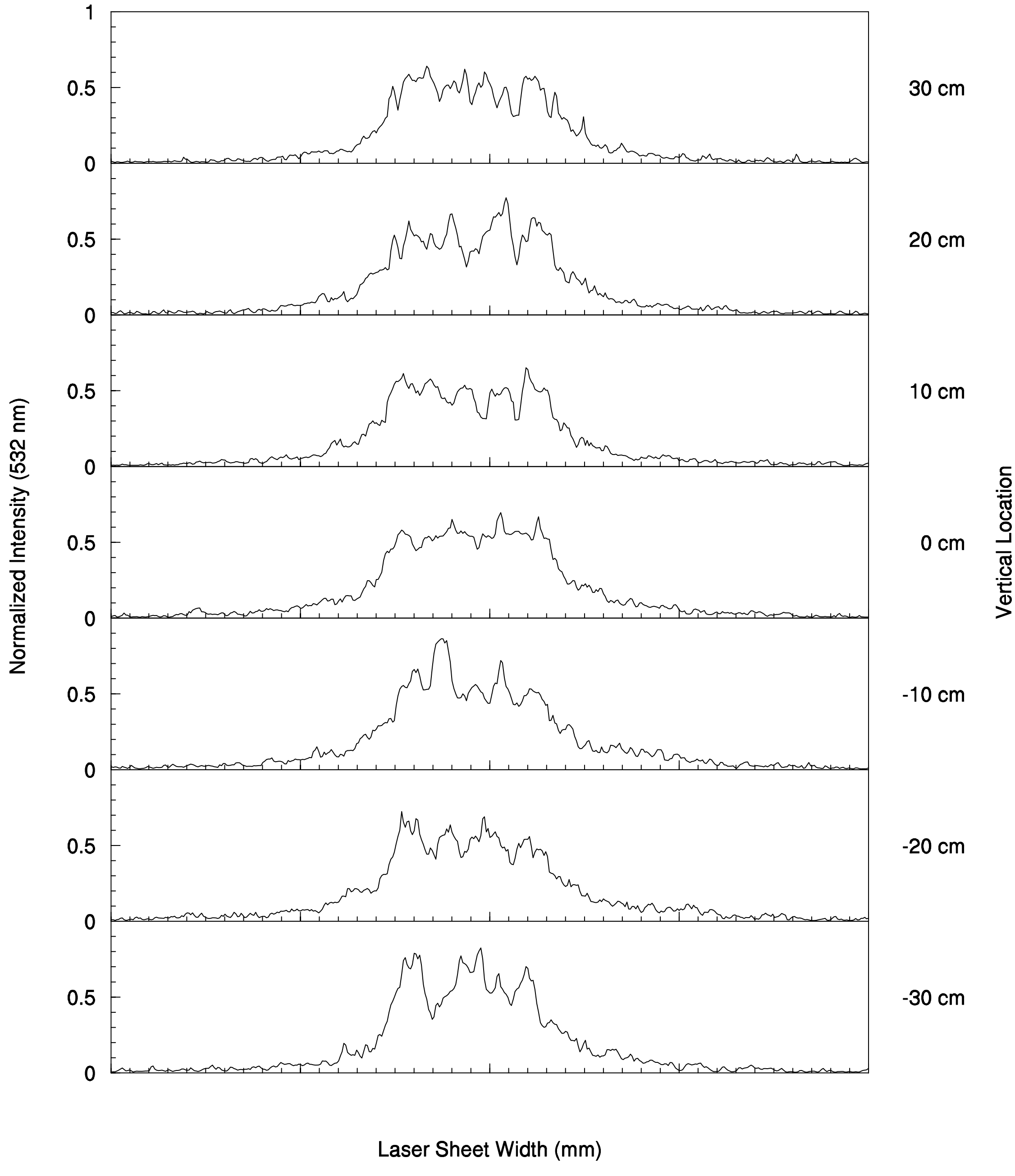

Figure A-4. Laser sheet power profile measured at the near edge of the droplet measurement region. Laser power is 7.20 W at 532 nm. 8 mm slit is installed after sheet forming optic. Beam sheet thickness is approximately 10.0 mm over the vertical range of 0.6 m.

APPENDIX B

Image Analysis Macro User's Guide

How to use "Macro216"?

By Kazuki Shiozawa

Macro216 is an Image-Pro Basic program which analyses a sprinkler image and reports the data such as the velocities, the positions, and the diameters of the droplets in the image. This manual is focused on the usage of the Macro216, and explains three basic steps.

Step 1: Set Up

First, you need to edit the Macro a little bit. Launch the Image-Pro and open up the image you want to analyze. Click **Macro** from the menu bar, go to **Macro…** and click **Change**. Select the Macro you want (in this case, Macro216) and hit **Edit**. Click the box called "Proc:" at the upper right corner of the window, and choose **"Execute"**. You'll see the following window.

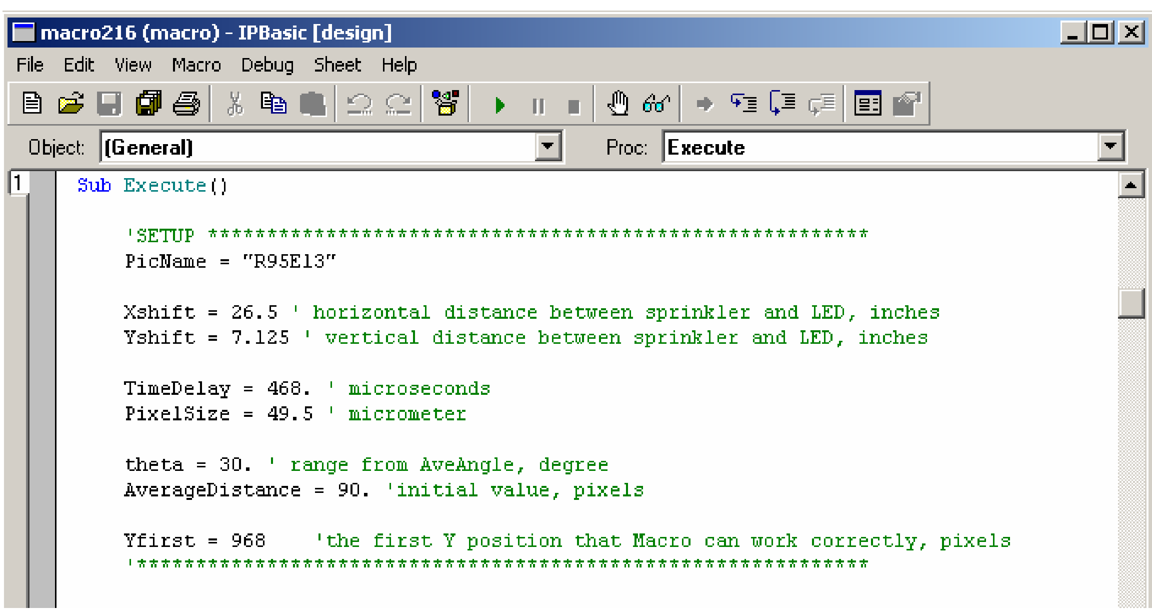

Now you need to set up the values in the window appropriately for your image. PicName is the name of your image. It can't be more than 15 characters unless you change the string size.

Xshift and Yshift are the horizontal and vertical distances between the LED and the sprinkler. Make sure you use the correct units.

Input TimeDelay and PixelSize, as appropriate for your image.

"AverageDistance" is the initial average value of the distance between all the droplet pairs. This value doesn't have to be accurate since the Macro automatically calculates a new average distance and replaces it.

We suggest setting the theta value between 20 and 30 degrees.

"Yfirst" is the vertical position where the Macro can first measure the droplets correctly. Later when you correct the error of the Macro, you don't have to do the drops above the "Yfirst" line. Therefore, you might not want to trust the data above this line (see Figure below).

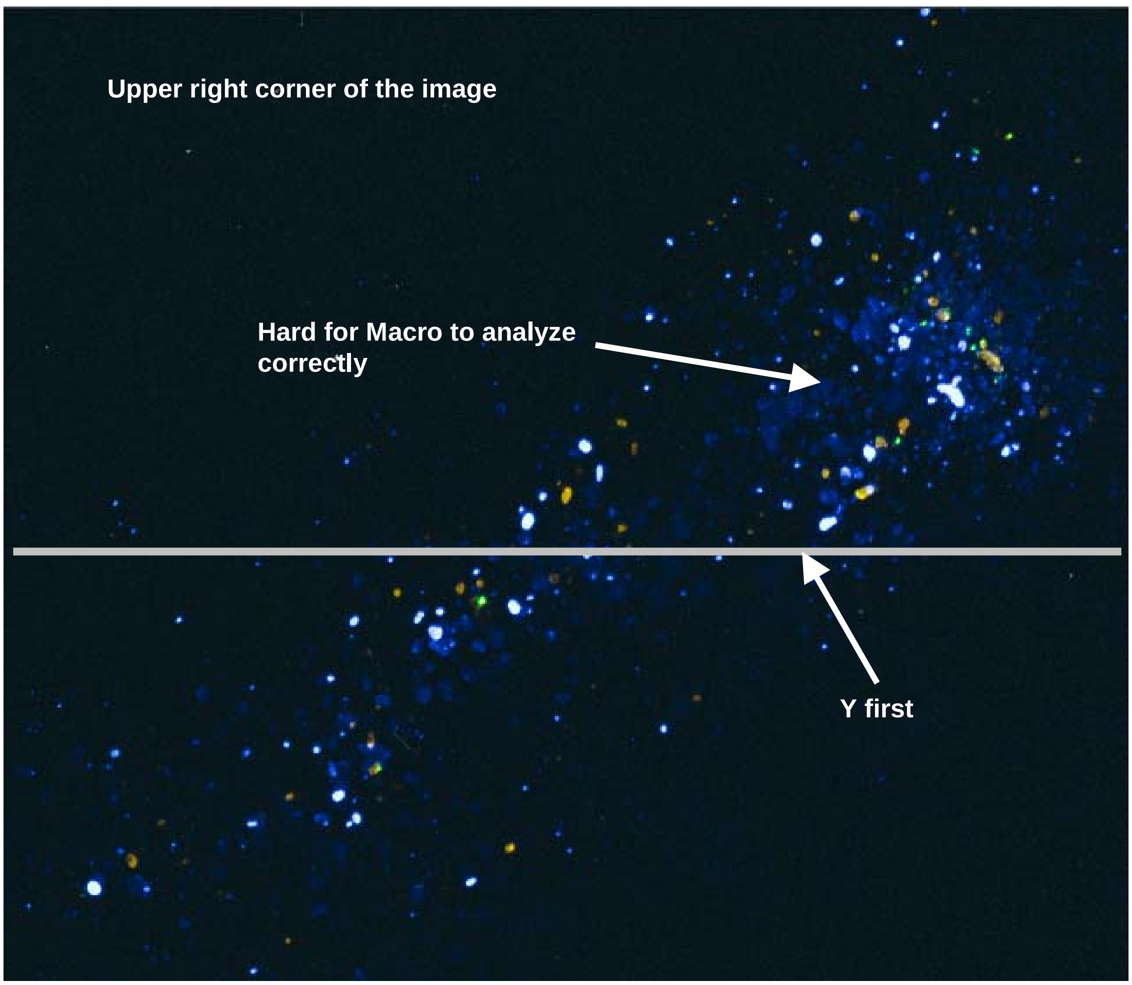

Step 2: Execute Macro

Now you're ready to execute the Macro! Go to **Macro** in the menu bar and select **Macro…**. Select "**Execute**" in the window and click "**Run**" (or simply go to **Macro** and choose "**Execute**").

Wait until the Macro finishes it up. It might take a couple of minutes, depending on the size of your image. In the most cases, the data you'll get is too large to fit in the output window. Therefore, Macro saves the data as a notepad, in the temp file in G directory (unless you change the destination). The file called "FileName velocity" gives you the velocity data, and the file called "FileName size" gives you the size data of the droplets. Following window shows an example of the velocity data.

Output Window

File Edit

```
* R95E13
* Origin Sprinkler
* Xsize(pixels)  2671
* Ysize  1951
* XLED(pixels)  0
* YLED  0
* Xshift(inches)  26.5
* Yshift  7.125
* TimeDelay(microseconds)  468
* OnePixel(micron)  49.5
* Theta(degree)  30
* FirstY(pixels)  968
* FirstY(m) -0.228891
Y index   X(meter)     Y(meter)     Velocity(m/s)   Diameter(micron) Angle(degree)   Xblue(meter)   Yblue
  1     -0.5698729   -0.1829567    5.934461     940.8403     60.95034    -0.5710868    -0.1836309
  2     -0.6011589   -0.1828638    4.956608     607.7565     59.46748    -0.602158     -0.183453
  3     -0.5565957   -0.1830306    5.296614     604.4528     61.27459    -0.5576826    -0.1836262
  4     -0.6586345   -0.1838978    1.846015     290.7692     56.96971    -0.6589966    -0.1841333
  5     -0.5726048   -0.1843219    4.714899     938.9828     57.17779    -0.573532     -0.1849199
  6     -0.6715039   -0.1853221    5.547597     538.5524     61.77142    -0.6726477    -0.1859361
  7     -0.5580049   -0.1858121    5.575756     490.7639     57.15926    -0.559101     -0.1865197
  8     -0.5562663   -0.186821     6.272614     859.9572     57.11906    -0.557499     -0.1876179
  9     -0.5576414   -0.1871124    6.084856     484.6093     56.98772    -0.5588354    -0.1878882
  10    -0.6304247   -0.1875377    5.601316     568.2555     61.33417    -0.6315748    -0.1881664
  11    -0.6573269   -0.1888258    3.589856     388.442      60.85493    -0.6580606    -0.1892349
  12    -0.6187643   -0.1892791    4.671064     364.6943     60.04105    -0.6197113    -0.189825
  13    -0.6082432   -0.1910073    5.732507     824.051      61.05069    -0.609417     -0.1916566
  14    -0.5908565   -0.1914188    5.824704     1014.627     59.3829     -0.5920295    -0.192113
  15    -0.5976875   -0.191184     4.237615     321.1985     57.57347    -0.5985245    -0.1917157
  16    -0.5856507   -0.191785     5.697614     545.4631     58.8492     -0.5867917    -0.1924746
  17    -0.5579356   -0.1916395    4.544407     277.2285     57.72782    -0.5588347    -0.1922073
  18    -0.5707985   -0.1919759    5.122401     374.0853     56.73045    -0.5718007    -0.1926335
  28    No match   X:  1.291667   Y:  460.9583   D:  5.872275   X,Ysprinkler(m):-0.673036062503815  -0.2037924375
  34    No match   X:  17.68   Y:  533.2   D:  7.211102   X,Ysprinkler(m):-0.67222483996582  -0.207368400390625
```

The output data gives you all the setup data used to analyze the image, followed by the droplet data.

Y index is the number on the yellow droplets in the window called "FileName Y" on your screen.

X and Y indicate the position of the droplet. The origin is the location of the sprinkler, and all the values are negative for our convenience.

X blue and Y blue indicate the location of the blue droplets. You might need this data for further analysis.

At the end of the data, Macro displays the droplets with no matches, and outputs the diameter and the X, Y positions of the droplets. It also gives you the X, Y positions of the yellow droplets from the sprinkler (X,Ysprinkler). Later you might use this information to check those "No match" droplets.

Troubles?

Case 1: Image-Pro shuts down by itself!

Solution: Simply re-start the Image-Pro, and try the Macro again. This is not a severe problem.

Case 2: The output window displays nothing!

Solution: Don't worry, just go to the temp file in G directory and find your data.

Case 3: There are too many "No match" droplets!

Solution 1: Are you looking at the output window of the Image-Pro? Go to the temp file of G directory and find the stored data.

Solution 2: Look at the window titled "FileName Y", and if it's not black and white, that means the Macro didn't work properly. After re-start the Image-Pro try the Macro again.

Solution 3: Look carefully where those "No match" droplets are. The image might contain a plastic bar used to hold the film when the image was scanned, and the plastic bar appears to be red, which is recognized as many yellow droplets by the Macro. You might want to trim your image and get rid of the plastic bar. Usually, they are at the edge of your image, so it might be hard to recognize them at first.

Solution 4: Your image might be a little too big. If your image is more than 270MB, the Macro might not work properly. If this is the case, try to trim your image so that the size goes down below 270MB. Usually such a big image has an unnecessary part (e.g., dark background with no droplets at the edges).

Solution 5: Sometimes the counting function in Image-Pro doesn't work for a certain image, and the reason hasn't been found. In this case, the output data is mostly "No match". You might just give up and analyze other images instead, or you can cut off the image and let the Macro analyze the partial image. You can tell the Macro is having a problem when it's counting all the droplets, because the display of counting is abnormal (see the following figure: top part is not counted properly).

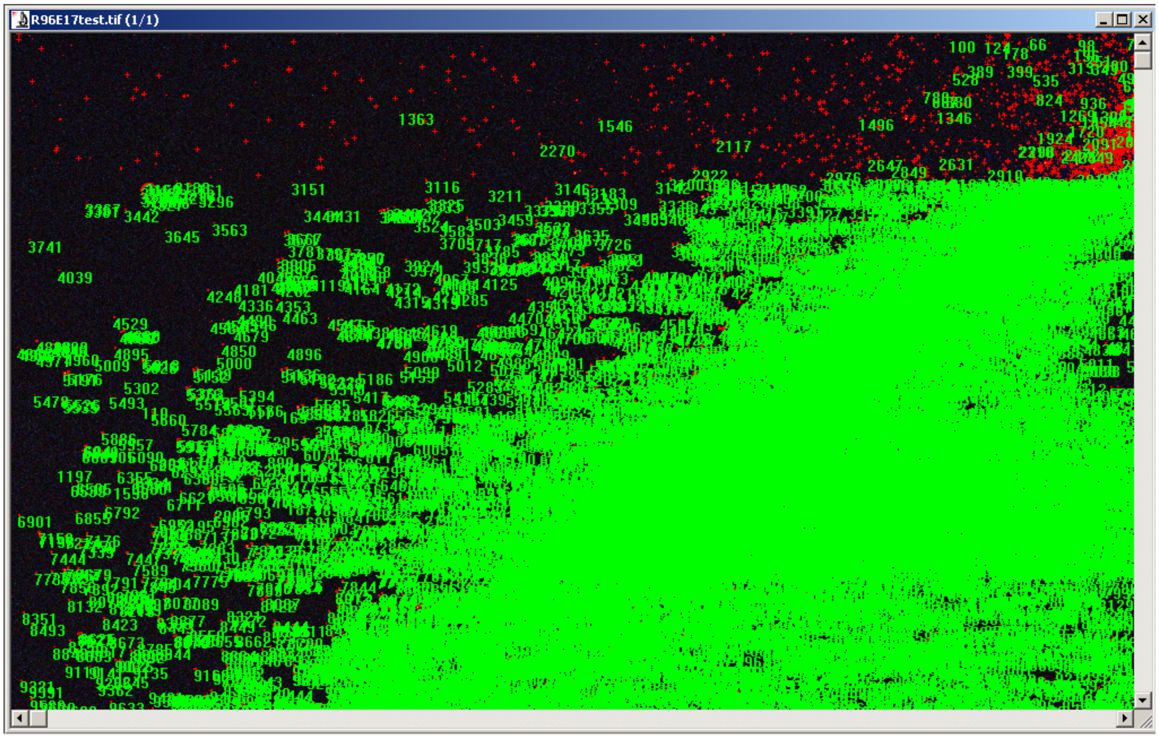

Step 3: Correct the output

After you run the Macro, you need to look at the original picture and find the overlapping droplets or the weird shaped droplets, because the Macro might have not analyzed them correctly. Here we illustrate several general cases, so that you'll get the basic idea of how to handle the errors of the Macro.

Case 1: A yellow drop and a blue droplet are overlapping

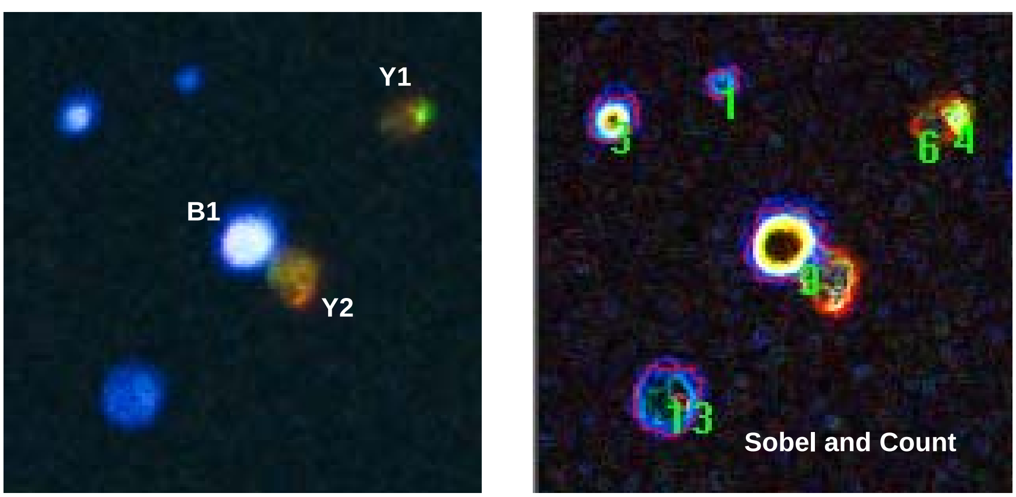

In the case of above, you see Y1 goes with B1, but the Macro actually outputs "No match" for Y1. This is because B1 is too close to Y2, so when the Macro first counts all the droplets, it counts B1 and Y2 together, and later the Macro treat this combined droplets as a yellow droplets. So there is no such a blue droplet as “B1”, and Y1 can’t find a match.

If B1 didn’t get erased, Y1 would have a match, but the diameter would be too big because B1 and Y2 are still combined. In this case measure the diameter of B1 by hand and replace the diameter for Y1.

Case 2: Two blue (or yellow) droplets are too close to each other

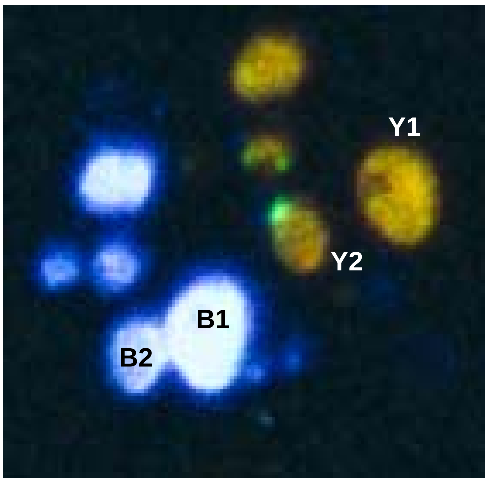

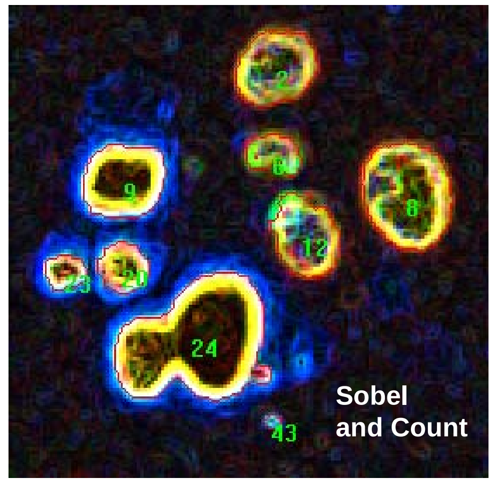

In the case of the above pictures, it looks like Y1 goes with B1 and Y2 goes with B2. But as you can imagine, B1 and B2 are counted together (24 in the right-hand side picture) and either one of Y1 or Y2 would take this combined blue droplet. In the worst case, if the combined blue droplets have more than the aspect ratio of 2, both B1 and B2 disappear and both Y1 and Y2 becomes “No match” (or Y1 might take the tiny droplet right next to B1).

Case 3: A blue droplet has a weird shape

Aspect Ratios

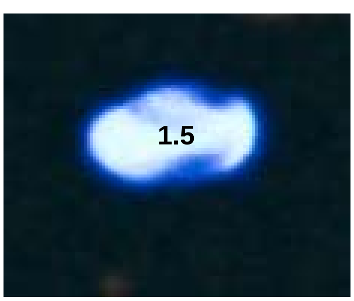

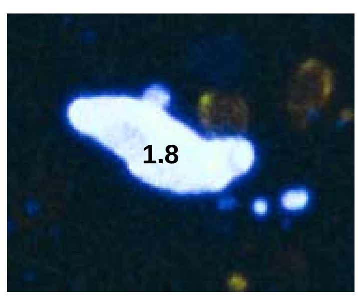

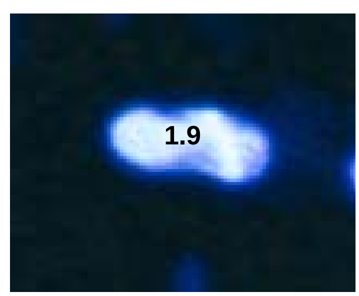

The above three images are weird shaped blue droplets. Their aspect ratios are less than 2 so they are not going to be a problem. If the aspect ratio was more than 2, however, the Macro will erase them as garbage, and some yellow droplets would become "No match".

You don't have to worry about weird looking yellow droplets, since the Macro won't erase them even though they have the aspect ratio of more than 2.

So… how should I correct the data?

If you find images like the examples above, you first have to find where they are in the window titled "FileName Y", and get their Y indexes. Make sure the Macro handled them correctly. If not, you need to measure the distance between the right droplet pairs, the angle between them, and the diameter of the blue droplet. Go to **Measure** and **Line Profile…** use the line profile and record the approximated values.

Next, open the output file and go to the bottom of the data set, and find the Y index of the droplet that you want to correct.

```
11   -0.6573269   -0.1888258    3.589856    388.442    60.85493   -0.6580606   -0.1892349
12   -0.6187643   -0.1892791    4.671064    364.6943   60.04105   -0.6197113   -0.189825
13   -0.6082432   -0.1910073    5.732507    824.051    61.05069   -0.609417    -0.1916566
14   -0.5908565   -0.1914188    5.824704    1014.627   59.3829    -0.5920295   -0.192113
15   -0.5976875   -0.191184     4.237615    321.1985   57.57347   -0.5985245   -0.1917157
16   -0.5856507   -0.191785     5.697614    545.4631   58.8492    -0.5867917   -0.1924746
17   -0.5579356   -0.1916395    4.544407    277.2285   57.72782   -0.5588347   -0.1922073
18   -0.5707985   -0.1919759    5.122401    374.0853   56.73045   -0.5718007   -0.1926335
28   No match   X:  1.291667   Y:  460.9583   D:  5.872275   X,Ysprinkler(m):-0.673036062503815  -0.2037924375
34   No match   X:  17.68   Y:  533.2   D:  7.211102   X,Ysprinkler(m):-0.67222483996582  -0.207368400390625
```

Let's suppose in this case, the one that you want to fix is Y index 34. Y index 34 shows X, Y, and D after "No match". These are X, Y locations (which corresponds to the image) and the diameter of the yellow droplet. These data might help you to find where the yellow droplet is in the image. Following "X, Ysprinkler" is the location of the yellow droplet from the sprinkler, and you will be using these values later.

Go ahead and erase "No match", X, Y, D, and "X,Ysprinkler(m):" (highlighted in the figure above), and add the data you measured by hand. Make sure you put the velocity, diameter, and angle in order after the X, Y positions from the sprinkler. The corrected output file should look like following (the highlighted values are the data you inputted):

```
11   -0.6573269   -0.1888258   3.589856   388.442     60.85493   -0.6580606   -0.1892349
12   -0.6187643   -0.1892791   4.671064   364.6943    60.04105   -0.6197113   -0.189825
13   -0.6082432   -0.1910073   5.732507   824.051     61.05069   -0.609417    -0.1916566
14   -0.5908565   -0.1914188   5.824704   1014.627    59.3829    -0.5920295   -0.192113
15   -0.5976875   -0.191184    4.237615   321.1985    57.57347   -0.5985245   -0.1917157
16   -0.5856507   -0.191785    5.697614   545.4631    58.8492    -0.5867917   -0.1924746
17   -0.5579356   -0.1916395   4.544407   277.2285    57.72782   -0.5588347   -0.1922073
18   -0.5707985   -0.1919759   5.122401   374.0853    56.73045   -0.5718007   -0.1926335
28   No match   X:  1.291667   Y:  460.9583   D:  5.872275   X,Ysprinkler(m):-0.673036062503815  -0.2037924375
34   -0.67222483996582  -0.207368400390625  6.5  1000  60
```

There should be at least one space between values you input. You don’t have to input Xblue and Yblue, these should be exact values and you can’t do it by hand.

Don’t forget to add the missing blue droplets in the lists of blue droplets in the size data file.

After you finish taking care of all the overlapping droplets and any other problems, erase the remaining “No match” droplets.

It sounds like a difficult job, but each image has only a few of those overlapping droplets below the “Yfirst” line. In addition, the measurements by hand don’t need to be very accurate.

Finally, when you transfer the data files to Excel, use “space” as a delimiter and don’t import the first two columns (you don’t need Y indexes any more).

APPENDIX C

Image Analysis Macro Reference Guide

What does “Macro216” do?

by Kazuki Shiozawa

Macro216 is an Image-Pro Basic program which analyzes a sprinkler image and obtains data such as the velocities, diameters, and positions of the droplets in the image. Macro216 has several sub functions in it, and the purpose of this report is to explain all the sub functions and the problems that the programmer experienced during its development.

SUMMARY

Macro216 analyzes a sprinkler image using the following basic steps.

Step 1: Macro first applies the sobel filter to the original image, and takes the data of all the droplets which have more than 78 (20,000 for 16bit images) intensity (HSI).

Step 2: Macro finds all the yellow droplets in the image, subtracts the yellow droplets from all the droplets measured in step 1, and obtains the blue droplets.

Step 3: Macro matches up the blue and yellow droplets and calculates the parameters of the droplet pairs.

Step 4: Macro outputs and saves all the requested droplet information.

DESCRIPTION OF THE SUB FUNCTIONS IN MACRO216

Sub Function 1: Execute

The sub function “Execute” merely executes all the following sub functions at once. It actually iterates the sub function called “GetVelocity” nine times to obtain the optimum average distance between the droplet pairs (see the sub functions “GetYellow” and “GetVelocity” for more info). Also, the users can change all the set up values in this sub function.

Sub Function 2: GetAll

This sub function counts all the droplets in the image, measures the sizes and the X, Y positions of the droplets.

The sub function "GetAll" first applies the sobel filter to the image. Figure 2.1 shows the droplet images before and after the sobel filter, and the line profiles (HSI) across the center of the blue droplet in each image. The sobel filter result represents the slope of the intensity; i.e., the maximum value of the line profile after the sobel filter corresponds to the biggest slope of the line profile before the filter. The purpose of the sobel filter is to get the maximum slope of the intensity profile to determine the size of the droplet.

Figure 2.1: Applying the sobel filter to measure the diameters of the droplets

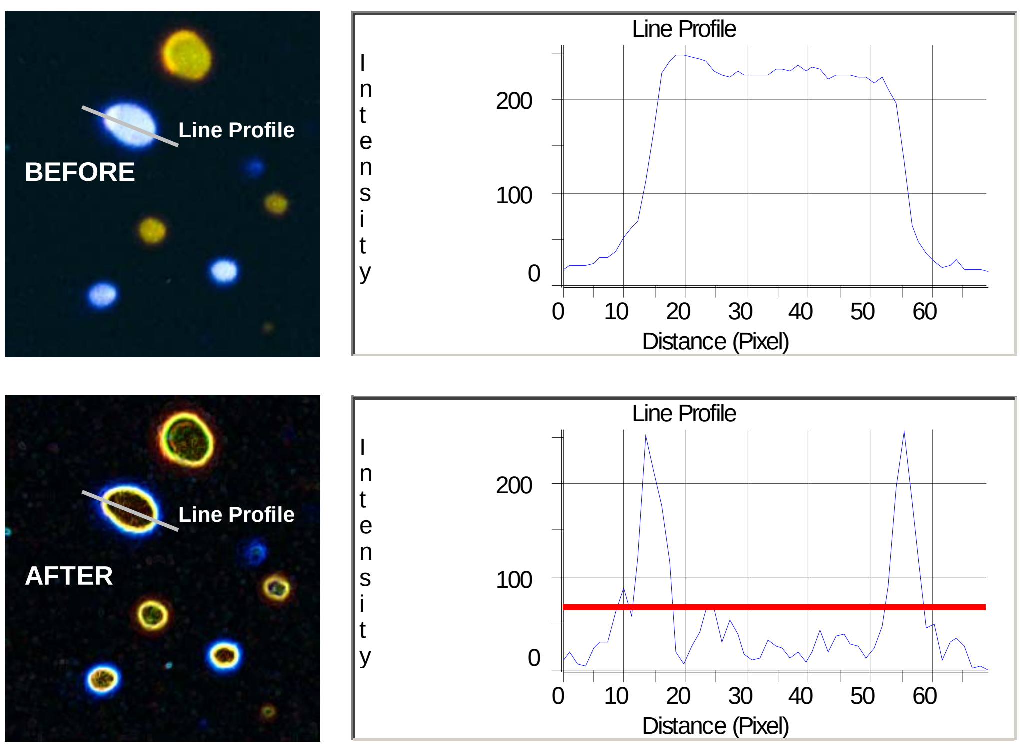

Although Image-Pro has the functions which measure the X and Y positions and the mean diameters of all the droplets, the function for the mean diameter measures the mean diameters of the outer walls of the droplets. Therefore, "GetAll" sub function measures the inner hole area of each droplet, calculates the inner diameter, and takes the average of the inner and outer diameters.

When "GetAll" measures the outer diameter and the hole area, the Macro sets up the HSI intensity range 78 (20,000 for 16bit images) and higher as the heavy red line in

Figure 2.1. This threshold allows us to eliminate the droplets that are out of the laser sheet.

In addition, “GetAll” measures the aspect ratio of each droplet. The aspect ratio is the ratio of the major axis and the minor axis of a droplet, and if the aspect ratio of the droplet is more than 2, “GetAll” excludes it as garbage. This allows us to eliminate most of the droplets out of the laser sheet, dust, or any other unknown materials in the image. Figure 2.2 shows some examples of “garbage” in a sprinkler image. The left-hand side pictures shows the droplets out of the laser sheet, and the right-hand side pictures show a piece of dust on the film. Although “GetAll” counted some parts of the garbage, it eliminated them later because they have a high aspect ratios.

Figure 2.2: Garbage and the aspect ratio

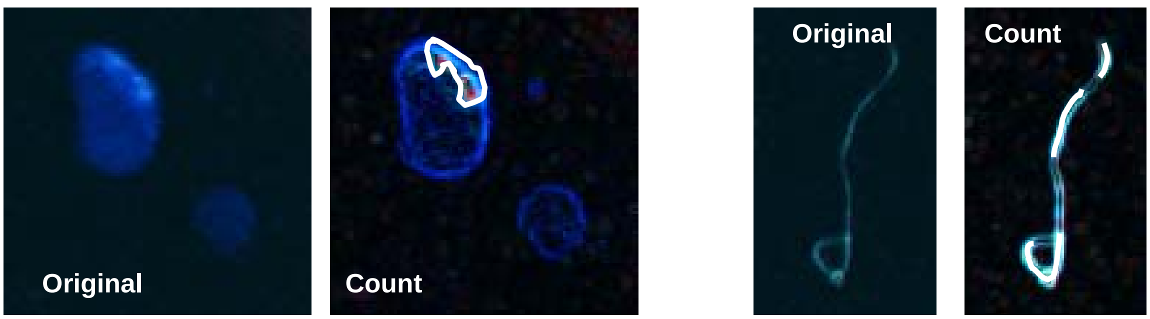

Sub Function 3: GetYellow

The sub function called “GetYellow” finds all the yellow droplets from the original image, and measures their X, Y positions and diameters.

Figure 3.1 shows the line profile of a blue droplet and a yellow droplet in hue mode. The yellow droplet has a much lower hue component compared to the blue droplet and the background, and this is how “GetYellow” extracts the yellow droplets from the original image, using segmentation.

Figure 3.1: Hue finds the yellow droplets

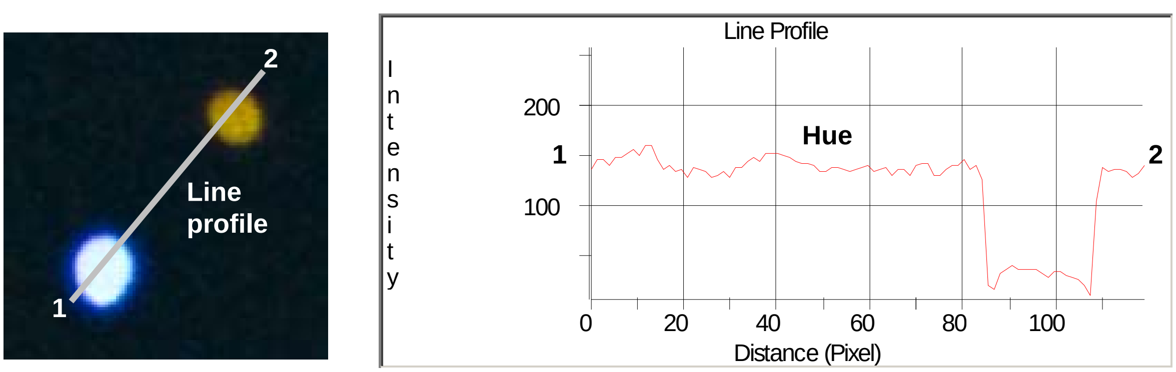

"GetYellow" now measures the X, Y positions and the diameters of the yellow droplets. The diameter measurement is done roughly because the diameters of yellow droplets will not be used in the final diameter results.

Next, "GetYellow" subtracts the yellow droplets from all the droplets measured in "GetAll", and separates the blue and yellow droplets.

Finally, "GetYellow" divides all the yellow droplets into three groups (see Figure 3.2), so that later on the Macro can measure the average distance between droplet pairs in each group region. Typically the droplets at the bottom of the image have shorter average distances than those at the top of the image.

Figure 3.2: The yellow drops divided into three groups

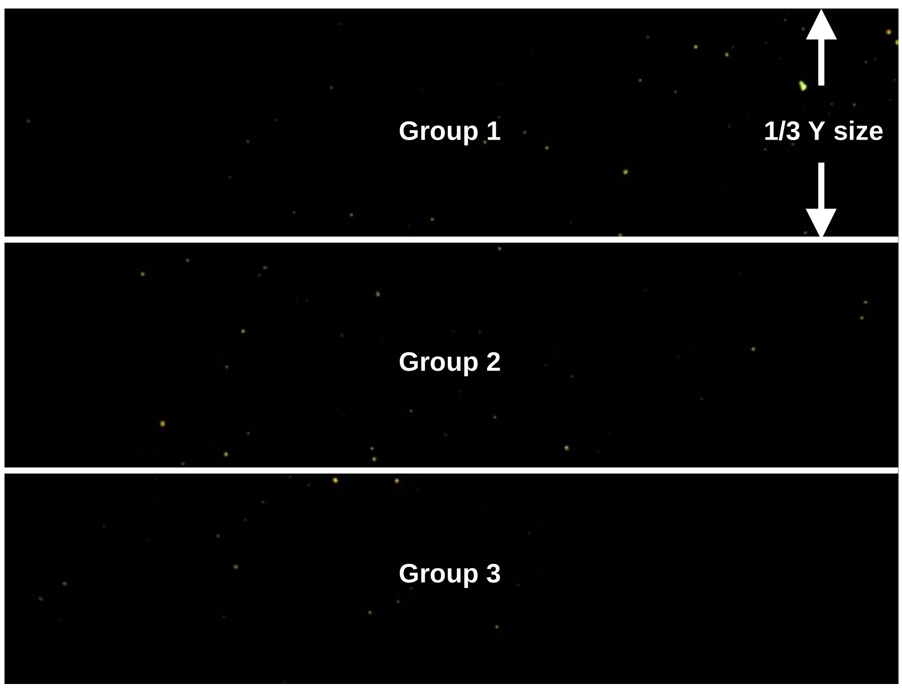

Sub Function 4: GetVelocity

The sub function called "GetVelocity" finds the pairs of the blue and yellow droplets, and calculates their average X, Y positions, velocities, diameters, and angles in relation to the South Pole.

There are 5 conditions for a blue droplet to be matched with a yellow droplet. Figure 4.1 shows an example of matching and some terms which are used in the "GetVelocity" sub function. The following are descriptions of terms and the conditions:

Y angle: This angle is the angle between the sprinkler and each yellow droplet. This value gives the approximate angle that a yellow droplet has with the corresponding blue droplet.

BY angle: This is the angle between a yellow droplet and a blue droplet.

Theta (θ): This is the upper and lower range from Y angle.

Figure 4.1: The terms used in "GetVelocity"

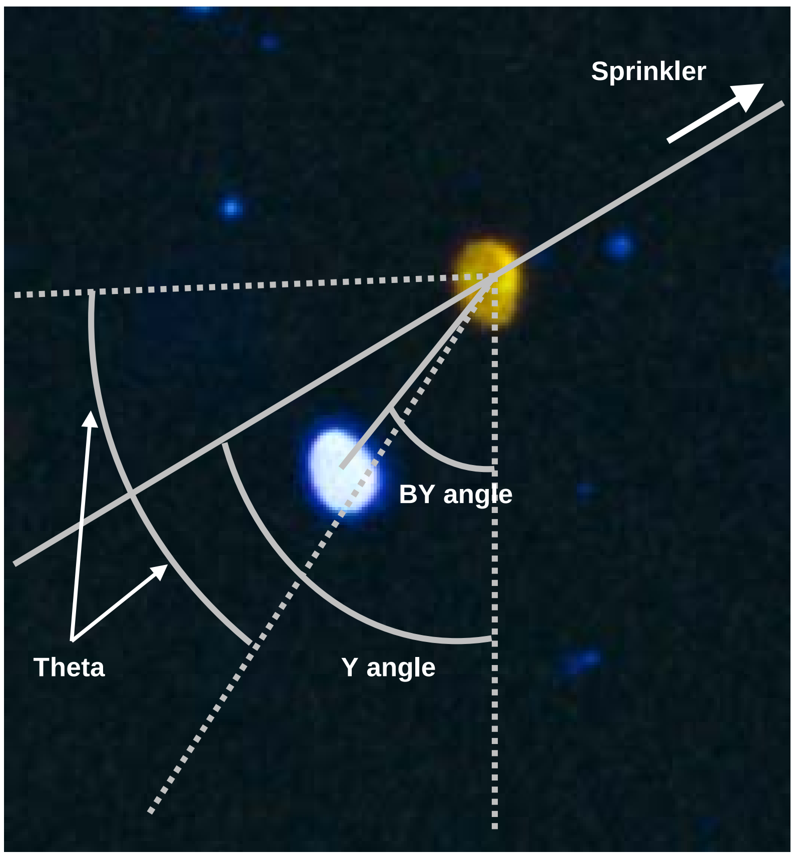

Condition 1: If the distance between the blue and yellow droplets is reasonable, condition 1 becomes True.

Condition 2: "GetVelocity" calculates an angle between the blue and yellow droplets (BY angle), and if the angle is within the range (Y angle - θ < BY angle < Y angle + θ), condition 2 becomes True (see Figure 4.1).

Condition 3: If the sizes of the yellow and blue droplets are reasonable, condition 3 becomes True.

Condition 4: If the yellow droplet already had a match, "GetVelocity" compares the angle and the distance of the old match and the new match, and if the new match is more appropriate, condition 4 becomes True. If the yellow droplet didn't have a match yet, condition 4 becomes True.

Condition 5: If a blue droplet was already taken by another yellow droplet, "GetVelocity" compares the angle and the distance of the old pairs and the new pairs, and if the new pair is more appropriate, "GetVelocity" cancels the old pair and condition 5 becomes True. If the blue droplet was not taken yet, condition 5 becomes True.

If all of the conditions above are satisfied, "GetVelocity" records the two matched droplets and their data, and calculates the average X, Y positions and the velocity. In addition, "GetVelocity" calculates the average distance of the droplet pairs in each group region (see Figure 3.2).

The "GetVelocity" sub function is iterated by the "Execute" sub function. Every time "GetVelocity" is executed, "Execute" clears all the data from the past, employs the new average distances from the previous iteration, and runs "GetVelocity" again to get better data. "GetVelocity" is iterated 3 times for each group region, which is enough to obtain the accurate value of the average distances.

Sub Function 5: Report

This sub function outputs and saves useful data obtained from the sub functions above, such as the average X, Y positions of the droplets, the velocities, the diameters, and the angles of the droplets. All the units are converted appropriately, and all the X, Y positions are adjusted to follow the coordinate system where the origin is the position of the sprinkler. After the data of the droplet pairs is output, "Report" outputs the yellow droplets with no matches. It gives the location and the diameter, so that the users can check those droplets.

PROBLEMS

The biggest problem with the current Macro is that it can't handle droplets that overlap other droplets. There is a way to solve this problem (but not completely) but it sacrifices the accuracy of the diameter measurement. Therefore, the analysis of those overlapping droplets must be done by hand. The percentage of overlapping droplets in the current work, however, is very small, although it depends on the particular image.

Another problem relating to the image analysis algorithm is the memory consumed by Image-Pro. After an image is closed, Image-Pro does not reallocate the memory. With large images, the memory quickly fills, leading to failure. The only way to clear the memory is to shut down and restart the Image-Pro software. In order to analyze 260 MB images, for example, the user must restart Image-Pro before analysis of each image.

APPENDIX D

Analysis Macros

1. Macro run within Image Pro Plus to analyze the calibration/verification images (macro216 calibration.scr):

```
' Name: Kazuki Shiozawa
' Dept: BFRL, NIST
' Date: May 13, 2002 -

Option Explicit

    'All (Blue and Yellow)
    Global Allnumber As Integer
    Global Allhole(12000) As Single
    Global Allxposition(12000) As Single
    Global Allyposition(12000) As Single
    Global AlloutD(12000) As Single
    Global Alldiameter(12000) As Single
    Global Allaspect(12000) As Single

    'Yellow
    global Mnumber As Integer 'M represents "maize"
    Global Mdiameter(2000) As Single
    Global Mxposition(2000) As Single
    Global Myposition(2000) As Single
    Global Mlist(2000) As Integer

    'final result
    Global PositionX(2000) As Single
    Global PositionY(2000) As Single
    Global Velocity(2000) As Single
    Global match(12000) As Single
    Global Diameter(2000) As Single
    Global Angle(2000) As Single
    Global SumDist As Single
    Global AveDist(3) As Single
    Global CountMatch As Integer
    Global Xblue As Single
    Global Yblue As Single

    'setups
    Global PicName As String * 12
    Global TimeDelay As Single
    Global PixelSize As Single
    Global theta As Single

    'iteration
    global i As Integer
```

```
    Global j As Integer
    Global k As Integer
    Global n As Integer
    Global z As Integer
    Global CountDown As Integer
    Global rememberK As Integer
    Global start As Integer

    'picture size, index6
    Global Xsize As Integer
    Global Ysize As Integer
    Global size(2) As Integer
    Global XLED As Integer
    Global YLED As Integer
    Global Xshift As Single
    Global Yshift As Single
    Global Xsprinkler As Single
    Global Ysprinkler As Single

    'temps
    Global Yangle As Single
    Global BYangle As Single
    global condition1 As Boolean
    global condition2 As Boolean
    Global condition3 As Boolean
    Global condition4 As Boolean
    Global condition5 As Boolean
    Global index As Integer
    Global distancebtw As Single
    Global AverageDistance As Single



Sub Execute()

    'SETUP *****************************************************
    PicName = "R92E04"
    XLED = 620 ' X position of LED, pixels
    YLED = 844 ' Y position of LED, pixels
    Xshift = 26.5 ' horizontal distance between sprinkler and LED, inches
    Yshift = 7.125 ' vertical distance between sprinkler and LED, inches

    TimeDelay = 609. ' microseconds
    PixelSize = 49.5 ' micrometer

    theta = 30.    ' range from AveAngle, degree
    AverageDistance = 60. 'initial value, pixels
    '**********************************************************

    For i = 0 To 2
        AveDist(i) = AverageDistance  'initiate
    Next i

    ret = ipdocget(getdocinfo,docsel_active,size(0)) 'get the size of the image
    Xsize = size(0)
    Ysize = size(1)
```

```
    Call GetAll()
    Call GetYellow()

End Sub

Sub GetAll()

    'getting all the droplets

    'sobel filtering
    ret = IpFltSobel()

    'range of selection
    ret = IpBlbSetAttr(BLOB_AUTORANGE, 0)
    ret = IpSegSetAttr(COLORMODEL, CM_HSI)
    ret = IpSegPreview(ALL_T_B)
    ret = IpSegSetRange(0, 0, 255)
    ret = IpSegSetRange(1, 0, 255)
    ret = IpSegSetRange(2, 78, 255)

    'select the parameters
    ret = IpBlbEnableMeas(BLBM_CENTRX, 1)
    ret = IpBlbEnableMeas(BLBM_CENTRY, 1)
    ret = IpBlbEnableMeas(BLBM_MEANFERRET, 1)
    ret = IpBlbEnableMeas(BLBM_HOLEAREA, 1)
    ret = IpBlbEnableMeas(BLBM_ASPECT, 1)

    'counting all the droplets
    ret = IpBlbSetAttr(BLOB_ADDCOUNT, 1)
    Allnumber = IpBlbCount()
    ret = IpBlbUpdate(4)
    ret = IpBlbData(BLBM_CENTRX, 0, Allnumber-1, Allxposition(0))
    ret = IpBlbData(BLBM_CENTRY, 0, Allnumber-1, Allyposition(0))
    ret = IpBlbData(BLBM_MEANFERRET, 0, Allnumber-1, AlloutD(0))
    ret = IpBlbData(BLBM_HOLEAREA, 0, Allnumber-1, Allhole(0))
    ret = IpBlbData(BLBM_ASPECT, 0, Allnumber-1, Allaspect(0))
    ret = IpBlbUpdate(0)
    ret = IpBlbDelete()
    ret = IpWsUndo(0)

    'getting a mean diameter, the average of inner and outer diameters
    For i = 0 To Allnumber -1
        Alldiameter(i) = (AlloutD(i) + ((Allhole(i)/3.1416)^0.5)*2.)/2.
    Next i

    'erasing the ones with aspect ratio more than 2
    i = 0
    While (i < Allnumber)
        If (Allaspect(i) > 2.) Then
            For j = i To Allnumber - 2
                Allxposition(j) = Allxposition(j+1)
                Allyposition(j) = Allyposition(j+1)
                Alldiameter(j) = Alldiameter(j+1)
                Allaspect(j) = Allaspect(j+1)
            Next j
```

```
            Allnumber = Allnumber - 1
        Else
            i = i + 1
        End If
    Wend

End Sub

Sub GetYellow ()

    'getting yellow droplets
    ret = IpAppSelectDoc(0)
    ret = IpSegSetAttr(COLORMODEL, CM_HSI)
    ret = IpSegSetRange(0, 0, 90)
    ret = IpSegSetRange(1, 0, 255)
    ret = IpSegSetRange(2, 0, 255)
    ret = IpSegCreateMask(MASK_BILEVELNEW, 0, 1)
    ret = IpWsChangeDescription(INF_NAME, PicName + "Y")

    'setup range of count
    ret = IpBlbSetAttr(BLOB_AUTORANGE, 1)
    ret = IpBlbSetAttr(BLOB_BRIGHTOBJ, 1)

    'select the parameters
    ret = IpBlbEnableMeas(BLBM_CENTRX, 1)
    ret = IpBlbEnableMeas(BLBM_CENTRY, 1)
    ret = IpBlbEnableMeas(BLBM_MEANFERRET, 1)

    'counting all the yellow droplets
    ret = IpBlbSetAttr(BLOB_ADDCOUNT, 1)
    Mnumber = IpBlbCount()
    ret = IpBlbUpdate(4)
    ret = IpBlbData(BLBM_MEANFERRET, 0, Mnumber-1, Mdiameter(0))
    ret = IpBlbData(BLBM_CENTRX, 0, Mnumber-1, Mxposition(0))
    ret = IpBlbData(BLBM_CENTRY, 0, Mnumber-1, Myposition(0))
    ret = IpBlbUpdate(0)

    'grouping yellow drops
    For i = 0 To Mnumber - 1
        If (Myposition(i) < Ysize/3) Then
            Mlist(i) = 0
        ElseIf (Myposition(i) < Ysize*2/3) Then
            Mlist(i) = 1
        Else
            Mlist(i) = 2
        End If
    Next i

    'finding blue droplets, all droplets - yellowdroplets = blue droplets
    For j = 0 To Mnumber - 1
        i = 0
        While (i < Allnumber)
            Distancebtw = ((Allxposition(i) - Mxposition(j))^2+(Allyposition(i) - Myposition(j))^2)^0.5
            If (Distancebtw < Mdiameter(j)/2.) Then
                For k = i To Allnumber - 2
                    Allxposition(k) = Allxposition(k+1)
```

```
                Allyposition(k) = Allyposition(k+1)
                Alldiameter(k) = Alldiameter(k+1)
            Next k
            Allnumber = Allnumber - 1
        Else
            i = i + 1
        End If
    Wend
Next j

ret = IpOutputShow(1)
'Debug.Print "Blue"
'Debug.Print " Index      X position     Y position      Diameter(pixel)"
For i = 0 To Allnumber - 1
    If (alldiameter(i) > 10) Then
        Debug.Print   Alldiameter(i)
    End If
Next i
'Debug.Print "Yellow"
'Debug.Print " Index      X position      Y position       Diameter"
'For i = 0 To Mnumber -1
'    Debug.Print "*"; i + 1; " *"; "       "; Mxposition(i); "       "; Myposition(i); "       "; Mdiameter(i)
'Next i

End Sub

Sub GetVelocity()

    condition1 = False
    condition2 = False
    condition3 = False
    condition4 = False
    condition5 = False

    SumDist = 0.'initiate temp values
    CountMatch = 0

    'get velocity
    For i = 0 To Mnumber-1
        If (Mlist(i) = z) Then  'one group per iteration
            match(i) = 0  'initiate
            angle(i) = 0
            rememberK = -1

            If (i < Mnumber*2/3) Then      'it makes macro a bit faster
                start = 0
            Else
                start = Allnumber/3
            End If

            For j = start To Allnumber - 1

                If ((Allyposition(j) - Myposition(i)) > AveDist(z)*5.) And (match(i) <> 0) Then  'it makes
macro faster
                    GoTo EndLoop
                End If
```

```
                    Distancebtw = ((Allxposition(j) - Mxposition(i))^2+(Allyposition(j) -
Myposition(i))^2)^0.5
                    If (Distancebtw >= AveDist(z)/4.0) And (Distancebtw <= AveDist(z)*1.75) And
(Allxposition(j) < Mxposition(i)) And (Allyposition(j) > Myposition(i)) Then
                        condition1 = True
                    Else
                        GoTo skip
                    End If

                    Yangle = (Atn((Xshift*10^4*2.54/PixelSize-(Mxposition(i)-XLED))/((Myposition(i)-
YLED)+Yshift*10^4*2.54/PixelSize)))*180/3.1416 'degree
                    BYangle = (Atn((Mxposition(i)-Allxposition(j))/(Allyposition(j)-
Myposition(i))))*180/3.1416 'degree

                    If    (BYangle < Yangle + theta) And (BYangle > Yangle - theta) Then
                        condition2 = True
                    Else
                        GoTo skip
                    End If

                    If (Alldiameter(j) > Mdiameter(i)/3.) Then    'big yellow drop can't take a small blue drop,
not vice versa
                        condition3 = True
                    Else
                        GoTo skip
                    End If

                    If (match(i) > 0) Then 'if yellow drop already had a match before...
                        If (Abs(distancebtw - AveDist(z)) < Abs((Velocity(i)*TimeDelay/PixelSize) -
AveDist(z))) Then       'better distance
                            If (Abs(BYangle - Yangle) < 10.) And (Abs(distancebtw-
(Velocity(i)*TimeDelay/PixelSize)) > AveDist(z)*0.2) Then
                                condition4 = True
                            End If
                        End If
                        If (Abs(BYangle - Yangle) < Abs(Angle(i) - Yangle)) Then      'better angle
                            If (Abs(AveDist(z) - distancebtw) < AveDist(z)*0.2 ) And (Abs(BYangle-
Angle(i)) > 5.)Then
                                condition4 = True
                            End If
                        End If
                        'but...
                        If (Abs(Diameter(i)-Mdiameter(i)) < Abs(Alldiameter(j)-Mdiameter(i))) Then
    'comparing size
                            If (Abs(Diameter(i)-Alldiameter(j)) > ((Diameter(i)+Alldiameter(j))/2.-
Abs(Diameter(i)-Alldiameter(j))/2.)) Then    'if the diameter difference is bigger than the diameter of the
small droplet
                                condition4 = False
                            End If
                        End If
                    Else
                        condition4 = True
                    End If

                    For k = 0 To i - 1
```

```
If (match(k) = j + 1) Then  'if the blue droplet is already taken
      condition5 = False
      If (Abs(Angle(k) - Yangle) > Abs(BYangle - Yangle)) Then    'better angle
            If (Abs(distancebtw - AveDist(z)) < AveDist(z)*0.2) And (Abs(BYangle-
Angle(k)) > 5.) Then
                  condition5 = True
            End If
      End If
      If (Abs((Velocity(k)*TimeDelay/PixelSize) - AveDist(z)) > Abs(distancebtw -
AveDist(z))) Then      'better distance
            If (Abs(BYangle - Yangle) < 10.) And (Abs(distancebtw-
(Velocity(k)*TimeDelay/PixelSize)) > AveDist(z)*0.2) Then
                  condition5 = True
            End If
      End If
      'but...
      If (Abs(Alldiameter(j)-Mdiameter(k)) < Abs(Alldiameter(j)-Mdiameter(i)))
Then      'comparing size
            If (Abs(Mdiameter(k)-Mdiameter(i)) > ((Mdiameter(k)+Mdiameter(i))/2.-
Abs(Mdiameter(k)-Mdiameter(i))/2.)) Then
                  condition5 = False
            End If
      End If
      If (condition1) And (condition2) And (condition3) And (condition4) And
(condition5) Then
            If (rememberK = -1) Then
                  match(k) = -match(k)  'cancel the old match
                  rememberK = k
            End If
      End If
      GoTo finish
Else
      condition5 = True
End If
Next k
finish:

'If (i = 258) And (condition1) And (condition2) And (condition3) And (condition4) And
(condition5) And (condition6) Then
' Debug.Print  j+1 'match(i)
'End If

If (condition1) And (condition2) And (condition3) And (condition4) And (condition5)
Then

      match(i) = j + 1
      PositionX(i) = (Mxposition(i) + Allxposition(j))/2.0
      PositionY(i) = (Myposition(i) + Allyposition(j))/2.0
      Velocity(i) = Distancebtw * PixelSize / TimeDelay ' m/sec
      Diameter(i) = Alldiameter(j)
      Angle(i) = BYangle

      SumDist = SumDist + Distancebtw
      CountMatch = CountMatch + 1

End If
```

```
                condition1 = False
                condition2 = False
                condition3 = False
                condition4 = False
                condition5 = False

                skip:

            Next j
            EndLoop:

            If (rememberK > -1) Then
                If (match(i) <> -match(rememberK))Then     'if the yellow drop once canceled a pair and
took different blue drop
                    match(rememberK) = -match(rememberK)    'valid old pair
                End If
            End If
        End If
    Next i

    'new average distance
    If (CountMatch <> 0) Then
        AveDist(z) = SumDist/CountMatch
    End If

End Sub



Sub Report()

    ret = IpOutputShow(1)
    ret = IpOutputClear()

    Debug.Print " * "; PicName
    Debug.Print " * "; "Origin: Sprinkler"
    Debug.Print " * "; "Xsize(pixels): "; Xsize
    Debug.Print " * "; "Ysize: "; Ysize
    Debug.Print " * "; "XLED(pixels): "; XLED
    Debug.Print " * "; "YLED: "; YLED
    Debug.Print " * "; "Xshift(inches): "; Xshift
    Debug.Print " * "; "Yshift: "; Yshift
    Debug.Print " * "; "TimeDelay(microseconds): "; TimeDelay
    Debug.Print " * "; "OnePixel(micron): "; PixelSize
    Debug.Print " * "; "Theta(degree): "; Theta
    Debug.Print " Bindex     X(meter)      Y(meter)       Diameter(micron)

    For i = 0 To Allnumber - 1
        Xsprinkler = (XLED - (Allxposition(i)))*PixelSize/10^6 + Xshift*0.0254     'meter
        Ysprinkler = ((Allyposition(i)) - YLED)*PixelSize/10^6 + Yshift*0.0254     'meter
        If (i < 9) Then
            Debug.Print "  ";
        ElseIf (i < 99) Then
            Debug.Print " ";
        End If
```

```
        Debug.Print i+1; "        "; -Xsprinkler ; "          ";-Ysprinkler ; "            "; Alldiameter(i)*PixelSize


        If (i = 349) Then  'append if there are too many droplets
            ret = IpOutputSave("G:\temp\" + PicName + "size.txt", 0)
            ret = IpOutputClear()
        ElseIf ((i Mod 350) = 349) And (i > 350)Then
            ret = IpOutputSave("G:\temp\" + PicName + "size.txt", S_APPEND)
            ret = IpOutputClear()
        End If

    Next i

    If (i > 349) Then
        ret = IpOutputSave("G:\temp\" + PicName + "size.txt", S_APPEND)
    Else
        ret = IpOutputSave("G:\temp\" + PicName + "size.txt", 0)
    End If

    ret = IpOutputClear()
    Debug.Print " * "; PicName
    Debug.Print " * "; "Origin: Sprinkler"
    Debug.Print " * "; "Xsize(pixels): "; Xsize
    Debug.Print " * "; "Ysize: "; Ysize
    Debug.Print " * "; "XLED(pixels): "; XLED
    Debug.Print " * "; "YLED: "; YLED
    Debug.Print " * "; "Xshift(inches): "; Xshift
    Debug.Print " * "; "Yshift: "; Yshift
    Debug.Print " * "; "TimeDelay(microseconds): "; TimeDelay
    Debug.Print " * "; "OnePixel(micron): "; PixelSize
    Debug.Print " * "; "Theta(degree): "; Theta
    Debug.Print "Y index    X(meter)           Y(meter)         Velocity(m/s)     Diameter(micron)
Angle(degree)     Xblue(meter)     Yblue

    For i = 0 To Mnumber-1
        If (match(i) < 1 ) Then
                If (i < 9) Then
                    Debug.Print "  ";
                ElseIf (i < 99) Then
                    Debug.Print " ";
                End If
                Debug.Print i + 1; "      No match      X: "; Mxposition(i); "       Y: "; Myposition(i); "
D: "; Mdiameter(i); "       X,Ysprinkler(m):"; -((XLED - (Mxposition(i)))*PixelSize/10^6 +
Xshift*0.0254); "  "; -(((Myposition(i)) - YLED)*PixelSize/10^6 + Yshift*0.0254)
        Else
            Xsprinkler = (XLED - (PositionX(i)))*PixelSize/10^6 + Xshift*0.0254  'meter
            Ysprinkler = ((PositionY(i)) - YLED)*PixelSize/10^6 + Yshift*0.0254  'meter
            Xblue = (XLED - (Allxposition(match(i)-1)))*PixelSize/10^6 + Xshift*0.0254   'meter
            Yblue = ((Allyposition(match(i)-1)) - YLED)*PixelSize/10^6 + Yshift*0.0254   'meter
                If (i < 9) Then
                    Debug.Print "  ";
                ElseIf (i < 99) Then
                    Debug.Print " ";
                End If
            Debug.Print i + 1;
```

```
            Debug.Print "       "; -Xsprinkler ; "        ";-Ysprinkler ; "           "; Velocity(i); "           ";
(Diameter(i) * PixelSize); "         "; Angle(i); "         "; -Xblue; "         "; -Yblue
        End If
        If (i = 119) Then
            ret = IpOutputSave("G:\temp\" + PicName + "velocity.txt", 0)
            ret = IpOutputClear()
        End If
        If ((i Mod 120) = 119) And (i > 120) Then
            ret = IpOutputSave("G:\temp\" + PicName + "velocity.txt", S_APPEND)
            ret = IpOutputClear()
        End If

    Next i

    If (i > 119) Then
        ret = IpOutputSave("G:\temp\" + PicName + "velocity.txt", S_APPEND)
    Else
        ret = IpOutputSave("G:\temp\" + PicName + "velocity.txt", 0)
    End If

End Sub
```

2. Macro run within Image Pro Plus to analyze sprinkler images (macro216.scr):

```
' Name: Kazuki Shiozawa
' Dept: BFRL, NIST
' Date: May 13, 2002 -

Option Explicit

    'All (Blue and Yellow)
    Global Allnumber As Integer
    Global Allhole(12000) As Single
    Global Allxposition(12000) As Single
    Global Allyposition(12000) As Single
    Global AlloutD(12000) As Single
    Global Alldiameter(12000) As Single
    Global Allaspect(12000) As Single

    'Yellow
    global Mnumber As Integer 'M represents "maize"
    Global Mdiameter(2000) As Single
    Global Mxposition(2000) As Single
    Global Myposition(2000) As Single
    Global Mlist(2000) As Integer

    'final result
    Global PositionX(2000) As Single
    Global PositionY(2000) As Single
    Global Velocity(2000) As Single
    Global match(12000) As Single
    Global Diameter(2000) As Single
    Global Angle(2000) As Single
    Global SumDist As Single
    Global AveDist(3) As Single
    Global CountMatch As Integer
    Global Xblue As Single
    Global Yblue As Single

    'setups
    Global PicName As String * 12
    Global TimeDelay As Single
    Global PixelSize As Single
    Global theta As Single

    'iteration
    global i As Integer
    Global j As Integer
    Global k As Integer
    Global n As Integer
    Global z As Integer
    Global CountDown As Integer
    Global rememberK As Integer
    Global start As Integer

    'picture size, index6
    Global Xsize As Integer
```

```
    Global Ysize As Integer
    Global size(2) As Integer
    Global XLED As Integer
    Global YLED As Integer
    Global Xshift As Single
    Global Yshift As Single
    Global Xsprinkler As Single
    Global Ysprinkler As Single
    Global Yfirst As Integer

    'temps
    Global Yangle As Single
    Global BYangle As Single
    global condition1 As Boolean
    global condition2 As Boolean
    Global condition3 As Boolean
    Global condition4 As Boolean
    Global condition5 As Boolean
    Global index As Integer
    Global distancebtw As Single
    Global AverageDistance As Single


Sub Execute()

    'SETUP ********************************************************
    PicName = "R113E05"

    Xshift = 24.3125 ' horizontal distance between sprinkler and LED, inches
    '19. + 1./16.  24.+5./16.     24.+1./8.  26.+1./16.

    Yshift =  10.9375' vertical distance between sprinkler and LED, inches
    '69.+9./16.-(51.+15./16.)    70.+1./16.-(59.+1./8.)        69.+5./8.-(61.+5./8.)  69.+5./8.-(58.+7./16.)

    TimeDelay = 520. ' microseconds
    PixelSize = 49.5 ' micrometer

    theta = 30.    ' range from AveAngle, degree
    AverageDistance = 100. 'initial value, pixels

    Yfirst = 0      'the first Y position that Macro can analyze correctly, pixels
    '************************************************************

    For i = 0 To 2
        AveDist(i) = AverageDistance  'initiate
    Next i

    ret = ipdocget(getdocinfo,docsel_active,size(0)) 'get the size of the image
    Xsize = size(0)
    Ysize = size(1)

    Call GetAll()
    Call GetYellow()

    CountDown = 9
```

```
    For n = 0 To 2     'iterate 3 times
        For z = 0 To 2     '3 parts, 3x3=9 iterations
            ret = IpOutputShow(1)
            Debug.Print CountDown; " more iterations... " ; AveDist(z); "pixels"
            Call GetVelocity()
            CountDown = CountDown - 1
        Next z
    Next n

    Call Report()

End Sub

Sub GetAll()

    'getting all the droplets

    'sobel filtering
    ret = IpFltSobel()

    'range of selection
    ret = IpBlbSetAttr(BLOB_AUTORANGE, 0)
    ret = IpSegSetAttr(COLORMODEL, CM_HSI)
    ret = IpSegPreview(ALL_T_B)
    ret = IpSegSetRange(0, 0, 255)
    ret = IpSegSetRange(1, 0, 255)
    ret = IpSegSetRange(2, 78, 255)

    'select the parameters
    ret = IpBlbEnableMeas(BLBM_CENTRX, 1)
    ret = IpBlbEnableMeas(BLBM_CENTRY, 1)
    ret = IpBlbEnableMeas(BLBM_MEANFERRET, 1)
    ret = IpBlbEnableMeas(BLBM_HOLEAREA, 1)
    ret = IpBlbEnableMeas(BLBM_ASPECT, 1)

    'counting all the droplets
    ret = IpBlbSetAttr(BLOB_ADDCOUNT, 1)
    Allnumber = IpBlbCount()
    ret = IpBlbUpdate(4)
    ret = IpBlbData(BLBM_CENTRX, 0, Allnumber-1, Allxposition(0))
    ret = IpBlbData(BLBM_CENTRY, 0, Allnumber-1, Allyposition(0))
    ret = IpBlbData(BLBM_MEANFERRET, 0, Allnumber-1, AlloutD(0))
    ret = IpBlbData(BLBM_HOLEAREA, 0, Allnumber-1, Allhole(0))
    ret = IpBlbData(BLBM_ASPECT, 0, Allnumber-1, Allaspect(0))
    ret = IpBlbUpdate(0)
    ret = IpBlbDelete()
    ret = IpWsUndo(0)

    'getting a mean diameter, the average of inner and outer diameters
    For i = 0 To Allnumber -1
        Alldiameter(i) = (AlloutD(i) + ((Allhole(i)/3.1416)^0.5)*2.)/2.
    Next i

    'erasing the ones with aspect ratio more than 2
    i = 0
```

```
    While (i < Allnumber)
        If (Allaspect(i) > 2.) Then
            For j = i To Allnumber - 2
                Allxposition(j) = Allxposition(j+1)
                Allyposition(j) = Allyposition(j+1)
                Alldiameter(j) = Alldiameter(j+1)
                Allaspect(j) = Allaspect(j+1)
            Next j
            Allnumber = Allnumber - 1
        Else
            i = i + 1
        End If
    Wend

End Sub

Sub GetYellow ()

    'getting yellow droplets
    ret = IpAppSelectDoc(0)
    ret = IpSegSetAttr(COLORMODEL, CM_HSI)
    ret = IpSegSetRange(0, 0, 90)
    ret = IpSegSetRange(1, 0, 255)
    ret = IpSegSetRange(2, 0, 255)
    ret = IpSegCreateMask(MASK_BILEVELNEW, 0, 1)
    ret = IpWsChangeDescription(INF_NAME, PicName + "Y")

    'setup range of count
    ret = IpBlbSetAttr(BLOB_AUTORANGE, 1)
    ret = IpBlbSetAttr(BLOB_BRIGHTOBJ, 1)

    'select the parameters
    ret = IpBlbEnableMeas(BLBM_CENTRX, 1)
    ret = IpBlbEnableMeas(BLBM_CENTRY, 1)
    ret = IpBlbEnableMeas(BLBM_MEANFERRET, 1)

    'counting all the yellow droplets
    ret = IpBlbSetAttr(BLOB_ADDCOUNT, 1)
    Mnumber = IpBlbCount()
    ret = IpBlbUpdate(4)
    ret = IpBlbData(BLBM_MEANFERRET, 0, Mnumber-1, Mdiameter(0))
    ret = IpBlbData(BLBM_CENTRX, 0, Mnumber-1, Mxposition(0))
    ret = IpBlbData(BLBM_CENTRY, 0, Mnumber-1, Myposition(0))
    ret = IpBlbUpdate(0)

    'grouping yellow drops and finding LED positions
    For i = 0 To Mnumber - 1
        If (Myposition(i) < Ysize/3) Then
            Mlist(i) = 0
        ElseIf (Myposition(i) < Ysize*2/3) Then
            Mlist(i) = 1
        Else
            Mlist(i) = 2
        End If

        If (Mdiameter(i) > 90.) And (Mxposition(i) < Xsize/4) And (Myposition(i) < Ysize/4) Then
```

```
            XLED = Mxposition(i)
            YLED = Myposition(i)
            Mlist(i) = -1
        End If

    Next i

    'finding blue droplets, all droplets - yellowdroplets = blue droplets
    For j = 0 To Mnumber - 1
        i = 0
        While (i < Allnumber)
            Distancebtw = ((Allxposition(i) - Mxposition(j))^2+(Allyposition(i) - Myposition(j))^2)^0.5
            If (Distancebtw < Mdiameter(j)/2.) Then
                For k = i To Allnumber - 2
                    Allxposition(k) = Allxposition(k+1)
                    Allyposition(k) = Allyposition(k+1)
                    Alldiameter(k) = Alldiameter(k+1)
                Next k
                Allnumber = Allnumber - 1
                GoTo jump
            Else
                i = i + 1
            End If
        Wend
        jump:
    Next j

    'ret = IpOutputShow(1)
    'Debug.Print "Blue"
    'Debug.Print " Index      X position     Y position      Diameter(pixel)"
    'For i = 0 To Allnumber - 1
    '           Debug.Print  "*"; i + 1; " *"; "       "; Allxposition(i); "       "; Allyposition(i); "       ";
Alldiameter(i)
    'Next i
    'Debug.Print "Yellow"
    'Debug.Print " Index      X position      Y position       Diameter"
    'For i = 0 To Mnumber -1
    '      Debug.Print "*"; i + 1; " *"; "       "; Mxposition(i); "       "; Myposition(i); "       "; Mdiameter(i)
    'Next i

End Sub

Sub GetVelocity()

    condition1 = False
    condition2 = False
    condition3 = False
    condition4 = False
    condition5 = False

    SumDist = 0.'initiate temp values
    CountMatch = 0

    'get velocity
    For i = 0 To Mnumber-1
        If (Mlist(i) = z) Then  'one group per iteration
```

```
match(i) = 0  'initiate
angle(i) = 0
rememberK = -1

If (i < Mnumber*2/3) Then       'it makes macro a bit faster
      start = 0
Else
      start = Allnumber/3
End If

For j = start To Allnumber - 1

      If ((Allyposition(j) - Myposition(i)) > AveDist(z)*5.) And (match(i) <> 0) Then  'it makes
macro faster
            GoTo EndLoop
      End If

      Distancebtw = ((Allxposition(j) - Mxposition(i))^2+(Allyposition(j) -
Myposition(i))^2)^0.5
      If (Distancebtw >= AveDist(z)/4.0) And (Distancebtw <= AveDist(z)*1.75) And
(Allxposition(j) < (Mxposition(i)+AveDist(z))) And (Allyposition(j) > Myposition(i)) Then
            condition1 = True
      Else
            GoTo skip
      End If

      Yangle = (Atn((Xshift*10^4*2.54/PixelSize-(Mxposition(i)-XLED))/((Myposition(i)-
YLED)+Yshift*10^4*2.54/PixelSize)))*180/3.1416 'degree
      BYangle = (Atn((Mxposition(i)-Allxposition(j))/(Allyposition(j)-
Myposition(i))))*180/3.1416 'degree

      If    (BYangle < Yangle + theta) And (BYangle > Yangle - theta) Then
            condition2 = True
      Else
            GoTo skip
      End If

      If (Alldiameter(j) > Mdiameter(i)/2.) Then    'big yellow drop can't take a small blue drop,
not vice versa
            condition3 = True
      Else
            GoTo skip
      End If

      If (match(i) > 0) Then 'if yellow drop already had a match before...
            If (Abs(distancebtw - AveDist(z)) < Abs((Velocity(i)*TimeDelay/PixelSize) -
AveDist(z))) Then       'better distance
                  If (Abs(BYangle - Yangle) < 10.) And (Abs(distancebtw-
(Velocity(i)*TimeDelay/PixelSize)) > AveDist(z)*0.2) Then
                        condition4 = True
                  End If
            End If
            If (Abs(BYangle - Yangle) < Abs(Angle(i) - Yangle)) Then      'better angle
                  If (Abs(AveDist(z) - distancebtw) < AveDist(z)*0.2 ) And (Abs(BYangle-
Angle(i)) > 5.)Then
                        condition4 = True
```

```
                End If
            End If
            'but...
            If (Abs(Diameter(i)-Mdiameter(i)) < Abs(Alldiameter(j)-Mdiameter(i))) Then
    'comparing size
                If (Abs(Diameter(i)-Alldiameter(j)) > ((Diameter(i)+Alldiameter(j))/2.-
Abs(Diameter(i)-Alldiameter(j))/2.)) Then    'if the diameter difference is bigger than the diameter of the
small droplet
                    condition4 = False
                End If
            End If
        Else
            condition4 = True
        End If

        For k = 0 To i
            If (match(k) = j + 1) Then  'if the blue droplet is already taken
                condition5 = False
                If (Abs(Angle(k) - Yangle) > Abs(BYangle - Yangle)) Then    'better angle
                    If (Abs(distancebtw - AveDist(z)) < AveDist(z)*0.2) And (Abs(BYangle-
Angle(k)) > 5.) Then
                        condition5 = True
                    End If
                End If
                If (Abs((Velocity(k)*TimeDelay/PixelSize) - AveDist(z)) > Abs(distancebtw -
AveDist(z))) Then       'better distance
                    If (Abs(BYangle - Yangle) < 10.) And (Abs(distancebtw-
(Velocity(k)*TimeDelay/PixelSize)) > AveDist(z)*0.2) Then
                        condition5 = True
                    End If
                End If
                'but...
                If (Abs(Alldiameter(j)-Mdiameter(k)) < Abs(Alldiameter(j)-Mdiameter(i)))
Then      'comparing size
                    If (Abs(Mdiameter(k)-Mdiameter(i)) > ((Mdiameter(k)+Mdiameter(i))/2.-
Abs(Mdiameter(k)-Mdiameter(i))/2.)) Then
                        condition5 = False
                    End If
                End If
                If (condition1) And (condition2) And (condition3) And (condition4) And
(condition5) Then
                    If (rememberK = -1) Then
                        match(k) = -match(k)  'cancel the old match
                        rememberK = k
                    End If
                End If
                GoTo finish
            Else
                condition5 = True
            End If
        Next k
        finish:

        'If (i = 281) And (condition1) And (condition2)And (condition3)Then
        '    Debug.Print  i+1; j+1; alldiameter(j); condition4; condition5
        'End If
```

```
                If (condition1) And (condition2) And (condition3) And (condition4) And (condition5)
Then

                    match(i) = j + 1
                    PositionX(i) = (Mxposition(i) + Allxposition(j))/2.0
                    PositionY(i) = (Myposition(i) + Allyposition(j))/2.0
                    Velocity(i) = Distancebtw * PixelSize / TimeDelay ' m/sec
                    Diameter(i) = Alldiameter(j)
                    Angle(i) = BYangle

                    SumDist = SumDist + Distancebtw
                    CountMatch = CountMatch + 1

                End If

                skip:

                condition1 = False
                condition2 = False
                condition3 = False
                condition4 = False
                condition5 = False

            Next j
            EndLoop:

            If (rememberK > -1) Then
                If (match(i) <> -match(rememberK)) Then   'if the yellow drop once canceled a pair and
took different blue drop
                    match(rememberK) = -match(rememberK)   'valid old pair
                End If
            End If
        End If
    Next i

    'new average distance
    If (CountMatch <> 0) Then
        AveDist(z) = SumDist/CountMatch
    End If

End Sub



Sub Report()

    ret = IpOutputShow(1)
    ret = IpOutputClear()

    Debug.Print " * "; PicName
    Debug.Print " * "; "Origin Sprinkler"
    Debug.Print " * "; "Xsize(pixels) "; Xsize
    Debug.Print " * "; "Ysize "; Ysize
    Debug.Print " * "; "XLED(pixels) "; XLED
    Debug.Print " * "; "YLED "; YLED
```

```
Debug.Print " * "; "Xshift(inches) "; Xshift
Debug.Print " * "; "Yshift "; Yshift
Debug.Print " * "; "TimeDelay(microseconds) "; TimeDelay
Debug.Print " * "; "OnePixel(micron) "; PixelSize
Debug.Print " * "; "Theta(degree) "; Theta
Debug.Print " * "; "FirstY(pixels) "; Yfirst
Debug.Print " * "; "FirstY(m) "; -((Yfirst - YLED)*PixelSize/10^6 + Yshift*0.0254)
Debug.Print " "          'spaces for upper/lower boundary
Debug.Print " "
Debug.Print " "
Debug.Print " "
Debug.Print " Bindex     X(meter)      Y(meter)       Diameter(micron)

For i = 0 To Allnumber - 1
    Xsprinkler = (XLED - (Allxposition(i)))*PixelSize/10^6 + Xshift*0.0254    'meter
    Ysprinkler = ((Allyposition(i)) - YLED)*PixelSize/10^6 + Yshift*0.0254    'meter
    If (i < 9) Then
        Debug.Print "  ";
    ElseIf (i < 99) Then
        Debug.Print " ";
    End If
    Debug.Print i+1; "       "; -Xsprinkler ; "         ";-Ysprinkler ; "          "; Alldiameter(i)*PixelSize


    If (i = 349) Then  'append if there are too many droplets
        ret = IpOutputSave("G:\temp\" + PicName + "size.txt", 0)
        ret = IpOutputClear()
    ElseIf ((i Mod 350) = 349) And (i > 350)Then
        ret = IpOutputSave("G:\temp\" + PicName + "size.txt", S_APPEND)
        ret = IpOutputClear()
    End If

Next i

If (i > 349) Then
    ret = IpOutputSave("G:\temp\" + PicName + "size.txt", S_APPEND)
Else
    ret = IpOutputSave("G:\temp\" + PicName + "size.txt", 0)
End If

ret = IpOutputClear()
Debug.Print " * "; PicName
Debug.Print " * "; "Origin Sprinkler"
Debug.Print " * "; "Xsize(pixels) "; Xsize
Debug.Print " * "; "Ysize "; Ysize
Debug.Print " * "; "XLED(pixels) "; XLED
Debug.Print " * "; "YLED "; YLED
Debug.Print " * "; "Xshift(inches) "; Xshift
Debug.Print " * "; "Yshift "; Yshift
Debug.Print " * "; "TimeDelay(microseconds) "; TimeDelay
Debug.Print " * "; "OnePixel(micron) "; PixelSize
Debug.Print " * "; "Theta(degree) "; Theta
Debug.Print " * "; "FirstY(pixels) "; Yfirst
Debug.Print " * "; "FirstY(m) "; -((Yfirst - YLED)*PixelSize/10^6 + Yshift*0.0254)
Debug.Print " "          ' spaces for upper/lower boundary
Debug.Print " "
```

```
    Debug.Print " "
    Debug.Print " "
    Debug.Print "Y index    X(meter)          Y(meter)        Velocity(m/s)     Diameter(micron)
Angle(degree)     Xblue(meter)     Yblue

    For i = 0 To Mnumber-1    'matches
        If (match(i) > 0 ) Then
            Xsprinkler = (XLED - (PositionX(i)))*PixelSize/10^6 + Xshift*0.0254 'meter
            Ysprinkler = ((PositionY(i)) - YLED)*PixelSize/10^6 + Yshift*0.0254 'meter
            Xblue = (XLED - (Allxposition(match(i)-1)))*PixelSize/10^6 + Xshift*0.0254   'meter
            Yblue = ((Allyposition(match(i)-1)) - YLED)*PixelSize/10^6 + Yshift*0.0254   'meter
                If (i < 9) Then
                    Debug.Print "  ";
                ElseIf (i < 99) Then
                    Debug.Print " ";
                End If
            Debug.Print i + 1;

            Debug.Print "      "; -Xsprinkler ; "        ";-Ysprinkler ; "          "; Velocity(i); "           ";
(Diameter(i) * PixelSize); "        "; Angle(i); "        "; -Xblue; "        "; -Yblue
        End If
        If (i = 119) Then
            ret = IpOutputSave("G:\temp\" + PicName + "velocity.txt", 0)
            ret = IpOutputClear()
        End If
        If ((i Mod 120) = 119) And (i > 120) Then
            ret = IpOutputSave("G:\temp\" + PicName + "velocity.txt", S_APPEND)
            ret = IpOutputClear()
        End If

    Next i

    If (i > 119) Then
        ret = IpOutputSave("G:\temp\" + PicName + "velocity.txt", S_APPEND)
        ret = IpOutputClear()
    Else
        ret = IpOutputSave("G:\temp\" + PicName + "velocity.txt", 0)
        ret = IpOutputClear()
    End If

    For i = 0 To Mnumber-1    ' no matches
        If (match(i) < 1 ) Then
            If (i < 9) Then
                Debug.Print "  ";
            ElseIf (i < 99) Then
                Debug.Print " ";
            End If
            Debug.Print i + 1; "      No match      X: "; Mxposition(i); "       Y: "; Myposition(i); "       D: ";
Mdiameter(i); "       X,Ysprinkler(m):"; -((XLED - (Mxposition(i)))*PixelSize/10^6 + Xshift*0.0254); "  ";
-(((Myposition(i)) - YLED)*PixelSize/10^6 + Yshift*0.0254)
        End If
    Next i
    ret = IpOutputSave("G:\temp\" + PicName + "velocity.txt", S_APPEND)

End Sub
```

```
Sub Convert()

    Dim Xs As Single
    Dim Ys As Single
    Dim Xl As Integer
    Dim Yl As Integer
    Dim Xp As Integer
    Dim Yp As Integer
    Dim dX As Single
    Dim dY As Single
    Dim sign As Integer
    Dim YorN As String * 10

    ret = ipstgetint("X,Ysprinkler(m) to X,Y pixels, enter 0   X,Y pixels to X,Ysprinkler, enter 1", sign, 0,
0, 1)

    ret = ipstgetint("Enter XLED(pixels)", Xl, 0, 0, 9999)
    ret = ipstgetint("Enter YLED(pixels)", Yl, 0, 0, 9999)
    ret = ipstgetfloat("Enter Xshift (in.)", dX, 26.5, 0, 100.0, 0.1)
    ret = ipstgetfloat("Enter Yshift (in.)", dY, 7.125, 0, 100.0, 0.1)
    ret = ipstgetfloat("Enter PixelSize (micron)", PixelSize, 49.5, 0, 100.0, 0.1)

    If (sign = 0) Then
        ret = ipstgetFloat("Enter POSITIVE Xsprinkler(m)", Xs, 0, 0, 10.0, 0.01)
        ret = ipstgetFloat("Enter POSITIVE Ysprinkler(m)", Ys, 0, 0, 10.0, 0.01)
        Xp = (dX*.0254-Xs)*10^6/PixelSize + Xl
        Yp = (Ys-dY*.0254)*10^6/PixelSize + Yl
        ret = Ipoutputshow(1)
        Debug.Print "************************************"
        Debug.Print "X LED: "; Xl; " pixels"
        Debug.Print "Y LED: "; Yl; " pixels"
        Debug.Print "X shift: "; dX; " in."
        Debug.Print "Y shift: "; dY; " in."
        Debug.Print "Pixel size: "; PixelSize; " micron"
        Debug.Print "X sprinkler: "; Xs; " meter"
        Debug.Print "Y sprinkler: "; Ys; " meter"
        Debug.Print "X pixel: "; Xp; "pixels"
        Debug.Print "Y pixel: "; Yp; "pixels"
    Else
        ret = ipstgetint("Enter X pixels", Xp, 0, 0, 19999)
        ret = ipstgetint("Enter Y pixels", Yp, 0, 0, 19999)
        Xs = (Xl - Xp)*PixelSize/10^6 + dX*0.0254
        Ys = (Yp - Yl)*PixelSize/10^6 + dY*0.0254
        ret = Ipoutputshow(1)
        Debug.Print "************************************"
        Debug.Print "X LED: "; Xl; " pixels"
        Debug.Print "Y LED: "; Yl; " pixels"
        Debug.Print "X shift: "; dX; " in."
        Debug.Print "Y shift: "; dY; " in."
        Debug.Print "Pixel size: "; PixelSize; " micron"
        Debug.Print "X pixel: "; Xp; " pixels"
        Debug.Print "Y pixel: "; Yp; " pixels"
        Debug.Print "Xsprinkler: "; -Xs; " m ("; -Xs*100/2.54; " in.)"
        Debug.Print "Ysprinkler: "; -Ys; " m ("; -Ys*100/2.54; " in.)"
    End If
```

```
    byebye:
End Sub
```

3. Macro run in Microsoft Excel/Visual Basic for generating random drop size and velocity pseudo data files (AngleDistributionMakerMacroV2.xls):

```
Option Explicit

Sub DeviationAngle()

' This subroutine randomly chooses the initial trajectory angle deviation
' from strike plate angle.  This is based on a cumulative normal probability
' function.  The output of 1000 simulated drops was used to reconstruct a
' cumulative angular distribution, and agreed with the known cumulative
' normal distribuition.  There were slight differences, ie. a slight shift
' of the result toward smaller drop sizes, but appeared to be due to
' rounding errors.

Dim sigma As Single
Dim MeanDeviationAngle As Single
Dim StrikePlateAngle As Single
Dim DeviationAngle As Single
Dim angle As Single
Dim probability As Single
Dim row As Integer
Dim i As Integer

Sheets("angle").Select

sigma = 4
MeanDeviationAngle = -7
StrikePlateAngle = 90
row = 1

For i = 1 To 23553
   Randomize
   probability = Rnd

   If probability > 0 And probability < 1 Then
      DeviationAngle = Application.NormInv(probability, MeanDeviationAngle, sigma)
   End If

   angle = StrikePlateAngle / 2 + DeviationAngle

   Cells(row, 4).Value = angle
   row = row + 1
Next

End Sub


Sub DropSize()

Dim gamma As Single
Dim k As Single
Dim VolFrac(1 To 300) As Double         'volume fraction "f3"
Dim NumFrac(1 To 300) As Double         'number fraction "f0"
Dim CumulNumFrac(1 To 300) As Double     'cumulative number fraction "F0"
```

```
Dim d As Single
Dim dia As Single
Dim f3overdiacube(1 To 300) As Double    'f3/dia^3
Dim sumf3overdiacube As Double          'summation(f3/dia^3)
Dim checksum1 As Double
Dim checksum2 As Double
Dim i As Single                        'loop count variable
Dim row As Integer
Dim size As Single
Dim probability As Single


k = 3.1
gamma = 1.9

' make table of volume fraction vs diameter
For d = 1 To 120
   dia = d * 25 / 1000  'diameter in mm
   VolFrac(d) = k * gamma * (dia ^ (gamma - 1)) * Exp(-k * (dia ^ gamma)) / 40
   Cells(d, 1).Value = dia
   Cells(d, 2).Value = VolFrac(d)
Next

' make checksum1 of volume fractions
For d = 1 To 120
   checksum1 = checksum1 + VolFrac(d)
Next
Cells(11, 7).Value = checksum1 'print to row 11, column G


' make table of number fractions
For d = 1 To 120
   dia = d * 25 / 1000  'diameter in mm
   f3overdiacube(d) = VolFrac(d) / (dia ^ 3)
   sumf3overdiacube = sumf3overdiacube + f3overdiacube(d)
Next

For d = 1 To 120
   NumFrac(d) = f3overdiacube(d) / sumf3overdiacube
   Cells(d, 3).Value = d
   Cells(d, 4).Value = NumFrac(d)
Next

' make checksum2 of number fractions
For d = 1 To 120
   checksum2 = checksum2 + NumFrac(d)
Next
Cells(11, 8).Value = checksum2 'print to row 11, column H


' make table of cumulative number fraction
For d = 1 To 120
   For i = 1 To d
      CumulNumFrac(d) = CumulNumFrac(d) + NumFrac(i)
      Cells(d, 5).Value = d
      Cells(d, 6).Value = CumulNumFrac(d)
```

```
    Next
Next
Cells(11, 9).Value = CumulNumFrac(120) 'print to row 11, column I


' randomly pick drop diameters
row = 1
For i = 1 To 400000
    Randomize
    probability = Rnd

    If probability > 0 And probability < 1 Then
        d = 1
        Do Until CumulNumFrac(d) > probability Or d > 120
            size = d * 25
            d = d + 1
        Loop
        If d > 1 Then size = size + 25
        If d = 1 Then size = 25
    End If

    ' reject drops less than 100 um
    If size >= 150 Then
        Cells(row, 15).Value = probability
        Cells(row, 16).Value = size
        row = row + 1
    End If
Next

End Sub
```

4. Macro run in Microsoft Excel/Visual Basic for predicting the water flux distribution on the floor under the sprinkler using measured sprinkler data (FloorLocationMacroV4.xls):

```
Option Explicit

Const g As Single = 9.81               'acceleration of gravity
Const airdensity As Single = 1.1774     'at 300K, Holman
Const waterdensity As Single = 998
Const airvisc As Single = 0.000018462   'dynamic viscosity of air at 300K, Holman
Const Pi As Single = 3.141592
Private YatZeroHorizVel As Single       'y coordinate where horizontal velocity=0
Private SprinklerHeight As Single       'height of sprinkler above floor plane or buckets
Private HorizDistInviscid As Single     'maximum horizontal travel distance neglecting drag


Sub Trajectory(VelocityFilename2, x0, y0, speed0, diameter, theta0, XatFloor)
    'Dim diameter As Single         'droplet diameter
    Dim h As Single                'interval (step size, seconds)
    Dim i As Integer               'step number
    Dim k1 As Single               'Runge-Kutta coefficients
    Dim k2 As Single
    Dim k3 As Single
    Dim k4 As Single
    Dim uavg As Single
    Dim vavg As Single
    Dim j As Single
    Dim tStar As Single     'characteristic time
    Dim k As Single        'coefficient from drag curve.  See Cd function.
    Dim IndexAtFloor As Single
    'Dim SummaryWorkBook As String
    'Dim Velocityworkbook As String
    'Dim endrow As Long
    'Dim FirstRow As Long
    'Dim Row As Single


    Dim time(0 To 1000) As Single
    Dim ThetaRad(0 To 1000) As Single          'droplet direction relative to south pole in radians
    Dim theta(0 To 1000) As Single            'droplet direction relative to south pole in degrees
    Dim speed(0 To 1000) As Single            'magnitude of velocity
    Dim x(0 To 1000) As Single               'horizontal position
    Dim y(0 To 1000) As Single               'vertical position
    Dim u(0 To 1000) As Single               'horizontal velocity
    Dim v(0 To 1000) As Single               'vertical velocity
    Dim t(0 To 1000) As Single               'time
    Dim uprime(0 To 1000) As Single           'horizontal accleration
    Dim vprime(0 To 1000) As Single           'vertical acceleration
    Dim xNormalized(0 To 1000) As Single
    Dim yNormalizedHeight(0 To 1000) As Single
    Dim yNormalizedZeroHorizVel(0 To 1000) As Single


    'SummaryWorkBook = "FloorLocationMacro.xls"
    'Velocityworkbook = ActiveWorkbook.Name
```

```
'endrow = Range("A64000").End(xlUp).Row
'FirstRow = Range("D1").End(xlDown).Row
'FirstRow = FirstRow + 1


'For Row = FirstRow To endrow

    'initial conditions
    SprinklerHeight = (82 - 6) / 12 * 0.3048    'high sprinkler position minus pan height
    h = 0.01
    k = 15.92

    'x(0) = Abs(Cells(Row, "A"))
    'y(0) = Abs(Cells(Row, "B"))
    'speed(0) = Cells(Row, "C")
    'diameter = Cells(Row, "D") / (10 ^ 6)
    'theta(0) = Cells(Row, "E")
    x(0) = x0
    y(0) = y0
    speed(0) = speed0
    theta(0) = theta0

    ThetaRad(0) = theta(0) * Pi / 180
    tStar = (4 * waterdensity * (diameter ^ 2)) / (3 * k * airvisc)


    'calculate initial velocities
    i = 0
    u(i) = speed(i) * Sin(ThetaRad(i))
    v(i) = speed(i) * Cos(ThetaRad(i))
    HorizDistInviscid = tStar * u(0)


    'begin trajectory calculations
    Do While u(i) > 0 Or y(i) / SprinklerHeight <= 1

        If u(i) > 0 Then
            YatZeroHorizVel = y(i)
        End If

        If y(i) / SprinklerHeight <= 1 Then
            IndexAtFloor = i
        End If

        '4th order Runge-Kutta Scheme
        k1 = h * horizaccel(diameter, u(i), v(i), speed(i))
        k2 = h * horizaccel(diameter, u(i) + 0.5 * h, v(i) + 0.5 * k1, speed(i))
        k3 = h * horizaccel(diameter, u(i) + 0.5 * h, v(i) + 0.5 * k2, speed(i))
        k4 = h * horizaccel(diameter, u(i) + h, v(i) + k3, speed(i))
        u(i + 1) = u(i) + (1 / 6) * (k1 + 2 * k2 + 2 * k3 + k4)

        k1 = h * vertaccel(diameter, u(i), v(i), speed(i))
        k2 = h * vertaccel(diameter, u(i) + 0.5 * h, v(i) + 0.5 * k1, speed(i))
        k3 = h * vertaccel(diameter, u(i) + 0.5 * h, v(i) + 0.5 * k2, speed(i))
        k4 = h * vertaccel(diameter, u(i) + h, v(i) + k3, speed(i))
        v(i + 1) = v(i) + (1 / 6) * (k1 + 2 * k2 + 2 * k3 + k4)
```

```
        'Trapezoidal Integration
        uavg = (u(i) + u(i + 1)) / 2
        vavg = (v(i) + v(i + 1)) / 2
        x(i + 1) = x(i) + h * uavg
        y(i + 1) = y(i) + h * vavg

        speed(i + 1) = Sqr((u(i + 1)) ^ 2 + (v(i + 1)) ^ 2)
        theta(i + 1) = (180 / Pi) * Atn(u(i + 1) / v(i + 1))

        time(i + 1) = time(i) + h

        i = i + 1

      Loop

      For j = 0 To i

        'calculate normalized droplet positions
        xNormalized(j) = x(j) / HorizDistInviscid
        yNormalizedHeight(j) = y(j) / SprinklerHeight
        yNormalizedZeroHorizVel(j) = y(j) / YatZeroHorizVel

      Next

      XatFloor = x(IndexAtFloor)

      'print iteration results to spreadsheet (for debugging)
        'Call dataout(VelocityFilename2, IndexAtFloor, time(IndexAtFloor), x(IndexAtFloor),
y(IndexAtFloor), _
          u(IndexAtFloor), v(IndexAtFloor), speed(IndexAtFloor), theta(IndexAtFloor), _
          xNormalized(IndexAtFloor), yNormalizedHeight(IndexAtFloor), _
          yNormalizedZeroHorizVel(IndexAtFloor))

  'Next

End Sub

Function horizaccel(diameter, u, v, speed)  'Horizontal equation of motion

  horizaccel = (-3 / 4) * Cd(speed, diameter) * (airdensity / waterdensity) * (1 / diameter) _
          * Sqr(u ^ 2 + v ^ 2) * u

End Function

Function vertaccel(diameter, u, v, speed)   'Vertical equation of motion

  vertaccel = g - (3 / 4) * Cd(speed, diameter) * (airdensity / waterdensity) * (1 / diameter) _
          * Sqr(u ^ 2 + v ^ 2) * v

End Function

Function Cd(speed, diameter) As Single       'Calculation of sphere drag coefficiect
                                             'From sprinkler scaling analysis.
  Dim k As Single
  Dim b As Single
```

```
    Dim Re As Single

    k = 15.92           'k and b are good for 1<Re<500. They are
    b = 0.584           'from a curve fit of Lapple drag plot.

    Re = airdensity * speed * diameter / airvisc

    If Re = 0 Then
        Cd = 0

    ElseIf Re > 0 And Re < 1 Then
        Cd = 24 / Re

    ElseIf Re > 500 Then
        Cd = 0.44

    Else: Cd = k / (Re ^ b)

    End If

End Function

Sub dataout(VelocityFilename2, i, time, x, y, u, v, speed, theta, xNormalized, yNormalizedHeight, _
                    yNormalizedZeroHorizVel)     'Copy result for each drop to "trajectories" sheet in
                                                 'FloorLocationMacro*.xls file for debugging

    Dim endrow As Integer

    'SummaryWorkBook = "trajectory.xls"
    'Trajectoryworkbook = ActiveWorkbook.Name

    Windows("FloorLocationMacroV4.xls").Activate
    Sheets("trajectories").Select

    endrow = Range("A64000").End(xlUp).row
    endrow = endrow + 1

    Range("A" & endrow).Value = VelocityFilename2
    Range("B" & endrow).Value = i
    Range("C" & endrow).Value = time
    Range("D" & endrow).Value = x
    Range("E" & endrow).Value = y
    Range("F" & endrow).Value = u
    Range("G" & endrow).Value = v
    Range("H" & endrow).Value = speed
    Range("I" & endrow).Value = theta
    Range("J" & endrow).Value = xNormalized
    Range("K" & endrow).Value = yNormalizedHeight
    Range("L" & endrow).Value = yNormalizedZeroHorizVel

End Sub
Sub MakeListOfFiles()
    Dim Filename As String
    Dim row As Long
    Windows("FloorLocationMacroV4.xls").Activate
    Sheets("resultfiles").Select
```

```
    Cells.Clear
    Filename = Dir("e:\Excel macro analysis\*.xls")
    Do While Filename <> ""
        If InStr(UCase(Filename), "VELO") > 0 Then
            row = row + 1
            Cells(row, 1).Value = Filename
        End If
        Filename = Dir
    Loop


End Sub

Sub AnalyzeAllData()
    Dim i As Integer
    Dim VelocityFilename2 As String
    Dim VelocityFullFileName2 As String
    Dim endrow2 As Long


    Windows("FloorLocationMacroV4.xls").Activate
    Sheets("resultfiles").Select
    endrow2 = Range("A64000").End(xlUp).row
    For i = 1 To endrow2
        Sheets("resultfiles").Select
        VelocityFilename2 = Cells(i, 1).Value
        VelocityFullFileName2 = "e:\Excel macro analysis\" + VelocityFilename2
        Workbooks.Open VelocityFullFileName2
        ImpactDistribution (VelocityFilename2)
        'Trajectory
        Workbooks(VelocityFilename2).Close False
    Next
End Sub

Sub ImpactDistribution(VelocityFilename2)

Dim endrow As Integer
Dim endrow2 As Integer
Dim FirstRow As Integer
Dim row As Integer
Dim x As Single
Dim y As Single
Dim speed As Single
Dim diameter As Single
Dim theta As Single
Dim XatFloor As Single
Dim dropvolume As Single
Dim totalvolume As Single
Dim pan As Integer

Dim volume(0 To 18) As Single


Windows(VelocityFilename2).Activate
    endrow = Range("A64000").End(xlUp).row
```

```
    FirstRow = Range("D1").End(xlDown).row
    FirstRow = FirstRow + 1

For row = FirstRow To endrow
    Windows(VelocityFilename2).Activate
    x = Abs(Cells(row, "A").Value)
    y = Abs(Cells(row, "B").Value)
    speed = Cells(row, "C").Value
    diameter = Cells(row, "D").Value / (10 ^ 6)
    theta = Cells(row, "E").Value

    Call Trajectory(VelocityFilename2, x, y, speed, diameter, theta, XatFloor)

    dropvolume = (4 / 3) * Pi * ((diameter / 2) ^ 3)

    If XatFloor >= 0 And XatFloor < 0.076 Then
            volume(0) = volume(0) + dropvolume * 2
        End If

    For pan = 1 To 18
        If XatFloor >= (pan * 0.152 - 0.076) And XatFloor < (pan * 0.152 + 0.076) Then
            volume(pan) = volume(pan) + dropvolume
        End If
    Next
Next

Windows("FloorLocationMacroV4.xls").Activate      'Output water volume total for pans
    Sheets("ImpactDist").Select
    endrow2 = Range("A64000").End(xlUp).row
    endrow2 = endrow2 + 1

'For pan = 0 To 18
'    Range(Chr(65 + pan) & endrow2).Value = pan
'Next

Range("A" & endrow2).Value = VelocityFilename2


For pan = 0 To 18
    totalvolume = totalvolume + volume(pan)
Next

For pan = 0 To 18
    Range(Chr(65 + pan + 1) & endrow2).Value = volume(pan) / totalvolume
Next


'make VelocityFilename2 active
'get initial drop data from VelocityFilename2
'run trajectory(x0, y0, speed0, theta0, diameter, velocityFilename2, XatFloor)
'calculate volume of drop
'put drop volume in appropriate collection pan
'loop back for all drops in image
'output to ImpactDist sheet in FloorLocationMacroV2

End Sub
```

5. Macro run in Microsoft Excel/Visual Basic for predicting the water flux distribution on the floor under the sprinkler using "pseudo data" (FloorLocationMacroV4b.xls):

```
Option Explicit

Const g As Single = 9.81              'acceleration of gravity
Const airdensity As Single = 1.1774     'at 300K, Holman
Const waterdensity As Single = 998
Const airvisc As Single = 0.000018462   'dynamic viscosity of air at 300K, Holman
Const Pi As Single = 3.141592
Private YatZeroHorizVel As Single       'y coordinate where horizontal velocity=0
Private SprinklerHeight As Single      'height of sprinkler above floor plane or buckets
Private HorizDistInviscid As Single     'maximum horizontal travel distance neglecting drag


Sub Trajectory(VelocityFilename2, x0, y0, speed0, diameter, theta0, XatFloor)
    'Dim diameter As Single         'droplet diameter
    Dim h As Double               'interval (step size, seconds)
    Dim i As Integer              'step number
    Dim k1 As Double               'Runge-Kutta coefficients
    Dim k2 As Double
    Dim k3 As Double
    Dim k4 As Double
    Dim uavg As Double
    Dim vavg As Double
    Dim j As Single
    Dim tStar As Double     'characteristic time
    Dim k As Double        'coefficient from drag curve.  See Cd function.
    Dim IndexAtFloor As Double
    'Dim SummaryWorkBook As String
    'Dim Velocityworkbook As String
    'Dim endrow As Long
    'Dim FirstRow As Long
    'Dim Row As Single


    Dim time(0 To 1000) As Double
    Dim ThetaRad(0 To 1000) As Double          'droplet direction relative to south pole in radians
    Dim theta(0 To 1000) As Double           'droplet direction relative to south pole in degrees
    Dim speed(0 To 1000) As Double           'magnitude of velocity
    Dim x(0 To 1000) As Double             'horizontal position
    Dim y(0 To 1000) As Double             'vertical position
    Dim u(0 To 1000) As Double             'horizontal velocity
    Dim v(0 To 1000) As Double             'vertical velocity
    Dim t(0 To 1000) As Double             'time
    Dim uprime(0 To 1000) As Double          'horizontal accleration
    Dim vprime(0 To 1000) As Double          'vertical acceleration
    Dim xNormalized(0 To 1000) As Double
    Dim yNormalizedHeight(0 To 1000) As Double
    Dim yNormalizedZeroHorizVel(0 To 1000) As Double


    'SummaryWorkBook = "FloorLocationMacro.xls"
    'Velocityworkbook = ActiveWorkbook.Name
```

```
'endrow = Range("A64000").End(xlUp).Row
'FirstRow = Range("D1").End(xlDown).Row
'FirstRow = FirstRow + 1


'For Row = FirstRow To endrow

    'initial conditions
    SprinklerHeight = (82 - 6) / 12 * 0.3048    'high sprinkler position minus pan height
    h = 0.01
    k = 15.92

    'x(0) = Abs(Cells(Row, "A"))
    'y(0) = Abs(Cells(Row, "B"))
    'speed(0) = Cells(Row, "C")
    'diameter = Cells(Row, "D") / (10 ^ 6)
    'theta(0) = Cells(Row, "E")
    x(0) = 0.001    'changed from x0 05/05/03
    y(0) = 0.001    'changed from y0 05/05/03
    speed(0) = 13.2   'changed from speed0 05/05/03
    theta(0) = theta0       'changed from theta0 05/05/03

    ThetaRad(0) = theta(0) * Pi / 180
    tStar = (4 * waterdensity * (diameter ^ 2)) / (3 * k * airvisc)


    'calculate initial velocities
    i = 0
    u(i) = speed(i) * Sin(ThetaRad(i))
    v(i) = speed(i) * Cos(ThetaRad(i))
    HorizDistInviscid = tStar * u(0)


    'begin trajectory calculations
    Do While u(i) > 0 Or y(i) / SprinklerHeight <= 1

        If u(i) > 0 Then
            YatZeroHorizVel = y(i)
        End If

        If y(i) / SprinklerHeight <= 1 Then
            IndexAtFloor = i
        End If

        '4th order Runge-Kutta Scheme
        k1 = h * horizaccel(diameter, u(i), v(i), speed(i))
        k2 = h * horizaccel(diameter, u(i) + 0.5 * h, v(i) + 0.5 * k1, speed(i))
        k3 = h * horizaccel(diameter, u(i) + 0.5 * h, v(i) + 0.5 * k2, speed(i))
        k4 = h * horizaccel(diameter, u(i) + h, v(i) + k3, speed(i))
        u(i + 1) = u(i) + (1 / 6) * (k1 + 2 * k2 + 2 * k3 + k4)

        k1 = h * vertaccel(diameter, u(i), v(i), speed(i))
        k2 = h * vertaccel(diameter, u(i) + 0.5 * h, v(i) + 0.5 * k1, speed(i))
        k3 = h * vertaccel(diameter, u(i) + 0.5 * h, v(i) + 0.5 * k2, speed(i))
        k4 = h * vertaccel(diameter, u(i) + h, v(i) + k3, speed(i))
        v(i + 1) = v(i) + (1 / 6) * (k1 + 2 * k2 + 2 * k3 + k4)
```

```
        'Trapezoidal Integration
        uavg = (u(i) + u(i + 1)) / 2
        vavg = (v(i) + v(i + 1)) / 2
        x(i + 1) = x(i) + h * uavg
        y(i + 1) = y(i) + h * vavg

        speed(i + 1) = Sqr((u(i + 1)) ^ 2 + (v(i + 1)) ^ 2)
        theta(i + 1) = (180 / Pi) * Atn(u(i + 1) / v(i + 1))

        time(i + 1) = time(i) + h

        i = i + 1

    Loop

    For j = 0 To i

        'calculate normalized droplet positions
        xNormalized(j) = x(j) / HorizDistInviscid
        yNormalizedHeight(j) = y(j) / SprinklerHeight
        yNormalizedZeroHorizVel(j) = y(j) / YatZeroHorizVel

    Next

    XatFloor = x(IndexAtFloor)

    'print iteration results to spreadsheet (for debugging)
        'Call dataout(VelocityFilename2, IndexAtFloor, time(IndexAtFloor), x(IndexAtFloor),
y(IndexAtFloor), _
            u(IndexAtFloor), v(IndexAtFloor), speed(IndexAtFloor), theta(IndexAtFloor), _
            xNormalized(IndexAtFloor), yNormalizedHeight(IndexAtFloor), _
            yNormalizedZeroHorizVel(IndexAtFloor))

    'Next

End Sub

Function horizaccel(diameter, u, v, speed) As Double 'Horizontal equation of motion


    horizaccel = (-3 / 4) * Cd(speed, diameter) * (airdensity / waterdensity) * (1 / diameter) _
                * Sqr(u ^ 2 + v ^ 2) * u

End Function

Function vertaccel(diameter, u, v, speed) As Double  'Vertical equation of motion

    vertaccel = g - (3 / 4) * Cd(speed, diameter) * (airdensity / waterdensity) * (1 / diameter) _
                * Sqr(u ^ 2 + v ^ 2) * v

End Function

Function Cd(speed, diameter) As Single       'Calculation of sphere drag coefficiect
                                             'From sprinkler scaling analysis.
    Dim k As Single
```

```
    Dim b As Single
    Dim Re As Single

    k = 15.92           'k and b are good for 1<Re<500. They are
    b = 0.584           'from a curve fit of Lapple drag plot.

    Re = airdensity * speed * diameter / airvisc

    If Re = 0 Then
        Cd = 0

    ElseIf Re > 0 And Re < 1 Then
        Cd = 24 / Re

    ElseIf Re > 500 Then
        Cd = 0.44

    Else: Cd = k / (Re ^ b)

    End If

End Function

Sub dataout(VelocityFilename2, i, time, x, y, u, v, speed, theta, xNormalized, yNormalizedHeight, _
        yNormalizedZeroHorizVel)        'Copy result for each drop to "trajectories" sheet in
                                        'FloorLocationMacro*.xls file for debugging

    Dim endrow As Integer

    'SummaryWorkBook = "trajectory.xls"
    'Trajectoryworkbook = ActiveWorkbook.Name

    Windows("FloorLocationMacroV4b.xls").Activate
    Sheets("trajectories").Select

    endrow = Range("A64000").End(xlUp).row
    endrow = endrow + 1

    Range("A" & endrow).Value = VelocityFilename2
    Range("B" & endrow).Value = i
    Range("C" & endrow).Value = time
    Range("D" & endrow).Value = x
    Range("E" & endrow).Value = y
    Range("F" & endrow).Value = u
    Range("G" & endrow).Value = v
    Range("H" & endrow).Value = speed
    Range("I" & endrow).Value = theta
    Range("J" & endrow).Value = xNormalized
    Range("K" & endrow).Value = yNormalizedHeight
    Range("L" & endrow).Value = yNormalizedZeroHorizVel

End Sub
Sub MakeListOfFiles()
    Dim Filename As String
    Dim row As Long
    Windows("FloorLocationMacroV4b.xls").Activate
```

```
    Sheets("resultfiles").Select

    Cells.Clear
    Filename = Dir("e:\Excel macro analysis\*.xls")
    Do While Filename <> ""
        If InStr(UCase(Filename), "VELO") > 0 Then
            row = row + 1
            Cells(row, 1).Value = Filename
        End If
        Filename = Dir
    Loop


End Sub

Sub AnalyzeAllData()
    Dim i As Integer
    Dim VelocityFilename2 As String
    Dim VelocityFullFileName2 As String
    Dim endrow2 As Long


    Windows("FloorLocationMacroV4b.xls").Activate
    Sheets("resultfiles").Select
    endrow2 = Range("A64000").End(xlUp).row
    For i = 1 To endrow2
        Sheets("resultfiles").Select
        VelocityFilename2 = Cells(i, 1).Value
        VelocityFullFileName2 = "e:\Excel macro analysis\" + VelocityFilename2
        Workbooks.Open VelocityFullFileName2
        ImpactDistribution (VelocityFilename2)
        'Trajectory
        Workbooks(VelocityFilename2).Close False
    Next
End Sub

Sub ImpactDistribution(VelocityFilename2)

Dim endrow As Integer
Dim endrow2 As Integer
Dim FirstRow As Integer
Dim row As Integer
Dim x As Single
Dim y As Single
Dim speed As Single
Dim diameter As Single
Dim theta As Single
Dim XatFloor As Single
Dim dropvolume As Single
Dim totalvolume As Single
Dim pan As Integer

Dim volume(0 To 18) As Single


Windows(VelocityFilename2).Activate
```

```
    endrow = Range("A64000").End(xlUp).row
    FirstRow = Range("D1").End(xlDown).row
    FirstRow = FirstRow + 1

For row = FirstRow To endrow
    Windows(VelocityFilename2).Activate
    x = Abs(Cells(row, "A").Value)
    y = Abs(Cells(row, "B").Value)
    speed = Cells(row, "C").Value
    diameter = Cells(row, "D").Value / (10 ^ 6)
    theta = Cells(row, "E").Value

    Call Trajectory(VelocityFilename2, x, y, speed, diameter, theta, XatFloor)

    dropvolume = (4 / 3) * Pi * ((diameter / 2) ^ 3)

    If XatFloor >= 0 And XatFloor < 0.076 Then
            volume(0) = volume(0) + dropvolume * 2
        End If

    For pan = 1 To 18
        If XatFloor >= (pan * 0.152 - 0.076) And XatFloor < (pan * 0.152 + 0.076) Then
            volume(pan) = volume(pan) + dropvolume
        End If
    Next
Next

Windows("FloorLocationMacroV4b.xls").Activate      'Output water volume total for pans
    Sheets("ImpactDist").Select
    endrow2 = Range("A64000").End(xlUp).row
    endrow2 = endrow2 + 1

'For pan = 0 To 18
'    Range(Chr(65 + pan) & endrow2).Value = pan
'Next

Range("A" & endrow2).Value = VelocityFilename2

For pan = 0 To 18
    totalvolume = totalvolume + volume(pan)
Next

For pan = 0 To 18
    Range(Chr(65 + pan + 1) & endrow2).Value = volume(pan) / totalvolume
Next

'make VelocityFilename2 active
'get initial drop data from VelocityFilename2
'run trajectory(x0, y0, speed0, theta0, diameter, velocityFilename2, XatFloor)
'calculate volume of drop
'put drop volume in appropriate collection pan
'loop back for all drops in image
'output to ImpactDist sheet in FloorLocationMacroV2

End Sub
```

APPENDIX E

Droplet Size and Velocity Data

Table E-1a. Droplet number fraction data.

strike angle (deg)	orifice dia (mm)	flow rate (gpm)	flow rate (L/s)	drop diameter size bin (µm) 100	200	300	400	500	600	700	800	900	1000	1100	1200	1300	1400	1500
60	4	3	0.189	0.026	0.332	0.356	0.114	0.055	0.035	0.024	0.017	0.012	0.008	0.006	0.005	0.003	0.003	0.002
60	4	5	0.315	0.024	0.403	0.383	0.094	0.04	0.021	0.012	0.008	0.005	0.003	0.002	0.001	8E-04	6E-04	3E-04
60	4	6	0.379	0.022	0.399	0.421	0.089	0.033	0.018	0.009	0.005	0.002	0.001	4E-04	2E-04	1E-04	8E-05	1E-04
60	6	6	0.379	0.03	0.383	0.325	0.089	0.045	0.03	0.02	0.016	0.012	0.011	0.008	0.005	0.007	0.004	0.003
60	6	9	0.568	0.022	0.347	0.42	0.116	0.045	0.022	0.012	0.007	0.004	0.002	0.001	8E-04	3E-04	2E-04	1E-04
60	6	10	0.631	0.022	0.366	0.429	0.107	0.039	0.018	0.009	0.005	0.002	0.001	4E-04	2E-04	2E-04	2E-05	0
60	8.5	6	0.379	0.04	0.382	0.296	0.104	0.048	0.029	0.021	0.015	0.011	0.01	0.007	0.005	0.004	0.005	0.003
60	8.5	10	0.631	0.032	0.377	0.335	0.092	0.045	0.027	0.018	0.012	0.011	0.009	0.008	0.006	0.005	0.004	0.003
60	8.5	12	0.757	0.024	0.356	0.371	0.104	0.048	0.026	0.019	0.012	0.01	0.007	0.006	0.004	0.003	0.003	0.002
90	4	3	0.189	0.038	0.407	0.302	0.102	0.051	0.032	0.02	0.016	0.01	0.007	0.005	0.003	0.002	0.001	9E-04
90	4	5	0.315	0.023	0.37	0.378	0.116	0.052	0.024	0.014	0.009	0.005	0.003	0.002	0.001	7E-04	4E-04	3E-04
90	4	6	0.379	0.024	0.389	0.392	0.11	0.044	0.021	0.011	0.006	0.002	8E-04	4E-04	1E-04	2E-04	3E-05	0
90	6	6	0.379	0.038	0.419	0.262	0.118	0.055	0.031	0.022	0.015	0.01	0.009	0.004	0.004	0.003	0.002	0.002
90	6	9	0.568	0.023	0.354	0.313	0.156	0.069	0.036	0.023	0.013	0.007	0.004	0.002	7E-04	2E-04	2E-04	4E-05
90	6	10	0.631	0.021	0.352	0.349	0.144	0.057	0.03	0.019	0.011	0.007	0.004	0.003	0.002	6E-04	4E-04	2E-04
90	8.5	6	0.379	0.041	0.402	0.2	0.118	0.064	0.04	0.028	0.019	0.017	0.014	0.012	0.009	0.007	0.007	0.005
90	8.5	10	0.631	0.034	0.384	0.237	0.125	0.067	0.04	0.027	0.022	0.015	0.01	0.007	0.006	0.006	0.005	0.003
90	8.5	12	0.757	0.028	0.34	0.218	0.15	0.078	0.052	0.033	0.023	0.019	0.014	0.01	0.006	0.005	0.005	0.005
90	8.5	12	0.757	0.034	0.392	0.252	0.137	0.063	0.036	0.024	0.015	0.011	0.009	0.007	0.004	0.003	0.003	0.002
120	4	3	0.189	0.034	0.414	0.379	0.078	0.036	0.02	0.013	0.009	0.005	0.004	0.002	0.002	0.001	6E-04	2E-04
120	4	5	0.315	0.021	0.391	0.386	0.119	0.038	0.019	0.01	0.006	0.003	0.002	0.002	6E-04	4E-04	3E-04	1E-04
120	4	6	0.379	0.022	0.433	0.376	0.106	0.032	0.016	0.007	0.003	0.002	7E-04	6E-04	3E-04	2E-04	9E-05	1E-04
120	6	6	0.379	0.038	0.408	0.29	0.086	0.046	0.03	0.022	0.018	0.013	0.011	0.008	0.006	0.005	0.004	0.003
120	6	9	0.568	0.025	0.364	0.394	0.117	0.043	0.021	0.012	0.008	0.005	0.004	0.002	0.002	0.001	8E-04	6E-04
120	6	10	0.631	0.016	0.316	0.46	0.104	0.045	0.022	0.013	0.008	0.005	0.004	0.003	0.002	9E-04	6E-04	6E-04
120	8.5	6	0.379	0.034	0.372	0.327	0.09	0.045	0.03	0.02	0.016	0.013	0.011	0.01	0.007	0.006	0.004	0.004
120	8.5	10	0.631	0.031	0.367	0.319	0.099	0.046	0.032	0.028	0.02	0.013	0.011	0.007	0.006	0.005	0.004	0.004
120	8.5	12	0.757	0.04	0.406	0.291	0.085	0.051	0.031	0.026	0.017	0.011	0.009	0.007	0.006	0.004	0.003	0.003

Table E-1b. Droplet number fraction data.

strike angle (deg)	orifice dia (mm)	flow rate (gpm)	flow rate (L/s)	drop diameter size bin (μm) 1600	1700	1800	1900	2000	2100	2200	2300	2400	2500	2600	2700	2800	2900	3000
60	4	3	0.189	0.001	0.001	4E-04	4E-04	4E-04	0	0	7E-05	0	1E-04	0	0	0	0	0
60	4	5	0.315	2E-04	1E-04	3E-05	3E-05	0	6E-05	0	0	0	0	0	0	0	0	0
60	4	6	0.379	0	0	0	0	0	0	0	0	0	0	0	0	0	0	0
60	6	6	0.379	0.003	0.002	0.002	0.002	0.001	1E-03	1E-03	5E-04	4E-04	6E-04	3E-04	5E-04	0	2E-04	0
60	6	9	0.568	7E-05	0	0	0	0	0	0	0	0	2E-05	0	0	0	0	0
60	6	10	0.631	2E-05	0	0	0	0	0	0	0	0	0	0	0	0	0	0
60	8.5	6	0.379	0.003	0.002	0.002	0.002	0.001	0.001	0.001	6E-04	0.001	9E-04	0.001	5E-04	3E-04	5E-04	7E-04
60	8.5	10	0.631	0.003	0.002	0.002	0.001	0.001	9E-04	9E-04	9E-04	5E-04	7E-04	8E-04	6E-04	4E-04	7E-04	2E-04
60	8.5	12	0.757	0.001	0.001	7E-04	8E-04	6E-04	5E-04	4E-04	2E-04	3E-04	2E-04	8E-05	1E-04	1E-04	9E-05	4E-05
90	4	3	0.189	1E-03	2E-04	3E-04	1E-04	0	0	6E-05	0	0	0	0	0	0	0	0
90	4	5	0.315	1E-04	5E-05	0	5E-05	3E-05	3E-05	3E-05	0	0	0	0	0	0	0	0
90	4	6	0.379	0	0	0	0	0	0	0	0	0	0	0	0	0	0	0
90	6	6	0.379	0.002	0.001	0.001	0.001	4E-04	8E-05	8E-05	0	0	1E-04	8E-05	0	0	0	0
90	6	9	0.568	8E-05	0	0	0	0	0	0	0	0	0	0	0	0	0	0
90	6	10	0.631	2E-05	0	4E-05	2E-05	0	0	0	0	0	0	0	0	0	0	0
90	8.5	6	0.379	0.003	0.003	0.003	0.001	0.001	0.001	3E-04	3E-04	4E-04	6E-04	2E-04	2E-04	2E-04	2E-04	2E-04
90	8.5	10	0.631	0.004	0.002	0.001	0.001	0.001	6E-04	5E-04	6E-04	3E-04	3E-04	2E-04	7E-05	2E-04	0	0
90	8.5	12	0.757	0.003	0.002	0.003	0.001	0.001	0.001	0.001	3E-04	6E-04	3E-04	4E-04	1E-04	0	1E-04	0
90	8.5	12	0.757	0.002	0.002	0.001	6E-04	1E-03	6E-04	3E-04	3E-04	3E-04	2E-04	0	6E-05	0	0	6E-05
120	4	3	0.189	3E-04	9E-05	4E-05	0	0	0	0	0	0	0	0	0	0	0	0
120	4	5	0.315	1E-04	3E-05	4E-05	0	2E-05	0	0	0	0	0	0	0	0	0	0
120	4	6	0.379	0	0	0	0	0	0	0	0	0	0	0	0	0	0	0
120	6	6	0.379	0.003	0.002	0.002	0.002	0.001	8E-04	9E-04	4E-04	2E-04	3E-04	1E-04	5E-05	2E-04	0	5E-05
120	6	9	0.568	3E-04	3E-04	9E-05	1E-04	2E-05	0	0	1E-05	2E-05	2E-05	0	2E-05	0	0	2E-05
120	6	10	0.631	3E-04	3E-04	6E-05	6E-05	3E-05	0	0	0	3E-05	0	3E-05	0	0	0	0
120	8.5	6	0.379	0.002	0.002	0.002	8E-04	9E-04	0.001	9E-04	6E-04	3E-04	2E-04	3E-04	5E-05	2E-04	0	2E-04
120	8.5	10	0.631	0.003	0.002	0.001	0.001	2E-04	5E-04	4E-04	2E-04	2E-04	0	6E-04	0	7E-05	0	2E-04
120	8.5	12	0.757	0.002	0.001	0.002	1E-03	6E-04	4E-04	5E-04	2E-04	5E-04	2E-04	2E-04	3E-04	8E-05	0	0

Table E-2a. Droplet volume fraction data.

strike angle (deg)	orifice dia (mm)	flow rate (gpm)	flow rate (L/s)	drop diameter size bin (µm) 100	200	300	400	500	600	700	800	900	1000	1100	1200	1300	1400	1500
60	4	3	0.189	2E-04	0.011	0.054	0.046	0.048	0.056	0.066	0.07	0.073	0.068	0.065	0.077	0.056	0.069	0.045
60	4	5	0.315	5E-04	0.039	0.136	0.097	0.09	0.088	0.084	0.078	0.076	0.062	0.064	0.05	0.037	0.031	0.019
60	4	6	0.379	7E-04	0.061	0.234	0.143	0.116	0.118	0.097	0.078	0.05	0.04	0.02	0.015	0.009	0.008	0.01
60	6	6	0.379	1E-04	0.007	0.024	0.019	0.02	0.026	0.028	0.035	0.04	0.046	0.048	0.039	0.066	0.044	0.05
60	6	9	0.568	5E-04	0.036	0.181	0.138	0.117	0.107	0.096	0.083	0.064	0.046	0.04	0.037	0.019	0.012	0.008
60	6	10	0.631	7E-04	0.05	0.236	0.162	0.131	0.112	0.096	0.08	0.05	0.035	0.019	0.01	0.013	0.002	0
60	8.5	6	0.379	1E-04	0.005	0.016	0.016	0.016	0.018	0.021	0.023	0.025	0.03	0.031	0.031	0.032	0.043	0.038
60	8.5	10	0.631	1E-04	0.006	0.02	0.016	0.017	0.019	0.021	0.022	0.028	0.031	0.039	0.039	0.041	0.044	0.044
60	8.5	12	0.757	2E-04	0.012	0.048	0.039	0.039	0.039	0.046	0.045	0.051	0.051	0.058	0.053	0.056	0.055	0.052
90	4	3	0.189	5E-04	0.018	0.064	0.058	0.063	0.074	0.077	0.096	0.084	0.087	0.075	0.065	0.052	0.05	0.036
90	4	5	0.315	5E-04	0.03	0.13	0.112	0.108	0.092	0.09	0.086	0.072	0.067	0.059	0.045	0.03	0.019	0.024
90	4	6	0.379	8E-04	0.048	0.214	0.165	0.144	0.125	0.11	0.086	0.045	0.025	0.017	0.006	0.012	0.003	0
90	6	6	0.379	3E-04	0.012	0.039	0.046	0.047	0.049	0.057	0.059	0.056	0.069	0.047	0.049	0.057	0.052	0.054
90	6	9	0.568	4E-04	0.024	0.104	0.135	0.129	0.124	0.128	0.112	0.088	0.064	0.045	0.021	0.009	0.008	0.002
90	6	10	0.631	4E-04	0.024	0.112	0.121	0.104	0.102	0.105	0.096	0.088	0.075	0.059	0.047	0.024	0.023	0.012
90	8.5	6	0.379	2E-04	0.005	0.013	0.021	0.024	0.027	0.031	0.033	0.044	0.051	0.056	0.055	0.055	0.07	0.059
90	8.5	10	0.631	2E-04	0.007	0.021	0.029	0.033	0.037	0.041	0.049	0.049	0.048	0.048	0.05	0.061	0.064	0.046
90	8.5	12	0.757	1E-04	0.006	0.02	0.031	0.034	0.04	0.042	0.043	0.057	0.055	0.056	0.047	0.048	0.052	0.056
90	8.5	12	0.757	2E-04	0.009	0.03	0.043	0.042	0.044	0.048	0.046	0.05	0.059	0.057	0.046	0.04	0.045	0.05
120	4	3	0.189	7E-04	0.038	0.124	0.075	0.075	0.078	0.085	0.09	0.073	0.077	0.07	0.064	0.06	0.037	0.014
120	4	5	0.315	6E-04	0.041	0.182	0.144	0.102	0.096	0.082	0.07	0.064	0.052	0.052	0.031	0.023	0.021	0.012
120	4	6	0.379	8E-04	0.06	0.237	0.174	0.117	0.106	0.077	0.059	0.055	0.024	0.027	0.022	0.019	0.01	0.012
120	6	6	0.379	2E-04	0.008	0.023	0.02	0.023	0.028	0.033	0.042	0.046	0.053	0.049	0.051	0.054	0.057	0.046
120	6	9	0.568	5E-04	0.027	0.125	0.1	0.081	0.074	0.07	0.071	0.061	0.063	0.051	0.053	0.047	0.039	0.035
120	6	10	0.631	3E-04	0.027	0.138	0.089	0.084	0.076	0.075	0.07	0.065	0.069	0.068	0.053	0.034	0.028	0.034
120	8.5	6	0.379	2E-04	0.007	0.025	0.02	0.021	0.026	0.029	0.036	0.043	0.047	0.062	0.06	0.059	0.053	0.055
120	8.5	10	0.631	2E-04	0.008	0.028	0.025	0.025	0.033	0.048	0.051	0.049	0.056	0.052	0.057	0.058	0.054	0.069
120	8.5	12	0.757	2E-04	0.01	0.027	0.023	0.031	0.034	0.046	0.045	0.043	0.05	0.056	0.055	0.051	0.047	0.054

Table E-2b. Droplet volume fraction data.

strike angle (deg)	orifice dia (mm)	flow rate (gpm)	flow rate (L/s)	drop diameter size bin (µm) 1600	1700	1800	1900	2000	2100	2200	2300	2400	2500	2600	2700	2800	2900	3000
60	4	3	0.189	0.057	0.042	0.021	0.03	0.027	0	0	0.007	0	0.011	0	0	0	0	0
60	4	5	0.315	0.017	0.012	0.004	0.005	0	0.011	0	0	0	0	0	0	0	0	0
60	4	6	0.379	0	0	0	0	0	0	0	0	0	0	0	0	0	0	0
60	6	6	0.379	0.049	0.046	0.04	0.052	0.039	0.04	0.049	0.029	0.026	0.045	0.029	0.045	0	0.02	0
60	6	9	0.568	0.007	0	0	0	0	0	0	0	0	0.01	0	0	0	0	0
60	6	10	0.631	0.003	0	0	0	0	0	0	0	0	0	0	0	0	0	0
60	8.5	6	0.379	0.035	0.036	0.048	0.051	0.039	0.048	0.048	0.025	0.053	0.047	0.06	0.033	0.019	0.044	0.067
60	8.5	10	0.631	0.044	0.042	0.043	0.034	0.045	0.035	0.04	0.04	0.03	0.041	0.059	0.043	0.035	0.069	0.015
60	8.5	12	0.757	0.044	0.05	0.022	0.036	0.037	0.027	0.025	0.023	0.019	0.022	0.009	0.013	0.009	0.015	0.005
90	4	3	0.189	0.05	0.012	0.021	0.009	0	0	0.008	0	0	0	0	0	0	0	0
90	4	5	0.315	0.009	0.006	0	0.007	0.004	0.006	0.005	0	0	0	0	0	0	0	0
90	4	6	0.379	0	0	0	0	0	0	0	0	0	0	0	0	0	0	0
90	6	6	0.379	0.059	0.05	0.063	0.064	0.022	0.009	0.007	0	0	0.022	0.012	0	0	0	0
90	6	9	0.568	0.006	0	0	0	0	0	0	0	0	0	0	0	0	0	0
90	6	10	0.631	0.002	0	0.004	0.002	0	0	0	0	0	0	0	0	0	0	0
90	8.5	6	0.379	0.051	0.049	0.063	0.031	0.04	0.041	0.012	0.016	0.019	0.037	0.016	0.015	0.021	0.024	0.018
90	8.5	10	0.631	0.07	0.048	0.043	0.039	0.043	0.029	0.026	0.037	0.023	0.022	0.014	0.005	0.019	0	0
90	8.5	12	0.757	0.045	0.04	0.065	0.039	0.041	0.043	0.035	0.02	0.032	0.01	0.022	0.01	0	0.013	0
90	8.5	12	0.757	0.053	0.059	0.049	0.031	0.049	0.036	0.024	0.027	0.026	0.017	0	0.008	0	0	0.011
120	4	3	0.189	0.023	0.009	0.005	0	0	0	0	0	0	0	0	0	0	0	0
120	4	5	0.315	0.013	0.005	0.006	0	0.004	0	0	0	0	0	0	0	0	0	0
120	4	6	0.379	0	0	0	0	0	0	0	0	0	0	0	0	0	0	0
120	6	6	0.379	0.063	0.051	0.05	0.06	0.04	0.036	0.052	0.028	0.018	0.023	0.013	0.005	0.021	0	0.007
120	6	9	0.568	0.022	0.026	0.009	0.014	0.003	0	0	0.004	0.005	0.005	0	0.006	0	0	0.008
120	6	10	0.631	0.02	0.031	0.007	0.008	0.006	0	0	0	0.007	0	0.009	0	0	0	0
120	8.5	6	0.379	0.049	0.045	0.053	0.03	0.036	0.052	0.048	0.037	0.018	0.019	0.03	0.005	0.014	0	0.023
120	8.5	10	0.631	0.066	0.067	0.035	0.044	0.01	0.027	0.022	0.012	0.014	0	0.054	0	0.011	0	0.024
120	8.5	12	0.757	0.045	0.036	0.082	0.039	0.027	0.02	0.034	0.016	0.037	0.013	0.023	0.045	0.01	0	0

Table E-3a. Droplet cumulative number fraction data.

strike angle (deg)	orifice dia (mm)	flow rate (gpm)	flow rate (L/s)	drop diameter size bin (µm) 100	200	300	400	500	600	700	800	900	1000	1100	1200	1300	1400	1500
60	4	3	0.189	0.026	0.357	0.713	0.827	0.882	0.917	0.941	0.958	0.97	0.978	0.983	0.989	0.992	0.995	0.996
60	4	5	0.315	0.024	0.427	0.811	0.905	0.945	0.966	0.979	0.986	0.991	0.994	0.997	0.998	0.999	0.999	1
60	4	6	0.379	0.022	0.421	0.842	0.93	0.964	0.982	0.991	0.996	0.998	0.999	0.999	1	1	1	1
60	6	6	0.379	0.03	0.412	0.737	0.826	0.871	0.901	0.921	0.937	0.949	0.96	0.968	0.973	0.98	0.983	0.987
60	6	9	0.568	0.022	0.369	0.789	0.905	0.95	0.973	0.985	0.992	0.995	0.997	0.998	0.999	1	1	1
60	6	10	0.631	0.022	0.388	0.817	0.924	0.963	0.981	0.991	0.996	0.998	0.999	1	1	1	1	1
60	8.5	6	0.379	0.04	0.422	0.718	0.821	0.869	0.899	0.92	0.935	0.946	0.956	0.963	0.968	0.973	0.978	0.981
60	8.5	10	0.631	0.032	0.409	0.744	0.835	0.88	0.907	0.926	0.938	0.948	0.957	0.965	0.971	0.976	0.98	0.984
60	8.5	12	0.757	0.024	0.38	0.751	0.854	0.902	0.928	0.947	0.959	0.968	0.975	0.981	0.985	0.988	0.991	0.993
90	4	3	0.189	0.038	0.445	0.747	0.849	0.9	0.932	0.952	0.969	0.979	0.986	0.991	0.994	0.996	0.997	0.998
90	4	5	0.315	0.023	0.393	0.771	0.887	0.939	0.963	0.977	0.986	0.991	0.995	0.997	0.998	0.999	0.999	1
90	4	6	0.379	0.024	0.413	0.805	0.914	0.959	0.98	0.991	0.996	0.998	0.999	1	1	1	1	1
90	6	6	0.379	0.038	0.457	0.718	0.837	0.892	0.923	0.945	0.961	0.97	0.979	0.983	0.987	0.99	0.992	0.994
90	6	9	0.568	0.023	0.377	0.69	0.846	0.915	0.951	0.974	0.986	0.993	0.997	0.999	1	1	1	1
90	6	10	0.631	0.021	0.373	0.722	0.866	0.923	0.953	0.972	0.983	0.99	0.995	0.997	0.999	0.999	1	1
90	8.5	6	0.379	0.041	0.444	0.644	0.762	0.826	0.867	0.895	0.914	0.931	0.946	0.957	0.966	0.973	0.98	0.984
90	8.5	10	0.631	0.034	0.418	0.654	0.779	0.847	0.887	0.914	0.936	0.95	0.961	0.968	0.975	0.98	0.985	0.988
90	8.5	12	0.757	0.028	0.368	0.586	0.736	0.814	0.866	0.899	0.922	0.942	0.955	0.965	0.971	0.977	0.981	0.986
90	8.5	12	0.757	0.034	0.426	0.678	0.815	0.877	0.914	0.938	0.953	0.964	0.973	0.98	0.984	0.987	0.989	0.992
120	4	3	0.189	0.034	0.448	0.828	0.906	0.941	0.962	0.975	0.984	0.989	0.993	0.996	0.997	0.999	0.999	1
120	4	5	0.315	0.021	0.412	0.799	0.918	0.956	0.976	0.986	0.991	0.995	0.997	0.998	0.999	0.999	1	1
120	4	6	0.379	0.022	0.455	0.831	0.938	0.97	0.985	0.992	0.996	0.998	0.999	0.999	1	1	1	1
120	6	6	0.379	0.038	0.445	0.735	0.821	0.867	0.897	0.919	0.937	0.951	0.962	0.969	0.976	0.98	0.985	0.987
120	6	9	0.568	0.025	0.389	0.783	0.9	0.943	0.965	0.977	0.985	0.989	0.993	0.995	0.997	0.998	0.999	0.999
120	6	10	0.631	0.016	0.332	0.792	0.896	0.941	0.963	0.976	0.984	0.989	0.993	0.995	0.997	0.998	0.999	0.999
120	8.5	6	0.379	0.034	0.406	0.732	0.822	0.867	0.897	0.917	0.933	0.946	0.957	0.967	0.975	0.98	0.984	0.988
120	8.5	10	0.631	0.031	0.397	0.717	0.815	0.861	0.893	0.921	0.941	0.954	0.965	0.972	0.978	0.983	0.986	0.99
120	8.5	12	0.757	0.04	0.446	0.737	0.822	0.874	0.905	0.93	0.947	0.958	0.967	0.975	0.98	0.985	0.988	0.99

Table E-3b. Droplet cumulative number fraction data.

strike angle (deg)	orifice dia (mm)	flow rate (gpm)	flow rate (L/s)	drop diameter size bin (µm) 1600	1700	1800	1900	2000	2100	2200	2300	2400	2500	2600	2700	2800	2900	3000	approx. median dia (µm)
60	4	3	0.189	0.998	0.999	0.999	0.999	1	1	1	1	1	1	1	1	1	1	1	240
60	4	5	0.315	1	1	1	1	1	1	1	1	1	1	1	1	1	1	1	219
60	4	6	0.379	1	1	1	1	1	1	1	1	1	1	1	1	1	1	1	219
60	6	6	0.379	0.989	0.991	0.993	0.994	0.996	0.996	0.997	0.998	0.998	0.999	0.999	1	1	1	1	227
60	6	9	0.568	1	1	1	1	1	1	1	1	1	1	1	1	1	1	1	231
60	6	10	0.631	1	1	1	1	1	1	1	1	1	1	1	1	1	1	1	226
60	8.5	6	0.379	0.983	0.986	0.988	0.99	0.992	0.993	0.994	0.995	0.996	0.997	0.998	0.999	0.999	0.999	1	226
60	8.5	10	0.631	0.987	0.989	0.991	0.992	0.993	0.994	0.995	0.996	0.997	0.997	0.998	0.999	0.999	1	1	227
60	8.5	12	0.757	0.995	0.996	0.997	0.997	0.998	0.998	0.999	0.999	0.999	1	1	1	1	1	1	232
90	4	3	0.189	0.999	0.999	1	1	1	1	1	1	1	1	1	1	1	1	1	218
90	4	5	0.315	1	1	1	1	1	1	1	1	1	1	1	1	1	1	1	228
90	4	6	0.379	1	1	1	1	1	1	1	1	1	1	1	1	1	1	1	222
90	6	6	0.379	0.996	0.997	0.998	0.999	1	1	1	1	1	1	1	1	1	1	1	216
90	6	9	0.568	1	1	1	1	1	1	1	1	1	1	1	1	1	1	1	239
90	6	10	0.631	1	1	1	1	1	1	1	1	1	1	1	1	1	1	1	236
90	8.5	6	0.379	0.988	0.991	0.994	0.995	0.996	0.997	0.998	0.998	0.998	0.999	0.999	0.999	1	1	1	228
90	8.5	10	0.631	0.991	0.993	0.995	0.996	0.997	0.998	0.998	0.999	0.999	1	1	1	1	1	1	235
90	8.5	12	0.757	0.989	0.991	0.994	0.995	0.996	0.997	0.998	0.998	0.999	0.999	1	1	1	1	1	261
90	8.5	12	0.757	0.994	0.995	0.997	0.997	0.998	0.999	0.999	0.999	1	1	1	1	1	1	1	229
120	4	3	0.189	1	1	1	1	1	1	1	1	1	1	1	1	1	1	1	214
120	4	5	0.315	1	1	1	1	1	1	1	1	1	1	1	1	1	1	1	223
120	4	6	0.379	1	1	1	1	1	1	1	1	1	1	1	1	1	1	1	212
120	6	6	0.379	0.99	0.993	0.994	0.996	0.997	0.998	0.999	0.999	0.999	1	1	1	1	1	1	219
120	6	9	0.568	0.999	1	1	1	1	1	1	1	1	1	1	1	1	1	1	228
120	6	10	0.631	0.999	1	1	1	1	1	1	1	1	1	1	1	1	1	1	237
120	8.5	6	0.379	0.991	0.993	0.994	0.995	0.996	0.997	0.998	0.999	0.999	0.999	1	1	1	1	1	229
120	8.5	10	0.631	0.993	0.996	0.997	0.998	0.998	0.999	0.999	0.999	0.999	0.999	1	1	1	1	1	232
120	8.5	12	0.757	0.992	0.994	0.996	0.997	0.998	0.998	0.999	0.999	0.999	0.999	1	1	1	1	1	219

Table E-4a. Droplet cumulative volume fraction data.

strike angle (deg)	orifice dia (mm)	flow rate (gpm)	flow rate (L/s)	drop diameter size bin (μm) 100	200	300	400	500	600	700	800	900	1000	1100	1200	1300	1400	1500
60	4	3	0.189	2E-04	0.012	0.065	0.111	0.16	0.216	0.282	0.352	0.425	0.492	0.557	0.634	0.691	0.759	0.804
60	4	5	0.315	5E-04	0.039	0.176	0.272	0.362	0.45	0.534	0.612	0.688	0.751	0.815	0.865	0.901	0.932	0.951
60	4	6	0.379	7E-04	0.061	0.296	0.439	0.555	0.673	0.769	0.848	0.898	0.938	0.958	0.973	0.982	0.99	1
60	6	6	0.379	1E-04	0.007	0.031	0.049	0.07	0.096	0.123	0.158	0.198	0.244	0.292	0.331	0.397	0.441	0.491
60	6	9	0.568	5E-04	0.036	0.217	0.355	0.472	0.579	0.675	0.757	0.822	0.868	0.907	0.944	0.963	0.975	0.983
60	6	10	0.631	7E-04	0.05	0.286	0.448	0.58	0.692	0.788	0.868	0.919	0.954	0.973	0.982	0.995	0.997	0.997
60	8.5	6	0.379	1E-04	0.005	0.021	0.037	0.053	0.07	0.091	0.115	0.14	0.17	0.202	0.233	0.265	0.308	0.345
60	8.5	10	0.631	1E-04	0.006	0.026	0.042	0.059	0.078	0.099	0.121	0.148	0.18	0.219	0.257	0.298	0.342	0.386
60	8.5	12	0.757	2E-04	0.012	0.06	0.1	0.139	0.177	0.223	0.269	0.32	0.371	0.428	0.481	0.537	0.592	0.644
90	4	3	0.189	5E-04	0.018	0.083	0.14	0.203	0.277	0.354	0.45	0.534	0.621	0.696	0.762	0.814	0.864	0.9
90	4	5	0.315	5E-04	0.03	0.16	0.272	0.38	0.472	0.562	0.647	0.719	0.786	0.845	0.89	0.92	0.939	0.963
90	4	6	0.379	8E-04	0.049	0.263	0.428	0.571	0.697	0.806	0.892	0.938	0.963	0.98	0.986	0.997	1	1
90	6	6	0.379	3E-04	0.013	0.052	0.098	0.145	0.193	0.251	0.31	0.365	0.434	0.481	0.53	0.587	0.639	0.693
90	6	9	0.568	4E-04	0.025	0.129	0.264	0.393	0.517	0.645	0.757	0.845	0.909	0.954	0.974	0.983	0.992	0.994
90	6	10	0.631	4E-04	0.025	0.137	0.258	0.362	0.464	0.569	0.665	0.753	0.827	0.887	0.933	0.957	0.98	0.992
90	8.5	6	0.379	2E-04	0.005	0.018	0.039	0.063	0.09	0.121	0.154	0.198	0.249	0.305	0.36	0.416	0.486	0.545
90	8.5	10	0.631	2E-04	0.007	0.028	0.057	0.09	0.126	0.167	0.216	0.265	0.313	0.361	0.411	0.472	0.536	0.582
90	8.5	12	0.757	1E-04	0.006	0.026	0.057	0.091	0.13	0.172	0.216	0.272	0.327	0.383	0.43	0.478	0.529	0.585
90	8.5	12	0.757	2E-04	0.009	0.04	0.082	0.124	0.169	0.217	0.263	0.313	0.371	0.428	0.474	0.514	0.559	0.609
120	4	3	0.189	7E-04	0.038	0.162	0.237	0.313	0.391	0.477	0.567	0.64	0.717	0.787	0.851	0.912	0.949	0.963
120	4	5	0.315	6E-04	0.042	0.224	0.368	0.471	0.567	0.649	0.719	0.782	0.834	0.886	0.917	0.94	0.96	0.972
120	4	6	0.379	8E-04	0.061	0.298	0.472	0.589	0.695	0.772	0.831	0.886	0.91	0.937	0.959	0.978	0.988	1
120	6	6	0.379	2E-04	0.008	0.031	0.051	0.074	0.102	0.135	0.178	0.224	0.276	0.326	0.377	0.431	0.488	0.535
120	6	9	0.568	5E-04	0.028	0.152	0.252	0.333	0.408	0.478	0.548	0.61	0.673	0.724	0.777	0.824	0.863	0.898
120	6	10	0.631	3E-04	0.028	0.166	0.255	0.34	0.415	0.491	0.56	0.625	0.694	0.761	0.815	0.849	0.877	0.911
120	8.5	6	0.379	2E-04	0.007	0.032	0.053	0.074	0.1	0.129	0.164	0.207	0.255	0.316	0.376	0.436	0.488	0.543
120	8.5	10	0.631	2E-04	0.009	0.037	0.062	0.087	0.12	0.167	0.218	0.268	0.323	0.375	0.432	0.49	0.544	0.612
120	8.5	12	0.757	2E-04	0.01	0.037	0.06	0.091	0.124	0.171	0.216	0.259	0.309	0.366	0.421	0.471	0.518	0.572

Table E-4b. Droplet cumulative volume fraction data.

strike angle (deg)	orifice dia (mm)	flow rate (gpm)	flow rate (L/s)	drop diameter size bin (µm) 1600	1700	1800	1900	2000	2100	2200	2300	2400	2500	2600	2700	2800	2900	3000	approx. volume median dia (µm)
60	4	3	0.189	0.861	0.903	0.924	0.954	0.982	0.982	0.982	0.989	0.989	1	1	1	1	1	1	1000
60	4	5	0.315	0.968	0.98	0.984	0.989	0.989	1	1	1	1	1	1	1	1	1	1	650
60	4	6	0.379	1	1	1	1	1	1	1	1	1	1	1	1	1	1	1	450
60	6	6	0.379	0.54	0.586	0.626	0.678	0.717	0.757	0.806	0.836	0.862	0.907	0.936	0.98	0.98	1	1	1500
60	6	9	0.568	0.99	0.99	0.99	0.99	0.99	0.99	0.99	0.99	0.99	1	1	1	1	1	1	530
60	6	10	0.631	1	1	1	1	1	1	1	1	1	1	1	1	1	1	1	450
60	8.5	6	0.379	0.381	0.417	0.465	0.516	0.556	0.604	0.652	0.677	0.729	0.777	0.837	0.87	0.888	0.933	1	1900
60	8.5	10	0.631	0.43	0.472	0.514	0.548	0.592	0.627	0.667	0.707	0.737	0.779	0.838	0.881	0.915	0.985	1	1800
60	8.5	12	0.757	0.688	0.739	0.76	0.796	0.833	0.861	0.886	0.908	0.927	0.949	0.958	0.971	0.98	0.995	1	1250
90	4	3	0.189	0.95	0.962	0.983	0.992	0.992	0.992	1	1	1	1	1	1	1	1	1	850
90	4	5	0.315	0.972	0.978	0.978	0.985	0.989	0.995	1	1	1	1	1	1	1	1	1	630
90	4	6	0.379	1	1	1	1	1	1	1	1	1	1	1	1	1	1	1	450
90	6	6	0.379	0.752	0.802	0.864	0.928	0.95	0.959	0.966	0.966	0.966	0.988	1	1	1	1	1	1150
90	6	9	0.568	1	1	1	1	1	1	1	1	1	1	1	1	1	1	1	600
90	6	10	0.631	0.994	0.994	0.998	1	1	1	1	1	1	1	1	1	1	1	1	650
90	8.5	6	0.379	0.597	0.645	0.708	0.74	0.779	0.821	0.833	0.849	0.867	0.905	0.921	0.936	0.957	0.982	1	1430
90	8.5	10	0.631	0.652	0.7	0.743	0.782	0.825	0.854	0.88	0.917	0.94	0.962	0.976	0.981	1	1	1	1350
90	8.5	12	0.757	0.63	0.669	0.735	0.773	0.815	0.857	0.893	0.912	0.944	0.955	0.977	0.987	0.987	1	1	1350
90	8.5	12	0.757	0.662	0.721	0.77	0.801	0.851	0.887	0.911	0.938	0.964	0.981	0.981	0.989	0.989	0.989	1	1300
120	4	3	0.189	0.986	0.995	1	1	1	1	1	1	1	1	1	1	1	1	1	750
120	4	5	0.315	0.985	0.99	0.996	0.996	1	1	1	1	1	1	1	1	1	1	1	550
120	4	6	0.379	1	1	1	1	1	1	1	1	1	1	1	1	1	1	1	430
120	6	6	0.379	0.597	0.648	0.698	0.758	0.798	0.834	0.885	0.913	0.931	0.954	0.967	0.972	0.993	0.993	1	1425
120	6	9	0.568	0.92	0.946	0.955	0.97	0.972	0.972	0.972	0.976	0.98	0.985	0.985	0.992	0.992	0.992	1	750
120	6	10	0.631	0.932	0.963	0.97	0.978	0.984	0.984	0.984	0.984	0.991	0.991	1	1	1	1	1	700
120	8.5	6	0.379	0.591	0.637	0.689	0.719	0.755	0.807	0.854	0.892	0.91	0.929	0.958	0.964	0.977	0.977	1	1430
120	8.5	10	0.631	0.679	0.746	0.781	0.825	0.835	0.863	0.885	0.897	0.911	0.911	0.965	0.965	0.976	0.976	1	1325
120	8.5	12	0.757	0.618	0.654	0.736	0.775	0.803	0.822	0.856	0.872	0.909	0.922	0.946	0.99	1	1	1	1370

Table E-5a. Magnitude of droplet velocity data (m/s).

strike angle (deg)	orifice dia (mm)	flow rate (gpm)	flow rate (L/s)	drop diameter size bin (µm) 100	200	300	400	500	600	700	800	900	1000	1100	1200	1300	1400	1500
60	4	3	0.189	0.00	6.08	4.28	5.31	6.44	7.19	7.60	7.99	8.21	8.50	8.73	8.74	8.85	8.89	8.88
60	4	5	0.315	0.00	11.14	8.54	9.60	11.37	12.43	13.15	13.81	14.02	13.94	14.66	14.58	14.52	14.51	14.50
60	4	6	0.379	0.00	12.09	10.82	11.50	13.20	14.17	14.78	15.40	15.87	15.77	17.41	15.64	16.81	19.26	16.77
60	6	6	0.379	0.00	6.55	5.43	5.92	6.92	7.65	8.00	8.44	8.55	8.85	8.99	9.05	9.24	9.45	9.54
60	6	9	0.568	3.92	9.39	8.17	9.49	11.33	12.31	13.15	13.55	14.16	14.44	14.72	15.16	15.74	15.81	15.18
60	6	10	0.631	9.67	11.99	9.92	11.18	12.93	13.86	14.68	14.98	15.48	16.51	16.48	16.57	15.65	15.52	0.00
60	8.5	6	0.379	4.82	5.11	4.08	3.97	4.54	4.88	5.02	5.19	5.49	5.44	5.52	5.48	5.70	5.77	5.79
60	8.5	10	0.631	7.97	7.30	5.77	5.87	6.68	7.16	7.57	7.66	7.85	8.16	8.17	8.24	8.46	8.45	8.62
60	8.5	12	0.757	0.00	8.66	7.04	7.55	8.91	9.69	10.19	10.56	10.89	11.19	11.57	11.64	11.67	11.85	11.97
90	4	3	0.189	0.00	6.35	4.82	5.84	6.86	7.66	8.04	8.24	8.29	8.55	8.62	8.97	8.77	8.56	8.87
90	4	5	0.315	0.00	12.99	11.21	11.24	12.85	13.98	14.83	15.34	15.89	15.92	15.81	16.96	16.67	15.01	16.30
90	4	6	0.379	0.00	16.43	13.81	13.50	14.93	15.82	17.14	17.44	17.46	19.13	18.67	22.21	22.40	20.51	0.00
90	6	6	0.379	14.41	9.50	7.51	6.83	8.12	9.08	9.61	9.98	10.29	10.36	10.55	10.82	11.05	11.05	11.06
90	6	9	0.568	0.00	17.25	17.43	14.97	16.39	17.74	18.07	18.58	19.02	19.22	18.72	18.41	22.63	18.00	19.39
90	6	10	0.631	22.72	15.22	14.10	12.56	13.92	14.67	15.42	16.15	16.10	17.29	17.14	17.59	18.56	17.96	16.89
90	8.5	6	0.379	4.58	5.48	5.18	4.13	4.66	5.10	5.33	5.44	5.69	5.74	5.86	5.86	5.92	5.95	6.10
90	8.5	10	0.631	0.00	9.07	8.48	7.21	7.76	8.63	8.88	9.25	9.44	9.52	9.57	9.47	9.90	9.78	9.94
90	8.5	12	0.757	6.37	11.69	10.66	9.27	9.78	10.53	11.17	11.35	11.58	11.68	11.91	12.09	11.74	12.09	12.47
90	8.5	12	0.757	0.00	10.12	9.46	8.01	9.32	10.28	10.85	11.20	11.46	11.84	11.97	12.17	12.56	12.59	12.83
120	4	3	0.189	9.07	8.70	5.32	5.54	6.95	7.52	8.18	8.49	8.79	8.99	9.37	9.51	9.55	9.44	9.49
120	4	5	0.315	0.00	13.77	11.35	11.40	12.34	13.58	13.89	14.98	15.63	15.97	16.20	16.12	16.01	19.08	17.20
120	4	6	0.379	0.00	17.51	15.37	14.26	15.40	16.77	18.70	18.63	19.03	22.01	21.39	21.67	20.90	20.86	0.00
120	6	6	0.379	0.00	8.45	6.36	5.86	6.86	7.50	7.95	8.33	8.58	8.93	8.98	9.19	9.47	9.43	9.56
120	6	9	0.568	13.42	12.60	11.41	10.28	11.39	12.74	13.49	14.02	14.44	14.96	15.23	15.20	15.97	15.66	15.91
120	6	10	0.631	9.79	13.46	10.82	10.30	11.64	12.68	13.35	14.37	14.84	15.56	16.47	15.65	16.11	15.72	17.81
120	8.5	6	0.379	0.00	4.85	4.06	3.89	4.47	4.78	5.01	5.26	5.40	5.52	5.77	5.72	5.79	5.92	6.16
120	8.5	10	0.631	9.23	9.06	7.31	6.57	7.39	8.01	8.31	8.76	9.03	9.14	9.39	9.76	9.41	9.85	9.57
120	8.5	12	0.757	8.14	10.82	8.47	7.81	8.22	9.48	9.95	10.40	10.28	10.84	11.33	11.36	11.44	11.67	11.80

Table E-5b. Magnitude of droplet velocity data (m/s).

strike angle (deg)	orifice dia (mm)	flow rate (gpm)	flow rate (L/s)	drop diameter size bin (μm) 1600	1700	1800	1900	2000	2100	2200	2300	2400	2500	2600	2700	2800	2900	3000
60	4	3	0.189	9.03	9.35	9.16	9.34	9.05	0.00	0.00	10.39	0.00	8.65	0.00	0.00	0.00	0.00	0.00
60	4	5	0.315	15.59	13.95	16.64	12.54	0.00	15.06	0.00	0.00	0.00	0.00	0.00	0.00	0.00	0.00	0.00
60	4	6	0.379	0.00	0.00	0.00	0.00	0.00	0.00	0.00	0.00	0.00	0.00	0.00	0.00	0.00	0.00	0.00
60	6	6	0.379	9.25	9.51	9.48	9.42	9.41	9.77	9.61	9.64	9.43	9.86	9.89	9.76	0.00	10.23	0.00
60	6	9	0.568	15.15	0.00	0.00	0.00	0.00	0.00	0.00	0.00	0.00	0.00	0.00	0.00	0.00	0.00	0.00
60	6	10	0.631	16.45	0.00	0.00	0.00	0.00	0.00	0.00	0.00	0.00	0.00	0.00	0.00	0.00	0.00	0.00
60	8.5	6	0.379	5.73	5.82	5.77	5.79	5.87	5.87	5.90	6.05	5.75	5.82	5.97	5.78	5.67	5.67	5.74
60	8.5	10	0.631	8.38	8.51	8.62	8.76	8.80	8.59	8.87	8.62	8.73	8.90	9.02	9.05	8.58	8.82	8.90
60	8.5	12	0.757	11.88	11.81	12.14	11.93	11.98	11.22	11.30	12.13	12.16	12.38	12.01	11.82	11.08	11.71	11.43
90	4	3	0.189	9.37	8.65	9.25	9.14	0.00	0.00	9.50	0.00	0.00	0.00	0.00	0.00	0.00	0.00	0.00
90	4	5	0.315	16.77	17.50	0.00	20.26	17.32	16.09	8.37	0.00	0.00	0.00	0.00	0.00	0.00	0.00	0.00
90	4	6	0.379	0.00	0.00	0.00	0.00	0.00	0.00	0.00	0.00	0.00	0.00	0.00	0.00	0.00	0.00	0.00
90	6	6	0.379	10.81	10.94	11.61	11.31	11.31	13.13	12.48	0.00	0.00	12.60	11.74	0.00	0.00	0.00	0.00
90	6	9	0.568	16.65	0.00	0.00	0.00	0.00	0.00	0.00	0.00	0.00	0.00	0.00	0.00	0.00	0.00	0.00
90	6	10	0.631	15.37	0.00	18.24	17.58	0.00	0.00	0.00	0.00	0.00	0.00	0.00	0.00	0.00	0.00	0.00
90	8.5	6	0.379	6.00	6.05	5.93	6.36	6.34	5.92	6.41	6.16	5.74	6.20	6.83	7.32	6.31	6.85	6.59
90	8.5	10	0.631	10.17	9.90	10.03	9.98	10.09	10.31	9.73	9.93	9.93	10.13	10.69	0.00	10.92	0.00	0.00
90	8.5	12	0.757	12.42	12.13	12.23	11.66	12.53	12.72	12.49	12.64	13.47	12.25	12.83	11.54	0.00	12.78	0.00
90	8.5	12	0.757	12.45	12.20	13.04	12.63	12.43	12.57	13.10	12.70	12.72	12.18	0.00	13.09	0.00	0.00	13.50
120	4	3	0.189	9.44	11.09	0.00	0.00	0.00	0.00	0.00	0.00	0.00	0.00	0.00	0.00	0.00	0.00	0.00
120	4	5	0.315	16.72	19.12	17.95	0.00	17.03	0.00	0.00	0.00	0.00	0.00	0.00	0.00	0.00	0.00	0.00
120	4	6	0.379	0.00	0.00	0.00	0.00	0.00	0.00	0.00	0.00	0.00	0.00	0.00	0.00	0.00	0.00	0.00
120	6	6	0.379	9.61	9.62	9.88	9.61	9.84	9.77	9.94	9.69	9.22	10.94	9.80	9.32	10.01	0.00	0.00
120	6	9	0.568	16.34	16.01	15.03	15.74	13.05	0.00	0.00	19.53	18.65	14.98	0.00	18.30	0.00	0.00	0.00
120	6	10	0.631	16.27	15.70	17.73	16.43	19.98	0.00	0.00	0.00	15.17	0.00	0.00	0.00	0.00	0.00	0.00
120	8.5	6	0.379	5.80	5.87	5.89	6.27	5.79	5.93	6.22	6.08	5.98	5.37	6.66	5.43	5.88	0.00	6.20
120	8.5	10	0.631	10.01	9.61	9.79	10.22	10.21	10.48	9.30	9.42	9.48	0.00	10.45	0.00	10.64	0.00	11.48
120	8.5	12	0.757	12.12	11.24	11.57	11.94	11.46	11.75	11.74	12.21	11.76	9.48	12.58	12.01	10.44	0.00	0.00

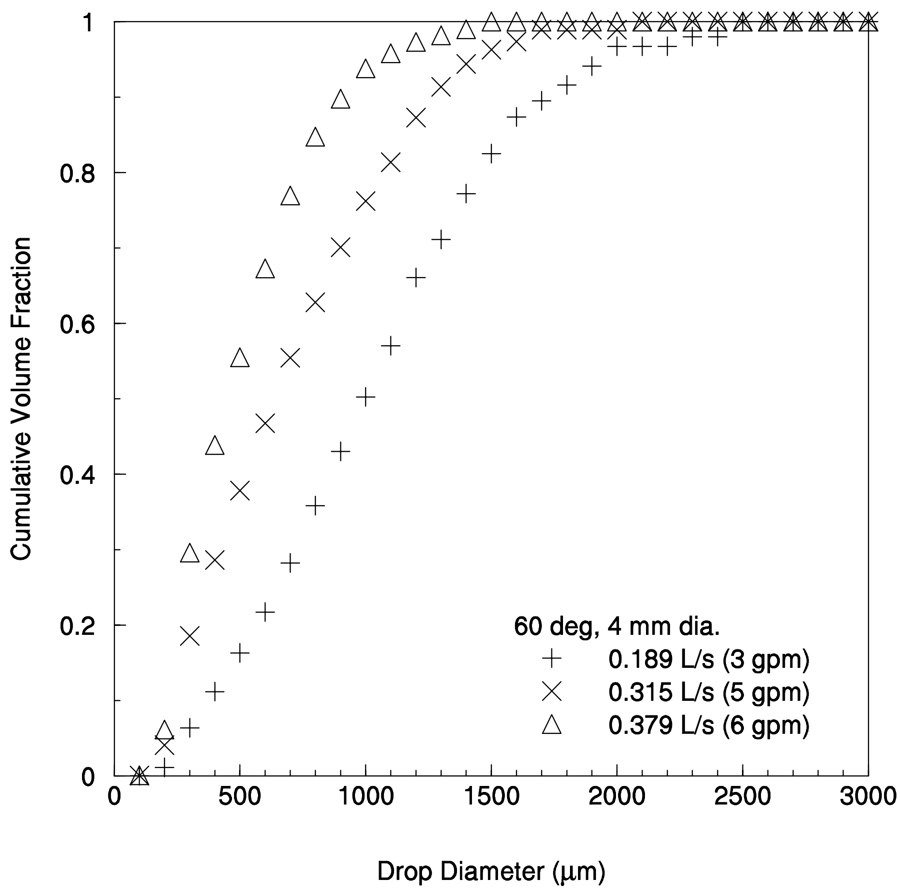

Figure E-1. Droplet cumulative water volume fraction function for a 4 mm nominal diameter orifice sprinkler with a 60 degree strike plate.

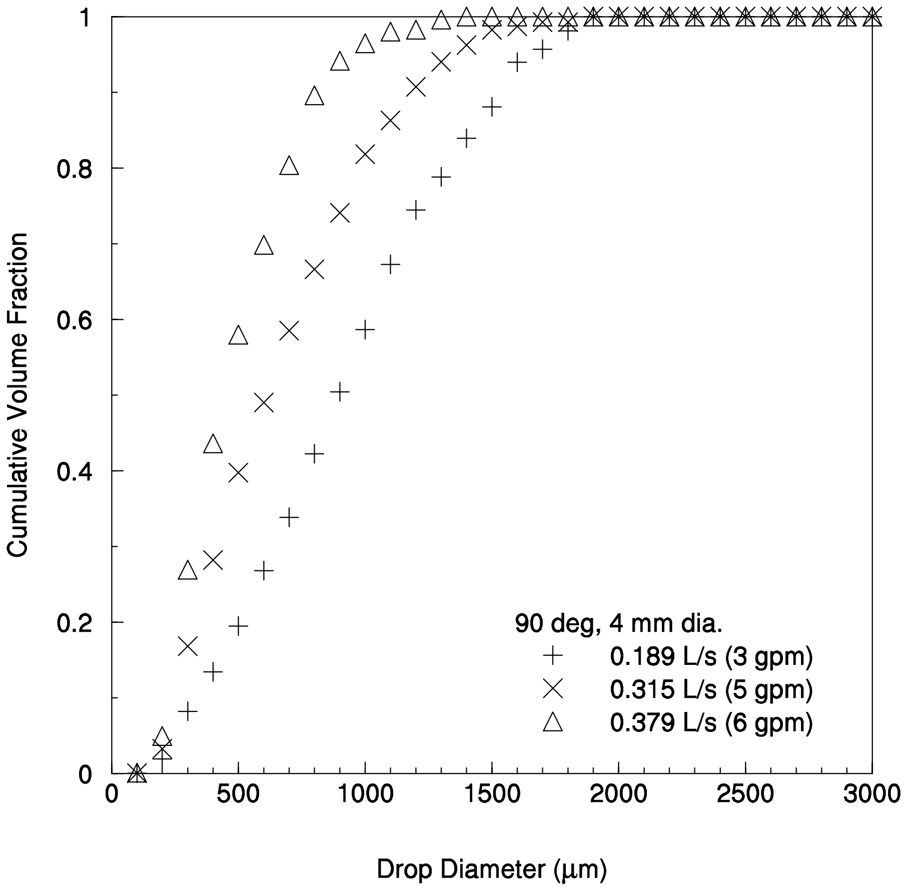

Figure E-2. Droplet cumulative water volume fraction function for a 4 mm nominal diameter orifice sprinkler with a 90 degree strike plate.

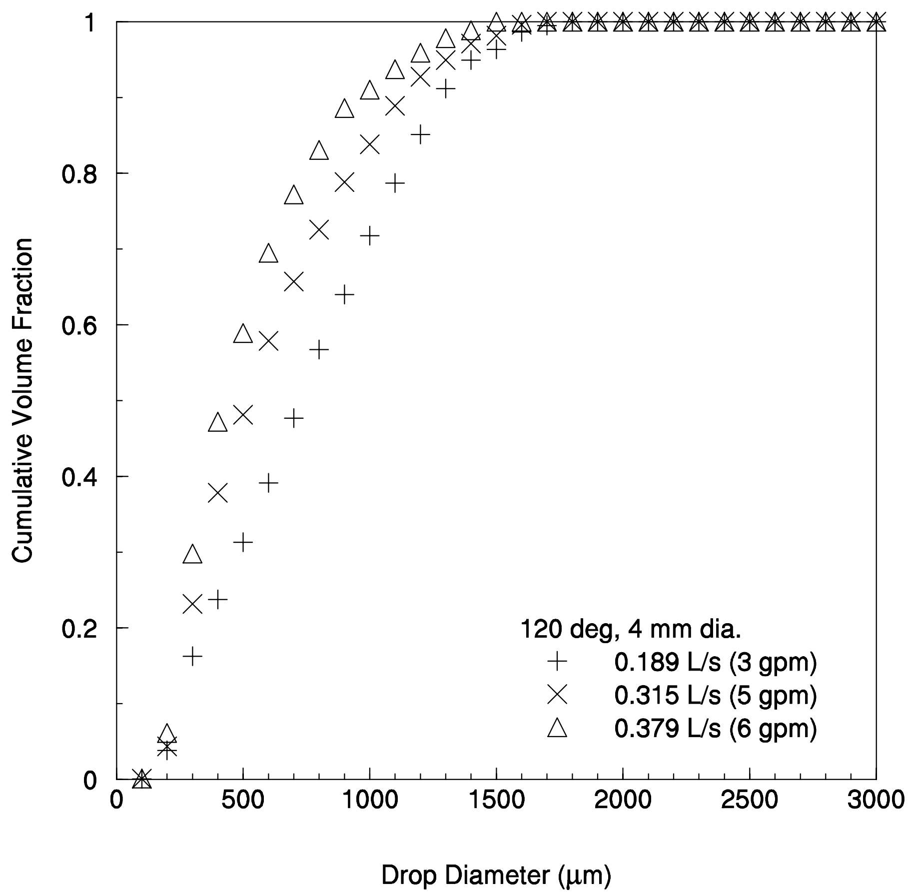

Figure E-3. Droplet cumulative water volume fraction function for a 4 mm nominal diameter orifice sprinkler with a 120 degree strike plate.

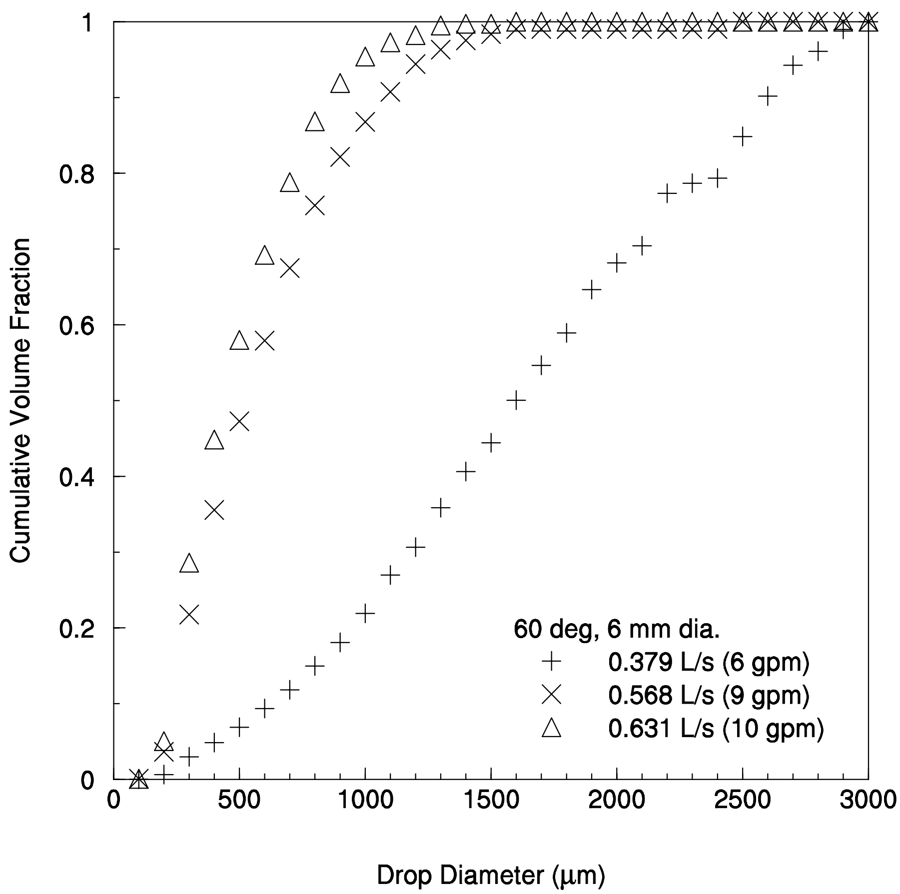

Figure E-4. Droplet cumulative water volume fraction function for a 6 mm nominal diameter orifice sprinkler with a 60 degree strike plate.

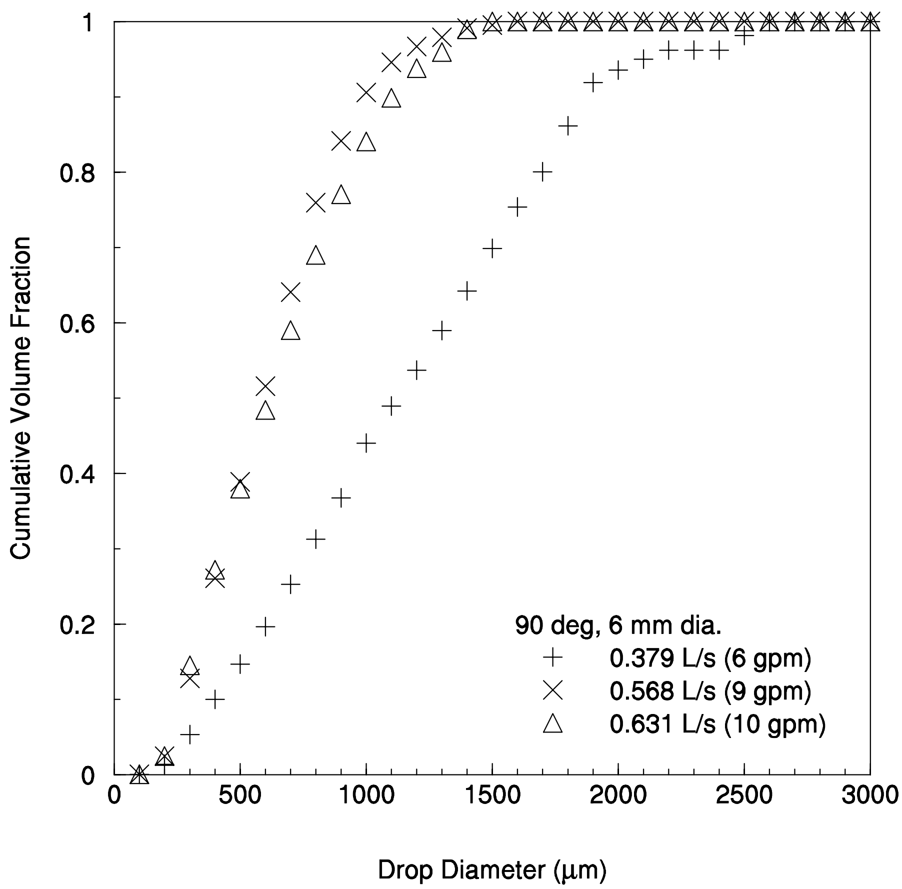

Figure E-5. Droplet cumulative water volume fraction function for a 6 mm nominal diameter orifice sprinkler with a 90 degree strike plate.

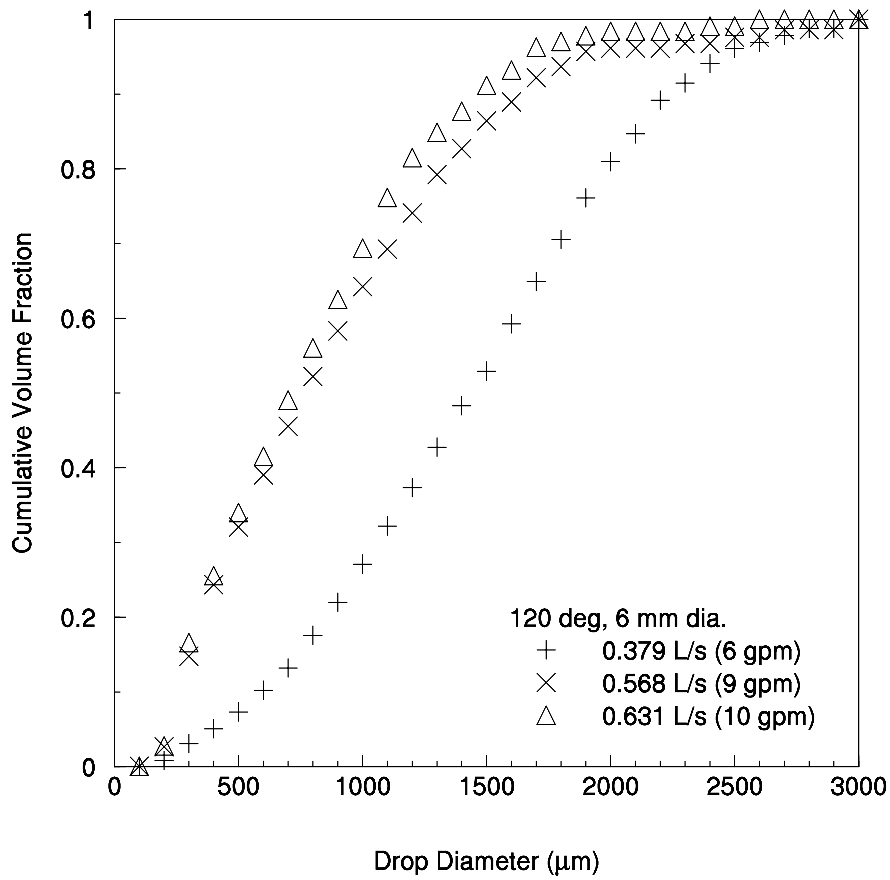

Figure E-6. Droplet cumulative water volume fraction function for a 6 mm nominal diameter orifice sprinkler with a 120 degree strike plate.

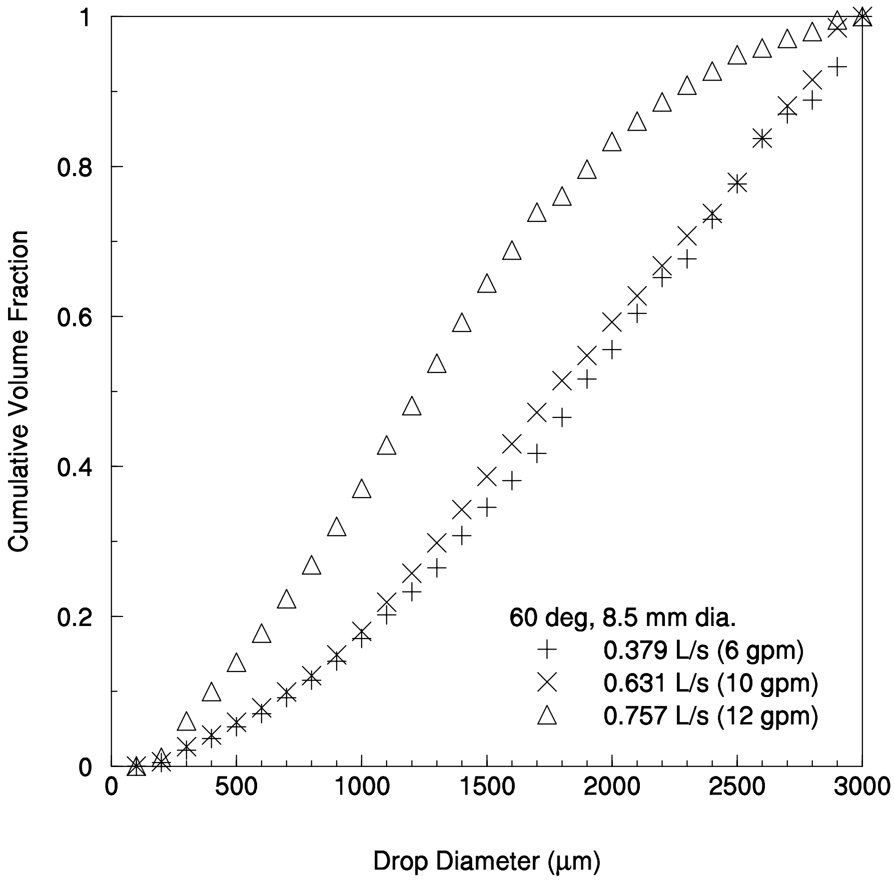

Figure E-7. Droplet cumulative water volume fraction function for a 8.5 mm nominal diameter orifice sprinkler with a 60 degree strike plate.

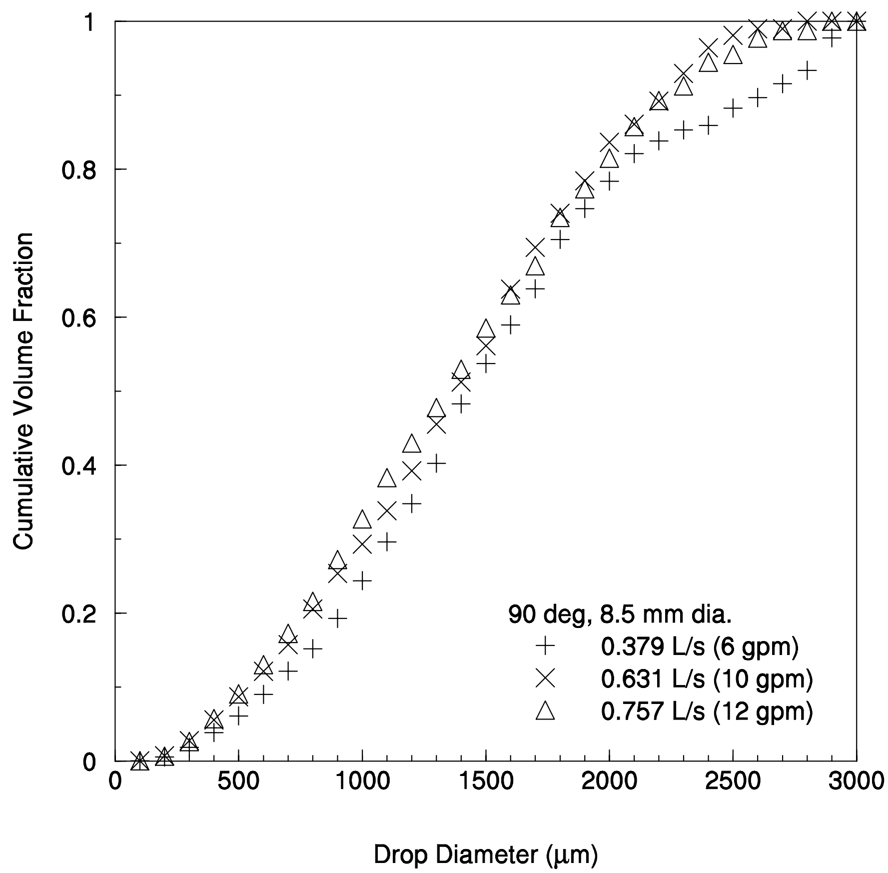

Figure E-8. Droplet cumulative water volume fraction function for a 8.5 mm nominal diameter orifice sprinkler with a 90 degree strike plate.

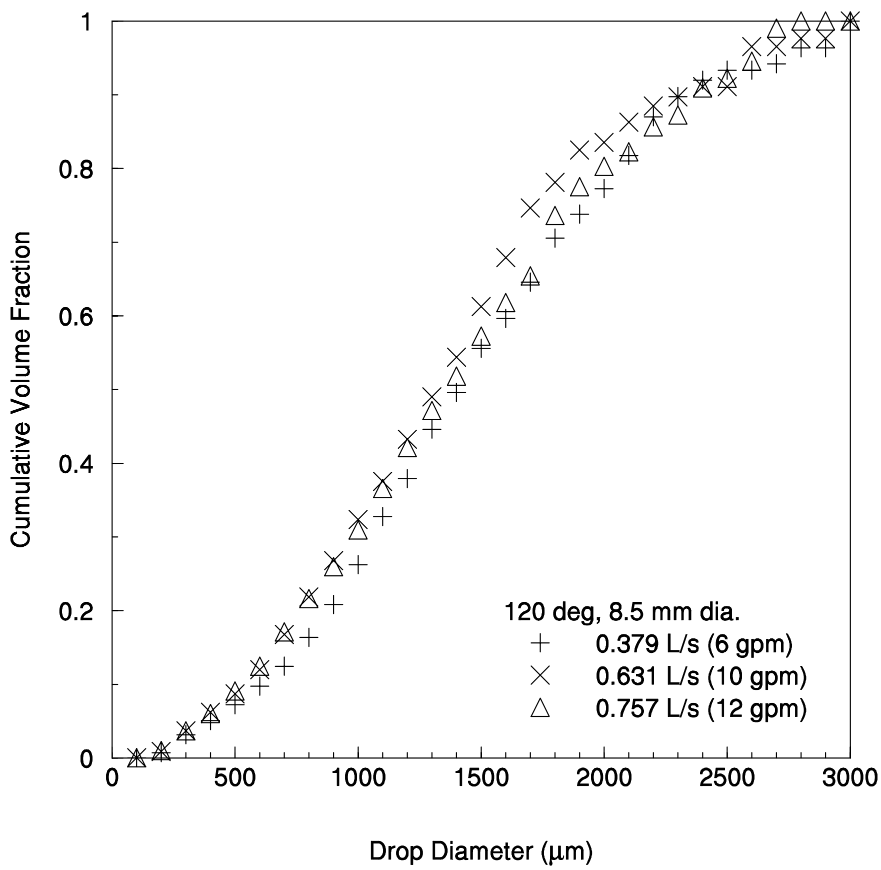

Figure E-9. Droplet cumulative water volume fraction function for a 8.5 mm nominal diameter orifice sprinkler with a 120 degree strike plate.

Table E-6. Sprinkler orifice Reynolds and Weber numbers for the operating condition combinations.

Re	We	strike angle (deg)	orifice dia. (mm)	flow (L/s)	flow (gpm)
5.78E+04	5.20E+03	60	8.5	0.37854	6
5.78E+04	5.20E+03	90	8.5	0.37854	6
5.78E+04	5.20E+03	120	8.5	0.37854	6
6.03E+04	1.18E+04	60	4	0.18927	3
6.03E+04	1.18E+04	90	4	0.18927	3
6.03E+04	1.18E+04	120	4	0.18927	3
8.12E+04	1.44E+04	60	6	0.37854	6
8.12E+04	1.44E+04	90	6	0.37854	6
8.12E+04	1.44E+04	120	6	0.37854	6
9.63E+04	1.44E+04	60	8.5	0.6309	10
9.63E+04	1.44E+04	90	8.5	0.6309	10
9.63E+04	1.44E+04	120	8.5	0.6309	10
1.16E+05	2.08E+04	60	8.5	0.75708	12
1.16E+05	2.08E+04	90	8.5	0.75708	12
1.16E+05	2.08E+04	90	8.5	0.75708	12
1.16E+05	2.08E+04	120	8.5	0.75708	12
1.22E+05	3.25E+04	60	6	0.56781	9
1.22E+05	3.25E+04	90	6	0.56781	9
1.22E+05	3.25E+04	120	6	0.56781	9
1.00E+05	3.28E+04	60	4	0.31545	5
1.00E+05	3.28E+04	90	4	0.31545	5
1.00E+05	3.28E+04	120	4	0.31545	5
1.35E+05	4.01E+04	60	6	0.6309	10
1.35E+05	4.01E+04	90	6	0.6309	10
1.35E+05	4.01E+04	120	6	0.6309	10
1.21E+05	4.72E+04	60	4	0.37854	6
1.21E+05	4.72E+04	90	4	0.37854	6
1.21E+05	4.72E+04	120	4	0.37854	6

Table E-7. Errors in sprinkler flow rate prediction from images.

strike angle (deg)	orifice dia. (mm)	flow rate (gpm)	flow rate (L/s)	sprinkler flow (gpm) calculated	measured	flow error (gpm)	Flow Error %
60	4	3	0.189	4.201	3	0.400	40.0
60	4	5	0.315	6.142	5	0.228	22.8
60	4	6	0.379	5.250	6	-0.125	12.5
60	6	6	0.379	10.402	6	0.734	73.4
60	6	9	0.568	5.555	9	-0.383	38.3
60	6	10	0.631	4.903	10	-0.510	51.0
60	8.5	6	0.379	8.853	6	0.476	47.6
60	8.5	10	0.631	12.806	10	0.281	28.1
60	8.5	12	0.757	11.755	12	-0.020	2.0
90	4	3	0.189	3.668	3	0.223	22.3
90	4	5	0.315	7.975	5	0.595	59.5
90	4	6	0.379	6.441	6	0.074	7.4
90	6	6	0.379	6.149	6	0.025	2.5
90	6	9	0.568	8.847	9	-0.017	1.7
90	6	10	0.631	13.796	10	0.380	38.0
90	8.5	6	0.379	10.740	6	0.790	79.0
90	8.5	10	0.631	12.548	10	0.255	25.5
90	8.5	12	0.757	15.050	12	0.254	25.4
90	8.5	12	0.757	10.768	12	-0.103	10.3
120	4	3	0.189	3.328	3	0.109	10.9
120	4	5	0.315	6.037	5	0.207	20.7
120	4	6	0.379	6.566	6	0.094	9.4
120	6	6	0.379	11.650	6	0.942	94.2
120	6	9	0.568	11.607	9	0.290	29.0
120	8.5	6	0.379	7.026	6	0.171	17.1
120	8.5	10	0.631	10.608	10	0.061	6.1
120	8.5	12	0.757	14.100	12	0.175	17.5

REFERENCES

Adrian, R.J. "Particle-Imaging Techniques for Experimental Fluid Mechanics." *Annual Review of Fluid Mechanics*, 1991. 23: 261-304.

Adrian, R.J. "Dynamic Ranges of Velocity and Spatial Resolution of Particle Image Velocimetry." *Meas. Sci. Technol.* 8 (1997) pp.1393-1398.

Bachalo, W.D. "Spray Diagnostics for the Twenty-First Century." *Atomization and Sprays*, Vol. 10, pp. 439-474, 2000.

Batchelor, G.K. An Introduction to Fluid Dynamics. The University Press, Cambridge, 1967.

Baum, H.R.; McCaffrey, B.J. "Fire Induced Flow Field: Theory and Experiment." Proceedings. Fire Safety Science. 2nd International Symposium. Tokyo, Japan, June 13-17, 1988. Hemisphere Publishing Company, 1989.

Biberman, L.M., ed. Perception of Displayed Information. Plenum Press, New York, 1973.

Cao, Z.M.; Nishino, K.; Torii, K. "Measurement of Size and Velocity of Water Spray Particles Using Laser-Induced Fluorescence Method." Proceedings of the 2nd Pacific Symposium on Flow Visualization, PSFVIP-2, Honolulu, USA, May 16-19, 1999.

Chan, T.S. "Measurements of Water Density and Drop Size Distributions of Selected ESFR Sprinklers." *Journal of Fire Protection Engineering*, 6(2), 1994, pp 79-87.

Dodge, L.G. "Comparison of Performance of Drop-Sizing Instruments." *Applied Optics*, Vol. 26, No. 7, April 1987.

Domann, R. and Hardalupas, Y. "Spatial Distribution of Fluorescence Intensity Within Large Droplets and its Dependence on Dye Concentration." *Applied Optics*, Vol. 40, No. 21, 20 July 2001.

Domann, R. and Hardalupas, Y. "A Study of Parameters that Influence the Accuracy of the Planar Droplet Sizing (PDS) Technique." *Part. Syst. Charact.* 18(2001) 3-11.

Downing, C.G. "The Evaporation of Drops of Pure Liquids at Elevated Temperatures: Rates of Evaporation and Wet-Bulb Temperatures." *AIChE Journal*, Vol. 12, No. 4, pp.760-766, 1966.

Dundas, P.H. "The Scaling of Sprinkler Discharge: Prediction of Drop Size." Prepared for Factory Mutual Research Corporation, Norwood, Massachusetts. FMRC Serial No. 18792, RC73-T-40, June 1974.

Eisenklam, P.; Arunachalam, S.A.; Weston, J.A. "Evaporation Rates and Drag Resistance of Burning Drops." Eleventh International Symposium on Combustion, pp. 715-727, 1967.

Everest, D.; Atreya, A. "PIV Measurements in Large-Scale Sprinkler Flows." Proceedings of the 2nd Pacific Symposium on Flow Visualization and Image Processing (PSFVIP-2), Honolulu, HI, USA, May 16-19, 1999.

Everest, D.; Atreya, A. "Simultaneous Measurements of Drop Size and Velocity in Large-Scale Sprinkler Flows Using Laser-Induced Fluorescence and Mie Scattering." *Journal of Flow Visualization and Image Processing.* (JFVIP) Vol. 10, pp. 1-19, 2003.

Fujicolor Portrait film, NPZ 800 Professional, Data Sheet, AF3-089E, Fuji Photo Film Co., Ltd., Tokyo, Japan 2001.

Guar, V.; Everest, D.; Atreya, A. "A Non-Intrusive Dye-Based Color Differentiation Technique for Particle Imaging Velocimetry (PIV) in Large-Scale Air Flows." Proceedings of ASME, 34th National Heat Transfer Conference, Pittsburgh, Pennsylvania, August 20-22, 2000.

Gunn, R. and Kinzer, G.D. "The Terminal Velocity of Fall for Water Droplets in Stagnant Air." *Journal of Meteorology*, Vol.6, 1949.

Herpfer, D.C. and Jeng, S. "Planar Measurements of Droplet Velocities and Sizes Within a Simplex Atomizer." *AIAA Journal*, Vol. 35 No. 1. January. pp. 127-132. 1997.

Hinds, W.C. Aerosol Technology: Properties, Behavior, and Measurement of Airborne Particles. 2nd Ed. John Wiley& Sons, Inc. New York, 1999

Holman, J.P. Experimental Methods for Engineers. McGraw-Hill Book Company, New York, 1989.

Huang, J.C.P. "The Break-up of Axisymmetric Liquid Sheets." *Journal of Fluid Mechanics*, Vol. 43, part 2, pp. 305-319, 1970.

Hubbard, G.L.; Denny, V.E.; Mills, A.F. "Droplet Evaporation: Effects of Transients and Variable Properties." *International Journal of Heat and Mass Transfer*, Vol. 18, pp. 1003-1008, 1975.

Kadambi, J.R., Martin, W.T., Amirthaganesh, S., and Wernet, M.P. "Particle sizing using Particle Imaging Velocimetry for two-phase flows." *Powder Technology* Vol. 100. pp. 251- 259. 1998.

Karter Jr., M.J., "Fire Loss in the United States During 2001." National Fire Protection Association, Quincy, MA November 2002.

Kincaid, D.C.; Soloman, K.H.; Oliphant, J.C. "Drop Size Distributions for Irrigation Sprinklers." Transactions of the American Society of Agricultural Engineers (ASAE), Vol. 39, No. 3, pp. 839-845, 1996.

Kodak Pro Films Technical Data, Pro 1000 PMZ, Eastman Kodak Company, Publication E-182, 1997

Kuo, K.K. Principles of Combustion. John Wiley & Sons, New York, 1986.

Lapple, C.E. and Shepherd, C.B. "Calculation of Particle Trajectories." *Industrial and Engineering Chemistry*, Vol. 32, No. 5, pp. 605-617, 1940.

Law, C.K. "The Theory for Monodisperse Spray Vaporization in Adiabatic and Isothermal Systems." *International Journal of Heat and Mass Transfer*, Vol. 18, pp. 1285-1292, 1975.

Law, C.K. "Adiabatic Spray Vaporization with Droplet Temperature Transient." *Combustion Science and Technology*, Vol 15, pp. 65-74, 1977.

Law, C.K. "Recent Advances in Droplet Vaporization and Combustion." *Prog. Energy Combust. Sci.*, Vol. 8, pp. 171-201, 1982.

Lawson, J.R.; Walton, W.D.; Evans, D.D. "Measurement of Droplet Size in Sprinkler Sprays." NBSIR 88-3715, National Bureau of Standards, Center for Fire Research, Gaithersburg, MD, February, 1988.

Lefebvre, A.H. Atomization and Sprays. Hemisphere Publishing Corporation, New York, 1989.

Madrzykowski, D.; Vettori, R.L. "Simulation of the Dynamics of the Fire at 3146 Cherry Road NE, Washington, D.C., May 30, 1999." NISTIR 6510, National Institute of Standards and Technology, Gaithersburg, MD, April, 2000.

McCaffrey, B.J.; Heskestad, G. "Robust Bidirectional Low-Velocity Probe for Flame and Fire Applications." Brief Communications. *Combustion and Flame*, Vol. 26, No. 1, pp. 125-127, February 1976.

McGrattan, K.B.; Baum, H.R.; Rehm, R.G.; Hamins, A.; Forney, G.P.; Prasad, K.; Floyd, J.E.; Hostikka, S. "Fire Dynamics Simulator (Version 3) - Technical Reference Guide." National Institute of Standards and Technology, Gaithersburg, MD, NISTIR 6783, November 2002.

McGrattan, K.B.; Forney, G.P.; Prasad, K.; Floyd, J.E.; Hostikka, S. "Fire Dynamics Simulator (Version 3) - User's Guide." National Institute of Standards and Technology, Gaithersburg, MD, NISTIR 6784, November 2002.

McGrattan, K.B.; Hamins, A.; Blevins, L.G. "Using Bench Scale Fire Measurements in Large Scale Simulations." NISTIR 6242, National Institute of Standards and Technology, Gaithersburg, MD, October 1998.

McGrattan, K.B.; Hamins, A.; Evans, D.D. "Sprinklers, Vent, and Draft Curtain Interaction: Modeling and Experiment." Proceedings. Fire Suppression and Detection Research Application Symposium. Research and Practice: Bridging the Gap. National Fire Protection Research Foundation. pp. 98-106. Orlando, Florida, February, 25-27, 1998.

Media Cybernetics, Image-Pro Plus Reference Guide, Silver Spring, MD. 2001.

Milke, J.A., Meeting Facilitator, "National Residential Fire Sprinkler Initiative, United States Fire Administration, Summary of Meeting, April 9-10, 2003" United States Fire Administration, Emmitsburg, MD, May 2003.

Narasimhan, C. and Gauvin, W.H. "Heat and Mass Transfer to Spheres in High-Temperature Surroundings." *The Canadian Journal of Chemical Engineering*, Vol. 45, pp. 181-188, August 1967.

Photodo AB, Lund, Sweden. www.photodo.com

Prahl, J.M. and Wendt, B. "Discharge Distribution Performance for an Axisymmetric Model of a Fire Sprinkler Head." *Fire Safety Journal*, 14 (1988) pp. 101-111.

Putorti Jr., A.D.; Belsinger, T.D.; Twilley, W.H. "Determination of Water Spray Drop Size and Speed from a Standard Orifice, Pendent Spray Sprinkler." FR4003, National Institute of Standards and Technology, Gaithersburg, MD, September, 1995, revised May 1999.

Putorti Jr., A.D.; Belsinger, T.D.; Twilley, W.H. "Determination of Water Spray Drop Size and Velocity from a Low Pressure, High Momentum, Water Mist Nozzle." FR4000, National Institute of Standards and Technology, Gaithersburg, MD, May, 1995.

Putorti Jr., A.D., Everest, D., and Atreya, A. "Simultaneous Measurements of Drop Size and Velocity in Large-Scale Sprinkler Flows Using Particle Tracking and Laser-Induced Fluorescence." NIST GCR 03-852, National Institute of Standards and Technology, Gaithersburg, MD July 2003.

Renksizbulut, M. and Yuen, M.C. "Experimental Study of Droplet Evaporation in a High-Temperature Air Stream." Transactions of the ASME, Vol. 105, pp. 384-388, May 1983.

Renksizbulut, M. and Yuen, M.C. "Numerical Study of Droplet Evaporation in a High-Temperature Stream." Transactions of the ASME, Vol. 105, pp. 389-397, May 1983.

Rohr, K.D. "U.S. Experience with Sprinklers." National Fire Protection Association, Quincy, MA, September 2001.

Sheppard, D.T., "Spray Characteristics of Fire Sprinklers." National Institute of Standards and Technology, NIST GCR 02-838, June 2002.

Sheppard, D.T., Gandhi, P.D., and Lueptow, R.M. "Predicting Sprinkler Water Distribution Using Particle Image Velocimetry." Proceedings. Research and Practice: Bridging the Gap. Fire Suppression and Detection Research Application Symposium. Fire Protection Research Foundation. February 23-25, 2000, Orlando, Florida, pp. 354-364, 2000.

Sheppard, D.T. and Lueptow, R.M. "Characterization of Fire Sprinkler Sprays Using Particle Imaging Velocimetry." Submitted to *Atomization and Sprays*, June 2003.

Smith, W.J. Modern Optical Engineering. McGraw-Hill, New York, third ed., 2000.

Solomon, K.H.; Zoldoske, D.F.; Oliphant, J.C. "Laser Optical Measurement of Sprinkler Drop Sizes." CATI Publication #961101, Center For Irrigation Technology, California Agricultural Technology Institute, California State University, Fresno, California, 1996.

Spalding, D.B. "Experiments on the Burning and Extinction of Liquid Fuel Spheres." *Fuel*, Vol. 32, pp. 169-185, 1953.

Spalding, D.B. Some Fundamentals of Combustion. Butterworths Scientific Publications, London, 1955.

Sparrow, E.M. and Gregg, J.L. "The Variable Fluid-Property Problem in Free Convection." *Transactions of the ASME*, Vol. 80, pp. 879-886, 1958.

Stengele, J.; Prommersberger, K.; Willmann, M.; Wittig, S. "Experimental and Theoretical Study of One- and Two- Component Droplet Vaporization in a High Pressure Environment." *International Journal of Heat and Mass Transfer*, Vol. 42, pp. 2683-2694, 1999.

Suiter, H.R.. Star Testing Astronomical Telescopes: A Manual for Optical Evaluation and Adjustment. Willmann-Bell, Richmond, VA, 1994.

Sujith, R.I.; Waldherr, G.A.; Jagoda, J.I.; Zinn, B.T. "On the Effect of Evaporation on Droplet Drag." *Journal of Fluids Engineering, Transactions of the ASME*, Vol. 118, pp. 862-864, December 1996.

Taylor, B.N. and Kuyatt, C.E. "Guidelines for Evaluating and Expressing the Uncertainty of NIST Measurement Results." NIST Technical Note 1297, 1994 Ed. National Institute of Standards and Technology, Gaithersburg, MD, September 1994.

Taylor, G. "The Dynamics of Thin Sheets of Fluid. I. Water Bells." *Proc. Royal Soc*. A, 253 (1959) pp. 289-295.

Taylor, G. "The Dynamics of Thin Sheets of Fluid. II. Waves on Fluid Sheets." *Proc. Royal Soc.* A, 253 (1959) pp. 296-312.

Taylor, G. "The Dynamics of Thin Sheets of Fluid. III. Disintegration of Fluid Sheets." *Proc. Royal Soc.* A, 253 (1959) pp. 313-321.

Taylor, G. "Formation of Thin Flat Sheets of Water." *Proc. Royal Soc.* A, 259 (1960) pp. 1-17.

Villermaux, E. and Clanet, C. "Life of a Flapping Sheet." *J. Fluid Mech* (2002) Vol. 462, pp. 341-363.

Walton, W.D.; McGrattan, K.B. "ALOFT-FT A Large Outdoor Fire Plume Trajectory Model - Flat Terrain Version 3.04." National Institute of Standards and Technology, Gaithersburg, MD. CD-ROM, NIST SP 924, 1998.

Walton, W.D.; McGrattan, K.B.; Mullin, J.V. "ALOFT-PC: A Smoke Plume Trajectory Model for Personal Computers." Arctic and Marine Oilspill Program (AMOP) Technical Seminar, 19th. Volume 2. Proceedings. June 12-14, 1996, Alberta, Canada, pp. 987-997, 1996.

Wendt, B. and Prahl, J.M. "Discharge Distribution Performance for an Axisymmetric Model of a Fire Sprinkler Head." NBS-GCR-86-517. Sponsored by U.S. Department of Commerce, National Bureau of Standards, Center for Fire Research, Gaithersburg, MD, 1986.

Widmann, J.F. "Characterization of a Residential Fire Sprinkler Using Phase Doppler Interferometry." NISTIR 6561, National Institute of Standards and Technology, Gaithersburg, MD, August, 2000.

Williams, C.S. and Becklund, O.A. Introduction to the Optical Transfer Function. John Wiley & Sons, New York, 1989.

You, H.Z. “Investigation of Spray Patterns of Selected Sprinklers with the FMRC Drop Size Measuring System.” Fire Safety Science-Proceedings of the First International Symposium, 1986, pp. 1165-1176.

Yuen, M.C. and Chen, L.W. “On Drag of Evaporating Liquid Droplets.” *Combustion Science and Technology*, Vol. 14, pp. 147-154, 1976.

Yuen, M.C. and Chen, L.W. “Heat-Transfer Measurements of Evaporating Liquid Droplets.” *International Journal of Heat and Mass Transfer*, Vol. 21, pp. 537-542, 1978.